Distribution Agreement

In presenting this thesis or dissertation as a partial fulfillment of the requirements for an advanced degree from Emory University, I hereby grant to Emory University and its agents the non-exclusive license to archive, make accessible, and display my thesis or dissertation in whole or in part in all forms of media, now or hereafter known, including display on the world wide web. I understand that I may select some access restrictions as part of the online submission of this thesis or dissertation. I retain all ownership rights to the copyright of the thesis or dissertation. I also retain the right to use in future works (such as articles or books) all or part of this thesis or dissertation.

Signature:

_____ _____

John D. Rolston Date

Multielectrode Interactions with the Normal and Epileptic Brain

By

John D. Rolston
Doctor of Philosophy

Graduate Division of Biological and Biomedical Science
Neuroscience

_____	_____
Robert E. Gross, M.D., Ph.D. Advisor	Steve M. Potter, Ph.D. Advisor
_____	_____
Elizabeth A. Buffalo, Ph.D. Committee Member	Brian Litt, M.D. Committee Member
_____	_____
Raymond Dingledine, Ph.D. Committee Member	Donald G. Rainnie, Ph.D. Committee Member

Accepted:

_____
Lisa A. Tedesco, Ph.D.
Dean of the James T. Laney School of Graduate Studies

_____
Date

Multielectrode Interactions with the Normal and Epileptic Brain

By

John D. Rolston
B.S., Columbia University, 2003

Advisors:
Robert E. Gross, M.D., Ph.D., and Steve M. Potter, Ph.D.

An abstract of
A dissertation submitted to the Faculty of the
James T. Laney School of Graduate Studies of Emory University
in partial fulfillment of the requirements for the degree of
Doctor of Philosophy in Neuroscience

Graduate Division of Biological and Biomedical Science
Neuroscience Program
2009

Abstract

Multielectrode Interactions with the Normal and Epileptic Brain

By John D. Rolston

Multielectrode recordings provide the unique ability to observe the brain's dynamics at multiple scales and from multiple locations. Using multielectrode arrays, I have carried out several investigations of both the normal and epileptic brain, and developed new technology to more easily interact with neural tissue.

First, using dissociated cultures of cortical neurons, I used a template-matching algorithm to uncover evidence of precisely timed repeating sequences of neuronal action potentials. These sequences, which have been observed in the intact brain and brain slices, are a potential mechanism of neural information processing.

My other experiments involved freely moving animals. Based on prior work with cell cultures, it is believed that closed-loop brain stimulation can suppress epileptiform activity in animals with seizures. Before this hypothesis could be tested, I had to develop a new recording and stimulation system capable of closed-loop microstimulation, along with new signal processing algorithms to improve the data we observed. The resulting system, NeuroRighter, is a freely available, open source platform with several advantages over existing commercial systems (none of which is capable of closed-loop stimulation).

With the new recording and stimulation system in place, I was able to characterize in detail the field potential and action potential dynamics underlying interictal spikes and seizures in the tetanus toxin model of temporal lobe epilepsy. Specifically, I found evidence of high-frequency oscillations in this model, which were restricted to interictal spikes and commensurate with entrained bursts of multiunit activity.

While distributed stimulation was ultimately ineffective at suppressing seizures and epileptiform bursting with the parameters we tested, we were nevertheless able to control neural activity in epileptic animals in novel ways. In particular, we provided the first evidence that high-frequency oscillations could be directly evoked with microstimulation. Such stimulation has potential applications in presurgical screening for epileptiform onset zones.

Multielectrode Interactions with the Normal and Epileptic Brain

By

John D. Rolston
B.S., Columbia University, 2003

Advisors:
Robert E. Gross, M.D., Ph.D., and Steve M. Potter, Ph.D.

A dissertation submitted to the Faculty of the
James T. Laney School of Graduate Studies of Emory University
in partial fulfillment of the requirements for the degree of
Doctor of Philosophy in Neuroscience

Graduate Division of Biological and Biomedical Science
Neuroscience Program
2009

Acknowledgements

I didn't expect to receive a PhD in neuroscience when I started at Emory. I entered the MD/PhD program as a physics student, set to study two-photon microscopy, but quickly changed to bioengineering, then biomedical engineering as I worked through the first two years of med school. This is symptomatic of a life of liking too many things. Even as I applied to college during high school, I sent half my applications requesting a major in astrophysics, and the other half computer science (computer science won). This probably explains why neither an MD nor PhD alone sounded fitting when I applied to graduate school.

But despite the peregrinations, the signs pointing toward neuroscience were always there. I remember taking an independent study course in high school, where I wrote one of my two term papers on consciousness (the other on astrophysics). In college, still interested in the brain, I did a research internship at the NIH, where I was advised by Dr. Adrian Danek, my first example of a clinician-scientist. Adrian's warmth, patience, and trust were remarkable, especially considering how inexperienced and young I was. He was my first scientific (and clinical) mentor, and I am deeply indebted—he showed me that the path I'm on existed.

With that encouragement, I applied again to the NIH for an internship the following summer. Adrian had returned to Germany, so I instead worked for Dr. Jason Kerr, in Dr. Dietmar Plenz's lab. Jason was every bit as fantastic as Adrian. He is one of the most gifted and honest scientists I know, and one of the best friends I've had. I don't think it's a stretch to say that without the opportunities he gave me, I wouldn't be where I am today.

Finishing college, I knew that I wanted to continue in neuroscience, but I didn't think a neuroscience program would prepare me for the brand of quantitative and computational neuroscience I subscribed to. Adrian and I worked on fMRI, and many of the neuroscientists and psychologists around us were hindered by the mathematics and programming involved in imaging data analysis. Those of us with quantitative backgrounds were sought after for help and collaborations. Working with Jason on calcium imaging, it was clear that carrying out the kind of analysis we were interested in, we'd need sophisticated quantitative machinery.

I wanted to study the brain, but I wanted to study it with the tools of physics and engineering. So I decided to get my PhD in one of these disciplines, rather than neuroscience. It wasn't until after I'd started my PhD in earnest that I realized how myopic I'd been. At this point, I had joined Dr. Steve Potter's lab and had begun taking classes in biomedical engineering. It became apparent that not only were the classes in BME softballs, but the items covered were not what I wanted to learn (the curriculum has since changed, so this analysis is dated). Worrying about my choice, I got unanimous advice from Steve and Dr. Allan Levey (former director of the MD/PhD program at Emory): if you want to learn something, teach it to yourself. You don't need classes when you have a library, the Internet, and two universities full of smart people.

With the patient support of the Emory Neuroscience program, I switched from BME to neuroscience in the winter between my first semesters. The flexibility and understanding of the MD/PhD program, especially Mary Horton and Dr. Chuck Parkos, was (and is) phenomenal. During my medical school interviews, it was clear that Emory was different from other institutions—the program seemed more engaged with the students, more willing to help them and more caring. Since joining Emory, these impressions were

borne out. The MD/PhD program has always been accessible and responsive, and never let me down.

Over the following four years in Steve's lab, I've been fortunate to work with wonderful people. Foremost is Steve himself. Two of Steve's best qualities are his honesty and openness. These traits are not common in the scientists I've met, but are the only way to comport yourself if you're truly involved in science for selfless reasons. In addition, Steve has been an extraordinarily supportive mentor, not only offering independence, but trusting me with it. Through Steve's lab, I had the fortune to discuss science with Radhika Madhavan, Doug Bakkum, Zenas Chao, Daniel Wagenaar, and Nathan Killian. Each helped me in my work at one point or another, and all became friends over time.

When I began my thesis project in earnest, it was because Steve had suggested I search for a scientist at Emory who knew about epilepsy. Through Dr. Ray Dingledine, I was pointed to Dr. Robert Gross. Bob is an MD/PhD neurosurgeon with a broad, encompassing perspective on science, medicine, and industry, and a great sense of humor. Despite a schedule packed with surgery and the management of essentially two unrelated labs, Bob has always stayed actively engaged in my projects, and is someone I turn to for advice almost weekly. What impresses me most about Bob is the vitality he shows in his career. Bob is managing two labs—one molecular biology and the other electrophysiology— and is involved with clinical research and trials. This is in addition to operating, seeing patients, teaching residents, and raising a family. Bob has become a great friend over the years, and I can't thank him enough for his help.

Through Bob's lab, I've met several others to whom I owe gratitude. Dr. Claire-Anne Gutekunst introduced me to hands-on biology, and, besides being a good friend, is someone who's always been willing to help me in my project in any way she could. Lissa

Jackson has been instrumental in getting things done at Emory, and has also become a good friend.

Throughout my thesis, I've been lucky to work with and talk with many other individuals at Emory and Georgia Tech. All the members of my thesis committee—Drs. Tig Rainnie, Beth Buffalo, Ray Dingledine, and Brian Litt (who's at UPenn)—have offered critical advice and support. I've also had the benefit of working in Tig's lab with Teresa Madsen. Teresa was starting extracellular recording from freely moving animals about the same time I was, and she and Tig allowed me to waste their time by dissecting their rig and asking their tech support guy questions. Their help and friendship was crucial at multiple points during my time at Emory.

At Tech, I've had the good fortune of meeting and working with Edgar Brown and Jim Ross. Edgar and Jim have always been willing to help me with electronics and engineering questions, and have become close friends over multiple mugs of maté.

I'm especially grateful to my fellow MD/PhD students, especially Orion Keifer and Nealen Laxpati. Both have helped me with my experiments over the years, lending me a hand when I was bogged down with data analysis, programming, or grant writing. Without their help my PhD would likely have been lonelier and definitely longer.

Outside Emory and Georgia Tech, I'm indebted to Dr Partha Mitra of Cold Spring Harbor Laboratory. After taking Partha's class in Neuroinformatics at Woods Hole, he invited me back as first a TA, then faculty. Those opportunities and the interactions they fostered have become an essential ingredient of my work.

Outside of the lab and academia, I have to thank my friends, family, and my wife, Erica, for all of their support. Erica is my best friend and has provided unconditional love and encouragement from my first day of medical school through the end. She's sustained me through this all, and I love her for it.

Lastly, and most importantly, I owe my parents everything. They remain my greatest role models. My every accomplishment is a result of their support.

This work was funded by the Wallace H. Coulter Foundation (http://www.whcf.org/), the Epilepsy Research Foundation (http://www.epilepsy.com/etp/scientific_research), a University Research Council grant from Emory University (http://www.emory.edu), the National Institute of General Medical Sciences (NIGMS; http://www.nigms.nih.gov/) (GM08169), and, from the National Institute of Neurological Disorders and Stroke (NINDS; http://www.ninds.nih.gov/), a Ruth L. Kirschstein National Research Service Award (NS060392), a translational research fellowship (NS007480), a career development award to Dr. Robert E. Gross (NS046322), and a research grant to Drs. Steve M. Potter and Robert E. Gross (NS054809). The funders had no role in study design, data collection and analysis, or preparation of the manuscript.

Brief Table of Contents

Table of Contents

Table of Figures

Chapter 1

Introduction

The human brain is arguably the most dynamic and complex organ in the body. Perhaps this is also why it is responsible for many of the body's—and mind's—most devastating diseases: schizophrenia, Alzheimer's, depression, addiction, and the rest. As scientists, we wish to understand how the brain's neural tissue, a mixture of known biochemical constituents (proteins, lipids, sugars), routinely carries out its extraordinary feats—feats like vision, movement, speech—and their elaborations—art, dance, literature. But we also want to learn what occurs when these functions are impaired. What is happening in the brain with schizophrenia or autism that makes it different?

Undergirding both questions is a fundamental desire to interact with—and control—the brain. Whether through new techniques to interrogate the brain (like the patch clamp or gene arrays), or through pharmaceuticals and medical devices, we have developed an array of means for both listening to the brain, and talking back. Many of these innovations are undeniably beneficial, like levodopa for Parkinson's disease; others more equivocal, like organophosphates or drugs of abuse.

Interestingly, this last aim of interacting with the brain is pursued in disjoint trajectories. That is, technologies are created to observe the brain—magnetic resonance imaging, electroencephalography, electron microscopy—and separate technologies are created to alter the brain—pharmaceuticals, brain stimulators, gene therapy. Truly interactive systems are uncommon, despite awareness of the potential benefits. The entire field of cybernetics, for example, was founded upon the idea that feedback is essential for understanding complex systems (Wiener, 1948).

Speech—one of the most successful closed-loop systems—is a good example of why feedback is powerful:

> Danny: Do you really want to go and live in that hotel for the winter?
> Wendy: Sure I do. It'll be lots of fun.
> Danny: Yeah, I guess so.[1]

When the first person asks something of the second, the second's answer alters the thinking of the first. The first individual's next comment reflects this. Thinking of this powerful system, it's easy to see how hopeful neuroscience experiments are. Analyzing spontaneous activity, for instance, is like standing mute in front of someone and waiting for them to speak. Stimulus-response experiments are like shouting the same (usually gibberish) phrase at a person and recording his or her perplexed responses.

There are notable exceptions to this tendency toward dichotomizing our interactions with the brain. Some experimental techniques, like the dynamic clamp (Goaillard and Marder, 2006), explicitly rely on real-time bidirectional communication with neurons. Devices similar to implantable cardioverter defibrillators are being used in patients with epilepsy to detect seizures, then respond with therapeutic electrical stimulation (Sun et al., 2008). Most relevant to the research in this dissertation, multiple labs are now developing brain-computer interfaces (BCIs) with bidirectional capabilities (O'Doherty et al., 2009; Rolston et al., 2009b; Venkatraman et al., 2009). A common trait of each of these tools is their complexity—implementing feedback is hard. Even when the technology is in place, hooking it meaningfully into a complex nervous system is even harder. Back to the example above, if you don't know the brain's language, you won't have a meaningful conversation. This is probably why closed-loop systems are still in their infancy, despite their theoretical advantages.

Whatever the current state of technology, scientists and biotechnology companies are always looking for an edge. If it provides an advantage, a new tool will be used. If it is

[1] Dialogue from *The Shining*. Dir. Stanley Kubrik. Warner Brothers Pictures (1980).

made simple to use, more people will take advantage of it. A case study is the discovery and exploitation of green fluorescent protein (GFP). GFP was first isolated from a bioluminescent jellyfish by Shimomura, who had no thoughts of using it as a tracer. But when scientists like Prasher and Chalfie heard of GFP's properties, they saw its utility in several lines of biological research, and quickly began using it to gain insight in cancer and bacteriology. These first uses of GFP were powerful, but demanding and non-trivial to replicate. But precisely because of its utility, GFP has since been incorporated into a large variety of pre-packaged vectors, commercially available from companies like Invitrogen. Closed-loop systems will likely follow similar trajectories before they see similar widespread use.

Three Questions

The concerns outlined above are ultimately the three areas in which neuroscience operates. Work, like the research in this dissertation, always applies to these three questions:

1. How does the brain work?
2. How does the brain *not* work?
3. How can we interact with it? (And more to the point, can we fix the diseased brain?)

These three questions are intertwined. Knowledge of normal and abnormal brain physiology are mutually informative. For example, the patient H.M. taught us about the role of the hippocampus in memory, while the modern neuropathological descriptions of degenerative diseases (amyotrophic lateral sclerosis, Huntington's, frontotemporal dementia, and all others) are only possible on the histological foundation laid by Ramon

y Cajal. Further, beneath every study of normal or abnormal physiology lies technology for interacting with the brain—Ramon y Cajal's histology was only possible with Golgi's silver stain; H.M.'s condition was an unfortunate outcome of a neurological surgery, the medial temporal lobectomy (which is still a crucial tool in treating epilepsy, despite its unintended misuse in this case). Lastly, technology is informed by the physiology it studies. For example, as part of routine pre-surgical workup, sodium amytal is perfused into alternate brain hemispheres (the Wada test) to determine the consequences of a lobectomy on each side—fallout from what H.M. taught us. These interactions are depicted graphically in the figure below.

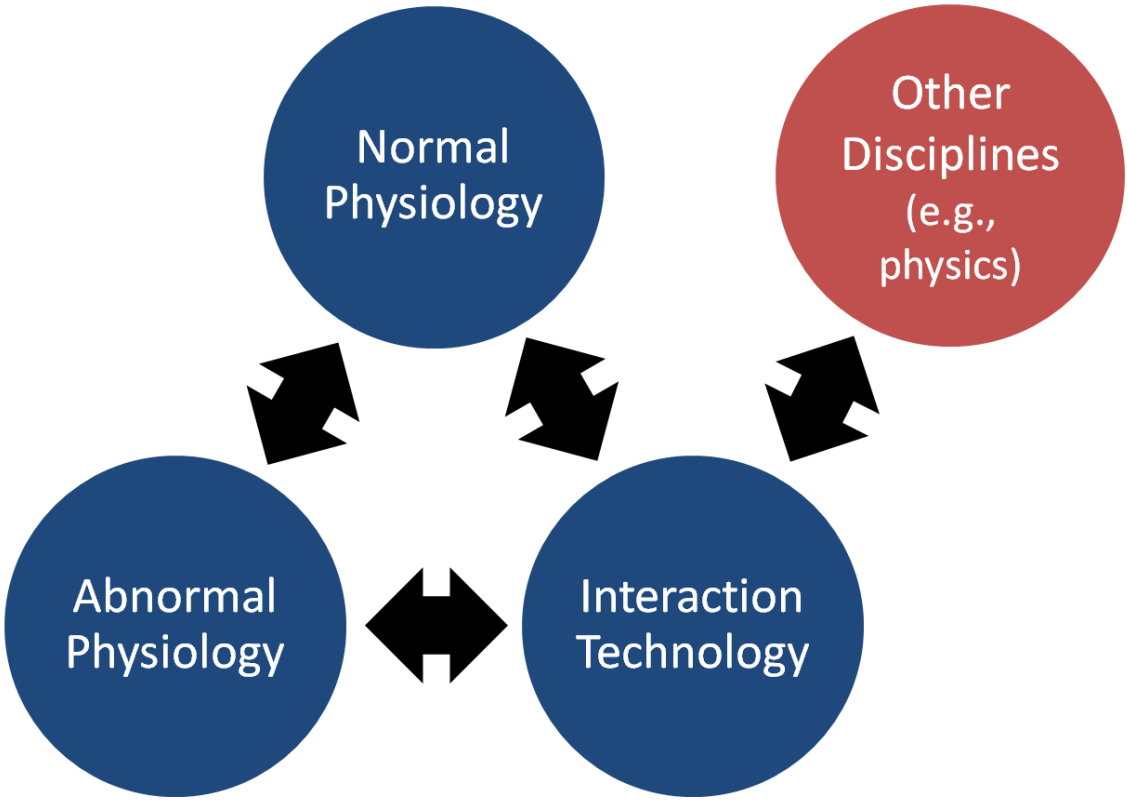

FIGURE 1-1. Normal brain function, abnormal brain function, and the technology for interacting with the brain are entwined pursuits. Other disciplines, like physics, math, and engineering, often exchange most of their ideas by way of new or improved interaction technologies, though there are examples of insights from other disciplines directly illuminating neurophysiology (for example, the discovery of DNA).

The research described in this dissertation is the product of these questions. While the neurophysiological focus varies, the technology used throughout carries a common thread: all of the work herein utilizes multielectrode recording (and often stimulation). Below, the technique of multielectrode recording will be described in more detail, followed by an overview of the remaining chapters.

Multielectrode Recording

Cells that control their intracellular ionic concentrations (as most live cells do) create an electric potential between the cell's interior and exterior: the membrane potential (Kandel et al., 2000). This is true for neurons, glia, liver cells, pancreatic cells, bacteria, and even plant cells. If a cell actively or passively changes these ionic concentrations, the membrane potential changes as well. Some cells have exploited these electrical changes as a means of intra- and extracellular signaling. For example, cardiac myocytes, connected by gap junctions, detect an increased membrane potential with voltage-gated calcium channels that, when opened, release calcium from internal stores and promote contraction of the heart muscle. Neurons have similar voltage-gated ion channels, along with ligand-gated channels and passive channels, providing a rich repertoire of fast signaling capabilities (Hille, 2001). These fast signals, in fact, are what most neuroscientists believe underlie the brain's unique functions. So, making sense of the complex overlapping electrical chatter of the brain's neurons is a primary goal in contemporary neuroscience. Many tools have been developed to this end, and many with the intent of measuring these voltages.

Voltage is always measured between two points; if what is being measured is nonmetallic, these points are called "electrodes" (Faraday, 1834). So the ideal way to measure membrane potential is with one electrode inside the cell, and one outside. And

this is in fact the basis of sharp penetrating electrodes and the patch clamp technique (specifically whole-cell patch clamp).

Since we believe that populations of interacting cells drive behavior, we wish to characterize these interactions. But the difficulty with these intracellular techniques is scale. Patching onto a single cell takes practice. Patching onto two cells simultaneously takes skill. Three cells is a feat. Four or more is heroic. Since even the simplest vertebrates have more than four neurons, different methods must be used to sample larger populations of neurons simultaneously.

This is where extracellular measurements become useful. At first, the temptation is to think that measuring extracellular voltages in reference to an extracellular electrode should always produce a measurement of zero volts. Fortunately, thanks to the resistance of the extracellular medium, this is not the case. Because of Ohm's law, $V = IR$, any current that flows between two points will produce a voltage. So the concern becomes, "When do currents flow?"

When an ion channel opens, and ions flow through it, this is an electrical current. Since ion channels open during postsynaptic potentials, action potentials, and glial potentials, all of these will be measured with a pair of extracellular electrodes.

Current Loops

The conservation of charge can be used to derive Kirchoff's current law: the total charge flowing into a node must equal the total charge flowing out. For ion channels (the nodes), this means that all the ions flowing out of the cell must have originated inside the cell (and vice versa). As an example, if an action potential is fired at the cell's axon hillock, sodium ions are entering the cell at that point (raising the membrane potential).

These ions flow into the cell and disperse throughout. Their presence perturbs other charged ions by electrostatic forces. Some of these other ions are repelled out of the cell through leak channels, and others (of opposite charge) are attracted inward. If the leak channels cannot accommodate all of the ions, the internal charge increases (i.e., an increased membrane potential), which in turn perturbs extracellular ions through capacitance. All of these flows cancel out so that the total current into the cell equals the total current outward—Kirchoff's current law.

All of this ionic action is distributed spatially throughout the cell—but since most of the cell surface area is made up of dendrites, this is where most of the return current shows up. Furthermore, if most of a cell's dendrites are on one side of a cell (as happens in the cortex and hippocampus), current dipoles develop (Figure 1-2).

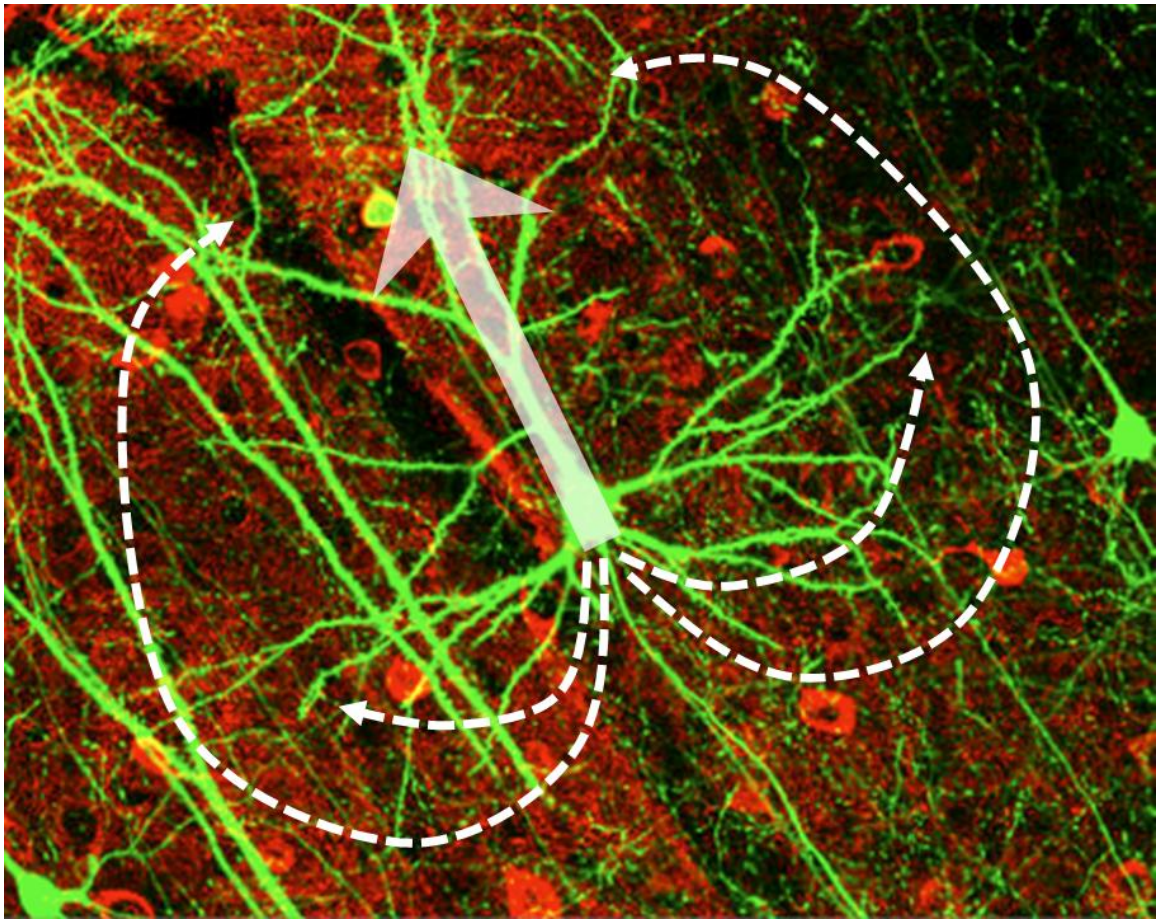

FIGURE 1-2. Current dipoles in a pyramidal cell. Current flows are shown with dashed white arrows. The dipole is indicated with the translucent solid arrow. The pyramidal cell, from the mouse visual cortex, is illuminated with GFP (green). [Image based on public domain file located at http://en.wikipedia.org/wiki/File:GFPneuron.png.]

Spatial and Temporal Synchrony

If two current dipoles are near each other, and they point in opposite directions (that is, anti-parallel), it is difficult to resolve them with extracellular electrodes (the dipoles "cancel out," in effect). However, if the dipoles are parallel and pointing in the same direction, they support each other. Therefore, structures with aligned dendritic fields are generally expected to produce larger electric fields when recorded. Areas without a bulk orientation, however, like subcortical nuclei, tend to have smaller electric fields.

This isn't to say that nothing will be recorded from nuclei like the amygdala or striatum. If an electrode is located near an axon hillock, for instance, its recording will be dominated by the nearby currents. More distant currents will have an effect, of course, but not as large an effect as the nearest cell. The difference between aligned cell layers and anisotropic layers is the chance that these more distant currents are on average going in the same direction as the closest dipole. If they are all pointing in random directions, they more or less cancel out, leaving only the closest to be measured. If they are all going in the same direction, they sum, leading to a very large reading. So the difference between areas with aligned dendritic fields (cortex) and scattered dendritic fields (nuclei) is really just the chance that dipoles from distant cells will be aligned with those of the closest cells. In an area like the cortex, the choices for a dipole are on the order of "up," "down," or "none." In the thalamus, dipoles can point in any direction.

The upshot is that two types of dipole synchrony exist:

1. Spatial. The dipoles point in the same direction
2. Temporal. The dipoles occur at the same time.

One is anatomical, the other functional. Both are measured (and conflated) by extracellular measurements.

Types of Signals

When an extracellular electrode is in the brain, what classes of signals are recorded? The most accurate answer is that any and all ionic currents are measured, whether from postsynaptic potentials, action potentials (APs), or glial cells. That being said, a few heuristics apply.

Action Potentials

APs are fast, lasting ~1 ms in duration. A 1 ms signal has a frequency of ~1 kHz (1/1 ms), so signals in this bandwidth are generally regarded as APs. Further, the highest current density of an AP is around the cell soma and axon hillock, so electrodes typically do not record APs unless they are near a cell body (Henze et al., 2000).

It should be stressed that a single extracellular electrode will usually be close to several cell somata, and hence the electrode has the ability to record APs from several cells. How can these cells be differentiated? Sometimes, the position of the electrode in relation to the soma will be different enough between cells that the APs have slightly different time course (the spikes have different shapes). Or, additionally, the cells themselves will produce APs with different shapes. In these cases, *spike sorting* can be used to classify the different waveforms as belonging to separate cells (Lewicki, 1998). (Unsorted signals are typically called *multiunit activity*, while sorted signals are called *single unit activity*.)

But spike sorting is not foolproof. There is nothing preventing two different cells from producing identical waveforms on an electrode. In this case, no amount of signal processing can distinguish the two classes of AP. The best recourse in these cases is to use multiple, closely spaced electrodes (*stereotrodes* or *tetrodes*). With multiple electrodes recording the same cells, there is a reduced chance that two cells will produce identical waveforms on *all* electrodes, which will permit spike sorting.

LFPs

Synaptic currents are slower than APs, generally 10s of ms (<100 Hz). Signals in this frequency band are generally called *field potentials*. When measured with microelectrodes (electrodes with tips around 1-50 μm in diameter), they are called *local field potentials* (LFPs). These signals often show their highest amplitudes in the dendritic fields, away from the cell bodies (Csicsvari et al., 2003).

Electrode Arrays

Given the complications induced by using extracellular electrodes (worries about sources, synchrony, etc.), what are the advantages? The primary one is simplicity. Just about any piece of metal can be used as an electrode, from a screw to a gold-plated tungsten wire (this is in fact what is used for the *in vivo* experiments described in the remainder of the dissertation). And to record cells, the electrode just needs to be near a cell—and there are lots of cells in the brain, so your chances are good! Intracellular recordings, on the other hand, require a single cell to be isolated and perforated. The cell can only survive for a few hours after such trauma, and finding another cell is a lengthy process. Extracellular electrodes can remain near cells for years, in comparison, without damaging the tissue (Suner et al., 2005).

Another prominent advantage of extracellular electrodes is their utility in freely moving animals. Extracellular electrodes can tolerate small movement while in the brain of a jumping and running rodent (Buzsaki, 2004) or primate (Santhanam et al., 2007). Intracellular electrodes are more susceptible to small changes in position that can easily break the electrode's seal or damage the cell (though this won't be the case forever; see (Lee et al., 2009)).

Since implantation of extracellular electrodes is fairly straight-forward, and localization is not as critical as with intracellular recordings, there is no barrier to inserting many electrodes—half a dozen to hundreds—at one time. And this is ultimately the most powerful use of extracellular electrodes: multielectrode arrays.

Because multielectrode arrays have multiple points of contact with the brain, they can record simultaneously from multiple cells. This ability to sample from neural populations brings us closer to our stated goal of monitoring populations of interacting cells.

To summarize, multielectrode arrays have the following advantages:

1. Easy to record from single cells (just have to be close)
2. Can be used for long times (on the order of years)
3. Usable in freely moving animals
4. Records multiple types of signal (APs, LFPs)
5. Spatially distributed sampling (recording different cells on each electrode)

However, they have the following disadvantages:

1. For a given electrode, it is unclear which cell is being recorded from, or even how many cells
2. Still not recording every cell in the entire brain

Chapter Summaries

As noted above, all of the remaining chapters utilize multielectrode arrays. Chapter 2 uses them to answer a question of basic neuroscience, involving candidate neural codes. Chapter 3 describes a potential application of arrays to epilepsy. Chapters 4-6 describe

new technologies to expand the utility of multielectrode arrays, using Chapter 3 as motivation. More detailed descriptions of each chapter follow:

Chapter 2 uses substrate-integrated multielectrode arrays (culture dishes with electrodes embedded in the bottom) to analyze the spontaneous activity of neural cultures. There are several candidate neural codes, one of them describing "synfire chains," or groups of cells that fire APs in precise temporal groups. There is evidence of this code from intact animals and brain slices, but we wondered if the code persisted in monolayer cultures, preparations where all the connections were disrupted and allowed to spontaneously rewire *in vitro*. Our evidence, using a template-matching algorithm, suggests that this phenomenon of repeating spatiotemporal patterns persists across many self-organizing neural systems.

Chapter 3 provides rationale for a novel treatment of epilepsy, which motivates many of the subsequent chapters in this dissertation. The treatment relies on work carried out by Daniel Wagenaar and Radhika Madhavan as part of their dissertations while working with Dr. Steve Potter (Wagenaar et al., 2005b). In essence, they showed that small pulses of stimulation distributed across a multielectrode array can completely suppress epileptiform bursting in neural cultures. Chapter 3 describes the many reasons why this approach should work in the intact brain as well, and the instantiation we envisaged for it.

Chapters 4 and 5 describe the NeuroRighter system, an integrated platform for closed-loop recording and stimulation from multielectrode arrays in freely moving animals. I created this system in an effort to carry out the experiments motivated by chapter 3.

Chapter 6 details a novel referencing algorithm for multielectrode recordings, either *in vivo* or *in vitro*, to reduce background noise and more easily record APs from single neurons.

Chapter 7 describes experiments with distributed microstimulation in epileptic rodents, using the tools from Chapters 4-6 and the motivation of Chapter 3.

Chapter 8 presents a characterization of the interictal activity present in the tetanus toxin model of epilepsy, specifically focusing on high-frequency oscillations (200-400 Hz oscillations in the local field potential). This chapter also shows our ability to elicit these oscillations with microstimulation.

Chapter 9, the last chapter, covers several additional experiments involving microstimulation in the rodent hippocampus, including a closed-loop experiment which attempted to control neural firing rates. These experiments were unsuccessful in answering their motivating questions, but postmortem analyses are provided that might prove useful to researchers examining similar phenomena.

The Appendices contain manuals for building and using the NeuroRighter hardware and software, along with additional details concerning it.

Chapter 2

Precisely Timed Spatiotemporal Patterns of Neural Activity in Dissociated Cortical Cultures[2]

[2] A version of this chapter has been previously published: J. D. Rolston, D. A. Wagenaar, and S. M. Potter (2007). "Precisely timed spatiotemporal patterns of neural activity in dissociated cortical cultures." *Neuroscience* 148(1):294-303.

Abstract

Recurring patterns of neural activity, a potential substrate of both information transfer and transformation in cortical networks, have been observed in the intact brain and in brain slices. Do these patterns require the inherent cortical microcircuitry of such preparations or are they a general property of self-organizing neuronal networks? In networks of dissociated cortical neurons—which lack evidence of the intact brain's intrinsic cortical architecture—we have observed a robust set of spontaneously repeating spatiotemporal patterns of neural activity, using a template-matching algorithm that has been successful both *in vivo* and in brain slices. The observed patterns in cultured monolayer networks are stable over minutes of extracellular recording, occur throughout the culture's development, and are temporally precise within milliseconds. The identification of these patterns in dissociated cultures opens a powerful methodological avenue for the study of such patterns, and their persistence despite the topological and morphological rearrangements of cellular dissociation is further evidence that precisely timed patterns are a universal emergent feature of self-organizing neuronal networks.

Introduction

The means by which information is reliably stored, propagated, and processed within biological neural networks is unknown, though several candidate mechanisms exist (Vogels et al., 2005). Of these theories, perhaps the most influential is that of Donald Hebb, who proposed information storage and processing via dynamically linked assemblies of cells, formed through simple activity-dependent learning rules (Hebb, 1949). Spontaneously recurring spatiotemporal patterns of neuronal action potentials, variously referred to as "motifs" (Ikegaya et al., 2004), "sequences" (Nadasdy et al., 1999), "synfire chains" (Abeles, 1991), and "information trains" (Frostig et al., 1984), might be an observable and quantifiable instantiation of Hebb's proposed cell assemblies. Such precisely timed patterns of neuronal action potentials are well-documented *in vivo* in various cortical structures (Abeles et al., 1993; Nadasdy et al., 1999; Ikegaya et al., 2004), and have also been shown in neocortical slices (Ikegaya et al., 2004). These preparations retain the brain's inherent microcircuitry, comprised of a specific laminar and columnar architecture ostensibly critical for normal function (Mountcastle, 1998). But is such structure crucial for the brain's elaboration of precisely timed activity patterns like those observed above?

Computational models of large-scale neuronal networks suggest that spontaneously recurring patterns of action potentials, termed "polychronous groups" by Izhikevich (Izhikevich, 2006), are an emergent property of loosely structured networks with realistic conduction delays governed by spike timing–dependent plasticity (STDP), and thus are not reliant on the brain's intrinsic cortical circuitry (Izhikevich et al., 2004; Izhikevich, 2006). But to our knowledge, the modeling work's conclusions have not been verified with unstructured networks *in vitro*. Is the Izhikevich model correct in implying

that precisely timed spatiotemporal activity patterns are produced independently of the brain's inherent cortical architecture?

To directly answer the above questions, we employed a well-established template-matching algorithm (Abeles and Gerstein, 1988) successfully utilized in two of the above-mentioned studies describing precisely timed activity patterns, one *in vivo* (Nadasdy et al., 1999) and one *in vitro* in brain slices (Ikegaya et al., 2004). This algorithm was applied to recordings of spontaneous action potentials from highly interconnected networks of dissociated cortical neurons, cultured on multielectrode arrays (Gross, 1979; Pine, 1980; Taketani and Baudry, 2006a). Such neuronal networks are well studied and their constituent neurons physiologically normal, but there is no evidence that dissociated networks retain or reestablish the brain's laminar and columnar microstructure (Dichter, 1978; Banker and Goslin, 1998). Moreover, the biological network's size (~50,000 cells) and diameter (~5 mm) approximates that used in the modeling study (100,000 model cells and an 8 mm radius) (Izhikevich et al., 2004). Finding comparable patterns in large networks of cultured dissociated cortical neurons to those found *in vivo* and in slices will provide strong evidence that such patterns are a general property of self-organizing neural networks and not dependent on the brain's intrinsic cortical microcircuitry, as it is constructed through the organism's development and experience.

Experimental Procedures

Cell culture

The data analyzed in this paper derive from a subset of the recordings described in Wagenaar et al. (2006b), where full details of the cell culture and recording conditions

may be found. Briefly, neocortex from embryonic (E18) Wistar rats, excluding the hippocampal anlage, was dissected according to NIH protocols, and dissociated in papain followed by trituration.

Approximately 50,000 cells were plated in a 5 mm diameter droplet on top of a multielectrode array (MEA) containing 59 electrodes arranged in a rectangular grid with 200 μm spacing. Cultures were maintained at 35 °C, 9% O_2, and 5% CO_2 in a DMEM-based medium for up to two months, which was partially replaced periodically. To avert infection and maintain the culture's osmolarity by preventing evaporation, the MEA dishes were covered with gas-permeable, water-impermeable Teflon membranes (Potter and DeMarse, 2001). Daily, 30 minutes of spiking activity was recorded using the MEA, inside the incubator where the cultures were maintained.

Extracellular recording

The MEA's signals were amplified and sent to a data acquisition computer, using a MultiChannel Systems MEA60 preamplifier and MC_Card A/D board (MultiChannel Systems, Reutlingen, Germany). Data acquisition and visualization was performed by our lab's custom-written software package, MeaBench[3] (Wagenaar et al., 2005a). Extracellular recordings were obtained from 59 electrodes on each MEA and action potentials (i.e., spikes) were detected using a threshold-based detector as upward or downward excursions beyond 4.5× the estimated RMS noise (Wagenaar et al., 2005a). Spike waveforms were stored and used to remove duplicate detections of multiphasic spikes. A variety of spike waveform shapes was observed on many electrodes, but distinct clusters in waveform space, as determined using the wavelet-based method of Quiroga et al. (2004), were typically not seen, presumably because many cells

[3] http://www.its.caltech.edu/~pinelab/wagenaar/meabench.html

contributed to the spike train at each electrode in these dense cultures, especially during bursts. Also during bursts, overlapping waveforms were a common occurrence, making spike sorting problematic. Thus, all results in this paper are based on unsorted multiunit data. Recordings were ultimately reduced to a series of ordered pairs, consisting of the precise time of each detected action potential's peak and the electrode on which it occurred.

Template-matching algorithm

The template-matching algorithm used here is identical to that in Ikegaya et al. (2004) and Nadasdy et al. (1999) and based on that of Abeles and Gerstein (1988). Briefly, a 200 ms template is constructed for each detected action potential. For the dataset's i^{th} spike occurring at time t_i on electrode e_i, a template $temp_i$ is constructed as a vector containing the latencies and electrode numbers of all spikes occurring within 200 ms of t_i. That is, $temp_i = <t_j - t_i, t_k - t_i, \ldots ; e_j, e_k, \ldots >$, where t_j, t_k, ... are less then t_i + 200 ms but greater than t_i. Each template from a spike detected on electrode e_i is then compared to all other templates from the same electrode. A match is declared when two latency/electrode pairs are identical within some specified precision (e.g., 1 ms), meaning that at least three matching spikes have recurred with a variation in firing times more tightly bound than the specified precision. These matches are later sorted into sequence families (see below). The matching process is repeated for all templates on all electrodes, resulting in the analysis of all the dataset's spikes (>10,000/min of recording).

The method, as described, would overestimate the number of sequences present in each dataset. As an example, say that a template consisting of spikes on electrodes 5, 10, 34, 7, and 8 recurs in a precise temporal order five times. The first run of the template-

matching algorithm would find four matches (i.e., repetitions) of the pattern as it serially searched through the data. When the algorithm eventually repeats with the second instance of the pattern as its reference template, it will find an additional three matches, and so on. Moreover, the algorithm would experience the same problem as it searched through subsets of the pattern's repetitions (e.g., {10, 34, 7, 8} and {34, 7, 8}). To alleviate this overcounting and to exactly replicate previous studies' implementations of the template-matching algorithm, matched spikes are removed from the dataset during each iteration of the algorithm, while mismatched spikes are retained, as in Ikegaya et al. (2004). Overcounting is thus prevented, while every spike is still analyzed at least once. As an added benefit, such spike removal results in a significantly faster implementation by reducing the dataset during each cycle of the algorithm. It took roughly 30 minutes to analyze one minute of multielectrode data on a standard desktop computer with MATLAB 7.2 (MathWorks, Natick, MA).

When several sequences match a given reference template, it is unclear *a priori* whether identical or different subsets of the template's spikes are matched. Due to this limitation of the algorithm, matches to one template form a collection of distinct subtypes or *sequence families* (e.g., one set of matches may be to spikes 2–5, while another may be to spikes 6–9, leaving only one spike, the trigger spike, in common between the two subtypes). Because we wish to identify repeating sequences of action potentials, and not repeating abstract templates, we conservatively collected instances of each sequence family separately by assigning a different sequence identification number to each family. Henceforth, *sequence family* will refer collectively to all instances of the same identified recurring spatiotemporal pattern of neural activity (i.e., all matches of a given subtype), and *sequence repetition* will refer to the individual occurrences of these families.

Shuffling

To evaluate the significance of our results, we ran the template-matching algorithm on shuffled versions of the same one-minute dataset and compared the number of identified sequences obtained from each. Two methods of shuffling were used, spike swapping and spike jittering (Figure 2-1). Spike swapping can be thought of as exchanging the electrode numbers of two randomly selected spikes, and repeating this process throughout the entire dataset. Formally, spike swapping takes the length *N* vector of electrode numbers from the dataset, where *N* is the total number of spikes, and then assigns a new electrode number from this vector by sampling without replacement. Thus, the dataset retains identical spike times after shuffling and an identical distribution of spikes per electrode per recording, but presumably lacks any biologically-induced correlations between spike times.

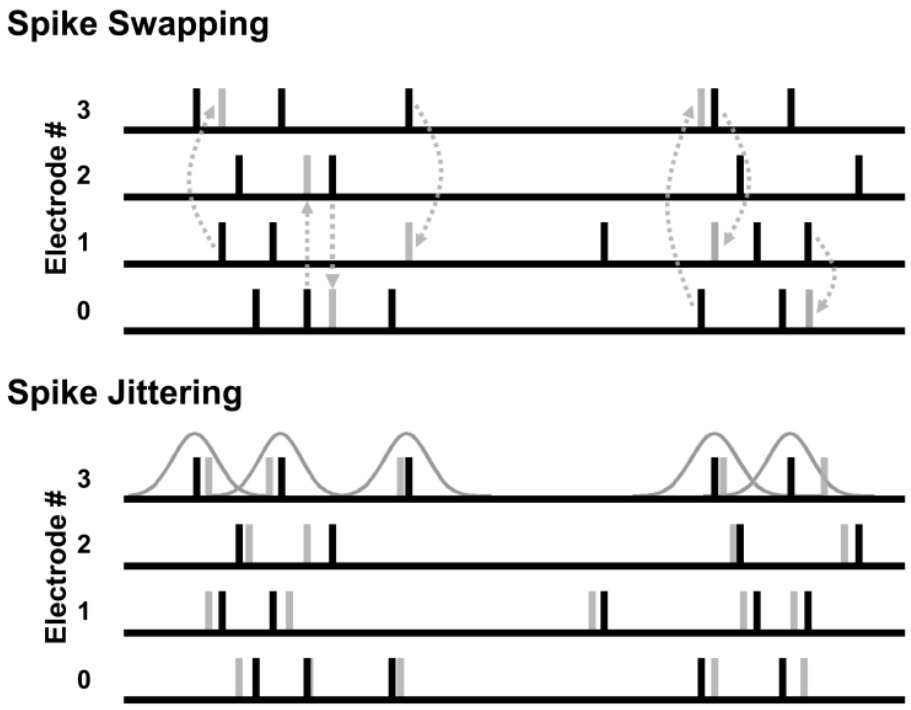

FIGURE 2-1 Shuffling methods. (Top) Spike swapping preserves the dataset's spike-timing distribution and electrode distribution. Note that swapping can be pair-wise (i.e., between two electrodes, as demonstrated with the two swaps to the

left) or higher-order (as demonstrated with the three-wise swap to the right). (Bottom) Spike jittering preserves population modulations in firing rate and each electrode's ISI distribution approximately, and the dataset's electrode distribution exactly.

Statistical Methods

The Wilcoxon signed-rank test was used to calculate significance by comparing the number of detected sequence families in each actual dataset to the number of detected sequence families in a single shuffled version of the same dataset. This captures the likelihood of all 10+ cultures having more sequence families than their shuffled counterparts, which is not expected by chance. Further, *p*-values were calculated directly for the three most frequently recurring sequence families in each culture by generating multiple shuffled datasets (see *Pattern Persistence* section above). When multiple comparisons were necessary, the Bonferroni adjustment, the most stringent correction for multiple comparisons (Bland and Altman, 1995), was used to protect against type I errors.

Results

Thirty minutes of spontaneous activity was recorded from each of 12 cultures, aged 21 DIV, derived from four separate platings (Wagenaar et al., 2006b). From these datasets, one minute (arbitrarily the 16th minute of recording time) was examined with a template-matching algorithm (see Methods) to determine the number of repeating sequences. The algorithm used a precision of 1 ms and a window size T = 200 ms, following Nadasdy et al. (1999). On average, 2993 ± 1077 unique sequence families were found in each recording, repeating 2.01 ± 0.1 times/min (range 2-6), consisting of 4.3 ± 6.3 spikes (range 3-475) and spanning 125 ± 55 ms. Several example sequences are shown in Figure 2-2.

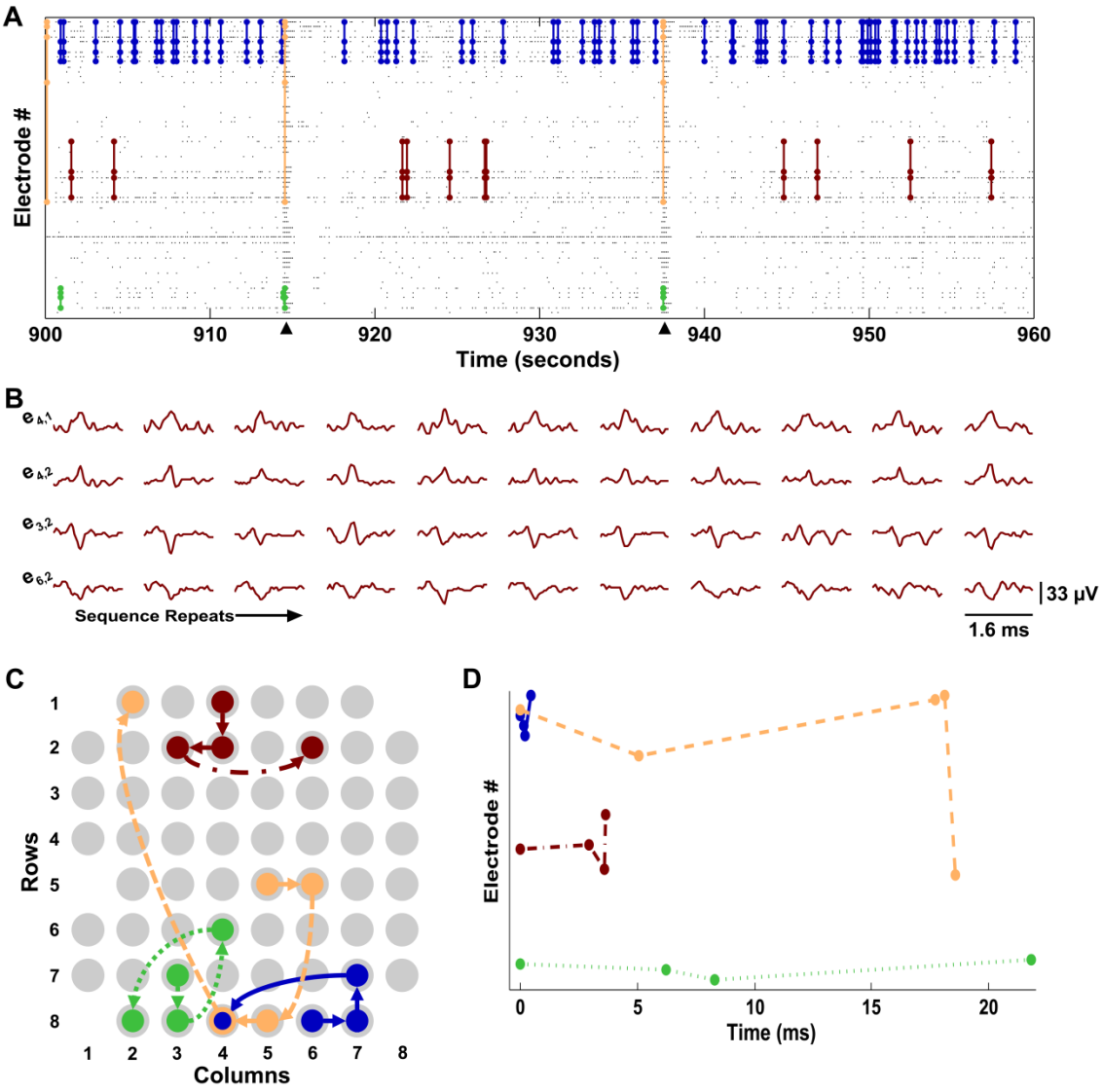

FIGURE 2-2 Precisely timed sequences of neural activity repeat spontaneously in networks of dissociated cortical neurons. (A) Raster plot showing sequence repetitions. Each gray dot represents an action potential detected on a specific electrode. Sixty-two instances (though fewer may be visible due to overlap) of a repeating four-spike sequence are traced in dark blue lines, seven instances of a five-spike sequence in orange, four instances of a four-spike sequence in green, and ten instances of a three-spike sequence in red. Arrowheads indicate population bursts. In this panel, the ordering of electrodes is not related to MEA geometry, but was chosen to avoid the overlapping of sequence traces. (B) Action potential waveforms for the eleven repetitions of the red sequence in A. Each row shows the waveforms recorded from one electrode and each column is one sequence repetition. Electrode labels indicate the column, row location of the electrode on the MEA (see panel C). (C) Spatial propagation of each sequence shown in A. Each electrode of the MEA is represented by a light gray circle. The dark blue solid arrows show the propagation of the dark blue sequence from A. The red dot-dashed arrows represent the red sequence depicted in panels A and B. The orange dashed

arrows represent the orange sequence depicted in panel A and the green dotted arrows represent the green sequence. Arrows indicate the sequence's origin and direction of propagation. The empty space at column 1, row 5 is the approximate location of the ground electrode. (D) The time course of the four sequence families, using the same color coding as panels A-C and the same line style as C. Electrode ordering as in panel A. These patterns were detected with a template-matching algorithm using a window size T = 200 ms and a precision of 1 ms (see **EXPERIMENTAL PROCEDURES**).

To demonstrate that the finding of precisely timed sequences was not limited to dissociated cultures at a particular developmental stage, we examined cultures aged 35 DIV as well. Using 11 cultures from three separate platings (8 from the previously analyzed 21 DIV cohort and three additional cultures), we found similar patterns to those observed at 21 DIV. In one minute of spontaneous activity, there were 1312 ± 341 unique sequence families per culture, repeating 2.1 ± 4 times (range 3-62), consisting of 8.0 ± 36.3 spikes (range 3-1408) and lasting 122 ± 61 ms.

The average time between sequence repetitions was 22.7 ± 16.7 seconds and many of the repetitions appeared to recur in close succession (Figure 2-3A). This tendency toward short inter-sequence intervals (the leftmost peak of Figure 2-3A) can be explained by cultured cortical networks' frequent display of brief, concerted increases in firing rate, known variously as "bursts," "population bursts," "barrages," and "network spikes" (Droge et al., 1986; Eytan and Marom, 2006; Wagenaar et al., 2006b), which may be similar to the UP states observed *in vivo* and in slices (Robinson et al., 1993; Steriade et al., 1993; Steriade, 2001). More than half of all sequence spikes occur during bursts, so it is not surprising that the time between sequences reflects this short length of bursts typical in cultures at these ages (~200 ms; leftmost peak of Figure 2-3A).

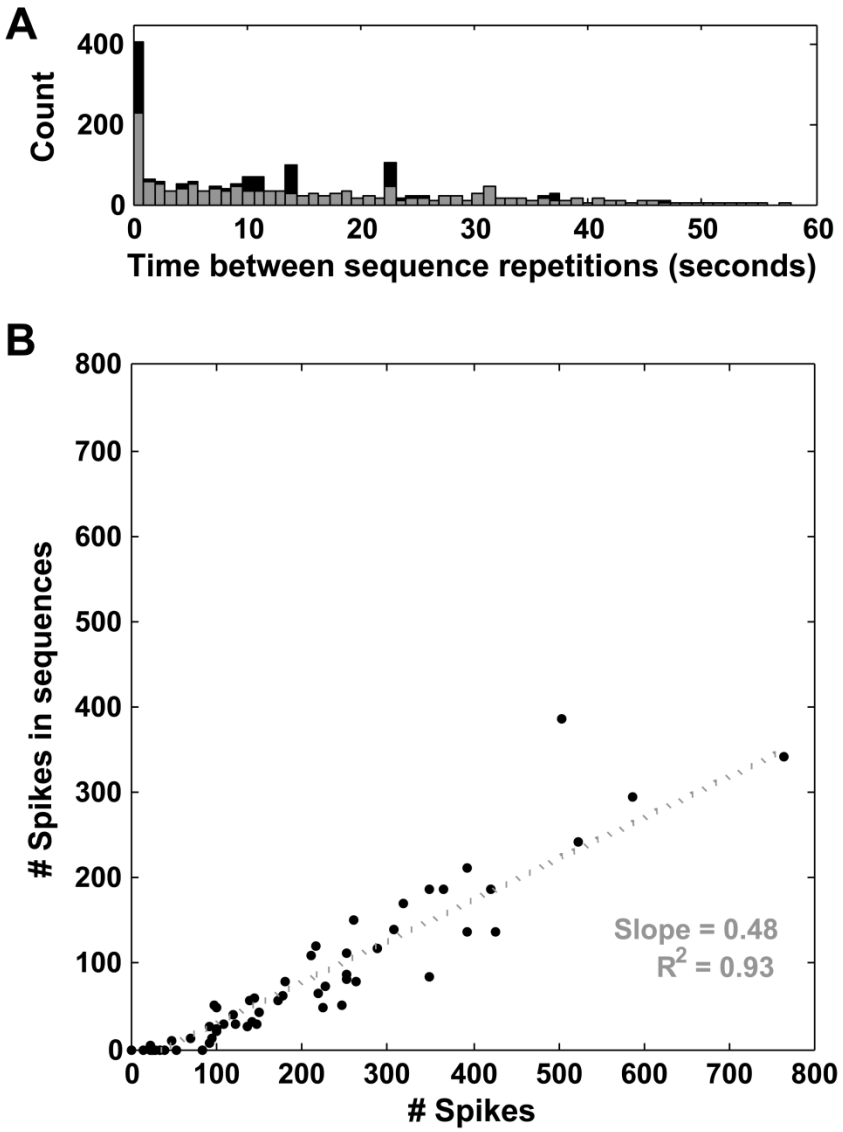

FIGURE 2-3. Properties of detected sequences. (A) Histogram of times between sequence repetitions. Sequences repeated with a mean interval of 22.7 ± 16.7 seconds, though many occur in close succession (left peak of histogram), due to the frequent occurrence of sequences in population bursts (see text). (B) Participation of each electrode in sequences, data from one representative culture. The total number of spikes detected on an electrode (x-axis) is plotted vs. the total number of spikes detected on the same electrode that take part in any sequence (y-axis). Each electrode is represented by one point. The slope of the best-fit line through these points can be used to estimate the percentage of spikes taking part in sequences on an electrode, 71% in this culture (R2 = 0.96) (if every spike detected on an electrode participated in a sequence, the best-fit line would have a slope of one).

Interestingly, the likelihood of a spike being part of a sequence appears to be roughly the same—or even a bit lower—during bursts as outside of bursts, despite a burst's greater concentration of spikes: Using the SIMMUX algorithm to detect population bursts (Wagenaar et al., 2005a), we determined that 52% of the spikes that were part of detected sequence repetitions occurred during bursts at 21 DIV, while of all spikes recorded at 21 DIV, 59% occurred in bursts. At 35 DIV, these numbers were 79% and 87%, respectively. These proportions—sequence spikes in bursts over all sequence spikes, and spikes in bursts over all spikes—are very nearly the same, suggesting that bursts do not potentiate sequence occurrence.

From looking at Figure 2-2, it is unclear whether some electrodes participate more frequently than others in the observed sequences. To investigate this in more detail, we made scatter plots, with the number of action potentials detected on each electrode as the abscissa and the number of action potentials taking part in sequence repetitions (from any sequence family) as the ordinate, representing each electrode as a point (Figure 2-3B). The slope of the best-fit line through these points provides an estimate of the percentage of each electrode's spikes that participate in sequences. If every spike detected on each electrode took part in a sequence, these points should fall on a line with slope 1. In the data shown in Figure 2-3B (from one representative culture), this slope is 0.71 ($R^2 = 0.96$). No discernible patterns emerged from this analysis across cultures (the slope changes from culture to culture, but the best-fit curve is always linear), suggesting that electrodes participate roughly with a constant proportion of their firing rates.

To determine the significance of detected sequences, we compared the number of observed sequence families to the number of observed sequence families in shuffled versions of the same data. Two shuffling methods were used, spike swapping and spike

jittering (see Experimental Procedures; Figure 2-1). Spike swapping is a balanced rearrangement of spikes over electrodes, leaving each electrode with precisely the same number of spikes, but occurring at different times. In essence, each spike's electrode number is reassigned to that of another spike, though each spike can give its electrode number to only one other spike. This method preserves both temporal and spatial population modulations, but fails to preserve the ISI distribution of individual cells. Spike jittering randomly perturbs the timing of each spike by an amount drawn from a Gaussian distribution of mean zero and standard deviation 2 ms. Because the perturbation has zero mean, the ISI distribution of each electrode is closely preserved, along with modulations in population activity. Additionally, the number of spikes per electrode remains unchanged, making spike jittering the more stringent of the two shuffling methods. There were more observed sequence families in the unshuffled data than in both spike swapped and spike jittered data ($P < 0.05$ and $P < 0.01$, respectively; Wilcoxon signed-rank test), indicating that the high number of observed sequences did not arise by chance.

Because of their precision and frequency of recurrence, it is appealing to interpret the observed precisely timed sequences as evidence of spatiotemporal attractors. Since sequences that recur frequently in our data are more likely to represent such attractors than those sequences that repeat only a few times, we can quantify this idea by tracking solely those sequences repeating three or more times, on the assumption that patterns recurring only twice are likely to be spurious. The number of such frequently repeating sequence families detected in the actual data was significantly higher than in spike swapped data ($P < 0.001$ at 21 DIV; $P < 0.005$ at 35 DIV) and these positive results were not affected by the choice of precision, 1 ms, as was determined by examining the data at various other precisions, from 2 to 20 ms (Figure 2-4A and Figure 2-5A). Similarly, the

number of detected sequence families was higher in actual data than in spike jittered data ($P < 0.01$ at 21 DIV; $P < 0.005$ at 35 DIV). However, unlike spike swapping, the results for spike jittering were affected by precision. Specifically, at a precision of ≥5 ms, the results became non-significant at 21 and 35 DIV ($P > 0.05$; Bonferroni-adjusted Wilcoxon signed-rank test). This is anticipated, however, because the Gaussian distribution used in spike jittering has a standard deviation of 2 ms, meaning that >95% of jittered spikes are within 4 ms (two standard deviations) of their original, unshuffled times. When using a precision ≥5 ms, this jittering should not be apparent. To account for this interplay between jittering and precision, we used an additional spike jittering kernel with a standard deviation of 20 ms. Surprisingly, a similar cutoff in precision was observed: at 21 DIV there were significantly more sequences in the actual data than jittered data at 1, 2, or 5 ms, but not ≥10 ms (Figure 2-4A; $P < 0.05$ and $P = 0.28$, Bonferroni-adjusted Wilcoxon signed-rank test) and at 35 DIV there were significantly more sequences at 1 and 2 ms, but not ≥5 ms (Figure 2-5A; $P < 0.05$ and $P = 0.59$, Bonferroni-adjusted Wilcoxon signed-rank test). This implies that frequently recurring sequence families in dissociated culture have an inherent precision of about or less than 5 ms, in agreement with the similar analysis of Beggs and Plenz on field potential patterns recorded in cultured slices (Beggs and Plenz, 2004).

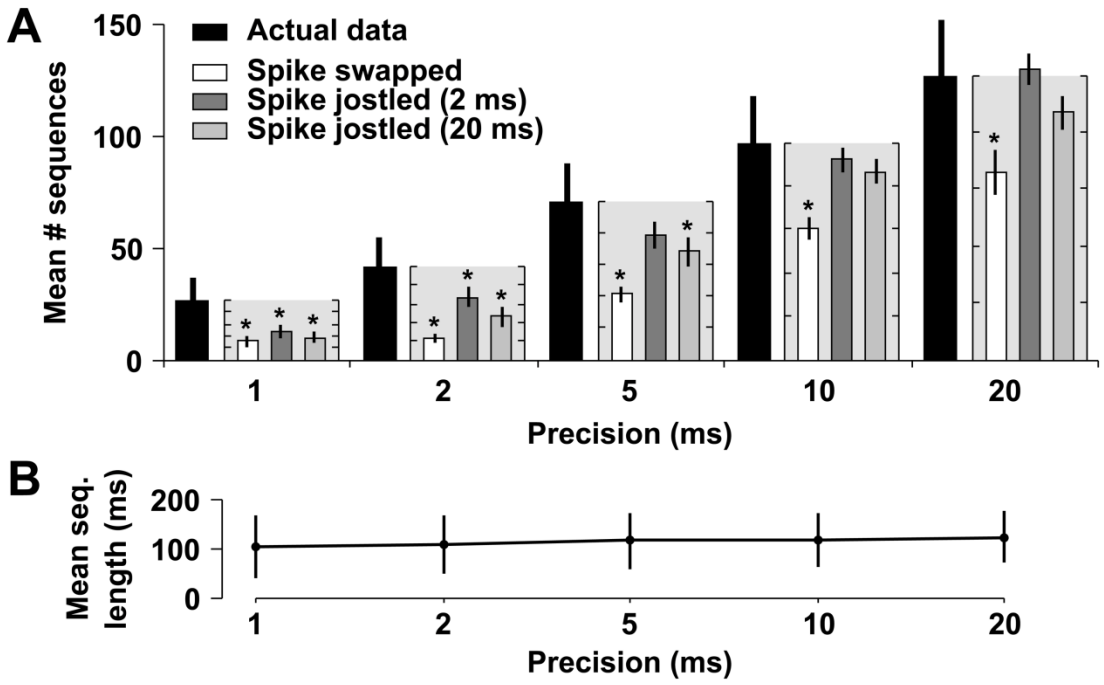

FIGURE 2-4. Sequences repeat more frequently in actual data from cultures aged 21 DIV than in shuffled data. The template-matching algorithm was run at various precisions (1, 2, 5, 10, and 20 ms) and the number of detected sequences was compared to the number of sequences observed in shuffled versions of the same dataset. (A) The mean number of detected sequence families repeating 3 or more times in the actual data (solid black bars, ±SEM), along with the mean percentage of these sequences explained by shuffled data (spike-swapped – white bars; jittered with 2 ms Gaussian kernel – dark grey bars; jittered with 20 ms Gaussian kernel – light grey bars). Percentages are calculated as the number of sequence families detected in shuffled data divided by the number detected in actual data, and the mean ±SEM of these ratios is plotted (light gray boxes next to black bars of unshuffled data) with the ordinate, ranging from 0-100%, scaled to the number of sequences detected in the actual data. Tick marks are at 20% intervals for these minor axes. Significant differences are indicated by asterisks. (B) Average length (±SD) of all detected sequences at each precision. The similarity between lengths indicates that our choice of precision does not affect the average length of detected sequences.

Ideally, the choice of precision should only affect the number and not the character of detected sequences. We therefore verified that the choice of precision did not affect the average length of detected frequently recurring sequences at either 21 or 35 DIV (Figure

2-4B and Figure 2-5B). Consequently, we feel confident that these sequences are not an artifact of particular precision choices, but instead may reflect the ongoing attractor-like dynamics of dissociated cortical networks.

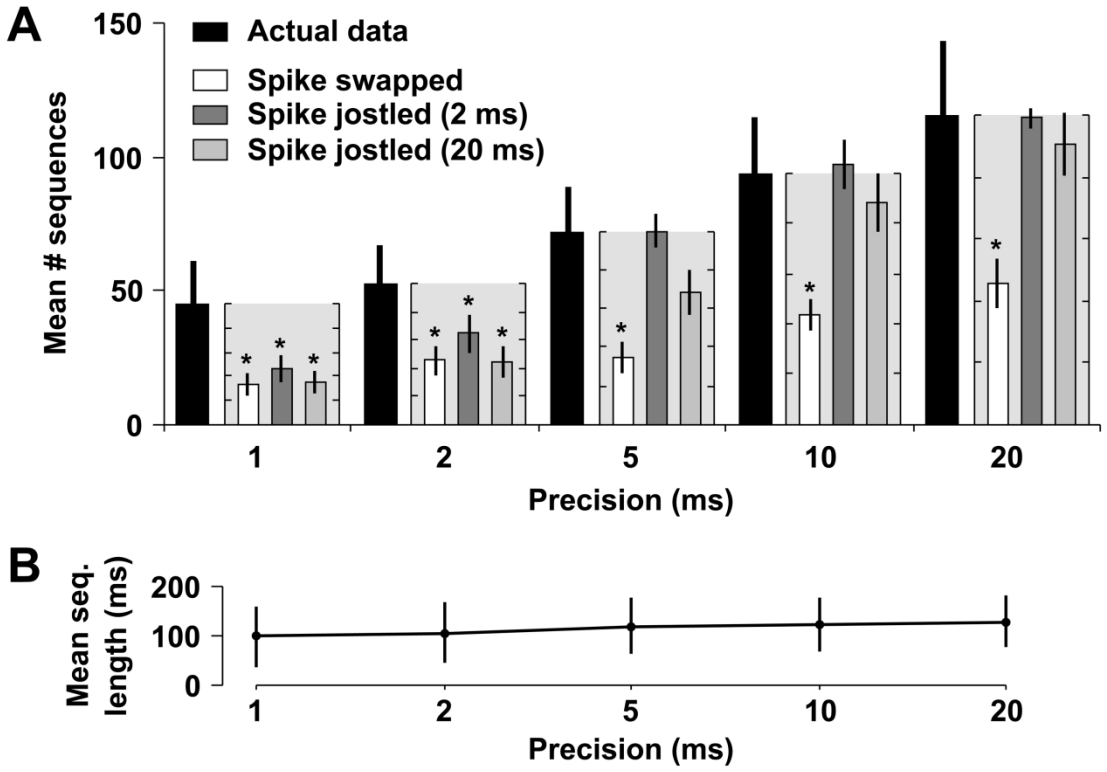

FIGURE 2-5. Sequences repeat more frequently in actual data than in shuffled data at 35 DIV. This figure mirrors **FIGURE 2-4**, but uses 11 cultures derived from 3 separate platings, aged 35 DIV, instead of 21 DIV. The observation of significant precisely timed sequences at both stages of development argues against any developmental transience of this phenomenon.

Since the above data were taken from short, one minute segments of larger recordings, we decided to track the detected patterns as they developed over longer times. To this end, we counted how often the three most frequently detected sequence families, from the original data, occurred in each of the ten one-minute data segments following the original data and, as a control, the original data itself. Because this method does not

discard matched spikes (in contrast to the template-matching algorithm above), its use as a control helps verify that our discovered sequences truly occurred more frequently than they would by chance. With these data, we compared the number of times the three most frequently recurring patterns occurred in the actual data versus spike-jittered (2 ms Gaussian kernel) versions of the same datasets, shuffling each dataset 20 times. Those cultures for which the actual data contained more sequence repetitions than all 20 shuffled versions of the same data can be said to contain significantly more sequence repetitions with $P < 0.05$. The number of cultures satisfying this criterion was graphed as a function of time segment (Figure 2-6), showing that, in more than half of the cultures, the three most frequently recurring sequences persist for at least ten minutes, and recur frequently during that time. Note that only one culture (at 21 DIV) failed the control validation.

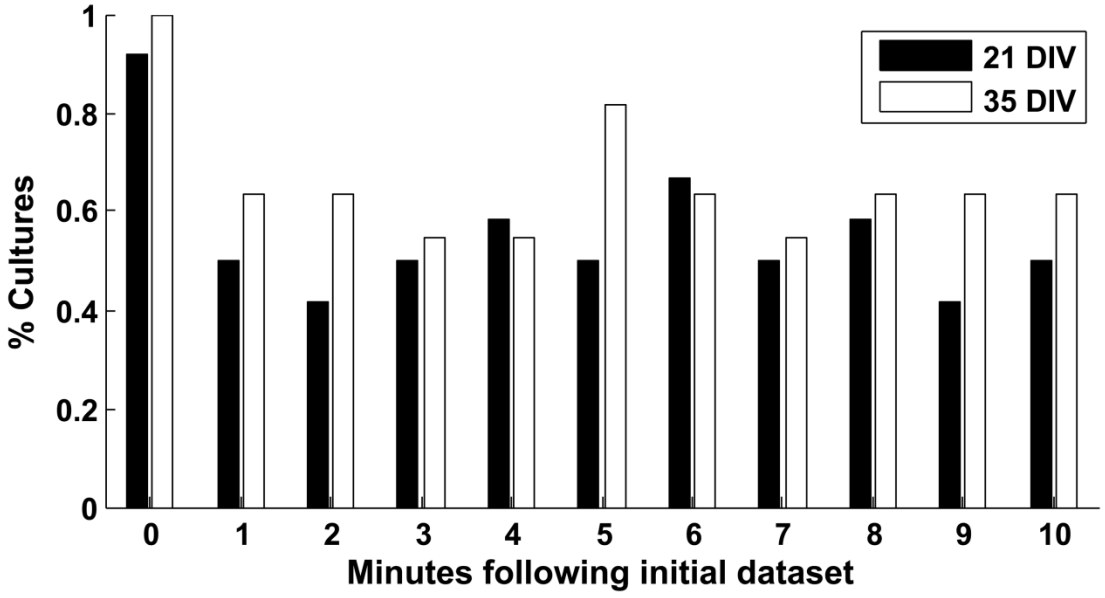

FIGURE 2-6. Persistence of detected sequences. The three most frequently recurring sequences were sought in actual data during the ten minutes following the 16th minute. The number of sequences observed in the actual data was compared to the number observed in 20 shuffled versions of the same data, using the most stringent shuffling method (i.e., spike jittering with a 2 ms Gaussian kernel). If the actual data had more observed sequences than any of the 20

shuffles, it was considered to contain significantly more of the three most frequently occurring sequences than shuffled data ($P < 0.05$). The percentage of cultures passing this test is shown for both 21 DIV (black bars) and 35 DIV datasets (white bars) for each minute. Most or all of the cultures (11 of 12 at 21 DIV, 12 of 12 at 35 DIV) passed this test at minute zero, even though the method for tracking persistence does not discard matched spikes, thus providing a control for the template-matching algorithm. These results suggest that the most frequently recurring patterns are stable over several minutes following their initial observation.

Discussion

We have shown the presence of persistently recurring, precisely timed sequences of action potentials in dissociated networks of cortical neurons, using an algorithm with noted success both *in vivo* in the rat hippocampus (Nadasdy et al., 1999) and *in vitro* in neocortical slices (Ikegaya et al., 2004). Examination of the persistence of these patterns suggests that the most frequently recurring sequences are maintained for at least several minutes following their initial observation. The patterns were observed throughout multiple developmental stages and were found to occur both within and outside network bursts.

Precisely timed sequences have a rich history of inquiry (Abeles, 1991; Herrmann et al., 1995; Aertsen et al., 1996; Bienenstock, 1996) and have been shown to be useful as substrates for computational learning rules (Gutig and Sompolinsky, 2006), suggesting that such sequences may fulfill the idea of dynamically linked cell assemblies postulated by Hebb decades ago (Hebb, 1949). Recently, precisely timed sequences of *bursts* of action potentials were described and characterized in dissociated cortical cultures grown on MEAs (Wagenaar et al., 2006a), although these patterns were limited to a defined developmental period, typically the second week *in vitro*. Also, the sequence of neural activation during bursts has been shown to be non-random and repetitive (Segev et al., 2004; Eytan and Marom, 2006; Madhavan et al., submitted). The idea that such patterns are a general property of self-organizing networks, rather than being limited to

developmentally and anatomically structured networks, is bolstered by computational studies of loosely-structured model neural networks of comparable size to our cultured neuronal networks (Izhikevich et al., 2004; Izhikevich, 2006). They found that recurring patterns of neural action potentials spontaneously developed in simulated networks as a result of the spike timing–dependent plasticity (STDP) learning rule (Dan and Poo, 2006), despite a wide range of parameters and varying degrees of thalamic afferentation (Izhikevich, 2006).

It has previously been suggested, by examining local field potentials (LFPs) with MEAs, that the neural networks of acute brain slices and organotypic cultures obey the principle of self-organized criticality (SOC) (Bak et al., 1987; Bak, 1996; Beggs and Plenz, 2003). Moreover, these precisely timed sequences of LFPs spontaneously recur, like the sequences we observed above (Beggs and Plenz, 2004). Might sequences of action potentials in dissociated cultures show similar behavior? One characteristic of critical processes is that their event sizes obey a power law probability distribution, $P(n) \approx n^{-\alpha}$, where n is the event size and $P(n)$ is the probability of observing a size n event. Fitting a power law to our distribution of sequence sizes, in terms of number of electrodes taking part in a sequence, results in an exponent $\alpha = -3.1 \pm 0.2$ (±95% confidence interval (CI)) using linear regression in log-log space ($R^2 = 0.97$; Figure 2-7A). However, when the same procedure is done on spike-swapped and spike-jittered data, similar fits are obtained ($\alpha = -3.2 \pm 0.2$, $R^2 = 0.97$ and $\alpha = -3.3 \pm 0.2$, $R^2 = 0.97$ for electrode-shuffled and spike-swapped data, respectively; Figure 2-7B-C). This suggests that the observed scale invariance of sequence sizes—in these data—does not prove anything inherent to significant pattern generation (Reed and Hughes, 2002; Bedard et al., 2006).

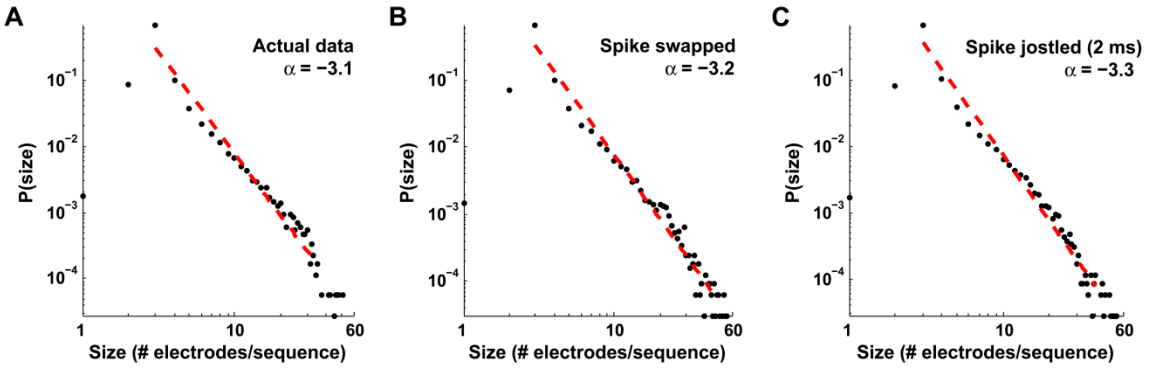

FIGURE 2-7. The distribution of sequence sizes obeys a power law probability distribution. When the number of electrodes taking part in each detected sequence is graphed against its probability of occurrence, the distribution can be fit by a power law (red dashed line), P(n) ~ n-α, where n is the event size, P(n) is its normalized frequency of occurrence in our datasets, and α is the power law's exponent. On log-log plots, such as these, graphed power laws appear linear, with slope α. For the observed sequences in the actual data α = -3.1 ± 0.2 (±95% CI, R2 = 0.97; A). However, we find similar scale invariance in our spike-swapped (α = -3.2 ± 0.2, R2 = 0.97; B) and spike-jittered data (α = -3.3 ± 0.2, R2 = 0.97; C), minimizing the importance of scale invariance in explaining our significantly repeating patterns.

Finding precisely timed sequences in cultures presents three important advances for the study of neural information processing. First, the observation of such sequences in dissociated cultures, combined with their illustration in multiple *in vivo* preparations and in brain slices, argues for their robustness, as evidenced by their persistence in multiple species and across various degrees of deafferentation, from simple anesthesia to surgical excision. Second, the further study of such sequences can now be performed in dissociated cultures, a simple preparation allowing detailed control of the culture's inputs and chemical environment, including relevant neuromodulators like dopamine (Lapish et al., 2007), as well as comprehensive long-term morphological imaging (Potter, 1996, 2005), potentially granting us a window into the morphological substrates underlying the formation of precisely timed sequences. Lastly, finding repeating sequences of neural action potentials in dissociated cultures argues against the necessity of innate cortical structure in their formation—not only are the sequences robust in the

sense of not requiring afferent input, just as in slices (MacLean et al., 2005), but they are robust in the sense that the neural network spontaneously self-organizes in a way that generates them. While the brain's intrinsic organization is likely to add new subtlety to these patterns, their existence appears to be a general feature of any self-organizing neuronal network. The reasons for such robustness are still unknown, but present an intriguing avenue for further research into repeating spatiotemporal patterns of neural activity.

Acknowledgments

We wish to thank Dieter Jaeger and Radhika Madhavan for helpful discussion, Sheri McKinney for technical assistance with cell culture, and our anonymous reviewers for suggesting significant improvements to the manuscript. This work was supported by the Emory University Graduate Division of Biological and Biomedical Sciences, the Whitaker Foundation, the Wallace H. Coulter Foundation, the NSF Center for Behavioral Neuroscience, NINDS grant NS38628, and NINDS/NIBIB grant EB00786.

Chapter 3

Distributed Microstimulation for Epilepsy[4]

[4] A version of this chapter has been previously published: John D. Rolston, Steve M. Potter, Robert E. Gross (2009) "Distributed Microstimulation for Epilepsy" in Schacter, S. C., Guttag, J., Schiff, S. J., Schomer, D. L., Summit Contributors (2009) "Advances in the Application of Technology to Epilepsy: The CIMIT/NIO Epilepsy Innovation Summit." *Epilepsy & Behavior* 16(1):3-46.

Electrical stimulation is a promising therapy for pharmacoresistant seizures, and is currently being tested in a variety of instantiations, such as deep brain stimulation (DBS) of subcortical nuclei, responsive stimulation of the cortex, and vagus nerve stimulation (Gross, 2004; Luders, 2004; Theodore, 2005). Each of these approaches uses a small number (usually ≤4) of large, millimeter-diameter electrodes, and relatively high currents and frequencies (several mA often at >100 Hz). While many of these methods have shown evidence of reducing seizure frequency, they so far have achieved seizure freedom in only a small number of patients.

We have taken an alternative approach, utilizing arrays of microelectrodes (dozens with <50 μm diameter) to directly stimulate epileptic foci with low frequency, low current pulses, asynchronously delivered across the span of the electrode array (Wagenaar et al., 2005b). This method was shown to be completely effective in suppressing epileptiform bursting in cultures of dissociated rat neocortex (Wagenaar et al., 2005b), a valuable model of the brain that reproduces some of its most nuanced features (Rolston et al., 2007a). Population bursting, which underlies interictal activity *in vivo* (Wyler et al., 1982), was suppressed in all cultures tested. For effective stimulation, only 25 electrodes were used of the 59 available, with each electrode stimulated at 2 Hz (50 Hz aggregate for the entire array). Stimulation was voltage-controlled and biphasic, using custom-made hardware (Wagenaar and Potter, 2004), and ranged from 100-900 mV per 400 μs phase. Optimal stimulation parameters for evoking neural responses had been previously determined (Wagenaar et al., 2004). Importantly, single electrode stimulation, like that used in conventional DBS, was incapable of suppressing bursting, even at higher stimulation voltages (Wagenaar et al., 2005b).

In an attempt to further optimize this protocol, we developed a closed-loop, state-control algorithm to adjust stimulation parameters in real time (Wagenaar et al., 2005b). State control uses the output of a system (e.g., neural activity) to change the activity of a controller, which acts to move the sensed output closer to a desired value (also called the reference value). In this case, the controller was multielectrode distributed stimulation, with stimulation voltage as the controller's free parameter. For input to the control algorithm, we monitored the array-wide firing rate, f (that is, the number of action potentials recorded from all electrodes per second), which can be viewed as a state variable of the neuronal network. Since higher voltage stimulation leads to increased neural firing rates *in vitro* (Wagenaar et al., 2004), we could control the firing rate by adjusting the voltage of ongoing stimulation, using the following control equation:

$$V_{new} \leftarrow V_{prev}\left(1-\varepsilon\frac{f-f_0}{f_0}\right)$$

where V_{new} is the stimulation voltage, V_{prev} is the previously used stimulation voltage, f is the observed array-wide firing rate, f_o is a target (reference) firing rate, and ε is a gain factor determining how quickly V reacts to f (typically, $\varepsilon = 0.02$).

This closed-loop approach again led to suppression of epileptiform activity, but did so with greater efficiency. Specifically, at a stimulation rate of 10 Hz aggregate with only 10 randomly selected electrodes (1 Hz per electrode), closed-loop stimulation suppressed epileptiform activity in >50% of cultures tested, compared to 20% with open-loop distributed stimulation at the same rate and electrode number. If electrodes were selected for efficacy in advance (rather than randomly), closed-loop stimulation was effective in 80% of cultures, compared to 60% of open-loop experiments in this reduced rate and reduced electrode number setup.

The primary advantages of the state-control approach are (1) reduced stimulation frequency and (2) a decreased need to find effective electrodes. These, in turn, lead to additional advantages beyond those already offered by open-loop distributed microstimulation: (1) reduced need for system programming post-implant (a frequent problem in contemporary DBS treatments), (2) increased battery life (due to lower voltages and stimulation rates), and (3) the potential to automatically compensate for brain changes or electrode impedance changes (e.g., if the brain adapts and requires larger stimulation voltages, or the electrode impedance increases yielding a similar effect, the algorithm will automatically provide increased stimulation voltages). Other advantages common to both open and closed-loop stimulation include increased fault tolerance (with more electrodes, there is increased physical redundancy) and relaxed placement requirements (more electrodes increase the probability of electrically affecting critical neural tissue).

Why should distributed stimulation suppress epileptiform activity? Neuronal cultures by definition lack the afferent and efferent connections they had *in vivo*. For reasons that are still unclear, such isolation causes a numerical increase and strengthening of recurrent synapses amongst the remaining neurons, perhaps in a homeostatic attempt to substitute for lost input (Buzsaki, 1986; Turrigiano, 1999; Houweling et al., 2005). *In vivo*, this might best be approximated by deafferentation epilepsy, where part of the neocortex is undercut, removing afferent drive and producing spontaneous seizures after a period of cortical reorganization (Echlin et al., 1959; Prince and Tseng, 1993). Furthermore, similar epileptiform activity occurs in the hippocampus when deafferented (Buzsaki, 1986; Buzsaki, 1989), and low-frequency “reafferentation” suppresses this activity (Barbarosie and Avoli, 1997). Distributed microstimulation may thus work by something akin to “reafferentation” of our cultures.

We are currently extending this work to behaving animals. We have developed a system for closed-loop stimulation and microwire array recording *in vivo* (Rolston et al., 2008) and are in the process of validating our protocols. In general, the rapid advances in real-time capabilities of computers and embedded systems, in tandem with progress in multielectrode recording and stimulation in awake animals (including humans), promise an exciting time for closed-loop strategies for treating a wide array of neurological and psychiatric disorders (Berger and Glanzman, 2005; DiLorenzo and Bronzino, 2008; Nicolelis, 2008).

Chapter 4

A low-cost multielectrode system for data acquisition enabling real-time closed-loop processing with rapid recovery from stimulation artifacts[5]

[5] A version of this chapter has been previously published: J. D. Rolston, R. E. Gross, S. M. Potter (2009). "A low-cost multielectrode system for data acquisition and real-time processing with rapid recovery from stimulation artifact." *Frontiers in Neuroengineering* 2:12. It is available online at http://www.frontiersin.org/neuroengineering/paper/10.3389/neuro.16/012.2009/

Abstract

Commercially available data acquisition systems for multielectrode recording from freely moving animals are expensive, often rely on proprietary software, and do not provide detailed, modifiable circuit schematics. When used in conjunction with electrical stimulation, they are prone to prolonged, saturating stimulation artifacts that prevent the recording of short-latency evoked responses. Yet electrical stimulation is integral to many experimental designs, and critical for emerging brain-computer interfacing and neuroprosthetic applications. To address these issues, we developed an easy-to-use, modifiable, and inexpensive system for multielectrode neural recording and stimulation. Setup costs are less than US$10,000 for 64 channels, an order of magnitude lower than comparable commercial systems. Unlike commercial equipment, the system recovers rapidly from stimulation and allows short-latency action potentials (<1 ms post-stimulus) to be detected, facilitating closed-loop applications and exposing neural activity that would otherwise remain hidden. To illustrate this capability, evoked activity from microstimulation of the rodent hippocampus is presented. The system is modular, in banks of 16 channels, and flexible in usage: while primarily designed for *in vivo* use, it can be combined with commercial preamplifiers to record from *in vitro* multielectrode arrays. The system's open-source control software, NeuroRighter, is implemented in C#, with an easy-to-use graphical interface. As C# functions in a managed code environment, which may impact performance, analysis was conducted to ensure comparable speed to C++ for this application. Hardware schematics, layout files, and software are freely available. Since maintaining wired headstage connections with freely moving animals is difficult, we describe a new method of electrode-headstage coupling using neodymium magnets.

Introduction

Perhaps the most widely used method for studying electrical population activity in neuronal networks is the multielectrode array (MEA), either as a microwire array *in vivo* (Buzsaki, 2004) or a substrate-integrated array *in vitro* (Taketani and Baudry, 2006b). While such passive recordings provide useful data, recent advances in basic science and therapeutic applications require active manipulation of tissue with electrical stimulation (Berger and Glanzman, 2005; Potter et al., 2006; Arsiero et al., 2007; Novellino et al., 2007; Kipke et al., 2008). Furthermore, nuanced, spatially precise stimulation will likely be critical for novel neural prostheses, for example, the hippocampal-cortical prosthesis proposed by Berger et al. (2005).

Interrogating and interacting with neural tissue at such a precise scale will benefit from systems that both stimulate and record from the same array of electrodes. Using the same electrodes for stimulation and recording permits greater spatial coupling for input and output mappings, and also reduces the total number of necessary electrodes. However, commercially available systems for conducting multielectrode recordings in freely moving animals (e.g., Plexon, Blackrock, Neuralynx) are neither designed nor tested for concurrent stimulation. Since some responses to electrical stimulation occur within 1 ms of stimulus offset (Olsson et al., 2005), the ability to recover rapidly from stimulation artifacts is essential for observing evoked activity without bias. Therefore, the ability to record neural activity—including single unit, multiunit, and local field potential (LFP) activity—within milliseconds of a stimulus pulse is crucial for driving the field of recurrent (closed-loop) brain computer interfaces forward (Potter et al., 2006; Kipke et al., 2008).

With this goal in mind, we developed a multiple-microelectrode recording system for use in freely moving animals that recovers rapidly (<1 ms) from stimulation artifacts. As a benefit of developing the hardware and software in-house, we are able to reduce the cost of this system to less than US$10,000 for 64 channels, and also release the hardware and software designs publicly with open-source licensing. Such licensing allows for easy adoption of our system by other laboratories, and encourages community modification and improvement. This current effort advances our previous work on creating low-cost, closed-loop technology for *in vitro* applications (the open-source MeaBench software (Wagenaar et al., 2005a), the RACS stimulation system (Wagenaar and Potter, 2004), and the artifact suppression algorithm SALPA (Wagenaar and Potter, 2002)), with the primary goal of supporting research in freely moving animals, but also modernizing and simplifying user interfaces and providing more hardware modularity.

For our current system, we minimized artifact duration and reduced system cost by reducing the number of amplification stages and the system gain. Most contemporary systems for multielectrode recording have two stages of amplification: a headstage amplifier, close to the animal or preparation, and a larger amplifier later in the signal chain (sometimes mislabeled as a “preamp”). This traditional two-stage acquisition model is unnecessary, however, given advances in amplifier miniaturization and A/D resolution. For instance, data acquisition cards with 16-bit resolution and a range of ±100 mV, like the M-Series cards from National Instruments, have theoretical resolutions of 3 nV. This resolution would be adequate in itself to record neural signals without amplification. Moreover, modern headstages with gains of 100 or 1000 increase the signal amplitude to levels in excess of what is necessary to record high resolution data, relaxing the requirements of A/D performance. These two advances obviate the need for a second stage of amplification, which represents an unnecessary cost, as well as

a potential source of artifact during experiments with electrical stimulation. Indeed, many experimental recording systems already rely on single, integrated amplifiers (Mavoori et al., 2005; Blum et al., 2007; Santhanam et al., 2007; Brown et al., 2008; Imfeld et al., 2008; Ye et al., 2008).

Below, we first describe our system and its components, based on the advances of high resolution A/D cards and high gain headstages. This is followed by a detailed characterization of system and software performance, including an analysis of stimulation artifacts, compared to those observed on a benchmark system (a commercially available Plexon system). These artifacts are further examined *in vivo*, illustrating field potential and action potential responses to microstimulation in the anesthetized and unanesthetized rodent hippocampus, along with data from a microstimulated epileptic animal. This data confirms the performance of the system (i.e., <1 ms recovery from artifact), speaks to the nature of population spikes (Andersen et al., 1971), and shows that high frequency oscillations (~300 Hz), an important phenomenon in epilepsy (Rampp and Stefan, 2006), can be triggered by microstimulation. Finally, we comment on the novelty of the design, compared to other systems described in the literature, and note an alternative configuration of the system which supports recording from substrate-integrated MEAs *in vitro*. Circuit designs, schematics, and software are all freely available online at http://www.johnrolston.com/.

System Design

System overview

The chief design criteria were 1) to obtain rapid recovery (<1 ms) from stimulation artifact, 2) produce a modular system which costs <$10,000 for 64-channels, and 3)

create open-source software that can run on a standard desktop computer. The resulting system for microelectrode recording from freely moving animals (Figure 4-1, case ❶) is composed of 1) a head-mounting amplifier (i.e., headstage), 2) stacked interface PCBs providing power to the headstage and analog filtering of the recorded signals, 3) a data acquisition card, 4) a standard desktop computer, and 5) control software. These components are described in detail below. Variants of the system are possible by replacing different components (e.g., Figure 4-1, case ❷ creates a hybrid Plexon system, and Figure 4-1, case ❸ shows an *in vitro* arrangement, using a MultiChannel Systems (Reutlingen, Germany) preamplifier).

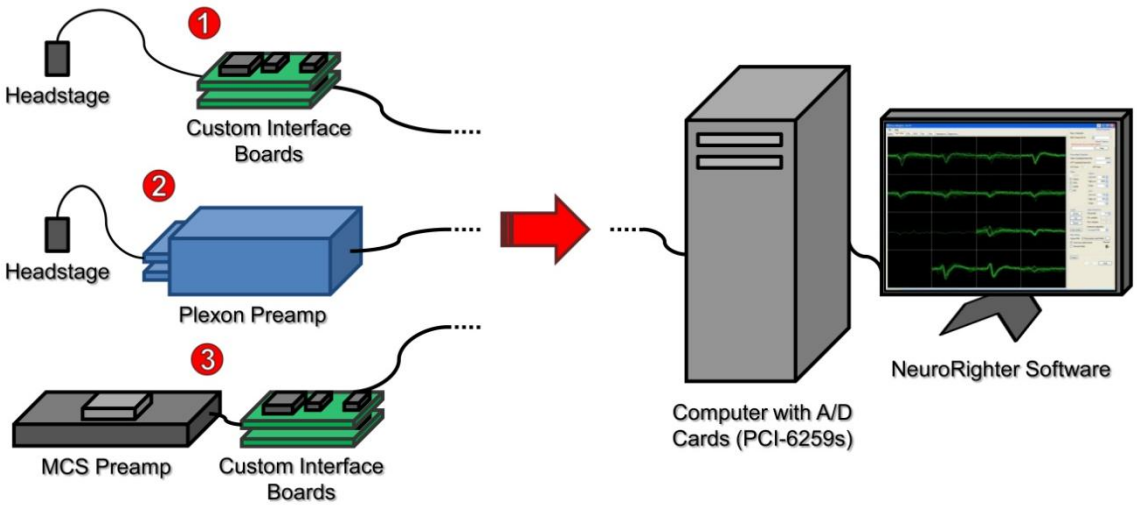

FIGURE 4-1. System Overview Illustrating Multiple Use Cases. ❶ A head-mounting amplifier (headstage) buffers multielectrode signals and sends them to custom interface PCBs. These boards provide filtered power to the recording headstage and an analog band-pass filter for the acquired neural signals. ❷ A Plexon headstage sends amplified neural signals to a Plexon preamplifier, which provides further amplification and band-pass filtering for the acquired signals. ❸ A MultiChannel Systems (MCS) preamplifier amplifies and filters neural signals from substrate integrate MEAs. Power is supplied by custom interface boards, as in ❶. In all cases, signals are digitized with a National

Instruments PCI-6259 data acquisition card, hosted by a standard desktop computer. Acquisition, visualization, and recording are controlled through our open-source NeuroRighter software.

Recording headstage

Neural signals are amplified by one or more 16-channel head-mounting amplifiers with 100× gain (Triangle Biosystems, Inc. (TBSI); Durham, NC, USA), suitable for recording from awake, behaving animals. The headstage weighs <0.75 g and utilizes an 18-pin Omnetics Nano connector with 6 guide posts to interface with microwire arrays (Omnetics Connector Corporation; Minneapolis, MN, USA). This is a standard connector, whose mate is used by probe manufacturers such as TDT (Tucker-David Technologies; Alachua, FL, USA), NBLabs (Denison, TX, USA), MicroProbe Incorporated (Gaithersburg, MD, USA), and Neurolinc Corporation (New York, NY, USA). Via an adaptor (available, for example, from Plexon Inc. (Dallas, TX, USA)), this connector can also interface with silicon probes from NeuroNexus Technologies (colloquially “Michigan probes”; Ann Arbor, MI, USA), which do not use Omnetics connectors. The recording headstage has 17 amplified inputs (16 signal channels and one reference channel) and a ground connection. The ground connection is ultimately connected to earth (i.e., “chassis” ground) further in the signal chain. The headstage provides 18 output channels: the 17 amplified inputs (16 signal channels and one reference) and one channel of “buffered ground” (which provides a buffered representation of the ground potential at the headstage). Either the buffered ground or reference channel can be used for subsequent differential amplification, recording, or data acquisition. The headstage has built-in filtering, with −3 dB points at 0.8 Hz and 22 kHz. Also, the headstage is DC-coupled, with a gain of 1× at 0 Hz.

Headstage stability: magnetic anchoring

Wired headstages, regardless of manufacturer, tend to unplug from the rat's microwire array connector during long recordings. Various methods exist for dealing with this (metal clips, locking headstages, plastic connector shrouds, etc.). We have employed high-strength magnets. Grade N45 neodymium magnets measuring 0.25 × 0.125 × 0.125 inches (CMS Magnetics; Plano, TX, USA) were attached to the microwire array's connector and the recording headstage's connector, so that the magnets would attract when the recording headstage and array were apposed (Figure 4-2). The magnets were fixed to their respective components with cyanoacrylate glue. This had no detectable effect on RMS noise levels ($P = 0.44$, paired t-test). This is to be expected, since the magnet is stationary in respect to the electrodes and recording headstage. The only movement relative to the magnetic field will come from the tethering wires, which make small-angle movements in relation to the field, originate ~20 mm distal to the magnets, and are oriented largely parallel to the magnetic field lines.

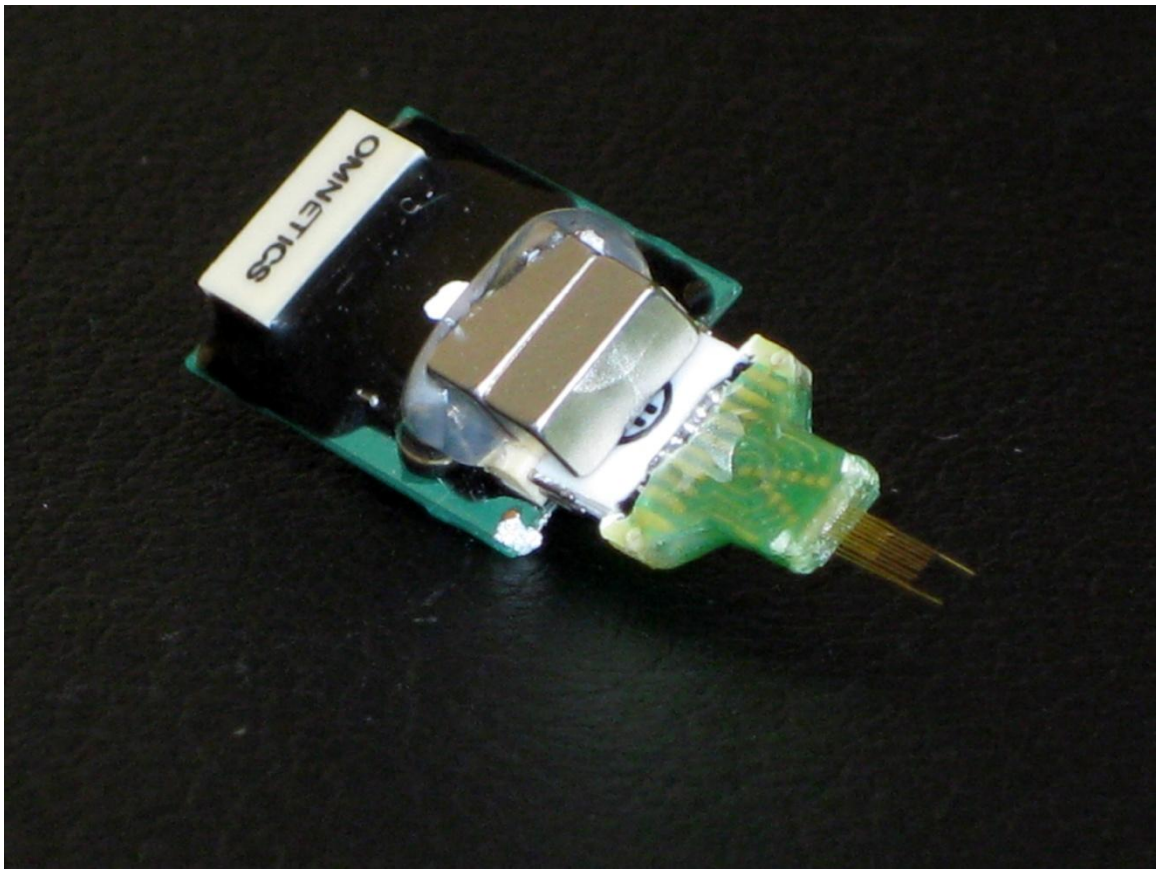

FIGURE 4-2. Neodymium magnets to secure headstage. Strong, "rare earth" magnets are glued to both the implanted microwire array, and the recording headstage. These magnets ensure a firm connection during normal animal movement, while nevertheless allowing the connection to break with sufficiently high forces (e.g., the experimenter's desire to end a recording, or an animal's particularly violent motions). A breakable connection helps to prevent loss of the acrylic headcap.

Interface boards

Design

The interface printed circuit boards (PCBs) are a collection of stacked boards with two or more levels (Figure 4-3A-B). The top board provides power supply filtering and voltage regulation to the remaining boards. The lower boards, of which there can be an arbitrary number, provide analog filtering for the acquired neural signals and provide further power supply filtering and voltage regulation for a recording headstage. Each of these

lower boards is linked to one 16-channel headstage. The boards communicate and send power via “stackthrough” connectors (Samtec; New Albany, IN, USA), making them readily modular for systems with higher channel count.

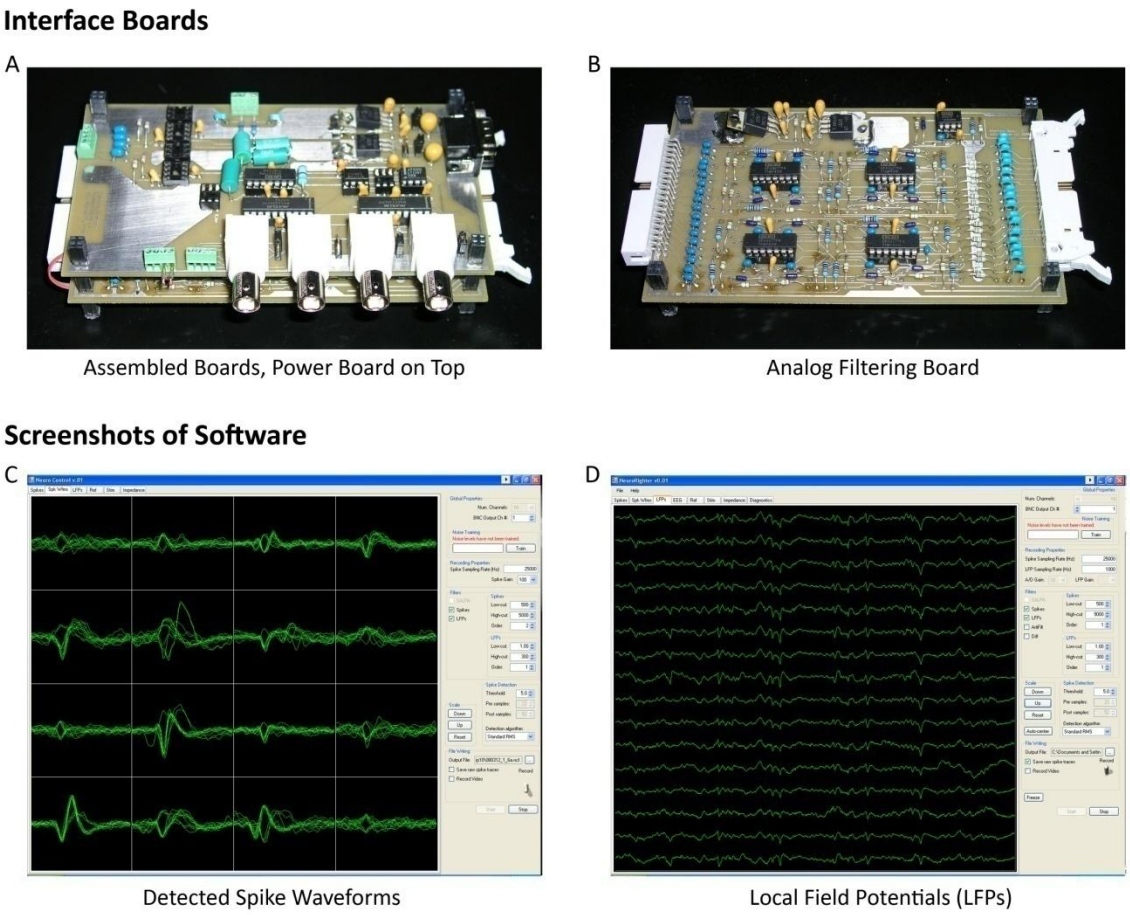

FIGURE 4-3. Photographs of Interface PCBs and Screenshots of NeuroRighter Software. (A) The stacking of one power board and an analog filter board is shown. Components on the power board handle power filtering and voltage regulation (upper right of board). Additional components are for future stimulation and EEG-recording applications (Rolston et al., 2007b, 2008), not described in this article. The power board and filtering board beneath are connected with stackthrough connectors. (B) Analog filtering boards provide a regulated power supply to each recording headstage and filter acquired data from each channel (including the reference channel) through a two-pole active high-pass filter (ICs, resistors, and capacitors on the board’s left and middle) and a passive one-pole low-pass filter (resistors and capacitors on right of board). (C) The open-source NeuroRighter software provides visualization of detected action potential (“spike”) waveforms across all recording channels (16, shown in a 4×4 grid). Multiple methods for action

potential detection are available. (D) LFPs are recorded from each channel by digitally band-pass filtering the raw data and downsampling. Five seconds of data are drawn for each of 16 channels. Recordings are from the hippocampus of an awake and behaving rat (see Experimental Methods).

PCB schematics and layouts were designed using version 2.1 of the free PCB123 software package (http://www.pcb123.com). The board layouts and schematics are available under the Creative Commons Attribution-Share Alike 3.0[6] license, which permits free modification and replication of the work.

The 4-layed PCBs measure 6 by 3.5 inches (15.2 x 8.9 cm) and use standard dual inline package (DIP) ICs and through-hole components, allowing users to easily assemble the boards by hand. The PCBs do not require solder masks or silkscreens, which would increase the boards' cost. The boards contain solely analog components, so division of grounds between analog and digital domains is unnecessary.

The interface boards are connected to the A/D cards by flat, 34-conductor, shielded cables (3M; St. Paul, MN, USA). The thirty-four conductors alternate between ground and signal, with the ground minimizing cross-talk between channels. The 17 signal-carrying lines are used for the 16 recording channels and one reference channel. The shielding around the entire cable is grounded, reducing unwanted electromagnetic interference (EMI).

Analog filtering.

To prevent aliasing and reduce noise, acquired neural signals (and the reference channel) are band-pass filtered within the interface board. The band-pass filter is composed of a two-pole active high-pass filter, followed by a passive low-pass filter (Figure 4-4). The active high-pass filter uses a voltage-controlled voltage-source (VCVS)

[6] http://creativecommons.org/licenses/by-sa/3.0/us/

topology (Horowitz and Hill, 1989), which requires one operational amplifier (op-amp) per channel. We selected the OPA4277 quad op-amp (Texas Instruments; Dallas, TX, USA) for its low noise (1.1 μV RMS noise from 1 Hz – 10 kHz), high precision (±10 μV typical), and wide power supply range (±2 to ±18 V). However, the pinouts of quad op-amp packages are standardized, so users may switch to compatible ICs if needed. High precision op-amps are used to ensure that signals are recorded with high fidelity.

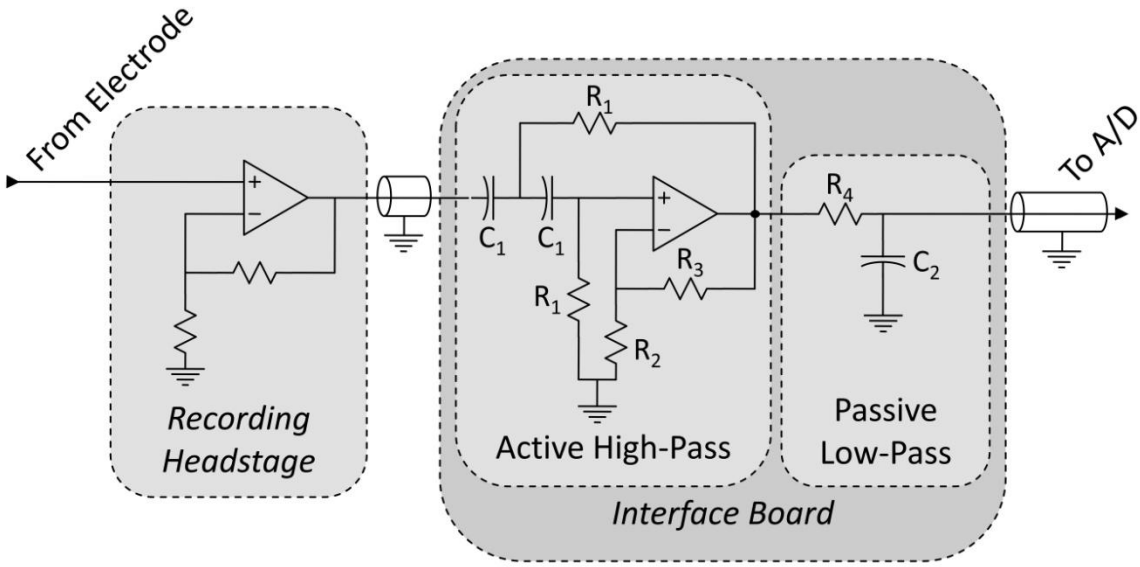

FIGURE 4-4. Signal Chain from Electrode to A/D Card. Signals originate from a microwire electrode and are amplified within the recording headstage in reference to a common ground. These signals propagate to the interface PCB, where they are band-pass filtered, and then to the A/D card. The band-pass filter is composed of a two-pole active high-pass filter (voltage-controlled voltage-source topology, as in (Horowitz and Hill, 1989)) and a one-pole passive low-pass filter. Resistors labeled R_1 and capacitors labeled C_1 determine the −3dB point of the high-pass filter, and R_4 and C_2 determine the −3dB point of the low-pass filter. R_2 and R_3 determine the nature of the high-pass filter (e.g., Butterworth, Bessel, etc.).

Filter poles are set by changing the circuit's capacitors and resistors (R_1, C_1, R_4 and C_2 in Figure 4-4). The −3dB point is determined by the equation $f_C = 1/(2\pi RC)$ for both the low- and high-pass filters, provided the active filter is a Butterworth filter (Horowitz and Hill, 1989). The class of high-pass filter (Butterworth, Bessel, Chebyshev) can be changed

by manipulating R_2 and R_3 (taking care to revise f_C, if creating a Bessel or Chebyshev filter, since doing so modifies the above equation by a constant depending on the filter's order) (Horowitz and Hill, 1989). For our purposes of recording action potentials and LFPs simultaneously, we prefer a band-pass filter from 1 Hz to 8840 Hz, with a Butterworth high-pass filter (Butterworth filters have the flattest possible passband (Horowitz and Hill, 1989)). For our setup, this corresponds to R_1 = 150 kΩ, R_2 = 100 kΩ, R_3 = 58.6 kΩ, R_4 = 180 Ω, C_1 = 1 μF, and C_2 = 100 nF.

Recalling the 0.8 Hz –3 dB point of the recording headstage, the –3 dB point of the entire system (recording headstage, interface boards, A/D card) can be calculated from the product of each stage's transfer function. For the one-pole filter of the recording headstage, the transfer function is

$$G(f) = \frac{100 * (2\pi f) * RC}{\sqrt{1 + \left((2\pi f)RC\right)^2}} \qquad (1)$$

where $G(f)$ is the gain at frequency f (in Hz) and RC = 0.2 for a filter with a –3 dB point at 0.8 Hz. The constant 100 accounts for the headstage passband gain. For the two-pole active filter, the transfer function is

$$G(f) = \frac{(2\pi f)^2}{(2\pi f)^2 + (2\pi f) * 2 * f_c + {f_c}^2} \qquad (2)$$

where $f_c = 1/(2\pi R_1 C_1) = 1$ for a –3 dB point at 1 Hz. The product of the transfer functions, when computed, yields a combined, system-wide –3 dB point of 1.4 Hz (the A/D card has negligible influence on the high-pass pole).

The system's VCVS filters provide a small gain. The gain depends on R_2 and R_3 in Figure 4-4 and is equivalent to $1 + (R_3/R_2)$. For our parameters, the gain is 1.6, leading to a system gain of 160.

It is important to ensure that the impedances of sources to the filter are low and the impedances of sinks are high to avoid loading the filter. The output impedance of the TBSI recording headstage is 158 Ω at 1 kHz (manufacturer's specifications)—much lower than the impedance of the high-pass filter. Similarly, the input impedance to the A/D card, the PCI-6259 (National Instruments; Austin, TX, USA), is >10 GΩ in parallel with 100 pF, much higher than the passive low-pass filter's impedance. These conclusions were verified in a PSPICE simulation which included the headstage and A/D card impedances. The simulation was conducted in OrCAD Capture CIS version 16 (Cadence Design Systems, Inc.; San Jose, CA, USA). The −3dB points were as expected and a gain of 1.6 was realized.

Power supply.

The interface boards have a wide supply range, ±2 to ±18 V, determined by the OPA4277 op-amps. The recording headstage, however, is constrained to a supply of ±2.25 to ±2.75 V. A supply voltage of ±2.5 V, therefore, would be adequate for the entire system. However, one of our design constraints is to minimize stimulation artifacts. While the TBSI headstage recovers from voltage transients outside its supply range within μs (see Results section below), it is possible that the OPA4277 op-amps, when configured as filters, might experience more lengthy saturation when input signals approach the power supply rails, leading to longer artifacts. To guard against this possibility, we utilize two separate bipolar supply voltages for the interface boards: one at ±2.5 V for the headstages and one at ±6 V for the remaining ICs (i.e., the components controlling

power supply and analog signal filtering). The additional headroom for the ICs helps minimize the chance of op-amp saturation.

The headstage power supply is regulated to ±2.5 V by one LM317 adjustable positive voltage regulator and one LM337 negative voltage regulator (ON Semiconductor; Phoenix, AZ, USA) per headstage. The regulators and their associated passive components further reduce power supply noise (0.025% line regulation; manufacturer's specifications). An additional pair of LM317 and LM337s is present on the power supply board (the top board) to regulate the power to the interface board ICs (i.e., the op-amps for analog filtering). This initial pair of regulators (but not those for the headstages on each analog filtering board) can be bypassed with jumpers, if desired. This might happen if, for instance, the only available power supply is <9V, in which case the regulators would not have the required voltage overhead to properly generate a ±6 V supply for the ICs.

In our setup, the system's ±6 V power supply is generated by two rechargeable 6 V, 20 amp-hour lead-acid batteries (Power-Sonic Corp.; San Diego, CA, USA). The ground of the system is tied to the common terminal of the two batteries, which is then tied to the chassis ground of the data acquisition computer (and hence, the A/D cards). Using batteries minimizes ground loops and line noise.

Data acquisition cards

One 32-channel PCI- or PCIe-6259 data acquisition card (National Instruments; Austin, TX, USA) is used for every set of two 16-channel recording headstages and corresponding interface boards. The 16-bit A/D cards have programmable ranges from ±100 mV to 10 V, and a maximum sampling rate of 1 MHz (for the aggregate of channels;

31,250 Hz per channel). With the 160× gain of the headstage and interface boards, these specifications correspond to a worst-case voltage resolution of 38 nV. The A/D cards take measurements either in reference to system ground ("referenced single-ended," in the National Instruments literature) or to a common reference for each bank of 16 channels ("non-referenced single-ended"). We prefer the latter arrangement, using the low-impedance, deinsulated 17th electrode of each microwire array as a reference electrode. Subtracting this common signal reduces movement artifact, stimulation artifact, and other common-mode interference. However, using an active reference increases RMS noise compared to a grounded reference (Figure 4-7; see Results below).

Software

To visualize, record, and process acquired neural signals, we created the *NeuroRighter* software application (Figure 4-3C-D). We had three goals for this software. First, it had to be easy to use and install, for neurobiologists with no programming experience and little time to debug a new application. Second, it had to be easily extensible, so that new features could be added both by us and other users. Lastly, it had to be fast and robust enough to run on conventional desktop computers.

To address the first goal, ease-of-use, we developed the application for the Windows XP and Vista operating systems, since these platforms combined account for roughly 90-95% of installed operating systems.[7] Also, the application is graphical and hosted as a single process, rather than separate client and server applications, again to streamline usage. To make the software extensible, it has been developed under the GNU Public

[7] All sites accessed October 2008: http://www.xitimonitor.com/; http://onestat.com/html/aboutus_pressbox58-microsoft-windows-vista-global-usage-share.html; http://www.w3schools.com/browsers/browsers_os.asp; http://w3counter.com/globalstats.php; http://marketshare.hitslink.com/

License[8] (GPL), version 3, making it and its derivatives free for noncommercial use. Because the software is open source, users can freely extend the code to suit their needs, and validate the code to protect against software errors, or "bugs" (Raymond, 2001). Lastly, the software was written in C#, a modern, type-safe, object-oriented language (Liberty and Xie, 2008), with aspects making it potentially easier to learn and program than the more widely used C/C++ (Wilkens, 2003; Chandra and Chandra, 2005).

Performance of C# compared to C/C++.

Some features of managed languages like C# incur a performance penalty (e.g., garbage collection). If this penalty is too high, it would conflict with our third goal of acceptable performance on a standard desktop computer. To ensure that C# performs acceptably for data acquisition software, we created test programs to evaluate the running time of a simple algorithm. The algorithm mimics a type of operation done on a large buffer of acquired data. In this case, random data is copied to a new array with an arithmetic operation. This is similar, for instance, to a filtering operation, though filtering will have more arithmetic operations. The pseudo-code follows:

```
//Create input and output arrays of size 64 x 25000 (channels x samples)
dataIn = double[64][25000]
dataOut = double[64][25000]

elapsedTime = 0 //keeps track of algorithm's running time

//Run a simple arithmetic operation on each sample of each channel.
//Repeat 1000 times.
do 1000 times
        startTime = current system time
        for i from 1 to 64 //for each channel
                for j from 1 to 25000 //for each sample
                        dataOut[i][j] = 1.01 * dataIn[i][j]
                end
        end
        stopTime = current system time
        elapsedTime = elapsedTime + (stopTime – startTime)
end
```

[8] http://www.gnu.org/copyleft/gpl.html

```
//Display averaged running time
print elapsedTime/1000
```

The runtime of the above algorithm in C++ was 9.34 ms, and in C# 9.25 ms, suggesting C# is as fast (actually, faster in this example) as C++ for typical operations in our domain.

Programming environment and libraries.

Software development was carried out with Visual Studio 2008 (Microsoft Corp.; Redmond, WA, USA) and the Measurement Studio 8.6 component libraries (National Instruments). Programming was conducted on an Intel Xeon 3.2 GHz computer with 2 GB of RAM and the XP, Vista 32-bit, and Vista 64-bit operating systems (to ensure compatibility with all three).

Real-time signal processing.

An overview of the signal processing sequence is given in Figure 4-5. Briefly, raw data, acquired at 25 kHz, are band-pass filtered into two separate streams: one for detecting action potentials and multi-unit activity, and another for following LFPs. Action potentials ("spikes") are best detected in a high frequency band, such as 500-9000 Hz. LFPs are band-passed typically from 1-500 Hz, and downsampled (the sampling rate is user-selectable; we prefer 2000 Hz). We generally record LFPs with a wide band (up to 500 Hz) to capture high frequency events, such as ripples and fast ripples (Rampp and Stefan, 2006). Frequency cut-offs for the digital filters are user-selectable for arbitrary frequencies, as are the number of poles for each filter.

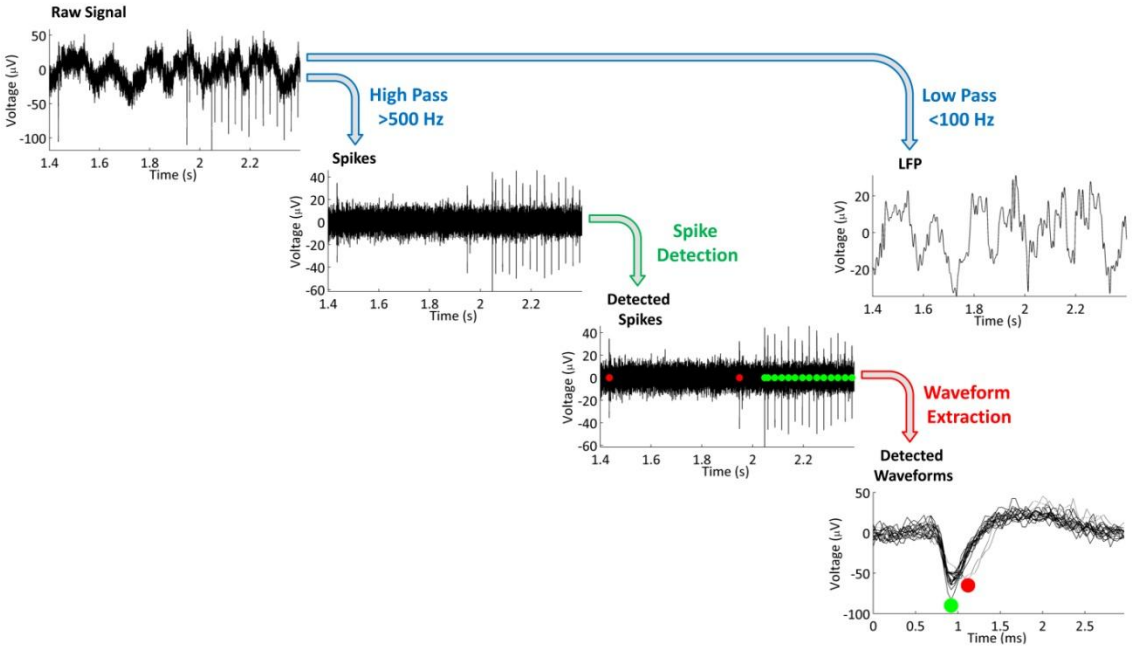

FIGURE 4-5. Signal Processing Steps. A raw signal is acquired, then split into two signals by digital filtering (blue arrows at top of figure). Low frequency data is downsampled and referred to as the local field potential (LFP). High frequency data is used to detect action potentials, or "spikes." A user-defined threshold is used to detect candidate spike waveforms (green arrow in middle of diagram). Detected action potentials are indicated with red and green circles. Multiple three ms waveforms are extracted (red arrow, lower right). The two colors, red and green, indicate that the spikes likely arise from different cells, given their different waveforms. Data were recorded with our system from the dorsal hippocampus (CA3) of an awake, behaving rat.

Action potentials are detected by locating points at which the filtered signal crossed a user-defined threshold. There are multiple methods available in the NeuroRighter software for calculating this threshold in real-time: fixed RMS, adaptive RMS, adaptive median (Quiroga et al., 2004), and Daniel Wagenaar's "LimAda" method (Wagenaar et al., 2005a). Spikes are detected when they cross $\pm(K \times Th)$, where K is a user-selected constant (typically 5.0), and Th is the threshold calculated by the selected method (e.g., fixed RMS). A user-determined number of sampling points, typically 75 (3 ms at a 25 kHz sampling rate), surrounding the threshold crossing are saved to file (for offline spike sorting (Lewicki, 1998)) and visualized (to assay the quality of recordings).

Experimental methods

Two sets of experiments were conducted: 1) artifacts were evaluated with either banks of resistors or MEAs submerged in artificial cerebrospinal fluid, using a Plexon system as a benchmark, and 2) artifacts were evaluated in vivo in anesthetized and unanesthetized animals.

Stimulation Artifact Testing

Tests for stimulation artifact were conducted with a custom-built stimulator, that can interface with conventional recording headstages, interposed between the headstage and electrodes (Rolston et al., 2007b). With this arrangement, we could monitor stimulation artifacts on the stimulating channel and neighboring channels. We used two systems for comparison: 1) a conventional system, consisting of a Plexon headstage (gain 1×) and preamplifier (gain 1000×) (Figure 4-1, scenario ❷) and 2) the system described in Section 2 above (Figure 4-1, scenario ❶). For each setup, we ran two experiments. First, ±10 μA and ±50 μA biphasic stimulation pulses (negative, cathodic phase first) were delivered when all inputs were connected through 560 kΩ resistors to ground (Plexon headstage tester unit; Plexon Inc.). Since the stimulator is interposed between the recording headstage and electrodes, the stimulation was delivered through the resistor to ground as well. Second, ±10 μA biphasic stimulation pulses (cathodic, negative phase first) were delivered through a microwire array (see section 3.1.1) submerged in artificial cerebrospinal fluid (ACSF; formulation as in Hammack et al. (2007)). This third arrangement approximates conditions *in vivo*. All pulses were 800 μs in length, with 400 μs per phase, a length determined by empirical measurements of stimulus efficacy (Wagenaar et al., 2004). Ten presentations of each pulse were recorded and pulses were

delivered at 0.25 Hz. Responses from non-stimulating electrodes were recorded by an adjacent electrode (175 μm distant).

Hereafter, we define an artifact as any non-physiological change in recorded signals induced by a stimulation pulse. With this definition, artifacts can last for appreciably long times, while still permitting useful information to be recovered before the artifact's end. For instance, by digitally filtering artifacts, action potentials can be detected before the influence of the stimulation pulse on the electrode has ceased (Wagenaar and Potter, 2002) (i.e., before the artifact has ended by our definition). On the other hand, there are components of an artifact that will never yield useful data, such as when the artifact induces amplifier saturation (or "railing"). To reconcile these ideas, we measured induced artifacts with two metrics, *desaturation* and *recovery*, covering the above described best and worst case scenarios. *Desaturation* refers to the point at which the amplifier output is no longer at the power supply rail, and when action potentials or other useful data could in principle be detected. *Recovery* refers to when the signals return and remain within 100 μV of baseline, which we see as a time when useful data is almost surely accessible if present, though perhaps requiring some form of filtering. The actual time at which action potentials could be recovered following a stimulation pulse falls somewhere between these two metrics, depending on the recording system and the filtering methods used.

Animal surgeries and recordings

To prove the system's functionality in awake, behaving animals, microwire array recordings were taken from the dorsal hippocampi of adult male Sprague-Dawley rats weighing >350 g (Charles River Laboratories; Wilmington, MA, USA). Animal work was conducted in accordance with the National Institutes of Health *Guide for the Care and*

Use of Laboratory Animals and approved by the Emory University Institutional Animal Care and Use Committee. Rats were anesthetized with 1.5-3.0% inhaled isoflurane and given a subcutaneous injection of buprenorphine (0.05 mg/kg) to minimize pain. A craniectomy was made over the right dorsal hippocampus, centered at 3.5 mm posterior and 2.8 mm lateral to bregma. The dura was incised with a sterile syringe needle and a microwire array (Tucker Davis Technologies) was implanted. The array had sixteen 33 μm diameter tungsten electrodes with polyimide insulation arranged in two rows of 8 electrodes, with 175 μm between electrodes within a row and 1 mm between rows. The two rows had different lengths, 4.0 mm and 2.7 mm, with the former directed at the CA3 region of the hippocampus, and the latter at the more dorsal CA1 region. The microwire arrays had integrated reference and ground wires, 2 mm longer and with the final 2 mm de-insulated, which were positioned collinear with the longer row of the array. The array was positioned at a 50° angle to midline (counter-clockwise rotation, with the posterior end swung laterally) to match the contours of the hippocampus. Electrodes were lowered while recording activity in order to attain correct positioning, usually ending when the longer electrodes were ~3 mm ventral to pia.

When the recordings stabilized, the craniectomy was sealed with cyanoacrylate glue (Loctite; Rocky Hill, CT, USA), skull screws were implanted (Plastics One; Roanoke, VA, USA), and dental acrylic (OrthoJet; Lang Dental; Wheeling, IL, USA) was applied to secure the array's connector. The rats returned to their normal housing, and rested and recovered post-operatively for 5-8 days before recordings began.

Epileptic animals

Epileptic animals were prepared as above, but with a single injection of 25 ng of tetanus toxin (Sigma Aldrich, St. Louis, MO, USA) in 0.5 μl phosphate buffered saline with 0.2%

bovine serum albumin (Jefferys and Walker, 2005). The injection, using a pulled glass pipette and a stereotactically mounted injector (Nanoject; Drummond Scientific Co., Broomall, PA, USA), was located in the dorsal hippocampus (3.3 mm posterior and 3.2 mm lateral to bregma, and 3.1 mm ventral to pia) and occurred immediately prior to the MEA implant. The needle was allowed to equilibrate for one minute prior to injection, the injection was delivered over 3 minutes, and the needle was left in place for 5 minutes following injection to prevent reflux. Animals exhibited spontaneous seizures within 3-9 days. No mortality or morbidity from the injections was observed, consistent with previous reports (Jefferys and Walker, 2005).

Results

We successfully created a low-cost system for multielectrode recording from awake, behaving animals (Figure 4-1, scenario ❶, and Figure 4-3). Sample data from a behaving rat's hippocampus is shown in Figure 4-5. Below, we characterize the system in detail, first analyzing noise levels, gain, cross-talk, then examining stimulation artifacts and how they compare to a benchmark commercial system. Finally, we illustrate the utility of the system by providing examples of the effects of microstimulation on single cell and LFP activity in the rodent hippocampus.

Noise

Electrode-referred noise spectra, with all inputs grounded, are shown in Figure 4-6. Root-mean-square (RMS) noise values are 6.1 ± 0.2 μV (mean ± standard error across channels) when using a grounded reference, and 8.4 ± 0.2 μV when using a true reference (i.e., an active reference). The increased noise when using a true reference arises from the superposition of the reference channel's RMS noise and that of the signal

channel (i.e., the combined noise should be a factor of √2 larger). The headstage manufacturer, Triangle Biosystems, specifies the broadband RMS noise as 6.2 μV, so our system is not introducing additional noise through the interface boards, cables, or A/D conversion process. When restricted to bands containing action potential data (>300 Hz; Figure 4-6B), the RMS noise levels are 3.9 ± 0.1 μV for grounded reference, 5.5 ± 0.1 μV for true reference, and 3.4 ± 0.02 μV when using a Plexon preamplifier and headstage (directly connected to our A/D cards; scenario ❷ in Figure 4-1).

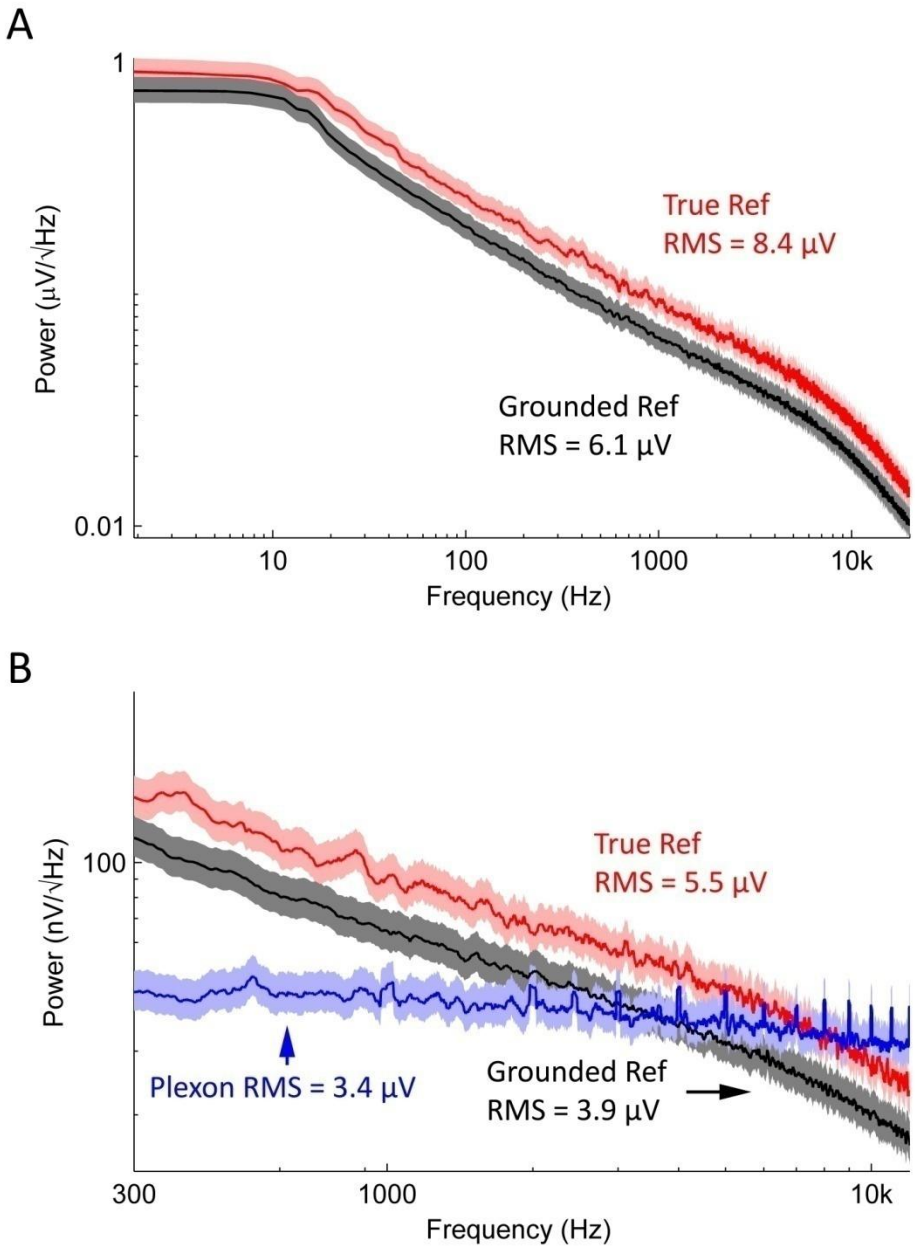

FIGURE 4-6. Noise Spectra. (A) Averaged, electrode-referred broadband spectra for a 16 channel system. Shading represents 95% confidence interval. The black curve depicts the noise spectrum with a grounded reference; the red curve shows data acquired with a true reference. (B) Noise spectra in the action potential frequency band, compared to noise spectrum from a Plexon preamplifier (blue), which has a 1-pole analog band-pass filter set to 300-8800 Hz. Red, black, and shading are as in (A). Note the harmonics present in the Plexon amplifier's spectrum. This is likely due to ground loops within the system, since the Plexon system is not battery-powered and has multiple paths to ground.

Gain and cross-talk

With manufacturer specifications and theoretical calculations, we computed a passband gain of 160× for our system, and confirmed this with a PSPICE simulation. We set the passband's –3 dB points (1.4 Hz and 8840 Hz) by choosing appropriate resistors and capacitors for the filters (see Section 2, System Design above). To verify the system's gain and –3 dB points, we used a custom-built stimulator (Rolston et al., 2007b) to deliver 100 μV amplitude sine waves in the range of 0.1 Hz to 12.5 kHz, and measured the waves' amplitudes when recorded by the system. The passband gain was 156× (43.9 dB), and the –3 dB points were located at 1.4 Hz and 8700 Hz, in agreement with our system design calculations.

We also wished to verify that the system's gain was constant across a range of input amplitudes. We tested this with a 1 kHz sine wave (the frequency range of action potentials) of varying amplitude, from 100 μV to 10 mV (the latter being far above what we expect to encounter in typical recordings). We observed an attenuation of 1 dB over this range (that is, the gain of a 10 mV input signal was measured to be ~140×, vs. the 100 μV signal's gain of 156×). This implies that recorded signal amplitudes will be reflected linearly over a wide range of physiological inputs.

Cross-talk was measured by sending a 1 mV 1kHz voltage-controlled sine wave to one channel, and recording from neighboring channels. For directly adjacent channels, the observed cross-talk was –66 dB. For non-adjacent channels, the cross-talk was slightly lower, –69 dB. This is in agreement with the headstage manufacturer's reported cross-talk (–63 dB for adjacent channels; personal communication with TBSI). Since the A/D card's specified cross-talk is –75 dB for adjacent channels, our measurements imply that

the headstage is the dominant source of cross-talk, rather than other elements of the signal chain.

Stimulation artifacts

Many conventional recording systems experience severe saturating transients when exposed to stimulation, making recording evoked neural responses difficult (Wagenaar and Potter, 2002). These artifacts stem from two sources: the electronics of the recording system and the electrode-tissue interface. The electronics can be pushed into unstable regimes when exposed to the large amplitude stimulation signals, and the stimulation electrode (since it is capacitively coupled to the extracellular medium) will require time to discharge following application of stimulus pulses (Blum et al., 2004).

Table 1. Stimulation Artifact Durations
Non-Stimulating Electrodes

Test Condition	**560 kΩ Resistor**	**ACSF**
System		
NeuroRighter		
Broadband[a]		
Recovery	<1 ms[e]	<1 ms
Desaturation	<1	<1
Spike Band[b]		
Recovery	<1	<1
Desaturation	<1	<1
Plexon		
LFP Band[c]		
Recovery	2	1300
Desaturation	<1	<1
Spike Band[d]		
Recovery	7	1.5
Desaturation	2.5	<1

[a]No digital filtering. Analog band-pass from 1.4 to 8800 Hz.
[b]Digital high-pass, 300 Hz.
[c]Analog band-pass, 1-500 Hz.
[d]Aanlog band-pass, 300-8800 Hz.
[e]All durations are in ms and in reference to stimulus offset.

To evaluate our system's artifacts, we compared the observed artifacts to those obtained using a benchmark Plexon system. To isolate the electronic component of the artifact, we used a custom-built stimulator (Rolston et al., 2007b), and delivered ±10 μA biphasic current-controlled pulses through 560 kΩ resistors connected to ground (see Section 3, Experimental Methods). Stimulating through a pure resistive load removes the capacitive effect of the electrode-tissue interface, leaving only the electronic component of the artifact. To gauge the combined effect of capacitive discharge and electronic components, we repeated these experiments (±10 μA biphasic current-controlled pulses) using a high-impedance (~200 kΩ) microwire array in ACSF. Artifact durations (in terms of recovery and desaturation; see Experimental Methods, above) are shown in Tables 1 and 2. Table 1 shows artifacts on neighboring, non-stimulated electrodes, while Table 2 shows artifacts recorded on the stimulating electrode. Average artifact waveforms for stimulation through a resistor are depicted in Figure 4-7, and waveforms for stimulation through a microwire array in ACSF are shown in Figure 4-8.

Table 2. Stimulation Artifact Durations

Stimulating Electrode

Test Condition	**560 kΩ Resistor**	**ACSF**
System		
NeuroRighter		
Broadband[a]		
Recovery	<1 ms[e]	1400 ms
Desaturation	<1	<1
Spike Band[b]		
Recovery	<1	6
Desaturation	<1	<1
Plexon		
LFP Band[c]		
Recovery	1500	1800
Desaturation	600	130
Spike Band[d]		
Recovery	7	70
Desaturation	3	1.1

[a]No digital filtering. Analog band-pass from 1.4 to 8800 Hz.
[b]Digital high-pass, 300 Hz.
[c]Analog band-pass, 1-500 Hz.
[d]Aanlog band-pass, 300-8800 Hz.
[e]All durations are in ms and in reference to stimulus offset.

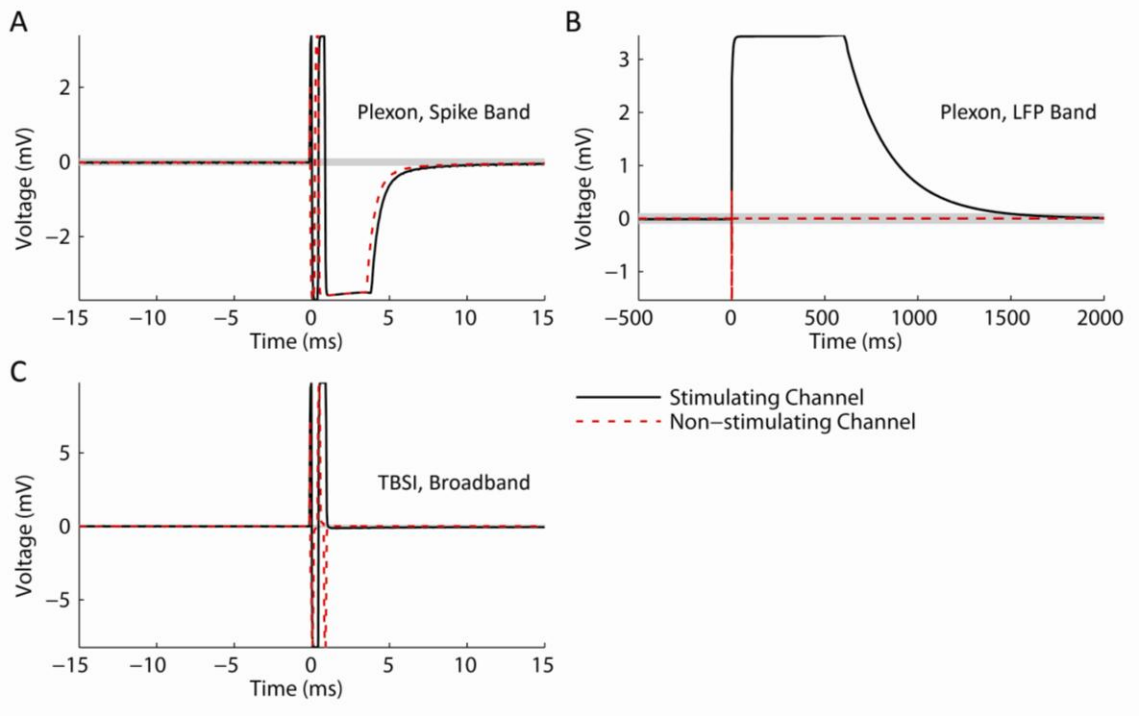

FIGURE 4-7. Stimulation through a 560 kΩ Resistor. A custom stimulator, interposed between the recording headstage and electrodes (which, in this case, were simulated by 560 kΩ resistors connected to ground), was used to evaluate stimulation artifacts on the stimulating electrode and neighboring electrodes. Stimuli lasting 800 μs were delivered at 0 ms. The average of 10 trials of ±10 μA biphasic stimuli (negative, cathodic phase first) are shown in each panel. 95% error bars are too small to be resolvable at this magnification, and are therefore not displayed. Gray bands represent the ±100 μV recovery window—see text for definition of recovery and desaturation. Artifact durations are provided in Table 1 for non-stimulated electrodes and Table 2 for stimulated electrodes. The analog band-pass filter of the Plexon spike band (A) is 300-8800 Hz. The Plexon LFP bandwidth is 1-500 Hz (B). No digital filtering is used for the TBSI-based NeuroRighter system (C).

In all cases, the NeuroRighter system performed better than the benchmark Plexon system. Additionally, the minimal artifact when stimulating through a pure resistive load suggests that artifacts observed when stimulating through electrodes in ACSF are purely due to capacitive discharge. Artifacts in ACSF on the Plexon system, however, are due to combined electronic and capacitive discharge effects.

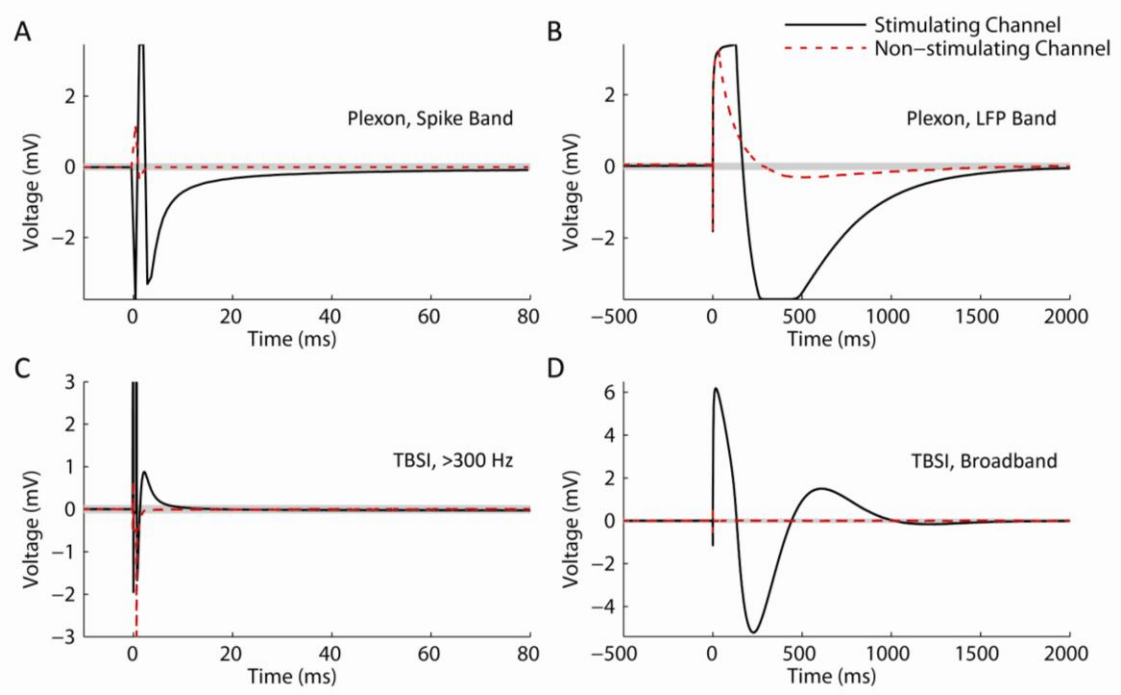

FIGURE 4-8. 10 µA Stimulation through a Microwire Array Immersed in ACSF. Biphasic (negative, cathodic phase first) pulses were delivered to each channel. The average of 10 trials is shown in each panel. 95% error bars are too small to be resolvable at this magnification, and are therefore not displayed. Gray bands represent the ±100 µV recovery window. Artifact durations for the non-stimulating electrodes are provided in Table 1, while durations for the stimulated electrode are shown in Table 2. (A) The Plexon system's spike band is 300-8800 Hz. (B) The LFP band is 1-500 Hz. (C) The TBSI headstage (NeuroRighter system) was digitally filtered >300 Hz to compare with the Plexon system's spike band. (D) No digital filtering was used for TBSI broadband recordings.

Responses to stimulation *in vivo*

The substantial reductions in stimulation artifacts under the well-controlled conditions above were encouraging, but it was important to demonstrate system performance under actual experimental conditions. We stimulated the CA1 hippocampal field of both awake and anesthetized rats at a range of current amplitudes (2, 4, 6, 8, 10, 15, 20, and 50 µA). Ten trials of each amplitude were presented in random order, to minimize neural adaptation. Responses were recovered on a non-stimulating electrode within 1 ms of stimulus offset, at stimulus amplitudes ≥4 µA (Figure 4-9A). More action potentials are recruited with higher stimulus amplitudes, culminating in a complex waveform at the

highest intensity (50 μA), in which individual action potentials are hard to discern. This complex waveform is likely the result of multiple action potentials superimposed, leading to the observed multimodal response that varies across trials (Figure 4-9A, top traces). Importantly, these short latency responses would be missed if using the Plexon system, since artifacts in that system exceed 1 ms.

Responses are recovered from the stimulating electrode within milliseconds, as well (Figure 4-10). Because the artifact is longer on the stimulating channel, directly evoked, low-jitter APs (Wagenaar et al., 2004; Bakkum et al., 2008a) are not recorded as they are on non-stimulating channels (cf. Figure 4-9). However, well-isolated APs are observed within 10 ms of the stimulation pulse at amplitudes ≤8 μA, and between 10-20 ms at amplitudes between 10-25 μA.

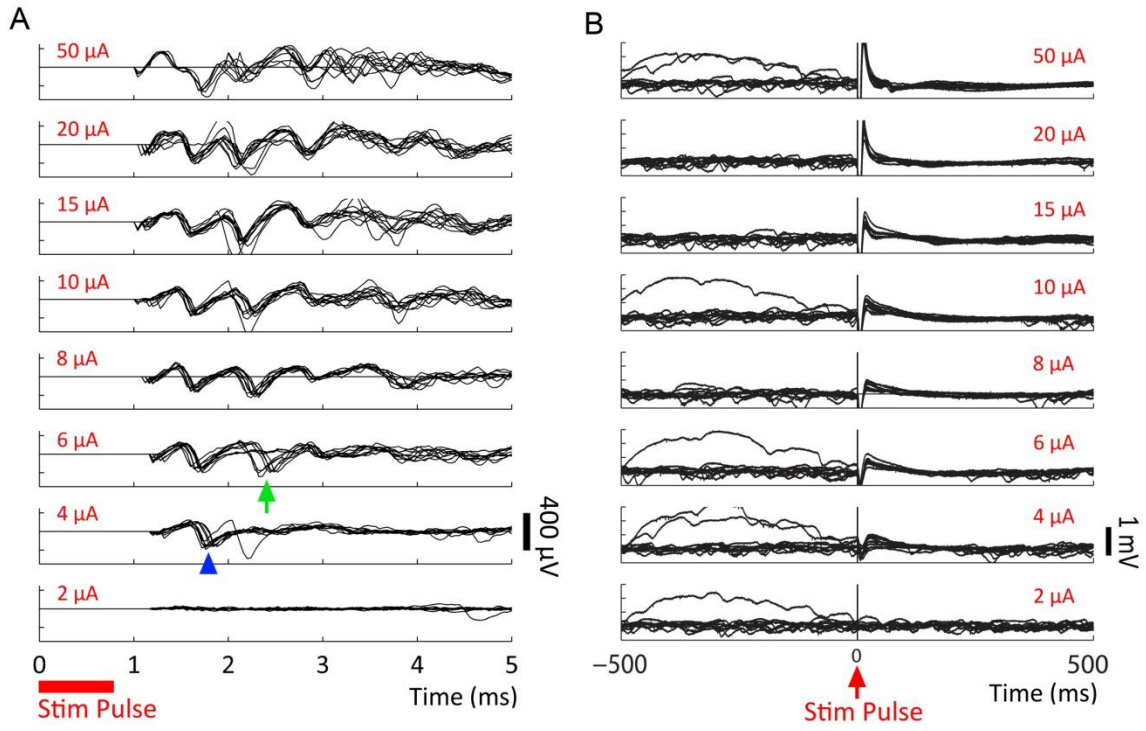

FIGURE 4-9. Directly evoked neural responses to stimulation *in vivo*. Responses to current-controlled microstimulation of increasing amplitude (amplitude shown in red) recorded from a non-stimulating electrode in an anesthetized rat's hippocampus (CA1). All pulses are cathodic, negative-phase first. Ten trials are overlaid in each panel. Trial amplitude was randomized during presentation. (A) The first evoked action potentials appear at ≥4 µA, within 1 ms of stimulus offset (blue arrowhead), followed by an additional response at ≥6 µA (green arrow). Artifacts are suppressed digitally using the SALPA algorithm (Wagenaar and Potter, 2002). (B) LFP responses show increasing durations of attenuation (flattening) in LFP activity with increasing stimulation currents, corresponding to inhibition of neuronal firing. Viewing these LFP responses would not be possible with the Plexon system, due to its long stimulation artifact.

We also successfully recorded LFPs during the same experiment (Figure 4-9B). In this case, a marked attenuation is induced in the recorded LFP responses, which increases in duration at higher stimulus amplitudes. There is also a sharp negative peak post-stimulation, followed by a broader positive deflection. These likely represent an initial depolarization of nearby tissue, followed by hyperpolarization (Andersen et al., 1971; Nunez and Srinivasan, 2006). These depolarizing peaks, likely "population spikes" (Andersen et al., 1971), appear at ≥4 µA, the same amplitudes that evoke action

potentials (Figure 4-9A). Furthermore, the noted attenuation in the LFP band appears only when the hyperpolarizing deflections are present, at ≥4 μA. Again, because other systems experience prolonged stimulation artifacts in the LFP band (Figure 4-7 and Figure 4-8), these results would be obscured if a different recording system were used.

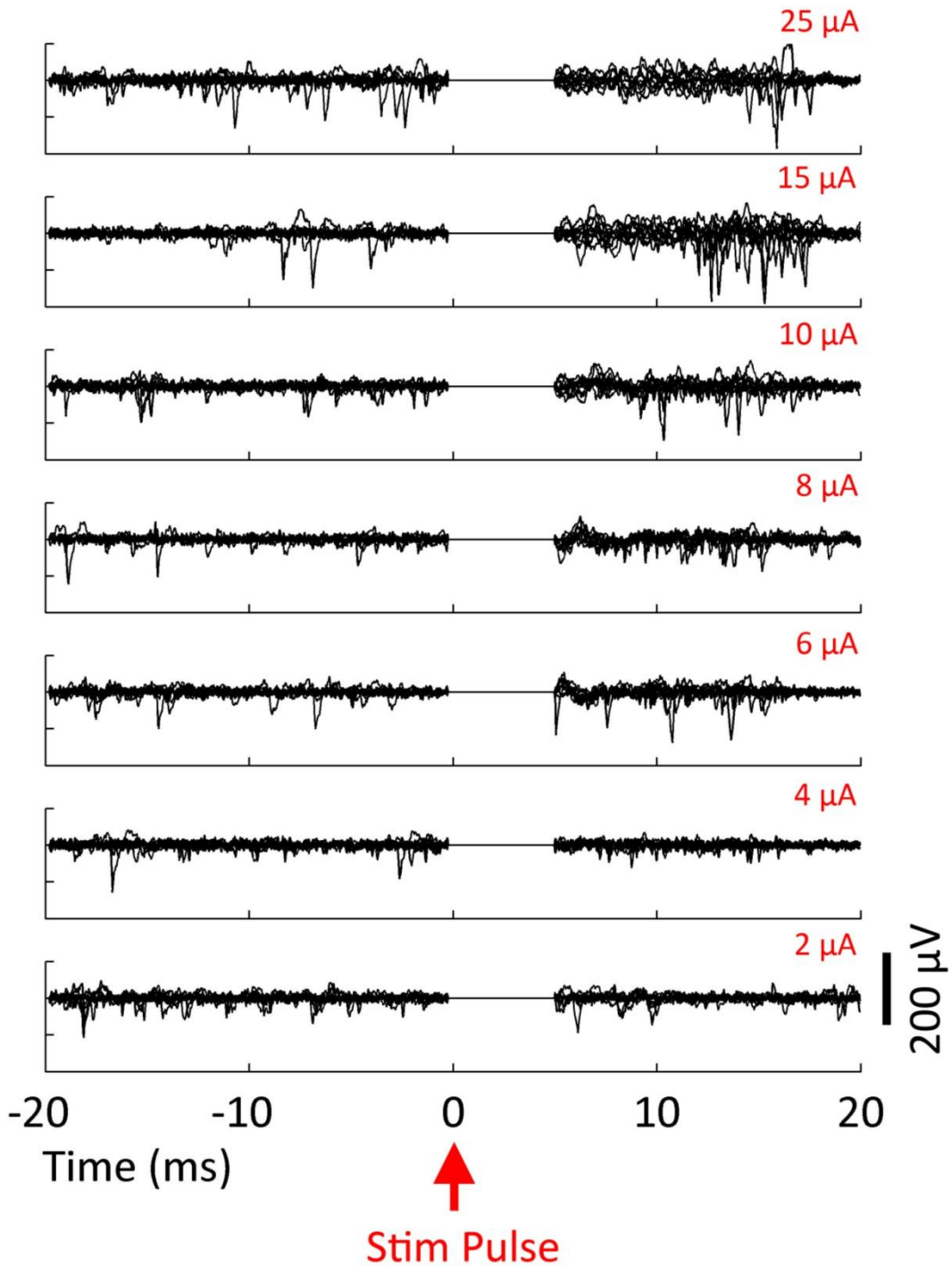

FIGURE 4-10. Evoked response recorded on the stimulating electrode. Biphasic current-controlled stimuli were delivered at time 0 ms to the hippocampus of an awake, behaving rat. Ten trials of each intensity are overlaid. Spontaneous APs are clearly visible before stimulation and evoked APs after blanking. The SALPA artifact suppression algorithm is used to digitally remove residual stimulation artifact, and to blank the channel for 5 ms.

As a final test of our system, we conducted microstimulation and recording in freely moving animals made epileptic with focal injections of tetanus toxin (Figure 4-11; see Experimental Methods above). Stimulation in CA3 of these animals evoked population spikes, created by the superposition of single cell activity, analogous to those observed previously in anesthetized rabbits and cats (Andersen et al., 1971). Interestingly, we also observed an increase in multiunit activity not associated with typical population spikes. Lastly, in 80% of the trials, microstimulation evoked high frequency oscillations at ~300 Hz, the fast ripple range (Rampp and Stefan, 2006). High frequency oscillations have been shown to occur in most models of epilepsy, as well as in human patients with epilepsy, but their mechanisms are still being investigated.

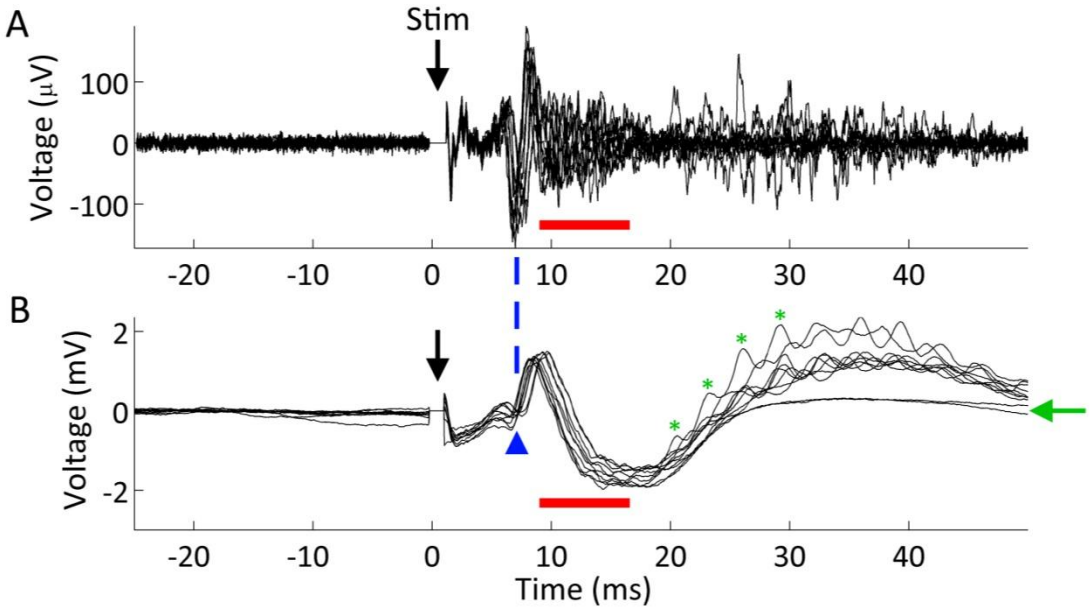

FIGURE 4-11. Microstimulation responses in CA3 of an epileptic animal. Simultaneously recorded (A) action potential traces (using the SALPA filter) and (B) LFP responses. Ten responses to a 20 μA biphasic pulse (negative phase first) are overlaid in both A and B. The stimulating electrode was located 175 μm distant in the same cell layer, CA3. As shown previously (Andersen et al., 1971), single cell activity underlies population spikes (blue arrowhead). However, we noted a high amount of multiunit activity following the population spike that is not clearly associated with any additional spike (red bars). Lastly, we observed evoked high

frequency oscillations at ~300 Hz (in the fast ripple range) in 80% of trials (green asterisks mark four periods of one such oscillation). The green arrow denotes the two traces where no fast ripples were evoked.

Software features and metrics

The NeuroRighter software was created for real-time data processing, visualization, and experimental control. Features include:

- Broadband multichannel recording
- Modular in 16-channel banks
- Arbitrary sampling rates, which can be different for LFPs and spikes
- Multiple adaptive spike detectors, with thresholds updated as often as every sample
- Stimulus artifact removal in real-time using SALPA (Wagenaar and Potter, 2002))
- Digital filtering with arbitrary frequency cut-offs and number of poles
- Data storage of raw broadband signals, detected spike waveforms, and/or LFPs
- Open source architecture
- Multi-threaded for scalability
- Digital re-referencing in real-time
- Ability to control peripherals (e.g., we have implemented control for the Cineplex video recording system and Plexon preamplifier programmable referencing)
- User-friendly, Windows-based graphical interface

Performance data for the software was obtained with the Reliability and Performance Monitor software, Version 6.0 (Microsoft Corporation). The software was tested when recording broadband data from 64 channels at 25 kHz per channel, with settings that resemble an intensive data processing experiment. Specifically, LFPs were obtained by

band-pass filtering the raw data with a digital 1-pole filter and downsampling to 2 kHz. The spike band was band-passed from the raw data with a 3-pole Butterworth filter (300-9000 Hz). Spikes were detected with an adaptive RMS threshold, recalculated every 50 ms for each channel. Surrogate spikes were generated by lowering the spike detection threshold, so that transient events would be labeled as spikes, leading to 2400 spikes s^{-1} or 40 s^{-1} per channel.

When file output was turned on, the data was saved to disk simultaneously in three formats: 1) raw data, which is every unprocessed sample from every channel, 2) spike data, which includes the time of each detected spike, the channel on which it occurred, and 3 ms of the spike's waveform, and 3) LFP data, which was sampled at 2 kHz for each channel. Results of these tests are reported in Table 3.

Table 3. Performance of NeuroRighter Software[a]

Metric	*Without File Writing*	*With File Writing*
CPU Usage	10%	24%
Memory Footprint	90 MB	105 MB
Disk Usage		
Raw Data	-	185 MB/min
Spike times/waveforms	-	9 MB/min
LFPs	-	18 MB/min

[a]Computer specifications as in section 2.5.2 above.

System cost

The system as described has a cost of less than US$10,000 (Table 4), including a desktop computer with monitor (which many labs already own). The minimum requirements for the computer will remain constant, so that the entry price for the computer will continue to fall as technology improves.

Table 4. 64-Channel System Costs[a]

Item	Quantity	Subtotal (USD)	Total (USD)
Computer (Dell)	1	858[b]	858
Recording headstage, with cables (TBSI)	4	1,095	4,380
PCBs (ExpressPCB)			
Power Supply	1 (2[c])	88.60	177.20[c]
Analog Filtering	4	51.10	204.40
A/D Cards (National Instruments)	2	1,259.10	2,518.20
Breakout Boxes & Cables for A/D Cards (National Instruments)	4	358.20	1,432.80
Circuit components (ICs, resistors, capacitors, etc.; Digi-Key and Samtec)	-	383.37	383.37
		Total:	9953.97

[a]Prices as of October 2008, except for recording headstages: November 2007. Vendors may have raised or lowered prices since this table was compiled. Prices were not rounded.

[b]Pricing for a Dell computer comparable to our development computer, with monitor included

[c]Minimum order of 2 boards

Discussion

We have constructed a fully featured data acquisition system for multiple microelectrode recordings. Our system meets its three design objectives: 1) artifacts <1 ms, 2) modular, customizable construction for <$10,000, and 3) open-source software capable of running on a standard desktop computer.

Recovery from stimulation

As shown in Figure 4-7A-B, the electronics of some commercially available data acquisition systems saturate during stimulation. Since artifacts prevent the recording of evoked neural signals, we wish to minimize them to collect the highest quality data possible. Artifacts outlasting the stimulation pulse are expected with traditional metal electrodes, which are capacitively coupled to the extracellular medium. However, the observed saturations in the Plexon hardware (Figure 4-7A-B) occur even when the impedance of the recorded source is purely resistive. This implies that the amplifiers and filters of the Plexon hardware are being driven into a saturated regime. Our system,

which has only a single stage of amplification (compared to the Plexon system's two stages), recovers within μs from the same stimulation pulses (Figure 4-7C). We believe this is due to the lower gain of our system and the single stage of amplification.

As noted above, a metal electrode stimulated in saline or tissue will suffer a prolonged baseline shift as the electrode's capacitance discharges following the stimulus. This will induce an artifact independent of the recording electronics. We would therefore expect our system, which showed negligible electronic artifact, to perform better when stimulated than the Plexon system, since an artifact on our system will be almost entirely due to electrode discharge, rather than hardware recovery (the Plexon system will have longer artifacts composed of both hardware recovery and electrode discharge). Indeed, this was the case when stimuli were delivered through a conventional microwire array immersed in artificial cerebrospinal fluid (ACSF; Figure 4-8).

What is the source of the additional artifact in the Plexon system? With an oscilloscope, we observed rapid recovery from stimulation pulses at the input of the Plexon preamplifier's differential instrumentation amps (LT1167; Linear Technology; Milpitas, CA, USA), but saturated signals at the preamplifier's output (as shown in Figure 4-7A-B). This implies that the Plexon recording headstage is not saturating, but the preamplifier is. In support of this, it has been shown that interposing a blanking circuit between the recording headstage and preamplifier greatly minimizes stimulation artifacts (Venkatraman et al., 2009). We have independently verified this with our own blanking circuitry for Plexon amplifiers.

In vivo microstimulation

Our ability to record LFPs and directly evoked action potentials within 1 ms of stimulation was verified in vivo, in both awake and anesthetized rats (Figure 4-9, Figure

4-10, and Figure 4-11). Directly evoked action potentials were recorded over a wide range of stimulus intensities (4-50 μA), and corresponding changes were observed in the LFP band, including a marked attenuation which increased in duration for increasing stimulus amplitudes (Figure 4-9). Importantly, the recorded short latency (<1 ms) neural responses would be obscured by artifacts in other systems (cf. Figure 4-8, which shows spike band artifacts lasting for 1.5 ms and LFP band artifacts lasting 1.3 seconds following stimulus offset). Additionally, we were able to recover responses within 10-20 ms from the stimulating electrode itself (Figure 4-10).

The system was further validated in a freely moving animal, made epileptic with a focal injection of tetanus toxin. Microstimulation evoked population spikes, analogous to those reported in Andersen et al. (1971). Differences between our experimental setup and that used by Andersen et al. exist, however: 1) our population spikes were evoked by stimulation in a cell layer (CA3) rather than a fiber bundle, such as the perforant path or mossy fiber pathway, 2) we studied freely moving rats, whereas Andersen et al. use anesthetized rabbits and cats, and 3) Andersen et al. expose the hippocampus by removing the overlying cortex, whereas our procedure leaves the overlying motor and sensory cortex intact. Nevertheless, the recorded single cell activity in CA3 closely matched the LFP population spike, as reported by Andersen et al. Interestingly, however, we also observed evoked multiunit activity that was not associated with a population spike in the LFP (red bars in Figure 4-11). Andersen et al. (1971) report some cases where unit activity precedes or follows the population spike, but not to this degree. The nature of this activity remains to be studied.

Another finding from our experiments with epileptic animals is that microstimulation can induce high frequency oscillations. Such oscillations have been repeatedly associated

with epileptiform activity in both humans and animal models (Rampp and Stefan, 2006), though their origin is still unclear. The potential to control these oscillations with microstimulation potentially provides a new experimental platform for further understanding such aberrant activity.

Customizability

Our system has a rich potential for customization for three reasons: 1) open source software, 2) open layouts and schematics, and 3) modular design. First, since the NeuroRighter software is open source, users can modify it to suit their needs, or to provide additional functionality. Second, our open circuit schematics and layouts were developed with free software (PCB123), allowing users to easily modify them. ICs can be changed to alternate models, different filters can be created, or the layout can be manipulated to improve recording characteristics. Lastly, the system is constructed in four largely independent layers: headstage, interface boards, A/D cards, and software. Any of these can be exchanged or modified to improve the system or add functionality. For example, we used the A/D cards and software to create a hybrid Plexon system with additional digital and analog control capabilities (Figure 4-1; see Section 5.4 below).

Hybrid Plexon system

Because our system is modular, it is possible to combine portions of our equipment with that of different vendors. As an example of this, we have successfully interfaced our system with both Plexon hardware for *in vivo* recordings and MultiChannel Systems (MCS) hardware for *in vitro* recordings (Figure 4-1). The advantages of our hybrid Plexon setup (Figure 4-1, case ❷) over the complete Plexon Multichannel Acquisition Processor (MAP) are cost and customizability. The NI A/D cards and our NeuroRighter program preclude the need for the large MAP box and the closed-source Plexon software,

both of which are costly. Additionally, since we record all data broadband, users have potentially greater access to the data's underlying structure. For instance, new action potential detection and sorting methods can be implemented in software and changed in real-time. The noise of this Plexon hybrid arrangement is comparable to that of our system (Figure 4-5), and we have added to the NeuroRighter software the ability to control a Cineplex video recording system and the Plexon preamplifier's programmable referencing. The primary drawback of this arrangement is the loss of online spike sorting, which is handled by the Plexon software. However, real-time sorting could be added as a module to the NeuroRighter software, using any number of published algorithms.

Hybrid MCS in vitro system

For *in vitro* recordings we developed an interface board for use with MultiChannel Systems (MCS) 64-channel preamplifiers (Figure 4-1, scenario ❸). The MCS amplifiers record from substrate-integrated multielectrode arrays, for use with neural or cardiac cell cultures. The interface board, in this case, is the same dimensions as the *in vivo* interface board and features the same stackthrough connectors, allowing it to be stacked beneath the power board (as in the *in vivo* setup). Our MCS interface board receives the MCS preamplifier's SCSI cable output, and passively relays the signal to standard header connectors. These connectors are identical to those used for the *in vivo* setup, permitting compatibility between the two systems. From this point, the signal chain is identical to the *in vivo* case described above. The electrode-referred noise (inputs grounded) of this hybrid system is 3.2 μV, broadband. In a conventional MCS system, our custom interface board, National Instruments A/D cards, and software would be replaced with an MCS A/D card (MC_Card) and MCS software (MC_Rack). The A/D cards we use are less expensive and have a greater resolution (16-bit vs. 14-bit), and our software is free and

open source. These two changes reduce the overall cost and permit greater customizability for an *in vitro* system.

Cost

The cost to construct a 64-channel version of our system was less than USD 10,000 (a 32-channel system will cost less than USD 6,000; Table 4). This compares favorably to the price of commercial systems: quotes we have received range from 4× to 10× the cost of our system. A savings of USD 30,000 to USD 90,000, or the ability to acquire multiple systems, will likely be of great use to many laboratories.

Software performance

We chose to implement our software in the C# programming language (Liberty and Xie, 2008), a modern and easy-to-use language similar to Java (Wilkens, 2003; Chandra and Chandra, 2005). Because C# is an open standard, the language has compilers for both Windows and Unix-based systems (via the Mono[9] and DotGNU[10] projects). Therefore, nothing prevents this software from being ported to Linux or the Unix-based Mac OS X. In fact, through the Mono project, C# programs can be ported to Mac OS X, Sun Solaris, BSD, and even the Nintendo Wii and iPhone OS. The only components that will require significant changes in NeuroRighter are the Measurement Studio libraries, created by National Instruments. The software currently uses these libraries to communicate with the National Instruments A/D hardware. However, since open source National Instruments drivers exist (e.g., the COMEDI drivers[11]), the Measurement Studio components can be replaced in future versions of the software.

[9] http://mono-project.com/Main_Page
[10] http://www.gnu.org/software/dotgnu/
[11] http://www.comedi.org/

A potential concern for writing numerically intensive applications in C# or other modern languages is speed. C#, like Java, is compiled to an intermediate language and not to native machine code. When a section of this code is executed, the Common Language Runtime (CLR) environment compiles the intermediate code to native code, which is then run normally. This just-in-time (JIT) compilation will be slower than native compilation (such as that used by C/C++). However, JIT compilation only occurs when the code is first executed. For a data acquisition program, where most code is executed repeatedly, essentially in an infinite loop terminated by the user, this performance penalty only occurs during the first reading of an A/D buffer. Consequently, the JIT penalty will be negligible in the context of a normal recording session. If the JIT penalty ever appears too costly, the intermediate language code can be compiled to native code with Microsoft's NGen.exe tool. Modern languages like C# and Java are believed to decrease the time required to develop and maintain applications. In the future, we hope these simplifications will provide more rapid implementation of new processing capabilities for data acquisition systems.

Comparison to other systems

There are a large number of recording systems described in the literature for conducting multielectrode recordings from behaving animals. Some of the most interesting designs, of late, involve telemetric devices capable of installation within the calvaria of active primates. The HermesB system (Santhanam et al., 2007) and the system described by Sodagar et al. (2007) both offer good performance with streaming data, but are limited to low channel counts. The HermesB system can only record from 2 channels, while the Sodagar system can record spikes from more, but only LFPs from 2 channels. Moreover, the resolution of the spikes recorded by the Sodagar system is only 5 bits. Our system has 16-bit resolution, and has been used in practice for 64 channels of simultaneous spike

and LFP acquisition. With software modifications, higher channel counts could easily be reached. Lastly, neither of these systems has been characterized to determine their responses to stimulation. The trade-off, as it stands, is in the convenience of wireless telemetry, which our system currently does not support.

The system developed by Mavoori et al. (2005), another implantable system, was designed for closed-loop stimulation and recording in primates. While stimulation artifacts were not completely characterized, the artifact on non-stimulating channels was cited as 2.5 ms. The NeuroRighter system outperforms this artifact length, and has twice the A/D resolution (16-bit vs. 8-bit). Additionally, the Mavoori system is currently too bulky to work with rodents, as it is enclosed in a 5.5 × 5 × 3 cm container.

Perhaps the most comparable system is that described by Venkatraman et al. (2009). This innovative setup uses a Plexon system equipped with custom-built blanking circuitry. This circuit disconnects the recording headstage output from the "preamplifier" input for 1 ms during and after stimulation. Because it acts at the preamplifier input (rather than the headstage), the device can be large without affecting recording from small, active rodents. The authors report the ability to record within 2 ms post-stimulation from non-stimulating electrodes, but do not report recordings from stimulating electrodes (Venkatraman et al., 2009). The NeuroRighter system, in contrast, recovers more quickly (<1 ms) on non-stimulating channels, can record from the stimulating channel within milliseconds, and costs significantly less, since no Plexon equipment needs be purchased.

Another comparable system is the CMOS-based stimulation/recording hardware described by Olsson et al. (2005). This system uses CMOS circuitry coupled to a silicon probe, and recovers from stimulation artifacts within 1 ms, like our system. This rapid

recovery comes at the cost of bandwidth—the widest range reported by Olsson is 10 Hz to 10 kHz, significantly attenuating low frequency LFPs. Other disadvantages of the system are its relatively high noise (9.2 μV RMS across 100 Hz – 10 kHz), its fixed reliance on silicon probes (whereas the NeuroRighter system can use a large variety of available probes, including silicon), and its CMOS design (making it difficult to replicate by other labs).

Several designs for artifact recovery that exist in the *in vitro* domain hold promise for *in vivo* work. For example, the active discharge circuitry illustrated by Brown et al. (2008) permits rapid artifact recovery, even on the stimulating electrode. This system, however, uses a patented CMOS design, making it non-replicable by different labs, and is not currently packaged for use with freely moving animals. Similar circuitry, based on sample and hold amplifiers, was proposed several years ago by Jimbo et al. (2003). This system by Jimbo, though, is based on larger, easy-to-solder DIP technology, leaving it unavailable in a miniaturized form suitable for freely moving animals. The NeuroRighter system performs as well as these systems, in terms of artifact length, on non-stimulating channels, but does not recover on the stimulating channel as quickly. However, the ability to use the NeuroRighter system in freely moving animals, and its open design, are both significant advantages.

Overall, we have found no system that is capable of use with small freely moving animals and that matches ours in terms of features that are important for increasingly popular closed-loop multi-electrode electrophysiology: rapid recovery from stimulation artifact, number of channels, and cost.

Conclusion

We believe that closed-loop systems, able to both stimulate and record from multiple electrodes, are essential for complete characterizations of neural activity. Since no commercially available system exists with this capability, we have designed our own, and are freely providing the means for its reproduction online (http://www.johnrolston.com). While the present article focuses on the system's recording characteristics, we have already integrated a head-mounted closed-loop stimulator. In the future, we hope to use the NeuroRighter system to fully document the effects of closed-loop microelectrode stimulation in awake, behaving animals. We also hope to continually improve the software and hardware, with the help of the neuroscience community, to offer features such as online spike sorting, novel digital filters, compression routines (Brinkmann et al., 2009), and other means of ensuring high-quality, easily analyzed data.

Multielectrode recording continues to be a useful means for interrogating the nervous system. But commercially available systems are expensive, and may prohibit some researchers from utilizing this powerful technique. Furthermore, closed-source software and proprietary circuit layouts and schematics prevent the research community from truly understanding their tools, and from making necessary improvements. We hope that the system we have described above and its superior recovery from stimulation artifact will not only be useful to a number of research labs, but also spur further innovations in real-time recording and stimulation technology. The neuroscience community is inventive and capable, and we will all benefit from the proliferation of inexpensive, easy-to-use, and powerful tools.

Conflict-of-Interest Statement

John Rolston received consulting fees from Axion Biosystems, which represent a competitor of the described system. We therefore do not see this as a conflict of interest. The other authors declare that the research was conducted in the absence of any commercial or financial relationships that could be construed as a potential conflict of interest.

Acknowledgments

We gratefully acknowledge the advice of E. Brown on circuit design, assistance with surgeries from C. A. Gutekunst, R. Hampson, and A. Goonawardena, assembly of the MCS interface board by C. Hales, construction of the rat enclosure by D. Rainnie, laboratory support from L. Jackson, and helpful discussions within the Gross and Potter labs. This work was funded by the Wallace H. Coulter Foundation, the Epilepsy Research Foundation, a Neurology/Biomedical Engineering seed grant from Emory University and Georgia Tech, a University Research Council grant from Emory University, and, from the National Institute of Neurological Disorders and Stroke, a Ruth L. Kirschstein National Research Service Award to JDR (NS060392), a translational research fellowship to JDR (NS007480), a career development award to REG (NS046322), and a research grant to SMP and REG (NS054809).

Chapter 5

Closed-loop Multielectrode Stimulator with Simultaneous Recording in Awake, Behaving Animals[12]

[12] A version of this chapter has been submitted for publication: John D. Rolston, Nealen G. Laxpati, Nathan J. Killian, Robert E. Gross, Steve M. Potter "Closed-loop Multielectrode Stimulator with Simultaneous Recording in Awake, Behaving Animals."

Abstract

Precise control of ongoing neural activity is a goal of modern neuroengineering, and such control is frequently sought using electrical stimulation. This control will likely be improved by coupling electrical stimulation to electrical recording, binding the two in a closed-loop system. To this end, we developed a closed-loop stimulator and microelectrode recording system for multielectrode arrays, with applications for both freely moving animals and *in vitro* preparations. This versatile system offers current- and voltage-controlled stimulation modes, along with push-button routines for electrolesioning and monitoring impedance spectra in real-time. The stimulator is compatible with many commercial recording systems, can stimulate from any electrode of an array, and allows simultaneous recording from all electrodes. Arbitrary stimulation waveforms can be pre-programmed or controlled by recorded neural activity. Both action potentials and local field potentials can serve as control signals for closed-loop stimuli. We present a sample closed-loop experiment in which electrical stimulation is triggered by the detection of interictal spikes in epileptic animals, and also present data from long-term monitoring of impedance spectra from chronically implanted arrays. Stimulator designs and software are open-source and freely available online.

Introduction

Simultaneous electrical stimulation and recording has been a boon for neuroscience, providing insight on synaptic plasticity (Dan and Poo, 2006), thalamic function (Steriade and Timofeev, 2003), learning in complex networks (Bakkum et al., 2008b; Chao et al., 2008), and more. Closed-loop systems, where observed neural activity controls electrical stimulation, have provided more insight still, proving useful for controlling epileptic seizures in humans (Fountas et al., 2005), suppressing aberrant bursting in neural cultures (Wagenaar et al., 2005b), and even illustrating new modes of learning and memory (Bakkum et al., 2008b).

Despite the appeal of closed-loop recording and stimulation, none of the currently available commercial systems was designed with closed-loop stimulation in mind. We therefore created our own system for use with multielectrode arrays. We had four primary goals for this device. First, stimulation should be available from any channel of a multielectrode array (MEA), affording precise control over a large field of neural tissue. Second, the electrodes should permit recording while stimulation is underway. Separate stimulation electrodes are not required. In general, responses to stimulation can occur within milliseconds of stimuli (Rolston et al., 2009b), and this information has shown utility in investigations of basic neurophysiological functions (Bakkum et al., 2008a). Systems with long stimulation artifacts or that use dedicated, stimulation-only electrodes may miss these responses. Third, the system should be versatile. For example, users should be allowed to rapidly alternate between voltage-controlled and current-controlled stimulation as they optimize their protocols. Similarly, stimulus waveforms of any complexity should be permitted, rather than a simple repertoire of biphasic rectangular pulses. This flexibility is important, for although current-controlled stimulation is more commonly used (Merrill et al., 2005), some studies, such as Wagenaar et al. (2004), have

shown greater efficacy of voltage- over current-controlled pulses. Additionally, Merrill et al. (2005) describe many cases where biphasic “square” pulses are inferior, with respect to consequent tissue damage, to more complex-shaped pulses. Lastly, the system should be readily accessible to the scientific community. Wide use is encouraged by compatibility with commercially available probes and recording systems—users will save both time and money if they are not required to replace existing, yet functional, recording equipment, or to begin using electrode arrays from a different manufacturer. Flexibility and accessibility are enhanced by free licensing of the system’s circuit designs and software code, so that its details are fully disclosed and customizable by others. Indeed, several open source solutions have already proven crucial for conduction neuroscience research across many sub-fields: e.g., SPM for functional neuroimaging (http://www.fil.ion.ucl.ac.uk/spm/software/), ImageJ for image processing and analysis (http://www.macbiophotonics.ca/imagej/), and Textpresso for text-mining scientific publications (Muller et al., 2004).

To satisfy the constraints described above, we developed an integrated system capable of simultaneous stimulation and recording from multielectrode arrays. Stimulation can be delivered to any of the recording electrodes of an array and artifacts are minimal, allowing the detection of action potentials within 1 ms of stimulus offset. The stimulator is highly flexible. Stimulation waveforms can be specified with 1 μs precision, and can be either voltage- or current-controlled. The stimulator provides diagnostic readouts, which monitor the voltage delivered during current-controlled stimulation, and the current during voltage-controlled stimulation. In a significant advance from other stimulators described in the literature, this information is used to calculate electrode impedance spectra in real-time.

The stimulator is compatible with many *in vivo* microwire arrays, including those from Neurolinc, TDT, Microprobe, NBLabs, and (with an adaptor) NeuroNexus. For *in vitro* studies, it interfaces directly with MultiChannel Systems (MCS) MEA1060 amplifiers. Stimulation control is fully integrated into our open-source NeuroRighter recording hardware and software (Rolston et al., 2009b), providing tight, millisecond-scale support for closed-loop stimulation experiments. For users with different recording equipment, the stimulator can be used without modification with recording systems such as those from TDT, Plexon, Blackrock Microsystems, Neuralynx, and MultiChannel Systems. Lastly, the open-source Windows-based control software is freely available online (http://www.johnrolston.com/), along with open-source circuit layouts and schematics.

Below we describe the design of the system, along with tests illustrating its utility for use with awake, behaving animals.

Design

The recording components of the system were described in detail previously (Rolston et al., 2009b). The stimulator itself can be used in a standalone mode, with our recording equipment (Rolston et al., 2009b), or in conjunction with recording equipment from different manufacturers. The stimulation system has two primary components: 1) A bidirectional interface, shared across *in vivo* and *in vitro* experiments and responsible for establishing stimulation waveforms, voltage and current monitoring, voltage to current conversion, and power supply filtering; and 2) stimulator modules and recording amplifiers, abutting or proximal to the experimental preparation, that differ depending on whether interfacing with substrate integrated multielectrode arrays (MEAs) or microwire arrays in freely moving animals (Figure 5-1). Analog stimulus waveforms are

generated by a multifunction data acquisition (DAQ) card, buffered and monitored in interface circuitry (Figure 5-1, right), and delivered to the stimulator modules (Figure 5-1, left). The modules have analog multiplexors, controlled by digital output from the multifunction DAQ, that select which channel receives the stimulus. Specific details for each component are provided below.

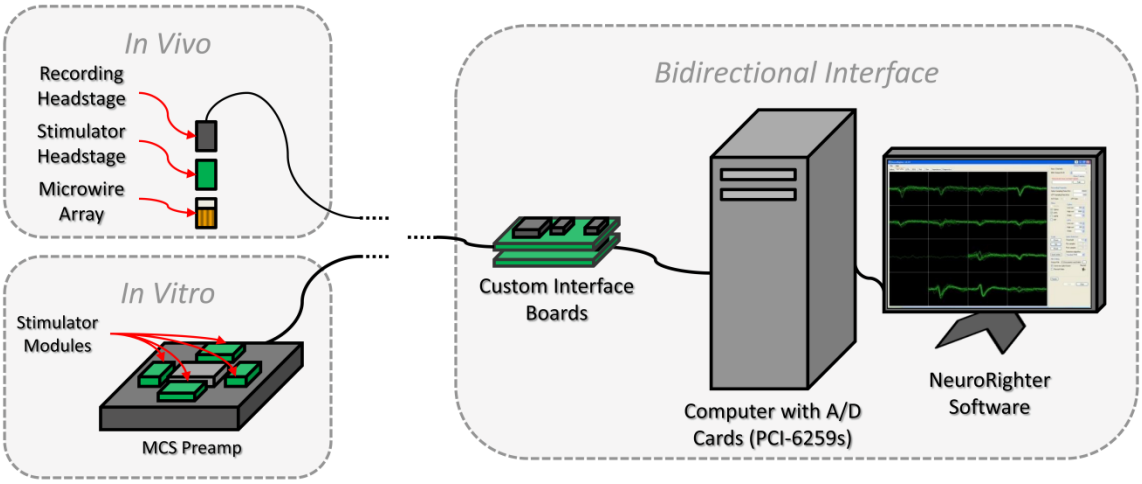

FIGURE 5-1. System schematic for closed-loop stimulation. The bidirectional interface (right side of figure) includes a desktop computer with multifunction A/D and D/A cards (for delivering stimulation and recording neural signals), controlled with the NeuroRighter software suite (Rolston et al., 2009b). The multifunction cards communicate with custom-designed interface boards, which provide stimulation control, impedance monitoring, power filtering, and analog signal filtering. The bidirectional interface can be used with behaving animals ("*In Vivo*", top-left panel) or neuronal slices or cultures ("*In Vitro*", bottom-left panel). For *in vivo* use, a head-mounted stimulator switch is interposed between the recording electrodes and the recording headstage. *In vitro*, individual stimulator modules are mounted on top of a MultiChannel Systems (MCS) amplifier.

Bidirectional interface

The shared system consists of a standard desktop computer with one or more PCI- or PCIe-6259 multifunction data acquisition cards (National Instruments; Austin, TX, USA), controlled by our open-source NeuroRighter software (Rolston et al., 2009b).

Stimulation commands consist of a digital signal, to control the analog multiplexors, and an analog signal which specifies the stimulus waveform with up to 1 μs precision.

On the interface board (Figure 5-2A), two banks of analog amplifiers separately control voltage-controlled and current-controlled stimulation (Horowitz and Hill, 1989; Wagenaar and Potter, 2004). Voltage-controlled stimulus waveforms from the PCI-6259 card are delivered to the appropriate bank of amplifiers via analog single-pole, double-throw switches (MAX333; Maxim Integrated Products, Inc.; Sunnyvale, CA, USA). The switches are controlled through software, using the PCI-6259's digital output.

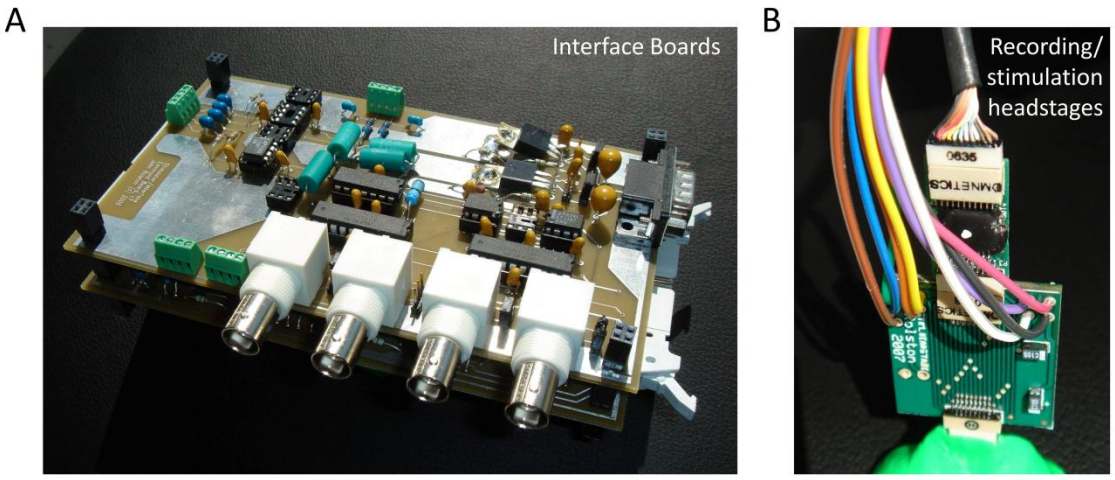

FIGURE 5-2. Photos of interface board, headstages, and modules. (A) The stimulation interface board has BNC posts and terminal strips for stimulation input/output and diagnostics. Circuitry for analog recording is stacked below (Rolston et al., 2009b). (B) For recordings in behaving animals, a microelectrode array is embedded in a acrylic headcap (green mound). The stimulation headstage connects with the array during experiments, and a recording headstage (top) connects to the stimulator. Extracellular signals pass through the stimulation headstage during normal recordings. During stimulation, a high-speed multiplexor connects one electrode with a stimulation signal from the interface boards.

In voltage-controlled mode, the software-specified stimulation waveform is buffered by an operational amplifier (OPA277, Texas Instruments; Dallas, TX, USA), while an

instrumentation amplifier (LT1167, Linear Technology; Milpitas, CA, USA) measures the voltage drop across a resistor, R_M (Figure 5-3A). By Ohm's law, the voltage drop across this resistor is proportional to the current flowing through the resistor (and hence stimulating electrode), making the output of the instrumentation amplifier proportional to the delivered stimulation current. Changing R_M (typically 100 Ω) alters the gain of this measurement. The instrumentation amplifier offers additional gain, controlled by the resistor R_G (typically 100 Ω, yielding a gain of ~500×).

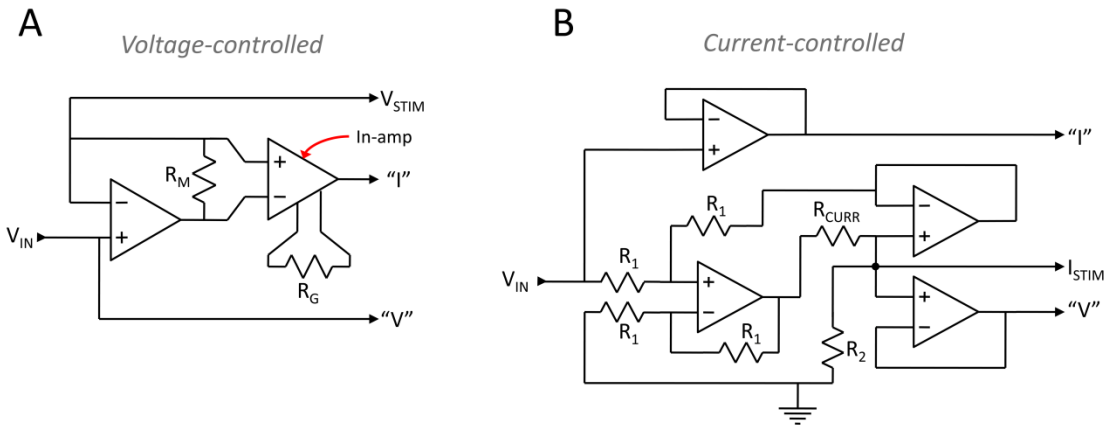

FIGURE 5-3. Circuit diagrams. Both voltage- and current-controlled stimulation are driven by a voltage-controlled analog waveform, V_{IN}, from a PCI-6259 multifunction DAQ. The desired circuit (voltage or current) is selected with analog SPDT switches by software (not shown). (A) For voltage-controlled stimulation, the input is buffered by an op-amp, after passing through a measurement resistor, R_M. To monitor the current delivered with the applied stimulation voltage, the voltage drop across R_M is measured by an instrumentation amplifier (in-amp), the output of which is proportional the stimulation current. The in-amp's gain is tuned with the resistor R_G. (B) For current-controlled stimulation, the voltage-controlled input is converted to current-controlled stimulaton across the resistor R_{CURR}, creating a current-controlled waveform with amplitude $I = V_{IN}/ R_{CURR}$. The four R_1 are high-precision 100 kΩ resistors, and R_2 is a 6.8 MΩ resistor to prevent runaway voltages. In both circuits, "I" refers to a voltage proportional to the delivered current, and "V" refers to a buffered copy of the delivered voltage. These are used for diagnostic purposes and for impedance measurements.

The voltage drop across R_M would lead to depressed stimulation voltages if left uncorrected. To compensate, the distal terminal of R_M is used as feedback for the buffering OPA277 operational amplifier (op-amp).

Current-controlled stimulation uses a set of four op-amps (OPA4277, Texas Instruments) and precision resistors (0.01%, 100 kΩ) to convert the voltage-controlled waveform from the PCI-6259 card to a current-controlled waveform for stimulation (Figure 5-3B). The converted current amplitude is inversely proportional to R_{CURR} (typically 100 kΩ), again according to Ohm's law ($I = V/R_{CURR}$). The voltage used to drive the desired current is monitored by buffering the current-controlled output with an additional op-amp (bottom right op-amp of Figure 5-3B: output "V"). This monitored voltage (from a known current) can be used to calculate impedance spectra (see "Impedance Measurements" below).

In both cases, voltage- or current-controlled stimulation, the final stimulation output is directed to a stimulation module by analog switches (MAX333). Each stimulation module contains one or more multiplexors which ultimately determine which channel is stimulated.

Stimulator modules

To enable simultaneous stimulation and recording, we use analog multiplexors (MAX306 or MAX308, Maxim, Inc.) to route stimulation pulses to the selected recording channel (Figure 5-4). When a channel is not being stimulated, the multiplexor output to that channel is closed, isolating the preamplifier and channel from the stimulation circuitry. Only at the precise moment of stimulation does the multiplexor open a path

from the stimulation circuitry to the recording electrode. Multiplexor switching times are <250 ns, permitting rapid switching between recording and stimulation. Details of the *in vivo* and *in vitro* instantiations of these modules are described below.

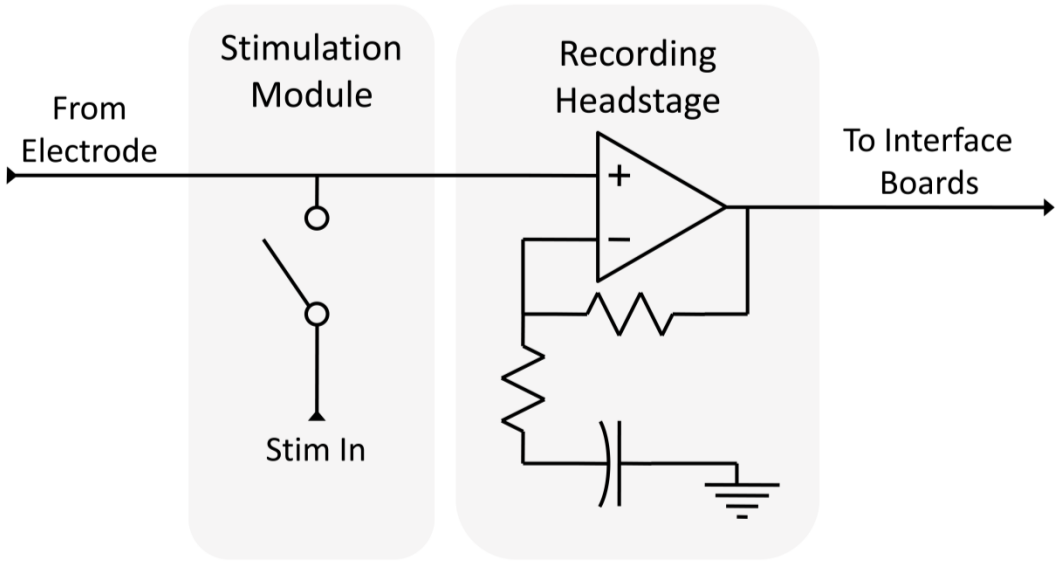

FIGURE 5-4. Circuit diagram for stimulator module and recording headstage. One representative channel is shown (the circuitry is identical for all recording channels). Signals pass from the recording electrode through the stimulation headstage or module and into the recording headstage, where the signals are amplified. The recording headstage output goes to the interface boards for filtering, then to an A/D card for digital conversion and computer analysis. When stimulated, the switch in the stimulation module is closed, directly connecting the electrode to the stimulation circuitry. Because of the recording headstage's high input impedance, stimulation current flows almost exclusively through the electrode. The switch is normally open (non-conductive), except at the precise moment of stimulation.

In vivo stimulator

In vivo, the stimulator headstage serves to route stimulation signals to a desired electrode, while allowing neural signals to pass through to the recording headstage when stimulation is not underway (Figure 5-2B). The headstage is a four-layer PCB (0.975 × 0.875 inches) designed using the free ExpressPCB software, version 6.1.4 (http://www.expresspcb.com/). Components are surface-mounted and consist of

Omnetics connectors, a 16-channel analog multiplexor (MAX306, Maxim, Inc.), and decoupling capacitors. The Omnetics connectors (A8783 and A9512, Omnetics Connector Corporation; Minneapolis, MN, USA) allow the stimulator to interface with most commercially available microwire arrays and recording headstages.

In vitro stimulator

The current stimulation system is backwards-compatible with our lab's previous *in vitro* stimulation hardware, the "Real-time All-Channel Stimulator", or RACS (Wagenaar and Potter, 2004). Therefore our stimulator can control stimulator modules from the RACS system, and the RACS system can control our *in vivo* stimulator headstages. Currently, we continue to utilize the stimulator modules described by Wagenaar et al. (2004) for our experiments in cell culture. These modules are two-layer PCBs designed using ExpressPCB. Each module has two 8-channel analog multiplexors (MAX308, Maxim Inc.) and decoupling capacitors, and interfaces with a MultiChannel Systems (MCS) preamp via exposed header pins.

Experimental methods

Rodent electrophysiology

Surgery

Animal work was conducted in accordance with the National Institutes of Health Guide for the Care and Use of Laboratory Animals and approved by the Emory University Institutional Animal Care and Use Committee. Adult male Sprague-Dawley rats weighing >350 g (Charles River Laboratories; Wilmington, MA, USA) were anesthetized with 1.5-3.0% inhaled isoflurane and given a subcutaneous injection of buprenorphine (0.05 mg/kg) to minimize pain. A craniectomy was made over the right dorsal hippocampus,

centered at 3.5 mm posterior and 2.8 mm lateral to bregma. The dura was incised with a sterile syringe needle. Rats were made epileptic by the injection of 25 ng of tetanus toxin (Sigma-Aldrich; St. Louis, MO, USA) into the dorsal hippocampus (3.3 mm posterior to bregma, 3.2 mm lateral to midline, and 3.1 mm ventral to pia) (Jefferys and Walker, 2005). The toxin was suspended in a total volume of 0.5 µl phosphate-buffered saline with 0.2% bovine serum albumin. The toxin was delivered using a pulled glass micropipette and a Nanoject II automatic injector (Drummond Scientific; Broomall, PA, USA). The tip of the micropipette was slowly lowered to the proper coordinates and allowed to sit for 1-2 minutes before the injection began (to allow the parenchyma to equilibrate following implantation). The toxin was then delivered slowly over the course of 3 minutes. The micropipette remained in place for an additional 5 minutes to prevent reflux.

Following the injection of tetanus toxin, a microwire array (Tucker Davis Technologies) was implanted. The array featured sixteen 33 µm diameter tungsten electrodes with polyimide insulation arranged in two rows of 8 electrodes, with 175 µm between electrodes within a row and 1 mm between rows. The two rows had different lengths, 4.0 mm and 2.7 mm, with the former directed at the CA3 region of the hippocampus and the latter at the more dorsal CA1 region. The microwire array had integrated reference and ground wires (6.0 mm long), which were positioned collinear with the longer row of the array. The array was positioned at a 50° angle to midline (counter-clockwise rotation, with the posterior end swung laterally) to follow the contours of the dorsal hippocampus. The array was lowered while recording neural activity in order to attain correct positioning, usually ending when the longer electrodes were ~3.5 mm ventral to pia.

The craniectomy was sealed with cyanoacrylate glue (Loctite; Rocky Hill, CT, USA), skull screws were implanted (Plastics One; Roanoke, VA, USA), and dental acrylic (OrthoJet; Lang Dental; Wheeling, IL, USA) was applied to secure the array's connector. The rats returned to their normal housing, and rested and recovered post-operatively for 5-8 days before recordings began. Spontaneous seizures began 6-9 days after the tetanus toxin injection.

Recording

Rats were recorded in a custom-built enclosure. The sampled extracellular waveform from each electrode was acquired at 25 kHz, and referenced to the integrated reference electrode. For spike detection, signals were filtered from 500 Hz to 9 kHz with a 1-pole bandpass filter. Local field potentials (LFPs) were computed from the raw data by band-pass filtering (1-500 Hz, 1-pole) and downsampling to 2 kHz. Stimulation artifacts (<1 ms in duration) were removed in real-time with the SALPA algorithm (Wagenaar and Potter, 2002).

Closed-loop experiment

To illustrate the closed-loop capabilities of the NeuroRighter system, we created a simple feedback stimulation experiment, where the hippocampus of a freely moving rat was stimulated upon the detection of an interictal spike in the LFP. Interictal spikes were defined as LFP deflections 7.5× baseline RMS. This simple detection method had a 100% specificity (compared to manual detection) when analyzing the 45 minutes preceding the stimulation experiment. A single, biphasic, current-controlled pulse (±10 μA, 400 μs pulse width per phase, cathodic phase first) was delivered to the electrode immediately upon interictal spike detection.

Impedance measurements

Impedances were measured by stimulating with sine waves of known amplitude (typically 1 μA) across a spectrum of frequencies. In current-controlled mode, the delivered voltage was measured using the diagnostic outputs of the board, and vice versa for voltage-controlled stimulation. At frequency f, the impedance is Z = V/I, where V is the RMS value of the measured voltage waveform and I is the RMS value of the delivered current waveform (for current-controlled measurements; these assignments are reversed if using voltage-controlled measurements). To reduce noise, a matched filter was digitally applied to the measured voltage or current waveform.

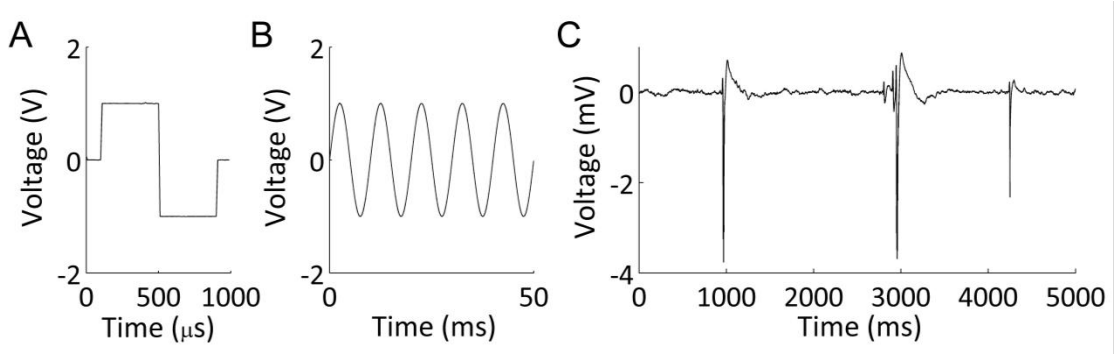

FIGURE 5-5. Sample stimulus waveforms. Arbitrary waveforms can be delivered to the stimulation electrodes with 1 μs resolution. A standard voltage-controlled biphasic pulse is shown in (A), a 100 Hz sine wave in (B), and a previously recorded LFP from an epileptic rat, now used as a stimulation signal, in (C).

Results

We created a system for closed-loop stimulation in behaving animals and *in vitro* preparations, able to stimulate with arbitrary current- or voltage-controlled waveforms to any channel of a multielectrode array. The waveforms have a 1 μs precision, making them suitable for creating standard biphasic pulses, sine waves (e.g., for impedance monitoring), or even for delivering pre-recorded extracellular field potentials as

stimulation (Figure 5-5). The ability to monitor the voltage used when delivering current-controlled stimuli, and the current delivered when using voltage-controlled stimuli, provides useful diagnostic information (Figure 5-6).

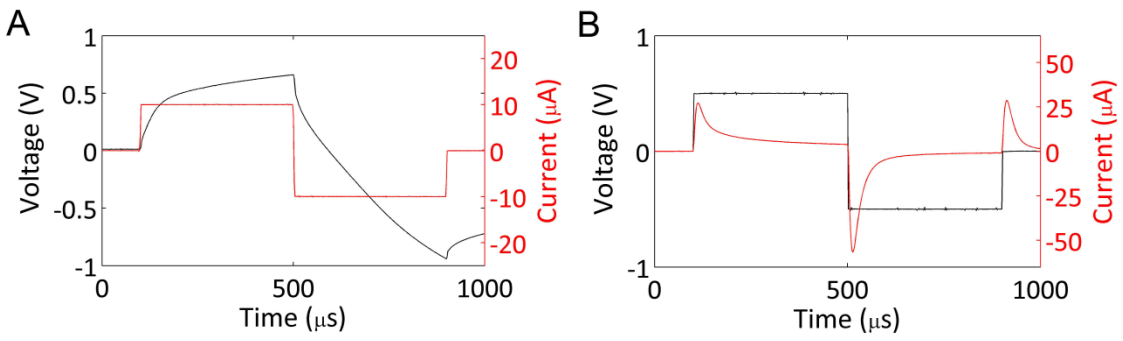

FIGURE 5-6. Dual current and voltage waveforms. Biphasic current-controlled (A) and voltage-controlled (B) pulses are delivered to an electrode in artificial cerebrospinal fluid (ACSF). The delivered voltage and currents are simultaneously monitored (black traces for voltage, red traces for current). (A) A 10 μA biphasic current-controlled pulse (red trace) produces a more slowly ramping voltage waveform (black trace). (B) A ±0.5 V biphasic voltage-controlled pulse (black trace) produces a current waveform (red trace) with sharp peaks at each change in voltage.

Animal experiments

We validated our system *in vivo* using freely moving rats with microwire arrays chronically implanted in the dorsal hippocampus (areas CA3 and CA1; see Experimental Methods). Rats were made epileptic with microinjections of tetanus toxin into the hippocampus, as part of ongoing experiments to suppress seizures with microstimulation. In these animals, stimulation readily evoked action potentials within 1 ms of stimulus offset (Figure 5-7).

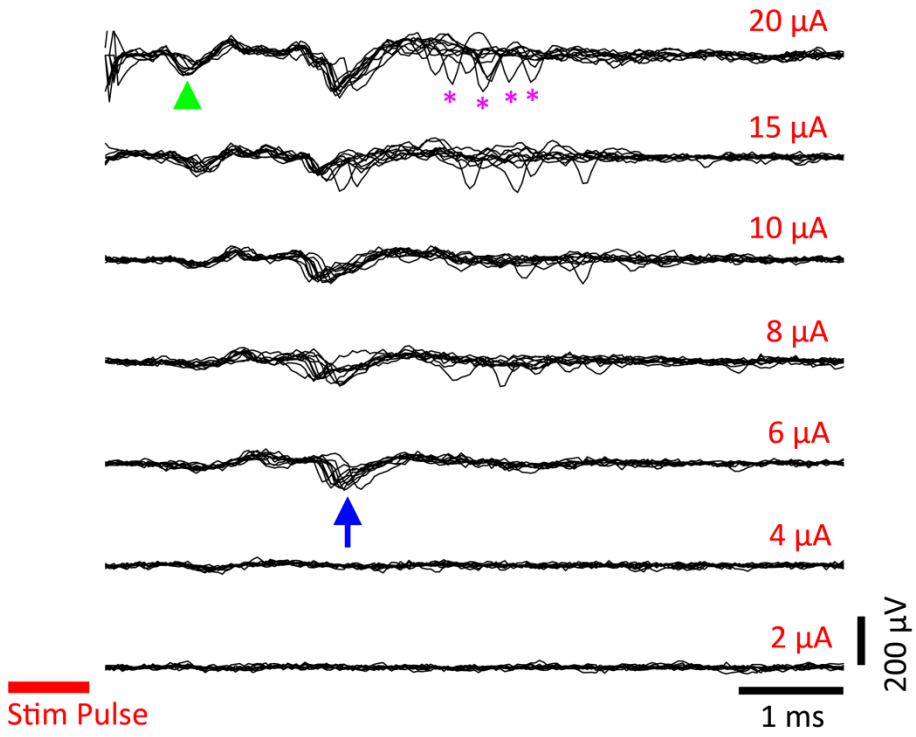

FIGURE 5-7. Hippocampal responses to current-controlled stimuli. Biphasic current-controlled stimuli (cathodic, negative phase first; 400 µs per phase) were delivered to an electrode in CA1, and responses were recorded as seen here in CA3. Ten trials of each stimulus amplitude are overlaid in each panel. Stimulus duration is indicated by the red bar. The first responses appear at ≥6 µA (blue arrow), with the lowest latency responses at 20 µA (green arrowhead). Additional, less consistent APs are recruited at high stimulation intensities (purple asterisks). All traces are filtered with the SALPA algorithm (Wagenaar and Potter, 2002). Stimuli were delivered at 1 Hz and in random order (to guard against neural adaptation).

Closed-loop experiment

To illustrate the closed-loop capabilities of the system, we tested a simple algorithm wherein the detection of an interictal spike (IIS) in the LFP triggered microstimulation (see Experimental Methods). Biphasic current-controlled pulses (±10 µA, cathodic phase first), which were shown to reliably evoke neural activity (Figure 5-7), were delivered to a single electrode immediately upon each detection. Despite the ability of microstimulation to evoke activity, IISs in CA3 and CA1 were not obviously affected by

stimulation (Figure 5-8A). The mean time between IIS detection and stimulation was 4.4 ± 1.2 ms (± standard deviation).

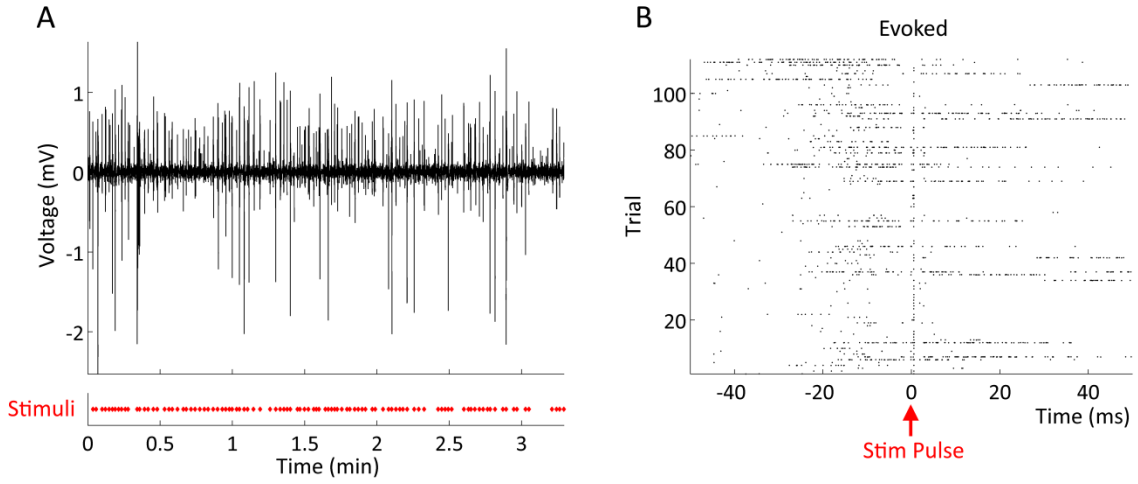

FIGURE 5-8. Closed-loop stimulation of a freely moving epileptic rodent. (A) The LFP of an electrode in CA3 was monitored for interictal spikes (IISs) and a single 10 µA biphasic current-controlled pulse was delivered upon detection (red X's in bottom panel). The displayed LFP trace (top panel) is from an electrode in CA1. (B) A raster plot of recorded action potentials (from any of the 16 electrodes) is shown, time-locked to the stimulus pulse. Action potentials are reliably evoked at low-latency following each pulse.

Impedance measurements

Impedance in vivo

The impedance of an electrode affects both its noise levels and ability to stimulate (i.e., the lower the impedance, the lower the voltage required to deliver a particular current). To monitor how these values change during implantation in freely moving animals, we measured the impedance spectrum of a microwire array in phosphate-buffered saline, then immediately after surgical implantation of the array, and then every few days for the following month (Figure 5-9). The impedance spectrum is fairly constant at low frequencies (<100 Hz; Figure 5-9A), but changes greatly in the higher frequency range (>100 Hz), the same range in which action potentials are most readily observed. The

greatest change is observed between PBS and implantation, where the impedance increases nearly 3-fold at 1 kHz (Figure 5-9A,C). But the impedance continues to increase over the first week following implantation (Figure 5-9C).

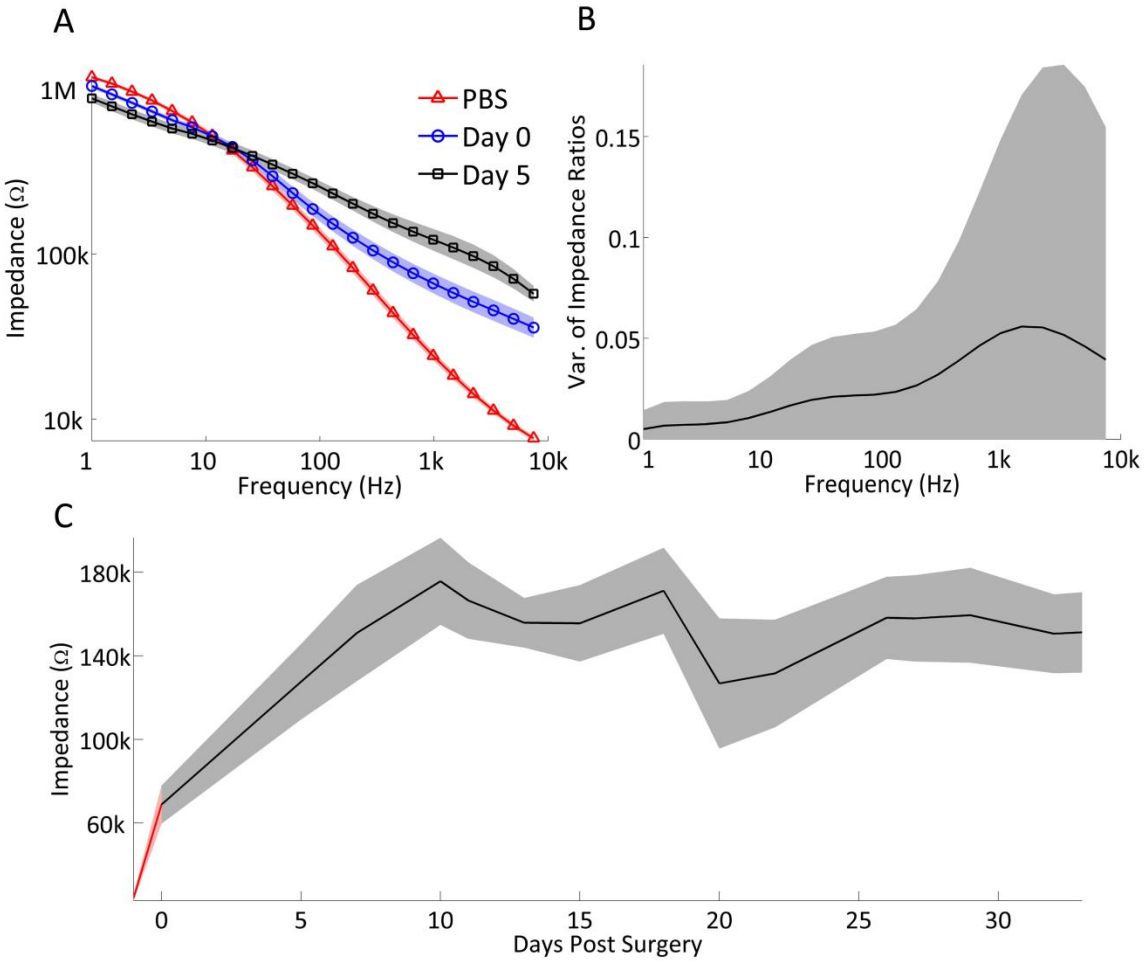

FIGURE 5-9. ***In vivo*** **impedance measurements from a chronically implanted microwire array in a rodent.** (A) Average impedance spectra across all 16 electrodes are shown when measured in phosphate buffered saline (PBS) immediately before implantation (blue curve), immediately after implantation (red curve), and 5 days post-surgery (blue curve). 95% confidence intervals are indicated by the pink, grey, and light blue shading. (B) The mean variability (across channels) of impedance ratios over time is shown for different frequencies (see text for description). The largest amount of variability is for frequencies >200 Hz. Shading indicates the standard deviation of the measured variability. (C) The average impedance (at 1 kHz) across channels is shown for different time points. Shading indicates 95% confidence intervals. The section in red indicates the mean impedance in PBS before surgical implantation.

When observing the impedance spectra of individual channels, we noted a large amount of variation at high frequencies (>100 Hz) across days. To quantify this, we calculated the variability, over time, of normalized impedance spectra. Specifically, a channel's impedance spectrum for each day was normalized to the average spectrum across days, creating a spectrum of ratios for each day (e.g., if the average impedance at 1 kHz was 100 kΩ, and the particular impedance on day 17 was 200 kΩ, the ratio would be 2 for day 17 at 1 kHz). The average spectrum did not include measurements in saline before implantation. We then calculated the variance over time of these spectra, to describe the level of variability at each frequency as the impedance evolved post-implantation. The resulting data were averaged across channels (Figure 5-9B), revealing a large increase in temporal variability localized to frequencies >200 Hz.

Impedance in vitro

The increase in impedance localized to high frequencies (>100 Hz) only occurs after implantation of the electrodes. This suggests that neural tissue is the prime factor for the increased impedance within this frequency band. As a further test of this, we repeated the impedance monitoring experiments using dissociated cultures of rat (embryonic day 18) neocortical neurons grown on substrate-integrated multielectrode arrays (Wagenaar et al., 2006b). Similar to the *in vivo* case, following culture plating there is an immediate increase in impedances >200 Hz (Figure 5-10A). Also, as was observed *in vivo*, the greatest amount of impedance variability through time is present in the frequencies between 100-10,000 Hz, the range most sensitive to the detection of action potentials (Figure 5-10B).

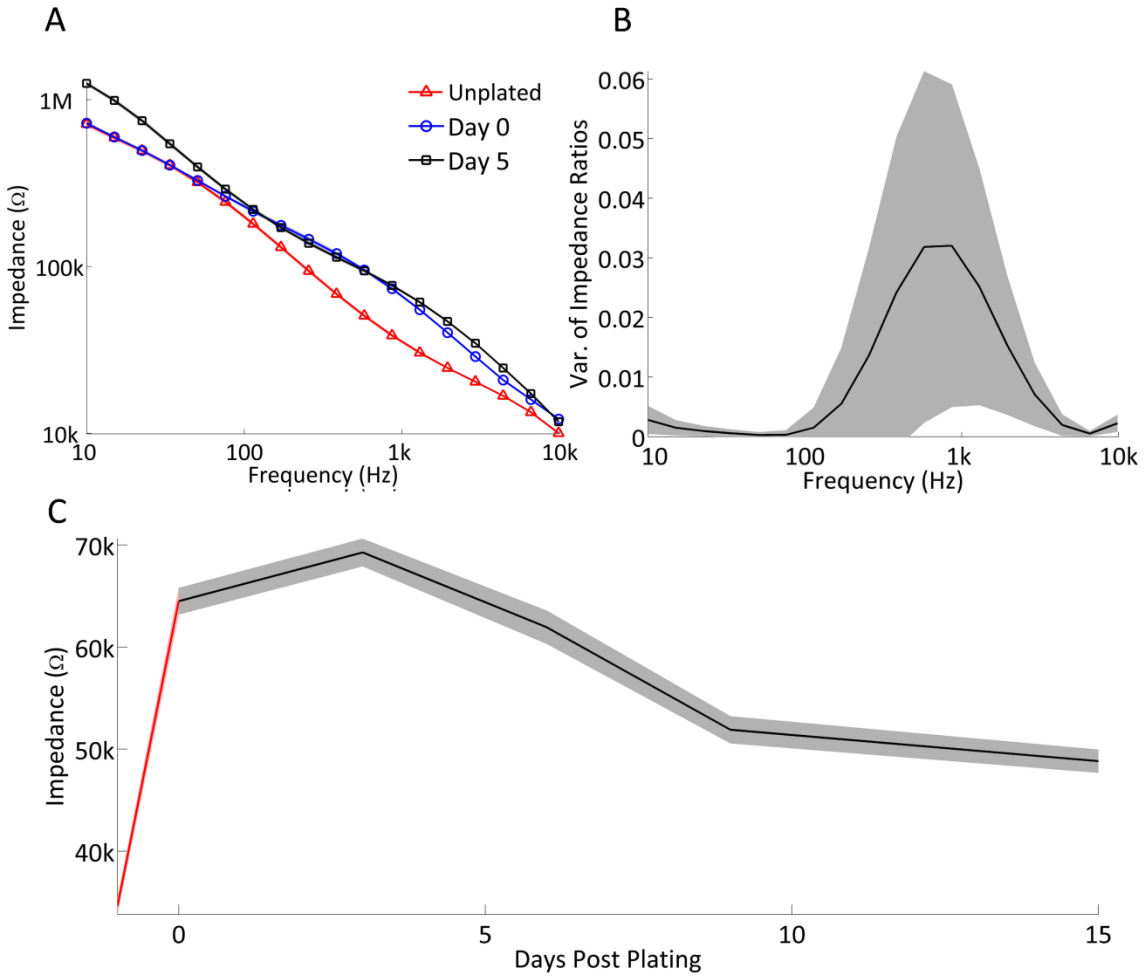

FIGURE 5-10. ***In vitro*** **impedance measurements from a substrate-integrated multielectrode array.** (A) Average impedance spectra across all 59 electrodes are shown when measured in culture medium (Dulbecco's Modified Eagle Medium along with 10% horse serum, sodium pyruvate, insulin and GlutaMax (Potter and DeMarse, 2001)) without plated cells (red curve), immediately after plating (blue curve), and 3 days post-plating (grey curve). 95% confidence intervals are indicated by the pink, grey, and light blue shading (the intervals are difficult to visualize due to their small magnitude). (B) The mean variability (across channels) of impedance ratios over time is shown for different frequencies (see text for description). The largest amount of variability is for frequencies >200 Hz. Shading indicates the standard deviation of the measured variability. (C) The average impedance (at 1 kHz) across channels is shown for different time points. Shading indicates 95% confidence intervals. The section in red indicates the mean impedance in culture medium in the MEA without cells.

Discussion

We created a versatile multi-channel, closed-loop system for use in both freely moving animals and *in vitro* experiments. The stimulator can deliver current- or voltage-controlled waveforms of arbitrary shape and can measure impedance spectra in real-time. Stimuli can be delivered to any of the recording electrodes with minimal artifact. The device can be used with our existing multielectrode recording hardware and software (Rolston et al., 2009b), our RACS stimulation hardware and software (Wagenaar and Potter, 2004), some commercial systems (e.g., Plexon, MultiChannel Systems), or in a stand-alone mode.

Comparison to existing systems

Experimental stimulation systems with some of these characteristics have been described previously: e.g., Venkatraman et al. (2009) in freely moving rodents, Mavoori et al. (Mavoori et al., 2005) in primates, and several for use with cell cultures (Wagenaar and Potter, 2004; Bontorin et al., 2007; Brown et al., 2008). Our system improves upon these previous devices in several ways. First, our system is more flexible, providing voltage and current-controlled modes and compatibility with a large number of systems and electrodes. It is also modular, allowing it to both stimulate and record from all electrodes in any given array. Second, our system performs real-time monitoring of impedance spectra, which can be used to gauge tissue responses to implanted electrodes (Williams et al., 2007) and to identify impaired electrodes (impedances will fall, for example, if an electrode becomes deinsulated). Of those systems of which we are aware, our system is the first to offer this capability. Third, our circuit schematics, layouts, and software are open-source and all freely available online. This contrasts with patented or commercial stimulators, like the stimulator described in Brown et al. (2008) or the commercial stimulator used by Venkatraman et al. (2009) . Having open-source designs

and software allows customization, and encourages other users to contribute improvements. Fourth, we use integrated recording and stimulation software. Using one application for both recording and stimulating allows tight communication between system components, providing a shorter time between detecting activity and delivering stimuli (i.e., shorter loop times). For example, our system has loop times 3-4× faster (shorter) than those of our previous closed-loop stimulator for *in vitro* studies (Wagenaar and Potter, 2004), and at least 2× faster than the closed-loop *in vivo* stimulator described by Venkatraman et al. (2009). An integrated application also grants the recording arm of the application detailed information about stimulation timing and characteristics. This information can be used for improved stimulus artifact suppression, filtering, or the cueing of recordings triggered by stimulus onset. Lastly, our system can be used *in vivo* or *in vitro*, providing a common interface for diverse experiments.

Closed-loop stimulation for epilepsy

Brief pulses of electrical stimulation have been shown to suppress afterdischarges in humans (Lesser et al., 1999), leading to a clinical trial of closed-loop stimulation for the suppression of seizures led by the company NeuroPace, Inc. (Fountas and Smith, 2007). These results prompt the question of whether lower amplitude pulses can suppress epileptiform activity in more local areas. To investigate, we delivered stimulation in response to the detection of spontaneous interictal spikes (IISs) in the hippocampus of epileptic rats exhibiting spontaneous seizures. First, we questioned whether short pulses of stimulation would modulate IISs recorded from a local electrode. In our preliminary investigations, stimulation to CA3 had no discernible effect on the interictal spikes recorded in CA3. This result might be consistent with our understanding of the origin of the LFP: low-frequency LFP signals (<50 Hz) are believed to arise due to synaptic input to an area (Buzsáki, 2006). Consequently, an effect might not be observed if stimulation

only affects the output of the tissue (action potentials), rather than the input (the low-frequency LFP). To see whether downstream areas were affected differently, we recorded simultaneously from CA1, which receives numerous direct projections from CA3 (Andersen, 2007). Here, too, we observed no discernible effect on IIS activity (Figure 5-8). Therefore, although stimulation evokes neural activity (Figure 5-7), the evoked activity did not appear to alter the ongoing IIS dynamics.

This is not to say that all microstimulation will be unable to alter the dynamics of IISs. Stimulation with higher amplitude currents, trains of stimuli (as is done for afterdischarges (Lesser et al., 1999)), or more electrodes, might be more effective in manipulating IIS activity. For example, it could be the case that a single pulse of microstimulation is not affecting enough neural tissue to override the prevailing epileptiform activity. Further characterization of the amount of tissue involved in IISs, as well as the volume of tissue activated by a stimulation pulse (Gross and Rolston, 2008), will be of great use in driving further experiments.

Impedance monitoring in vivo and in vitro

Measuring microelectrode impedance is important for three reasons—noise, stimulation, and impedance spectroscopy. One prominent source of noise in microelectrode recordings is thermal noise, also called Johnson-Nyquist noise. This noise arises from the inevitable movement of matter at temperatures above absolute zero, and is quantified by the formula $v^2 = 4k_BTZ$, where v is the noise amplitude (in units of voltage per √Hz), k_B is Boltzmann's constant, T is the temperature, and Z is the impedance. As can be appreciated from the equation, the higher the impedance, the greater the noise. Because electrode impedance is largely influenced by electrode surface area, impedance has become conflated with tip diameter and electrode size when discussing

microelectrodes in neuroscience. The two, however, are independent quantities, and the ideal microelectrode (for recording single cells) would have an infinitesimal surface extent and an impedance of zero (Ross et al., 2004).

Regarding stimulation, the current delivered with a stimulation pulse is dependent on an applied voltage and the electrode impedance (Ohms's law: $I = V/Z$). Therefore, with a lower electrode impedance, more current can be delivered with lower voltages. Using lower voltages results in smaller stimulation artifacts and potentially less tissue damage (Merrill et al., 2005).

Traditional electrode impedance spectroscopy (EIS) uses measured impedance spectra to query the nature of a measured substance (e.g., chemical rate constants, diffusion constants, doping density of semiconductors, etc.) (Barsoukov and Macdonald, 2005). The application of EIS to neuroscience is an emerging technique, mostly applied to determining the tissue reaction to implanted electrodes (Merrill and Tresco, 2005; Lempka et al., 2009).

By monitoring impedance spectra over time, we reached two conclusions. First, the measured impedance in saline at frequencies important for the detection of action potentials (~1 kHz) is a large underestimate of the true impedance in tissue (Figure 5-9 and Figure 5-10). In our *in vivo* setup, the impedance at 1 kHz increased nearly three-fold, from 24.3 kΩ to 68.8 kΩ, immediately upon implantation. A similar increase of 34.6 kΩ to 64.4 kΩ was observed with substrate-integrated MEAs *in vitro*. This increased impedance, which is confined to high frequencies, is likely due to the increased impedance of neural tissue as compared to saline, in agreement with the study of Lempka et al. (2009), which shows predominant tissue reactance between 100 Hz and 10 kHz. These differences in impedance between saline and tissue should be kept in mind

by microelectrode users when calculating quantities like the voltage required to generate a particular stimulation current.

A second conclusion is that the tissue component (100 Hz – 10 kHz) of impedance is more variable over time than the impedance at lower frequencies (Figure 5-9B, Figure 5-10B). This is likely due to changes in gliosis, as well as the dynamics of protein adsorption on the electrode surface. *In vivo*, high-frequency impedance changes might also be due to the dynamics of tissue swelling (this effect will not likely be present *in vitro*). Because impedances at lower frequencies are ostensibly not as affected by tissue, their impedances vary less over time.

Conclusions

We describe above a novel, open-source, closed-loop neural stimulator, capable of simultaneous stimulation and recording from microelectrode arrays both in freely moving animals and cell cultures. It is our hope that the system's free availability, push-button impedance spectroscopy, and ready-made stimulation routines will provide a useful experimental platform for the ongoing investigation of recurrent brain-computer interfaces.

Conflict of Interest Statement

John Rolston received consulting fees from Axion Biosystems, which represent a competitor of the described system. We therefore do not see this as a conflict of interest. The other authors declare that the research was conducted in the absence of any

commercial or financial relationships that could be construed as a potential conflict of interest.

Acknowledgments

We wish to thank Dr. Claire-Anne Gutekunst for help with rodent surgeries and histology. This work was funded by the Wallace H. Coulter Foundation (http://www.whcf.org/), the Epilepsy Research Foundation (http://www.epilepsy.com/etp/scientific_research), a Neurology/Biomedical Engineering seed grant from Emory University and Georgia Tech (http://www.bme.gatech.edu/), a University Research Council grant from Emory University (http://www.emory.edu), the National Institute of General Medical Sciences (NIGMS; http://www.nigms.nih.gov/) to JDR and NGL (GM08169), and, from the National Institute of Neurological Disorders and Stroke (NINDS; http://www.ninds.nih.gov/), a Ruth L. Kirschstein National Research Service Award to JDR (NS060392), a translational research fellowship to JDR (NS007480), a career development award to REG (NS046322), and a research grant to SMP and REG (NS054809). The funders had no role in study design, data collection and analysis, decision to publish, or preparation of the manuscript.

Author Contributions

The stimulation hardware and software was designed by J. D. Rolston. Rodent surgeries were performed by JDR and N. G. Laxpati. Impedance measurements were performed by NGL in rodents and N. J. Killian in culture. Data was analyzed by JDR. JDR and NGL

analyzed the impedance data. The paper was written by JDR, S. M. Potter, and R. E. Gross. Experiments were designed JDR. The project was conceptualized by JDR, REG, and SMP.

Chapter 6

Common Median Referencing for Improved Action Potential Detection with Multielectrode Arrays[13]

[13] © 2009 IEEE. Reprinted, with permission, from *31st Annual International Conference of the IEEE Engineering in Medicine and Biology Society*, "Common Median Referencing for Improved Action Potential Detection with Multielectrode Arrays," J. D. Rolston, R. E. Gross, S. M. Potter.

Abstract

Referencing is frequently used to remove common-mode signals from multielectrode data, in both freely moving animals and *in vitro* preparations. For action potential (AP) detection, referencing by subtracting the common average signal has been shown to increase AP signal-to-noise ratio (SNR). This method fails, however, when large transients occur on individual electrodes, as occurs during electrical stimulation or with large APs during spontaneous recordings. To deal with these cases, we propose using the common median as a reference. The common median has an improved SNR for AP detection (leading to more isolated single units and more detected APs per unit) and, unlike common average referencing, does not generate spurious APs when processing large single-electrode transients.

Introduction

Noise in multielectrode recordings has several origins, e.g., thermal noise due to electrode impedance, electromagnetic interference from nearby electronics, and biological signals that are not of interest to the investigator. This noise hinders our ability to detect signals of interest, such as action potentials (APs) or local field potentials (LFPs). Referencing (i.e., subtracting one time-varying signal from another) is one approach to dealing with such noise, functioning by removing common-mode signals (e.g., biological noise, 50/60 Hz noise) that are shared across the electrode and reference (Nunez and Srinivasan, 2006). Frequent choices of reference in freely moving animals are low-impedance skull screws, stainless steel wires, or a high-impedance microelectrode, carefully selected so as not to actively record single cells (which would otherwise show up on the referenced channels with inverted polarity).

It was recently reported that using the average signal across microelectrode channels was superior to alternative references in terms of noise reduction (Ludwig et al., 2009). While useful, the average reference has undesirable properties, namely that large signals on a single channel will skew the average toward outlying values. These large values then pollute the referenced channels, leading to spurious AP detections or large baseline shifts.

These problems become acute when conducting experiments involving microelectrode stimulation, a well-used experimental paradigm (Wagenaar et al., 2005b; Jackson et al., 2006; Bakkum et al., 2008b; Kipke et al., 2008; Venkatraman et al., 2009). Stimulation pulses are typically on the order of 100 mV – 10 V, which is 10^3-$10^5\times$ as large as a typical extracellular AP. Recording electronics typically do not amplify linearly in this regime,

but the signals on the stimulating electrode nevertheless dominate any computed average.

As an alternative to common average referencing, we propose common median referencing. The median is less susceptible to influence from outliers, as compared to the mean, yet is statistically equivalent when the inter-channel variability is Gaussian. When non-Gaussian, the median provides a better approximation of the distribution's center.

Methods

Surgery

All work with animals was conducted in accordance with the National Institutes of Health Guide for the Care and Use of Laboratory Animals and approved by the Emory University Institutional Animal Care and Use Committee. Adult male Sprague-Dawley rats (350-450 g) were anesthetized with isoflurane, several anchoring skull screws were implanted, and a craniotomy was drilled over the right dorsal hippocampus. After removing the dura, a 16-channel microwire array with two rows of 8 electrodes (row 1, 4 mm long; row 2, 2.8 mm long) was carefully lowered into craniotomy, with the longer row of the array targeted to the CA3 region, and the shorter row to CA1. Proper depth (usually 3-4 mm ventral to pia) was determined by monitoring electrophysiological recordings during implantation, using our lab's custom recording hardware and software, the NeuroRighter system (Rolston et al., 2008). The craniotomy was then sealed with dental acrylic and the rat was allowed to recover for 5-8 days before recordings began.

Recording

Rats were tethered to a 100× gain recording headstage and a custom-built stimulator (Rolston et al., 2008), but otherwise freely mobile in a Plexiglas enclosure. Extracellular signals, acquired at 25 kHz, were band-pass filtered from 1-9000 Hz in hardware. In software, the signals were split into two streams: spikes (filtered from 500-5000 Hz) and LFPs (1-500 Hz, downsampled to 2 kHz). Data was stored for offline analysis, which was conducted using MATLAB r2008. Spikes were detected as threshold crossings of ≥5× RMS, unless otherwise specified. Spikes were sorted using superparamagnetic clustering across wavelet coefficients with the Wave_clus software (Quiroga et al., 2004).

Results

We first describe theoretical results for signal contamination and attenuation with common average referencing, then present empirical data to illustrate the advantages of common median referencing over average referencing in practice.

Theoretical Contamination and Attenuation

Each signal s_i contributes $1/N$th of the average reference signal's amplitude, where N is the number of electrodes averaged. Two effects are noted. First, each s_i is attenuated by a factor of $1 - 1/N$, since its contribution to the average is now being subtracted from itself. Second, the inverse of the signal will now be present on all channels with an attenuation of $1/N$ (Figure 6-1).

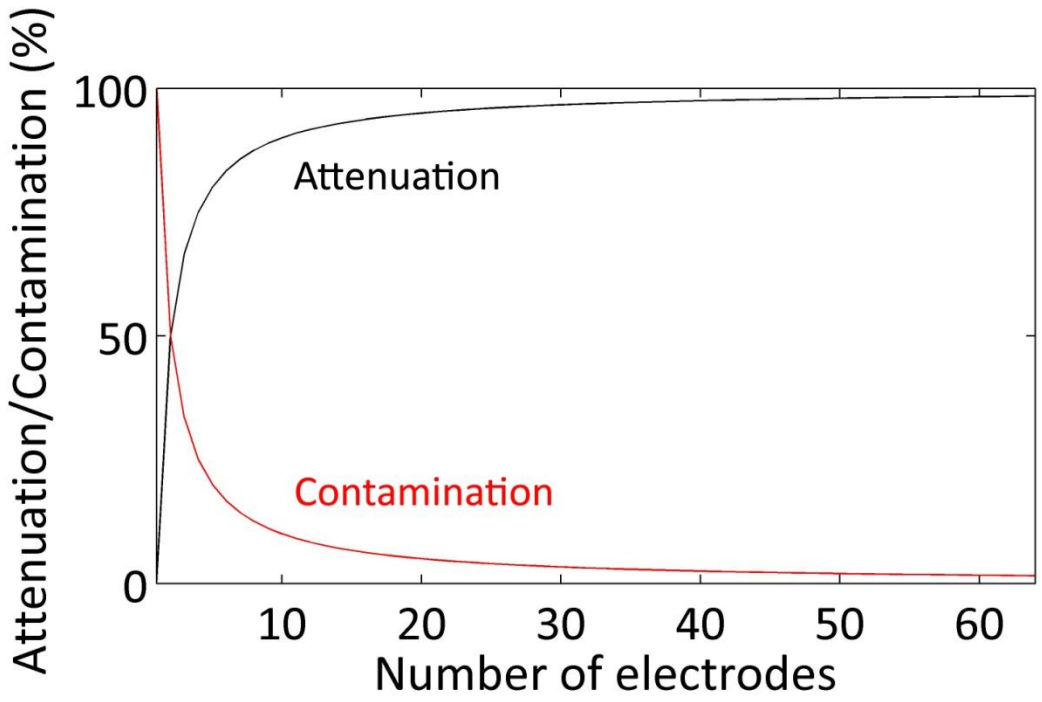

FIGURE 6-1. Theoretical attenuation (black) and contamination (red) of channels with common average referencing.

These results show that, for example, using a 10-electrode array and common average reference, that a 100 μV AP would be attenuated to 90 μV, and that a "phantom" 10 μV AP would show up on every other channel.

Spontaneous Experimental Data

Is the worry of contamination well founded, or are the spurious spikes too attenuated to be detected as APs? Empirical data suggests that the worry of induced spurious spikes is real. For example, a recording from an anesthetized rat hippocampus, using 16 electrodes, shows threshold-crossing contamination when large APs are detected (Figure 6-2). That is, with common average referencing, the "bleed-through" of an AP on one channel causes a spurious action potential on all other channels. These spurious APs cross the 3.5× standard deviation threshold, from Ludwig et al. (Ludwig et al., 2009), in

11/16 channels, and the 5× threshold in 1/16 channels (not including the channel of the actual AP in either case). This same type of contamination occurred 22 times in 5 sample minutes of recording. These problems do not occur with median referencing (0 times in 5 minutes).

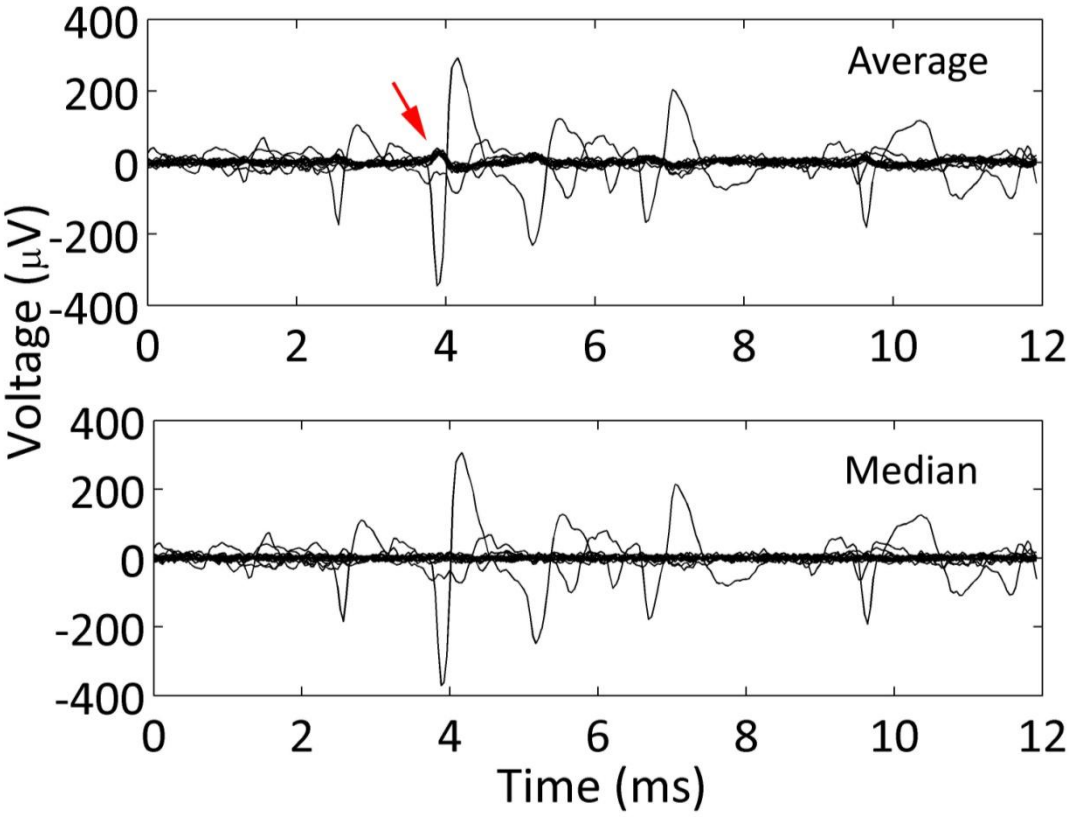

FIGURE 6-2. Contaminated traces with common average referencing vs. common median referencing. A large action potential on a single channel dominates the mean, creating spurious APs on all other channels (red arrow) when using average referencing (top). These problems do not occur with median referencing (bottom).

Stimulation Data

While the spurious spikes are problematic in spontaneous data, a more notable problem arises with electrical stimulation. When delivering a stimulus pulse to a single electrode,

the resulting artifact is referred to all other channels when using common average referencing (Figure 6-3).

The data shown in Figure 6-3 is broadband filtered (1-9000 Hz). If purely interested in APs, a much tighter band-pass would likely be used (e.g., 500-5000 Hz), in which case the prolonged baseline shift would be less notable. In either case, however, common median referencing is impervious to these contamination artifacts.

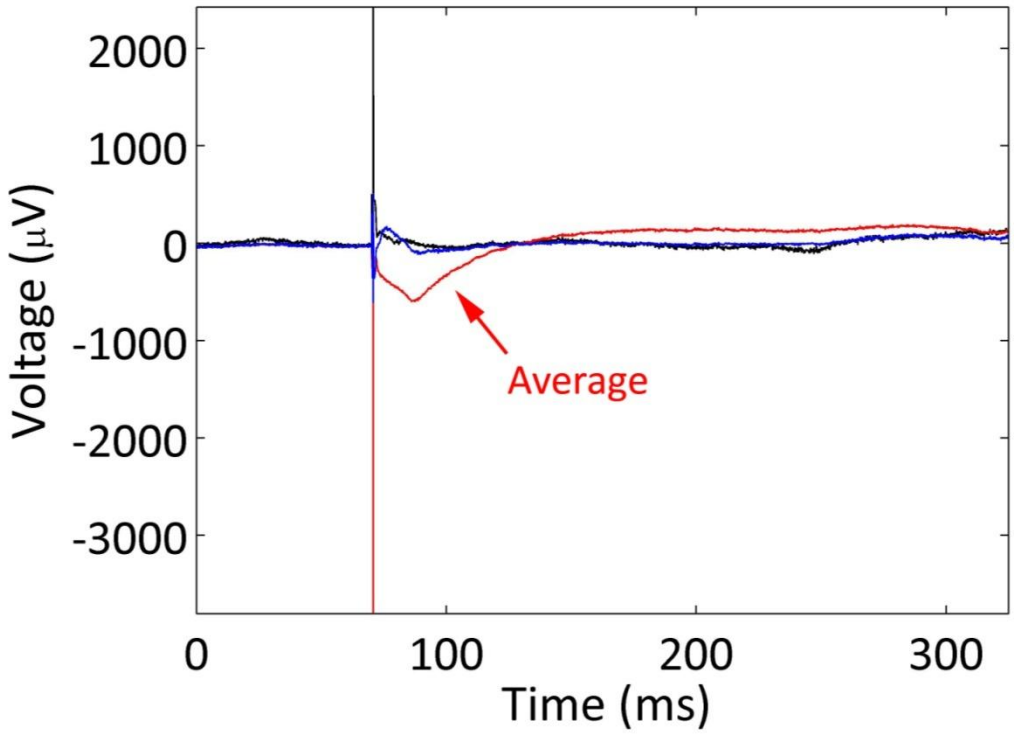

FIGURE 6-3. Stimulus artifact contamination. The original trace (black) shows minimal baseline shift following the stimulation pulse. The common average reference (red trace) reflects the long baseline shift from the stimulating electrode. Common median referencing (blue trace) avoids this problem.

Noise Reduction

To assay the effectiveness of the two referencing modes (average vs. median), we computed the RMS noise value for referenced band-pass filtered signals (500-9000 Hz),

suitable for detecting APs. The data (duration of 2 minutes) was acquired from 16 electrodes in the hippocampus of a freely moving rat.

Common average referencing had a mean RMS of 6.1 ± 0.5 μV across electrodes, common median referencing 6.2 ± 0.6 μV (compared to 7.3 ± 0.6 μV for unreferenced data). The median reference RMS value is significantly greater (by 0.1 μV) than the average reference RMS ($P < 0.01$, Wilcoxon sign-rank test). However, it should be recalled that with median referencing there is no statistical attenuation of signals. Thus, while the RMS noise for each channel using median referencing is higher than that of average referencing, the SNR is still greater with median referencing. As an example, given the above empirical RMS values from 16 electrodes, an AP with 100 μV amplitude will be attenuated to 94 μV using common average referencing (or 15× the RMS noise level. For median referencing, the same AP (unattenuated) is 16× the RMS noise level.

Detection Performance

Using 5 minutes of spontaneous recordings from three animals (16-channel arrays in the dorsal hippocampus; see Methods), we compared the effectiveness of common average and common median referencing. The data was referenced separately according to both methods, APs were detected (using 5× the RMS threshold of the referenced data, specific to each channel and each referencing method), and APs were sorted with superparamagnetic clustering of the wavelet decomposition (Quiroga et al., 2004).

With common median referencing, 0.66 additional well-sorted units were detected per dataset, on average (Figure 6-4). Additionally, across sorted units, there was an average increase of 10% in the number of detected APs (Figure 6-4). In no cases did common median referencing perform worse than common average referencing.

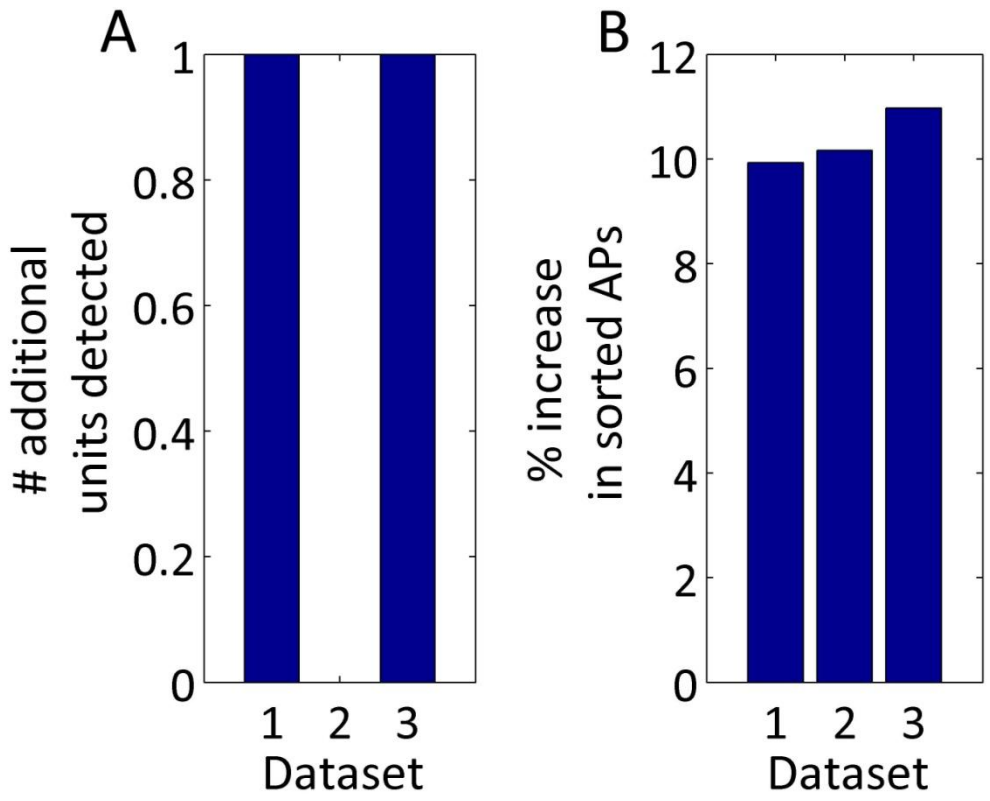

FIGURE 6-4. AP detection is improved with common median referencing vs. common average referencing. (A) Additional units are detected with spike sorting in 2/3 datasets, using common median referencing. (B) More APs are detected from sorted units with common median referencing as compared to common average referencing.

Discussion

Multielectrode recordings have provided useful insights into normal and pathological brain function (Buzsaki, 2004). Biophysical and electromagnetic noise sources, however, are a constant nuisance that obscure target neural signals. A simple method for reducing correlated noise (common-mode noise) is digital or analog referencing (Nunez and Srinivasan, 2006). Such referencing often selects a single electrode with low activity as a representation of background noise. This method is highly sensitive, however, to any uncorrelated noise on the reference channel, such as APs, stimulus artifacts, or other localized biological transients. In the field of electroencephalography (EEG), common

average references have routinely been used as one means of preventing uncorrelated noise from affecting referenced channels (Nunez and Srinivasan, 2006). This method was recently applied to multi-microelectrode arrays to improve the detection of APs, with an identical rationale (Ludwig et al., 2009).

The mean of a statistical sample, especially when there is a small sample size, is dominated by any occurring outliers. For multielectrode neural recordings, this translates to large APs from one electrode appearing on referenced electrodes (Figure 6-2) or baseline shifts from stimulus artifacts contaminating signals from other electrodes (Figure 6-3). The median provides a more stable representation of a distribution's central tendency that is less affected by large transients on a few channels.

While the median provides an improved estimate of the common signal, the RMS noise of this estimate is higher for the median referenced signals than for the average referenced signals. This is expected, in fact, since for most probability distributions, the absolute value of the median is guaranteed to be less than or equal to the mean (W. R. van Zwet, 1979; Abadir, 2005). Therefore, since the referencing signal has lower power, the referenced signal will have a slightly higher power than the comparable averaged referenced signal. This higher power will lead to an improved SNR of the median referencing scheme as compared to the average referencing scheme, even before accounting for the average referencing scheme's signal attenuation. Indeed, when analyzing data from multiple animals, common median referencing resulted in more isolated single units and more APs per unit than common average referencing (Figure 6-4).

While a common median reference is readily computed in real-time (e.g., we routinely use it during 64-channel recordings with our NeuroRighter software (Rolston et al.,

2008)), it nevertheless takes longer to calculate than the simpler common average reference. When scaling to very high channel counts (e.g., 1000s to tens of 1000s of electrodes (Frey et al., 2009)), computationally simpler methods might be advantageous. Yet robust statistics are still crucial for high performance. In these cases, hybrid methods might be used (e.g., removing outliers, then computing a common average (Stark and Abeles, 2007)) that preserve the spirit of a robust statistic (Huber and Ronchetti, 2009), but are less computationally expensive.

Conclusion

Empirically and theoretically, median referencing leads to a higher SNR for APs, and prevents false positive detections of spurious APs or other transients (e.g., stimulus artifacts). The method is simple and easily computed in real-time during data acquisition.

Acknowledgments

We gratefully acknowledge technical support from Claire-Anne Gutekunst, Lissa Jackson, and the Gross and Potter labs.

Chapter 7

Seizures and Interictal Spikes are Altered by Distributed Microstimulation

Abstract

Distributed microstimulation has been shown to completely suppress epileptiform bursting both in cell culture and neural network simulations. Using a rodent model of epilepsy, we tested whether distributed microstimulation could also suppress epileptiform bursting and seizures in freely behaving animals. Microwire arrays were chronically implanted in the dorsal hippocampi of rats made epileptic by focal injections of tetanus toxin. After the rats developed spontaneous seizures, multiple frequencies of distributed stimulation (10, 20, 50, and 100 Hz) were delivered across the array in randomized 30 minute epochs, with 30 stimulation-free minutes between each test. Seizure and interictal spike rates were compared across the non-stimulated and stimulated epochs. Across animals, distributed microstimulation increased interictal spike rates and seizure rates at all tested frequencies. Interestingly, however, the largest increase in the interictal spike rate (with 10 Hz stimulation) coincided with the lowest increase in seizure rate. This trend may indicate an inverse relationship between interictal spike rate and seizure rate.

Introduction

The rationale for examining distributed microstimulation as a treatment for epilepsy is discussed in detail in Chapter 3. Briefly, dissociated cultures of neocortical neurons grown on multielectrode arrays (MEAs) exhibit frequent barrages of neuronal activity, similar to epileptiform bursts (Wagenaar et al., 2006b). Similar bursts occur in large-scale neuronal network models with roughly the same number of neurons (Chao et al., 2005). In both cases, low-voltage microstimulation, when distributed over many electrodes (≥10) was able to completely suppress these bursts (Chao et al., 2005; Wagenaar et al., 2005b).

Can a similar approach suppress epileptiform bursting (i.e., interictal spikes) *in vivo*? To test this, we used chronically implanted microwire arrays to approximate the substrate-integrated multielectrode arrays used to suppress bursts *in vitro*. Since normal animals do not exhibit epileptiform bursts or seizures, we induced chronic epilepsy in rats by injecting small quantities of tetanus toxin into the dorsal hippocampus, producing a model of temporal lobe epilepsy. Electrode arrays were implanted peri-focally. Below, we show that, while we were able to influence epileptiform bursting and seizures with distributed stimulation, we were unable to suppress bursting as was done *in vitro*. However, we note an interesting inverse relationship between interictal spike rate and seizure rate at the lowest frequency of stimulation (10 Hz).

Methods

Rodent Surgeries

To evaluate distributed microstimulation *in vivo*, multielectrode arrays were chronically implanted in 8 male Sprague-Dawley rats (>350 g; Charles River Laboratories;

Wilmington, MA, USA), made epileptic with focal injections of tetanus toxin. All animal work was conducted in accordance with the National Institutes of Health *Guide for the Care and Use of Laboratory Animals* and approved by the Emory University Institutional Animal Care and Use Committee. Rats were anesthetized with 1.5-3.0% inhaled isoflurane and given a subcutaneous injection of buprenorphine (0.05 mg/kg) to minimize pain. A craniectomy was made over the right dorsal hippocampus, centered at 3.5 mm posterior and 2.8 mm lateral to bregma. The dura was incised with a sterile syringe needle and a single injection of 25 ng of tetanus toxin (Sigma Aldrich, St. Louis, MO, USA) in 0.5 μl phosphate buffered saline with 0.2% bovine serum albumin (Jefferys and Walker, 2005) was delivered. The injection, using a pulled glass pipette and a stereotactically mounted injector (Nanoject; Drummond Scientific Co., Broomall, PA, USA), was located in the dorsal hippocampus (3.3 mm posterior and 3.2 mm lateral to bregma, and 3.1 mm ventral to pia) and occurred immediately prior to the MEA implant. The needle was allowed to equilibrate for one minute prior to injection, the injection was delivered over 3 minutes, and the needle was left in place for 5 minutes following the injection to prevent reflux.

A microwire array (Tucker Davis Technologies; Alachua, FL, USA) was implanted after the tetanus toxin injection. The array had sixteen 33 μm diameter tungsten electrodes with polyimide insulation arranged in two rows of 8 electrodes, with 175 μm between electrodes within a row and 1 mm between rows. The two rows had different lengths, 4.0 mm and 3.0 mm, with the former directed at the CA3 region of the hippocampus, and the latter at the more dorsal CA1 region. The array had stainless steel wires for ground and reference electrodes, which were wound around stainless steel skull screws at the time of surgery. The reference screw was located slightly posterior to lambda, over the cerebellum.

The array was positioned at a 50° angle to midline (counter-clockwise rotation, with the posterior end swung laterally) to match the contours of the hippocampus. Electrodes were lowered while recording activity in order to attain correct positioning (Gross et al., 2006), usually ending when the longer electrodes were ~3 mm ventral to pia.

When the recordings stabilized, the craniectomy was sealed with cyanoacrylate glue (Loctite; Rocky Hill, CT, USA), skull screws were implanted (Plastics One; Roanoke, VA, USA), and dental acrylic (OrthoJet; Lang Dental; Wheeling, IL, USA) was applied to secure the array's connector. The rats returned to their normal housing, and rested and recovered post-operatively for 5-8 days before recordings began. All animals exhibited spontaneous seizures within 3-9 days. No mortality or morbidity from the injections was observed, consistent with previous reports (Jefferys and Walker, 2005).

Distributed Stimulation

When the rodents began exhibiting seizures, distributed microstimulation was delivered in an attempt to control their interictal spikes and seizures, using the closed-loop stimulator described in Chapter 5. 12 of 16 electrodes were selected in each animal (6 from each row of the array) for stimulation, leaving 4 electrodes unstimulated (to provide redundant measures of neural activity unperturbed by direct stimulation artifacts). Stimulation pulses consisted of biphasic ±10 μA pulses (cathodic phase first), which were previously shown effective in evoking neural activity in epileptic animals (Rolston et al., 2009b) (and Chapter 5). Stimulation was delivered asynchronously to the 12 electrodes in a randomly determined order at an aggregate frequency f (that is, each electrode was individually stimulated at a frequency of $f/12$). In these experiments, f was varied between 10, 20, 50, and 100 Hz.

The experimental design is depicted in Figure 7-1. Briefly, 30 minute epochs consisting of either no stimulation or stimulation at one of the test frequencies were presented. The frequencies were randomly selected without replacement, so that all frequencies were tested.

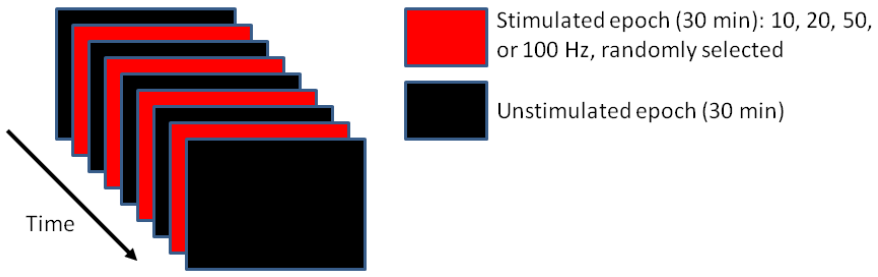

FIGURE 7-1. Experiment design. Distributed microstimulation was delivered in 30 minute epochs (red frames) at a randomly selected stimulation frequency (10, 20, 50, or 100 Hz). Stimulated epochs were interleaved with non-stimulated epochs (black frames). Stimulation frequencies were selected without replacement, so that all stimulation frequencies were tested.

Electrophysiology

Electrophysiological recordings were made using the NeuroRighter system (Rolston et al., 2009b). Extracellular voltage traces were recorded from all 16 electrodes in each animal, referenced in hardware to a cerebellar screw. The recordings were sampled at 25 kHz with a bandwidth of 1-9000 Hz (Rolston et al., 2009b). Recordings were processed offline in Matlab (MathWorks, Inc.; Natick, MA, USA) and custom software written in C#.

Post-processing consisted of removing the stimulation artifacts by clipping 2 ms of the raw waveform surrounding the stimulation time (5 samples before and 45 samples after) and interpolating the remaining points (Heffer and Fallon, 2008), digitally filtering the resulting artifact-free trace between 1-500 Hz (1-pole filter), and downsampling to 2500

Hz. Since interictal spikes last 10s to 100s of milliseconds, we were easily able to observe them in the reconstructed traces (Figure 7-2).

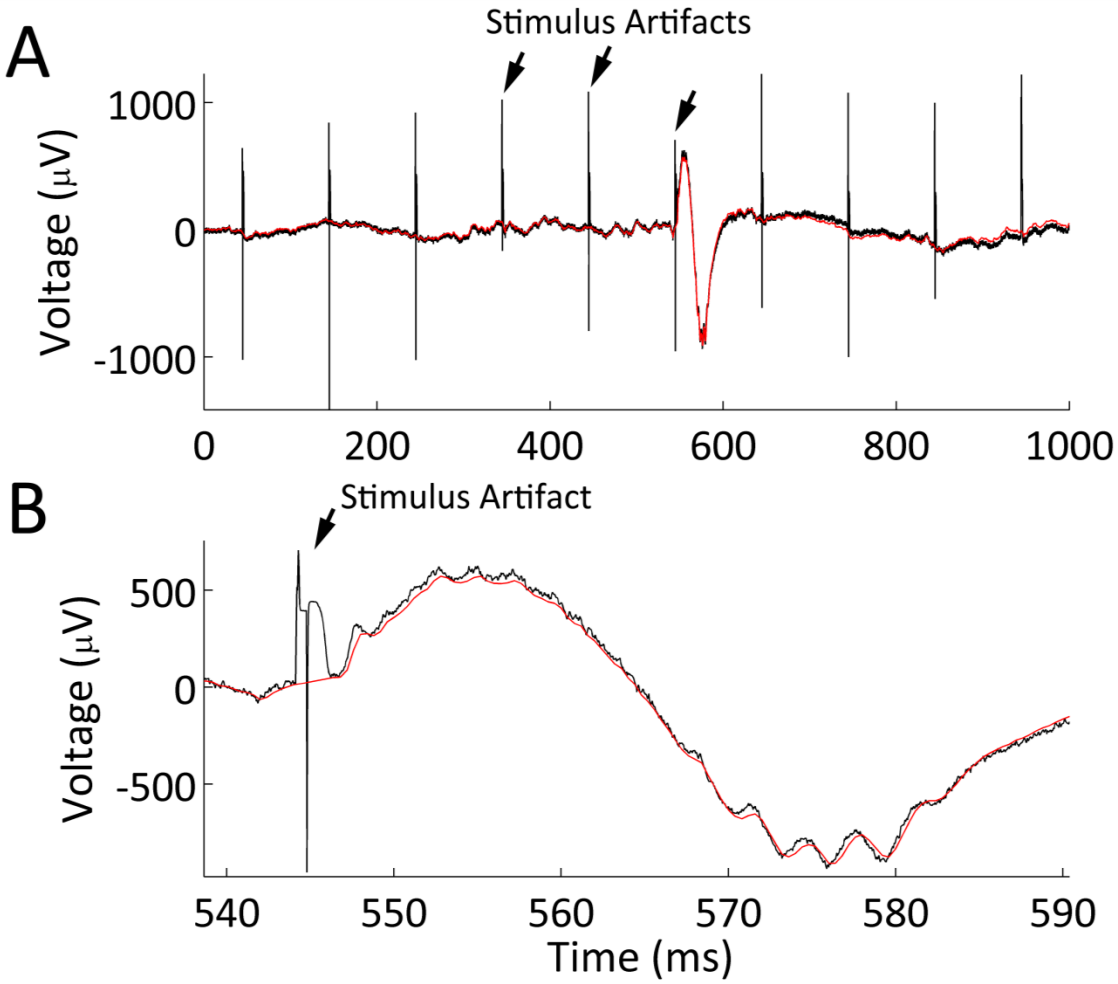

FIGURE 7-2. Artifact removal. To remove stimulation artifacts on non-stimulated channels, 2 ms around each stimulation pulse were clipped and the removed data interpolated from the uncorrupted neighboring points (see text). (A) Raw data (black) is shown before artifact removal and after filtering (red trace). Three of the periodic stimulation pulses are indicated with black arrows. (B) Magnification of the interictal spike (IIS) in (A), showing the removed stimulation artifact at the IIS's onset.

Interictal Spike and Seizure Detection

Interictal spikes were detected by first band-pass filtering the signal from 10-100 Hz (4^{th} order zero-phase filter), then estimating the baseline noise using the median of the

absolute value, divided by 0.6745 (Donoho and Johnstone, 1994; Quiroga et al., 2004). Interictal spikes were detected as deviations beyond 7.5× this baseline. To ensure the threshold was commensurate across epochs, IISs were detected using the average threshold across epochs for each animal.

Seizures were marked by hand, since they were far fewer in number (~1-2 per hour) than interictal spikes (one every 5-10 seconds).

Results

Eight rats were made epileptic with focal injections of tetanus toxin into the dorsal hippocampus. Each rat was also implanted with a 16-channel microwire array (see Methods). Once the animals began exhibiting seizures (5-10 days after surgery), distributed microstimulation was delivered in an effort to affect the number of IISs and seizures.

Results are depicted in Figure 7-3. Because the IIS and seizure rates are variable across animals, rates were normalized to the baseline, non-stimulated rate, yielding ratios of IIS rates and seizure rates. A ratio of 1 would imply no difference between stimulated and unstimulated epochs; ratios <1 imply a reduced rate; and ratios >1 imply a worsening of IIS or seizure rates.

In all cases, IIS rates and seizures rates were elevated above baseline. Within the data, there appears to be a trend in that the greatest increase in IIS rate occurs at 10 Hz, while the lowest increase in seizures also occurs at 10 Hz. Indeed, the difference between IIS rates (not ratios) at 10 Hz is significantly different than IIS rates at other stimulation frequencies (P = 0.025, two-sided rank-sum test). Similarly, the seizure rate with 10 Hz

stimulation is significantly lower than that of other frequencies (P = 0.034, two-sided rank-sum test). However, this is not a simple linear relationship: neither the correlation coefficient between stimulation frequency and IIS rates nor the correlation between stimulation frequency and seizure rates was significant. Additionally, no correlation was found between IIS rate and seizure rate, independent of stimulation frequency.

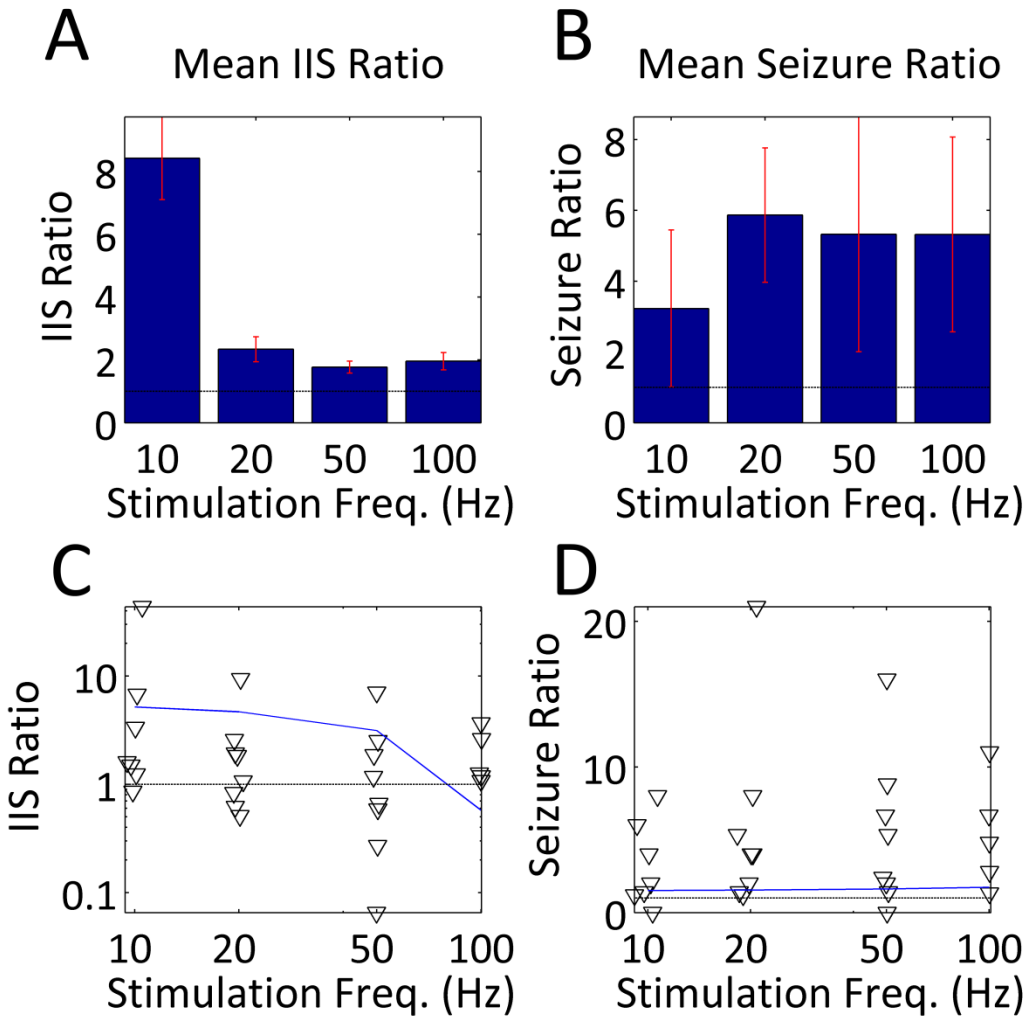

FIGURE 7-3. Results of distributed microstimulation. (A) Ratios of IIS rates (compared to baseline) are shown for each stimulation frequency. Red error bars depict 95% confidence intervals (not standard error). A ratio of 1 is indicated by the horizontal black line. In all cases, the IIS rate is significantly elevated beyond baseline. (B) Ratios of seizure rates (per 30 minute epoch, compared to baseline) are shown for each stimulation frequency. Red lines indicate 95% confidence intervals. In all cases, the seizure rate is elevated above baseline (ratio of 1, indicated by horizontal black line). (C) Log-log

plot of IIS ratios for each animal as a function of stimulation frequency. (Log-log chosen to better visualize outliers and main group simultaneously.) Data from a single animal is depicted as a hollow triangle. The linear best-fit line is shown in blue (its non-linear appearance is due to the log-log plot). A ratio of 1 is indicated by a horizontal black line. (D) A semi-log plot of seizure ratios as a function of stimulation frequency is shown (log of the abscissa). Data from a single animal is depicted as a hollow triangle. The linear best-fit line is shown in blue (its non-linear appearance is due to the log-log plot). A ratio of 1 is indicated by a horizontal black line.

Discussion

Distributed microstimulation increased interictal spike rates and seizure rates at all tested frequencies (10, 20, 50, and 100 Hz). Therefore, distributed microstimulation, as conducted here, does not appear to be viable treatment for epilepsy. It should be stressed, however, that only a small set of parameters was tested. Some of the more important free parameters are listed below, along with commentary.

1. Number of electrodes. The motivation behind distributed microstimulation is that it either a) keeps enough neurons in a refractory period or relative refractory period to prevent them from participating in bursts or b) keeps cells depolarized such that low-threshold calcium currents are not activated, which would lead to bursting (Xu and Clancy, 2008). Perhaps influencing a larger area of the hippocampus, using more electrodes, would yield better control.
2. Geometry of array. As noted above, more tissue might need to be affected to suppress seizures. A wider spacing of electrodes might go some way in accomplishing this.
3. Anatomical locations. The hippocampus is a large structure, and we targeted only a small portion of the dorsal aspect. Perhaps it will be easier to affect the entirety of different structures, for example the subthalamic nucleus (Loddenkemper et al., 2001) or anterior nucleus of the thalamus (Jobst, 2009).

4. Pulse amplitude. 10 μA pulses were used in this study, since they have been shown to reliably evoke neural activity (Rolston et al., 2009b). In the case of placing more cells in a refractory period, increasing the current to evoke more APs is essential, thus higher amplitude pulses might prove useful. On the other hand, elevating the membrane potential to inactivate T-type calcium channels (Xu and Clancy, 2008) might be readily accomplished by subthreshold stimulation (though, suprathreshold stimulation might evoke APs, which in turn depolarize downstream cells, without evoking further APs, accomplishing something similar).
5. Pulse trains. Brief trains of pulses, often at 200 Hz, have been shown in neocortex to more readily evoke activity (Butovas and Schwarz, 2003; Venkatraman et al., 2009). Perhaps a similar approach could be tried in the hippocampus.

Previous experiments with stimulation of the hippocampus support the current results. For example, Goddard showed early on that low-intensity stimulation (as low as 6 μA) delivered at 20-200 Hz could induce seizures in normal animals, providing the basis for the kindling model of epilepsy (Goddard, 1967). Godard's experiments used stimulation delivered from a single electrode, however, while distributed stimulation uses multiple electrodes to reach the same aggregate frequencies. This might be irrelevant, though, if all of the electrodes influence the same region of tissue—that is, they appear to the neural network as a "single electrode."

Concerning the reduced rate of seizures at lower stimulation frequencies, this again has been anticipated. Several groups, in fact, have reported reduction in seizure rates with low-frequency stimulation, from 0.1-5 Hz (Gaito, 1980a, b; Gaito et al., 1980;

D'Arcangelo et al., 2005; Jahanshahi et al., 2009). This is consistent with the lower seizure rate observed at 10 Hz of distributed microstimulation compared to higher rates.

Little work has been done, on the other hand, analyzing the effect of stimulation on interictal spike rate. While the present data provides only a weak correlation between IIS rate and seizure rate, the fact that the lowest seizure rates (at 10 Hz) coincide with the highest IIS rates provides circumstantial evidence that the two might be inversely related. Indeed, such a relationship has been shown to exist *in vitro* (Avoli, 2001), but only at low stimulation rates (0.25-1.5 Hz).

Conclusion

Distributed microstimulation is able to alter the dynamics of epileptic neural networks in freely moving animals. However, when delivered at 10-100 Hz, these alterations act to increase interictal spike rates and seizure rates. Interestingly, however, there appears to be a separation of effects at 10 Hz, the lowest frequency studied, in that seizure rates are at their lowest, while interictal spike rates are at their highest during these stimulation epochs.

Acknowledgements

I gratefully acknowledge assistance with animal surgeries from Nealen G. Laxpati and animal histology from Dr. Claire-Anne Gutekunst, Eric N. Stewart, and N. G. Laxpati.

Chapter 8

Presence and production of high-frequency oscillations in the tetanus toxin model of epilepsy

Abstract

High-frequency oscillations (~300 Hz), observed in the electroencephalogram or as local field potentials, are an emerging biomarker for epileptic tissue. Yet the mechanism by which HFOs are produced is unknown, and their rarity makes them difficult to study. Here, I present the first evidence of HFOs in the tetanus toxin model of epilepsy, a model with reduced latency to spontaneous seizures compared to alternative models. I then show how population bursts of action potentials (which occur during interictal spikes) are phase-locked with these oscillations, and that HFOs associate almost exclusively with high-amplitude interictal spikes. Lastly, I show that HFOs can be produced by electrical microstimulation of the hippocampus, providing the first evidence that these oscillations can be controlled temporally by external means.

Introduction

Epilepsy is a debilitating neurological disorder affecting nearly 1 in every 100 people (Brodie et al., 1997). Despite our best pharmacological treatments, up to a third of patients continue to have seizures (Cockerell et al., 1995; Kwan and Brodie, 2000). Surgical resection is a potentially curative option for some of these refractory patients, but surgical planning requires accurate localization of epileptogenic tissue prior to its removal. To this end, electroencephalography (EEG) and intracranial electrocorticography (ECoG) are routinely used to delineate pathologically active tissue prior to resection. These methods, undesirably, rely on recording infrequently occurring seizures, sometimes requiring weeks to months of continuous in-patient monitoring, and presenting obvious inconvenience and costs to the patient. In comparison, the more frequently occurring interictal spikes (IISs) are useful in diagnosing seizure disorders, but have poor localizing capabilities (Hufnagel et al., 2000; Rosenow and Luders, 2001).

High-frequency oscillations (HFOs) in the 200-400 Hz band are pathological field potentials detected in the local field potential (LFP), EEG, or ECoG and are highly specific to epileptic regions in animal models and patients with epilepsy (Engel et al., 2009). Moreover, a recent study has shown that HFOs are a more accurate predictor of the seizure onset zone (i.e., seizure focus) than are interictal spikes (Jacobs et al., 2008). As such, HFOs have potential as a more readily ascertainable biomarker for epileptic tissue than IISs or infrequent seizures.

Despite these implications, little is known about the mechanisms of HFOs. Thus, evoking the oscillations on demand in a high-throughput animal model will have clear experimental benefits. We address this in two ways. First, we describe the presence of HFOs in an additional animal model of epilepsy, the tetanus toxin model, which has

advantages over the status-epilepticus models currently used to study HFOs. Second, we find that HFOs are reliably triggered by electrical microstimulation, providing access to a more consistent evaluation of their presence and experimental perturbation. We use this model to address two questions concerning the nature of HFOs: 1) what is their relationship to IISs, and 2) what is their relationship to multiunit activity?

Methods

Surgery

Surgical methods are identical to those described in Chapter 4 and Chapter 5. Briefly, male Sprague-Dawley rats were stereotactically injected with 25 ng of tetanus toxin into the dorsal hippocampus to induce chronic seizures. At the same time, a 16-channel microwire array (33 μm diameter; TDT, Inc.) was implanted with 8 electrodes each in CA3 and CA1 of the dorsal hippocampus.

Electrophysiology

Electrophysiological recordings were made using the NeuroRighter system (Rolston et al., 2009b). Extracellular voltage traces were recorded from all 16 electrodes in each animal, referenced in hardware to a skull screw overlying the cerebellum. The recordings were sampled at 25 kHz with a bandwidth of 1-9000 Hz (Rolston et al., 2009b). The raw data was digitally processed in real-time to separate local field potentials (LFPs) from action potentials (APs). To record the LFP, the raw recording was band-pass filtered from 1-500 Hz (3-pole Butterworth) and downsampled to 2000 Hz. To detect APs, the raw recording was band-pass filtered from 500-5000 Hz (3-pole Butterworth), the common median reference was subtracted across channels (Rolston et al., 2009a) (Chapter 6), and spikes were detected in real-time by finding deviations greater or less

than 5× the signal's RMS noise (the RMS estimate was local to each channel, and updated in real-time).

Further processing was conducted offline in Matlab (MathWorks, Inc.; Natick, MA, USA) and custom software written in C#.

Interictal spike and HFO detection

Interictal spikes (IISs) were detected by band-pass filtering the LFP between 10-100 Hz (4^{th} order zero-phase Butterworth), producing a signal $V(t)$. IISs were identified as excursions of this signal $\geq 7.5 \times \text{median}(|V(t)|) / 0.6745$ (Donoho and Johnstone, 1994), a robust estimate of the standard deviation (which is equivalent to the RMS noise in signals with no DC offset, as is the case with this high-pass filtered data). To ensure that detected IISs were generated locally to each electrode, all detection was carried out using one electrode's LFP subtracted from a neighbor's electrode. This referencing helped minimize common mode interference (identical referencing was done for the HFO detection described below).

High-frequency oscillations were detected by band-pass filtering the LFP between 200-400 Hz (4^{th} order zero-phase Butterworth), squaring each sample, low-pass filtering the result below 200 Hz (2-pole zero-phase), and taking the square root of each sample. Low-pass filtering in this case is acceptable since the band-pass filtered signal is first squared (rectified) (Stark and Abeles, 2007). The median of the signal was then subtracted, producing a time-varying signal $H(t)$ which provided an estimate of the energy in the 200-400 Hz band at any given time. HFOs were then detected by finding excursions $\geq 5 \times \text{median}(|V(t)|) / 0.6745$ (as was done with IIS detection). Additionally, events were rejected if they persisted less than 15 ms. We also tried using

spectrograms, and monitoring the power between 200-400 Hz, but found that such a method is frequently confounded by sharp transients—sharp peaks (like those in interictal spikes) resemble Dirac delta functions, and consequently have increased power at all frequencies in their Fourier transforms. Having a minimum duration of elevated energy (as we do) helps guard against such detections.

Microstimulation

To test the effects of microstimulation on HFOs, we stimulated each animal (after all spontaneous recordings) with randomly distributed current-controlled pulses, using the stimulator described in Chapter 5. Pulses had amplitudes of ±2, 4, 6, 8, 10, 15, 20, or 50 μA (cathodic phase first) and pulse widths of 800 μs. Each pulse amplitude was delivered to each electrode a total of 10 times (i.e., 10 trials for each amplitude and electrode combination). To prevent neural adaptation to repeated pulses, the trial order (trial × electrode × pulse amplitude) was randomized (e.g., electrode 5 at 10 μA, then electrode 1 at 2 μA, etc.).

The resulting data was then searched for HFOs, using the automated method described above, for the 100 ms before and 100 ms after each stimulus pulse. The 5 ms immediately before and 5 ms immediately after each stimulus was blanked (samples set to zero) to avoid contamination by artifact (artifacts usually lasted 1-2 ms (Rolston et al., 2009b)).

Results

By injecting a small quantity of tetanus toxin (25 ng) into the dorsal hippocampi of 8 male Sprague-Dawley rats, we induced epilepsy with a temporal lobe focus, characterized by chronic spontaneous seizures and frequent interictal discharges. The rats were also

implanted with 16-electrode microwire arrays targeted by microelectrode mapping (Gross et al., 2006) to the dorsal hippocampus. These electrodes were used to record both the hippocampal local field potential (LFP) and multiunit activity (i.e., action potentials from multiple neurons; Figure 8-1).

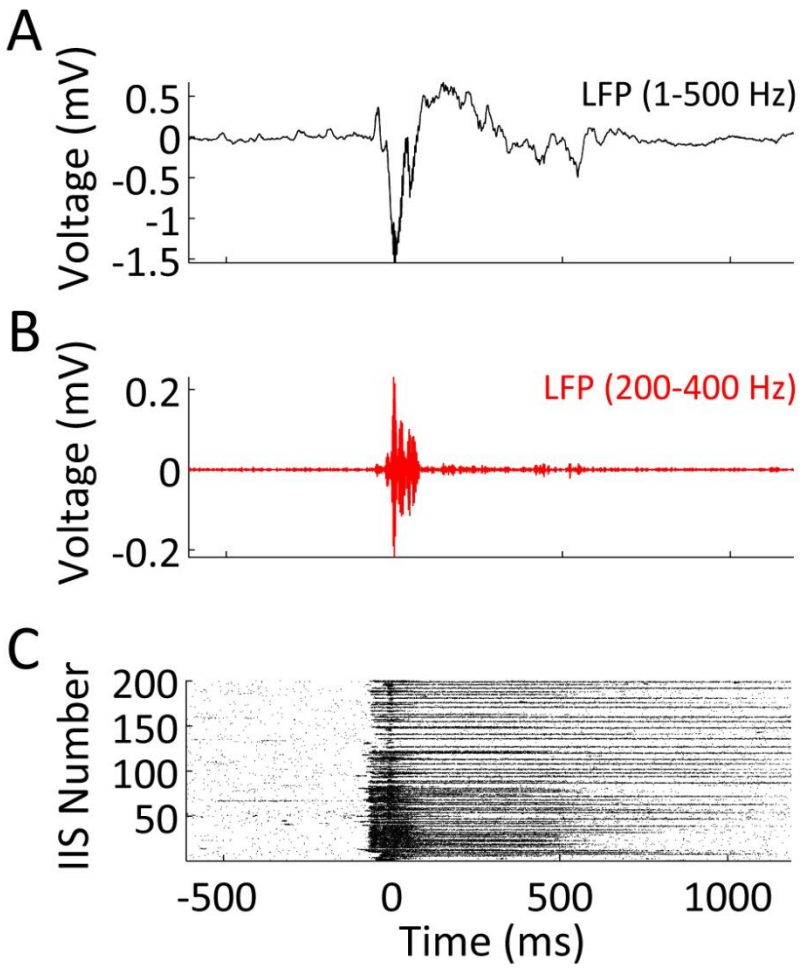

FIGURE 8-1. Interictal spikes (IISs) coincide with high-frequency oscillations (HFOs) and population bursts. (A) The LFP shows a sample IIS recorded in the frequency band of 1-500 Hz. (B) Filtering the LFP between 200-400 Hz shows a large increase in fast-ripple power during the negative peak of the IIS. (C) A raster of multiunit activity, aligned to the peak of all detected IISs (in this recording), shows a high degree of bursting during the IIS.

In all epileptic animals studied, LFP power spectra revealed large increases in power in the "fast ripple" range defined as 200-400 Hz, representing the presence of high-

frequency oscillations (HFOs; Figure 8-1 and Figure 8-2). Spectrograms of the LFP further revealed that these HFOs temporally coincided with interictal spikes (IISs; Figure 8-2B-C). Moreover, multiunit activity (MUA) showed the presence of large-scale population bursting during interictal spikes, coinciding with—but not limited to—HFOs (Figure 8-1C).

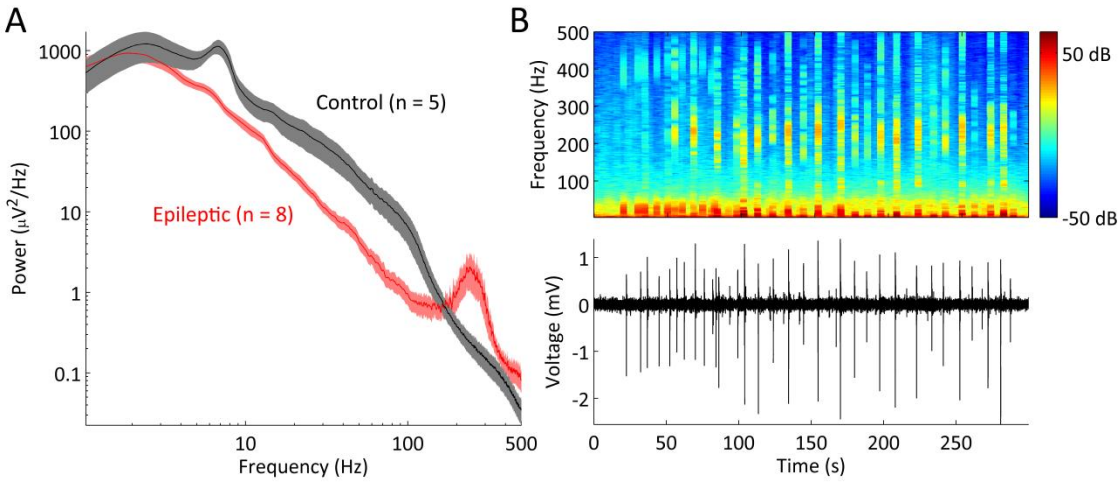

FIGURE 8-2. High-frequency oscillations are present and coincide with interictal spikes. (A) The average power spectrum of 5 non-epileptic animals (black) is shown in comparison to 8 epileptic animals (red). The epileptic animals show a large peak in the fast ripple frequency band of 200-400 Hz. Standard error is indicated by shading. (B) A spectrogram shows the HFO power is limited to defined bursts (top). By comparing the spectrogram to the time-domain LFP trace (bottom), a relationship between HFOs and IISs is suggested.

To quantify these observations, we used automated methods to detect both IISs and HFOs, and then determined the number of HFOs occurring within IISs. Across the 8 animals, 1999 HFOs were identified and 97.6% occurred during IISes. However, of the 9000 IISs detected, only 10.2% coincided with one or more HFOs (Figure 8-3A).

To see if there were differences in the IISs that contained HFOs and those that did not, we examined the peak amplitude of each IIS (absolute value) and compared those

containing and those not containing HFOs. IISs without HFOs had a mean amplitude of 544 μV, compared to IISs with HFOs that had an average amplitude of 1.8 mV, a 3.3-fold increase (Figure 8-3B). This difference was highly significant ($P < 0.0001$, Wilcoxon sign-rank test).

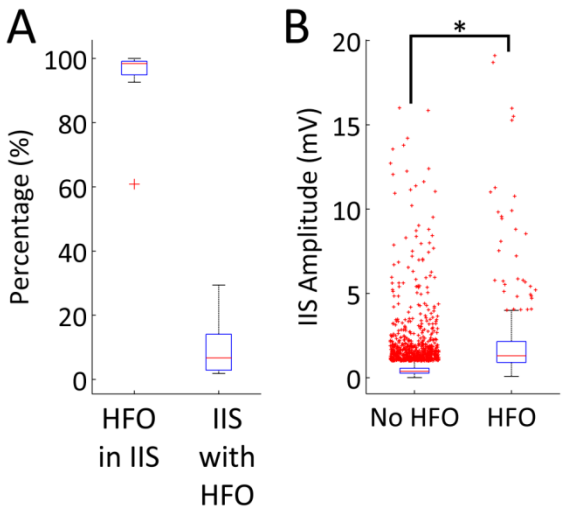

FIGURE 8-3. HFOs are predominantly localized to large IISs. (A) Box-plots (Tukey, 1977) show that most HFOs are within IISs, and only a small percentage of IISs contain HFOs. (B) The peak amplitude of IISs not containing HFOs is compared to those containing HFOs. The large number of "outliers" in the fourth quantile indicates a skewed distribution of IIS amplitudes. Nevertheless, the two groups are significantly different ($P < 0.0001$, Wilcoxon sign-rank test, no data points were excluded for any reason).

Since we observed that IISs coincide with population bursts (Figure 8-1C), we next asked whether these bursts were correlated to HFOs. To find bursting at particular frequencies, we calculated the spike-field coherence (SFC) between the population multiunit activity and the LFP in sliding windows (Mitra and Bokil, 2008) (Figure 8-4A-B). We then averaged the coherence in the HFO band (200-400 Hz) and compared the SFC during HFOs to that during IISs without HFOs, and both to the baseline (non-HFO, non-IIS) SFC. The mean SFC during HFOs (across all 8 animals) was 0.50 ± 0.07 (coherence values range from 0—no coherence—to 1—complete phase-locking), which was

significantly greater than the SFC during non-HFO-containing IISs (0.34 ± 0.02) or baseline (0.33 ± 0.02) (Wilcoxon sign-rank test, $P < 0.01$; Figure 8-4C).

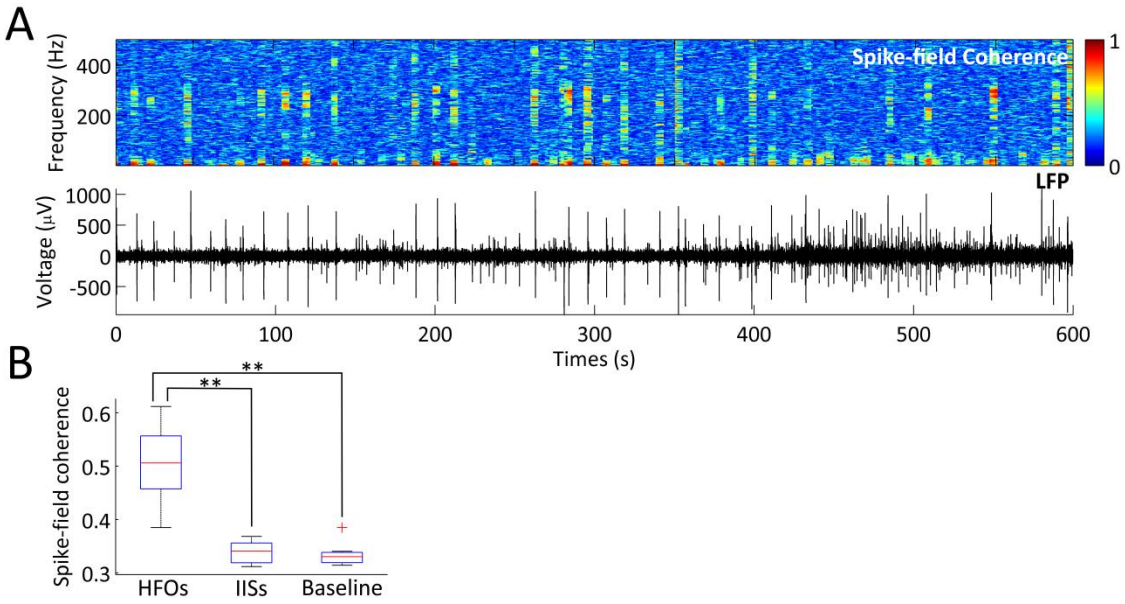

FIGURE 8-4. Spike-field coherence (SFC) is increased during HFOs. (A) A cohereogram between the LFP and multiunit activity (top) shows increases in coherence limited to the HFO frequency range. These increases in SFC appear associated with a subset of IISs, as shown in the time-locked LFP trace (bottom). (B) SFC in the HFO bandwidth (200-400 Hz) is increased during HFOs as compared to IISs or baseline recordings (Wilcoxon sign-rank test, $P < 0.01$), as is indicated in this box plot of mean SFC for each animal.

The sporadic nature of HFO occurrence makes them difficult to study. We therefore sought a method by which HFOs could be more reliably generated. Using microstimulation of the implanted array, we screened 7 epileptic animals (single session per animal; each exhibiting spontaneous HFOs) with a variety of pulse amplitudes (2-50 μA; see Methods). We then searched the 100 ms after each stimulus pulse for HFOs, along with the 100 ms preceding each pulse. In 6 of the 7 animals tested, there were significantly more HFOs present after stimulus pulses than before ($P < 0.001$, χ^2 test), showing that microstimulation evokes HFOs with short latency (Figure 8-5). To test the

specificity of these results, we also stimulated 3 control animals in an identical fashion. While some spurious detections of HFOs occurred in these non-epileptic animals, there was no significant difference between pre- and post-stimulus counts (Figure 8-5B). Because we stimulated using a range of current amplitudes, we were also able to analyze the number of HFOs evoked as a function of intensity. This analysis revealed a clear dependence on stimulus amplitude (higher amplitudes evoke more HFOs), with >25% of the evoked HFOs due to 50 μA stimuli (Figure 8-5C).

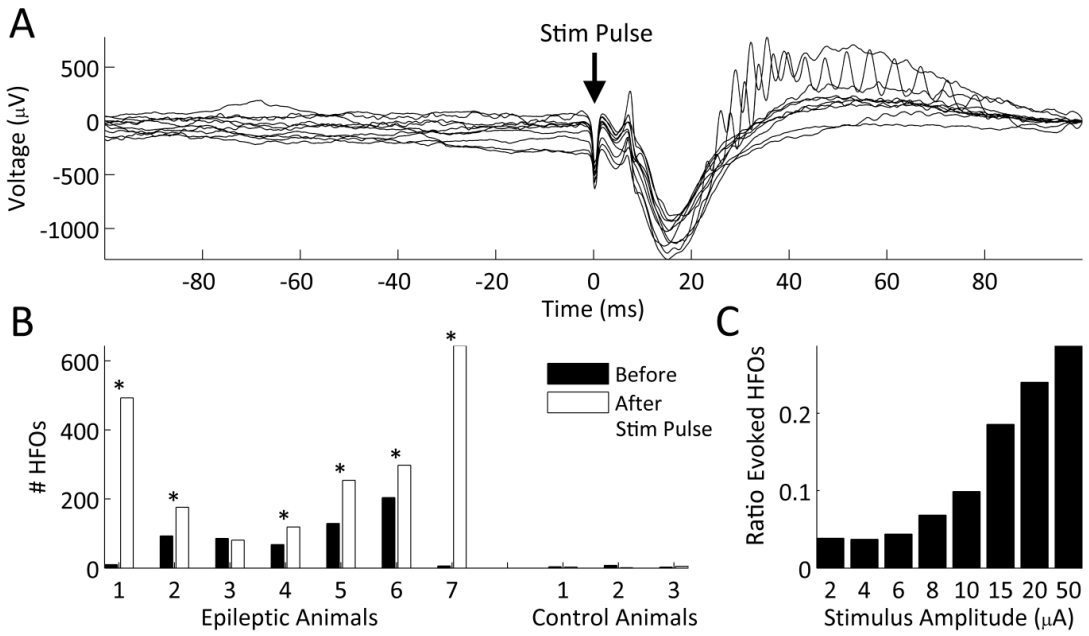

FIGURE 8-5. Microstimulation evokes HFOs. (A) The LFP in response to a microstimulation pulse of 20 μA is shown (10 trials are overlaid). HFOs can be seen in a subset of responses. (B) Across animals, more HFOs are observed in the 100 ms immediately after each stimulus pulse (white bars) than in the 100 ms preceding the pulse (black bars). Significance ($P < 0.001$, χ^2 test) is indicated with asterisks. While spurious HFOs were detected in non-epileptic control animals, these animals never exhibited a significant increase in HFOs. (C) The proportion of HFOs generated by each pulse amplitude is indicated, showing that increasing amplitudes evoke progressively more HFOs.

Discussion

High-frequency oscillations (HFOs) are poorly understood phenomena related to epileptogenic neural networks. They have been observed in both animal models of spontaneous seizures (Bragin et al., 2004; Foffani et al., 2007) and, by several independent labs, in patients with epilepsy (Bragin et al., 1999; Worrell et al., 2004; Urrestarazu et al., 2006; Jacobs et al., 2008).

To date, only two animal models have been used to study HFOs in the fast ripple band: kainic acid injection (Bragin et al., 2004) and pilocarpine injection (Foffani et al., 2007). Both are status epilepticus models that induce hippocampal sclerosis, and both exhibit

seizure-free latent periods of weeks to months before the onset of spontaneous seizures (Pitkanen et al., 2006). We therefore asked whether a non-status model, without hippocampal sclerosis, might also produce HFOs. The tetanus toxin model of temporal lobe epilepsy (Jefferys et al., 1995), in existence for over a century (Roux and Borrel, 1898), satisfies these criteria (non-status, non-lesional) and, as shown above, produces frequent HFOs amenable to study. Because it is a model of non-lesional temporal lobe epilepsy (Mellanby et al., 1977; Jefferys et al., 1992; Benke and Swann, 2004), it is an appropriate model for patients likely to undergo intracranial monitoring for localization of the epileptic focus (patients with clear lesions often do not require invasive recordings). The tetanus toxin model also produces seizures within 3-9 days of toxin injection (compared to weeks or months with status models), shortening the waiting period between surgery and acquisition of data. Finally, the tetanus toxin model has a near complete success rate in inducing seizures, as compared to status models, reducing the number of animals required for each study. Finding HFOs in this model, as we did, provides an attractive preparation for their further experimental investigation and, importantly, one with a different etiology than the existing status models. The fact that HFOs can arise from multiple non-overlapping etiological models is further evidence of their generality in ictogenesis.

The relationship between interictal spikes (IISs) and HFOs has not been definitively established. In the tetanus toxin model of epilepsy, 98% of HFOs occur within IISs. This is very different than the rate (48%) reported by Jacobs et al. (2008) in humans, but more in line with that of Worrell et al. (2008), who reported 84%. Numerous differences exist between these studies—etiology, species, HFO and IIS detection methods, electrode size (micro- vs. macroelectrodes), and electrode location, to name a few—so comparisons are fraught with nontrivial caveats. Regardless, the association between IISs and HFOs is

theoretically appealing. IISs represent large-scale depolarizations of neural tissue (de Curtis and Avanzini, 2001). If HFOs indicate the synchronized bursting of pyramidal cells (Bragin et al., 2000; Rampp and Stefan, 2006; Foffani et al., 2007; Engel et al., 2009), these discharges would be more likely to occur when groups of pyramidal cells are depolarized, as in IISs. Indeed, we see evidence of this from three pieces of data: 1) HFOs are more likely to occur during IISs, 2) larger IISs are more likely to coincide (possibly evoke) HFOs (Figure 8-3), and 3) HFOs are more likely to occur when cells are depolarized exogenously with microstimulation (Figure 8-5).

Is the bursting of pyramidal cells what is being recorded when HFOs are detected? Using spike-field coherence (SFC), we measured the phase-locked firing of hippocampal neurons in relation to the HFO frequency band (200-400 Hz). SFC was significantly greater than baseline during HFOs. Thus, populations of neurons are bursting in a phase-locked manner to HFOs when they occur. Nevertheless, with extracellular recording, it is difficult to determine the source of an extracellular voltage (i.e., whether an HFO reflects synaptic currents or the lower frequency signature of synchronously discharging action potentials from individual cells). However, the point might be moot: if cells are firing at 300 Hz (as a population, not necessarily individually), they would likely produce postsynaptic potentials at 300 Hz as well. Ultimately, the best method for determining the source of the oscillations in each preparation is either single-cell electrophysiology (Foffani et al., 2007), which can unequivocally dissociate input (membrane potential) from output (action potentials), or imaging with voltage- or calcium-sensitive dyes, which have single cell and single action potential resolution (Kerr and Denk, 2008).

Aside from the spontaneous recording of HFOs in the tetanus toxin model, we were able to reliably evoke HFOs using microstimulation (Figure 8-5). Such control of HFOs has not yet been reported, perhaps due to the difficulty in recording from the same electrodes used to stimulate (Rolston et al., 2009b).

This ability to electrically evoke HFOs has several potential uses. First, automated methods could be developed to microstimulate neural tissue and monitor for HFOs. If successful, such a technique would be useful for determining epileptic onset zones when preparing patients for resective surgery. While still invasive, a reliable version of this procedure could be done in a single session, rather than awaiting spontaneous seizures during weeks of expensive and time-consuming in-patient monitoring. Though a similar approach could be developed with spontaneous HFOs, artificially increasing their rate could allow for more rapid or reliable tests. Second, since HFOs appear to be related to epileptogenesis in animal models (Bragin et al., 2004), microstimulation could be used to create high-throughput screening of pharmaceutical or other interventions. That is, if a drug reduced the number of HFOs, that fact could be quickly established via a stimulation study, in lieu of passive recordings. HFOs could also be evaluated directly in terms of epileptogenicity or ictogenicity—for example, by artificially elevating their rate, one could test their relationship to either the beginning of seizures or number of seizures in an animal model. Lastly, researchers could use this technique to further study the mechanism of HFO generation. When an HFO is evoked with a stimulus pulse, for example, its origin is partially known (cells were depolarized by the stimulus, leading, by unknown intermediating events, to the HFO). When the neural circuitry is then altered (e.g., via optogenetic methods (Zhang et al., 2007) or chemical neuromodulators), changes in the evoked HFOs can be scrutinized for effects (e.g., latency, number, morphology, etc.). Whatever the case, all such applications will require further study of

evoked HFOs, both to validate their relevance to epilepsy in humans and to characterize them more fully. But despite the difficulty of the many experiments outlined above, by providing a novel form of control over HFOs, these experiments are now possible.

Conclusion

High-frequency oscillations (HFOs) in the range of 200-400 Hz have been repeatedly associated with epileptic tissue in humans and some animal models. We have now confirmed their presence in an additional animal model, the tetanus toxin model of chronic epilepsy, which has unique and useful advantages compared to other preparations. Using this model, we described a high association between HFOs and interictal discharges, and also associated HFOs with phase-locked bursts of neural action potentials, offering some insight into their mechanism. Lastly, we showed that HFOs could be evoked with microstimulation, providing the first evidence that these oscillations can be temporally controlled using exogenous interventions.

Acknowledgments

I gratefully acknowledge the Nealen G. Laxpati for assistance with rodent surgeries. I also thank Dr. Claire-Anne Gutekunst, Eric N. Stewart, and N. G. Laxpati for conducting rodent histology.

Chapter 9

Observations of the Effects of Microstimulation in the Rodent Hippocampus

Abstract

Microstimulation of the hippocampus has the potential to control neural activity in precise, reliable ways, perhaps leading to new treatments for disease or a better understanding of this important brain region. Nevertheless, the fundamental responses of the hippocampus to electrical microstimulation in freely moving animals are unknown. We attempted to address this in part by stimulating in normal and epileptic rats, first examining the response to isolated stimuli of varying amplitude, then trains of pulses of varying rates, and finally by a closed-loop experiment to determine optimal stimulation rates for driving maximal responses. None of these experiments successfully addressed their motivating question, but it is hoped that the following analyses will provide guidance for other researchers interested in this area.

Introduction

Electrical microstimulation offers a potentially powerful means of controlling the nervous system. But before this technique can be optimally used, its precise effects must be carefully characterized. That is, constructing a "palette" of stimulus-response pairs will allow researchers to construct nuanced protocols for shaping neural activity.

To date, little work has been done to characterize the way in which the hippocampus responds to microstimulation. The most progress was made with studies carried out in cats and rabbits in the 1960s and 70s, by hippocampal pioneers such as Eric Kandel (Kandel et al., 1961), Per Andersen, and Tim Bliss (Andersen et al., 1971). They monitored stimulation effects by recording either intracellularly or extracellularly, and stimulated predominantly in fiber bundles, such as the perforant path or fornix (though Kandel also stimulated the subiculum directly). The major conclusions of these studies were the finding of "population spikes" (compound, overlapping action potentials recorded primarily in the stratum pyramidale), fEPSPs (field excitatory postsynaptic potentials—negative deflections of the extracellular potential in the stratum radiatum, positive in the stratum pyramidale, corresponding to current sinks in the apical dendrites, and perisomatic sources, respectively (cf. Chapter 1)), and that fornix stimulation produces a large amount of inhibition following an initial excitatory response. These experiments were, however, conducted in anesthetized animals with most of their overlying cortex aspirated.

Since this early work, further progress in intact animals has been minimal, perhaps in part due to the advent of the slice preparation (Kerkut and Wheal, 1981), which provides a simplified system in which things like stimulation and electrophysiological responses can be easily monitored. Another cause might be the trend toward multielectrode

recordings in the rodent and primate hippocampus (Nicolelis, 2008), for which compatible stimulators are uncommon. In any case, detailed characterizations of the effects of neural microstimulation, along the lines of those produced for the neocortex by Butovas et al. (2003) and Histed et al. (2009), are absent. Furthermore, studies of the effect of microstimulation in unanesthetized animals are especially lacking (all of the above studies were conducted in anesthetized animals), despite the well-described differences in neural activity in both states (Greenberg et al., 2008).

To address these goals of characterizing microstimulation, we conducted four related experiments in epileptic and non-epileptic rats. These experiments sought to answer the following:

1. What is the effect of single pulses of microstimulation on neural action potentials (APs) and local field potentials (LFPs)?
2. What is the maximum rate of stimulation that still evokes reliable firing from hippocampal neurons?
3. Can a closed-loop algorithm determine the optimal stimulation frequency for evoking the maximal neural response (in terms of population firing rate)?
4. Can microstimulation timed to interictal spikes (IISs) affect them?

This final question was addressed in Chapter 5. The remainder of this chapter addresses the first three. It must be noted, though, that these are ultimately incomplete experiments. Each experiment had limitations that prevented the motivating question from being satisfactorily answered. However, I hope that the results I present, and their analyses, will prove a useful guide for future students pursuing similar research.

Methods

The general methods of rodent surgery, microstimulation and extracellular recording are described in Chapter 4, Chapter 5, and Chapter 6. Specific methods for each experiment are detailed below.

Single Pulse Stimulation

For each animal (4 non-epileptic and 8 epileptic), a sequence of stimulation pulses was delivered at 1 Hz. Each electrode was stimulated with ±2, 4, 6, 8, 10, 15, and 20 μA current-controlled biphasic pulses (cathodic, negative phase first) with durations of 400 μs per phase. Each pulse amplitude was delivered 10 times to each electrode. The combinatorial expansion of these parameters (electrode × stimulus amplitude × trial) created a sequence of pulses that was randomized before presentation. Randomizing helped ensure that neural adaptation was minimized between pulses.

Data were analyzed by examining all 10 responses to each stimulation amplitude from each recording electrode. APs were examined by using an artifact suppression algorithm on the raw data, the SALPA algorithm (Wagenaar and Potter, 2002), then referencing the resulting data by its common median to reduce common mode interference (Rolston et al., 2009a). LFPs were displayed by zero-phase filtering the raw data between 1-500 Hz (4-pole Butterworth).

Single Electrode Stimulation Trains

Four non-epileptic animals were studied. Each electrode was stimulated with ±10 μA biphasic pulses (negative, cathodic phase first), 400 μs per phase, at frequencies of 1, 2, 5, 10, 20, 50, 100, and 200 Hz. Each train lasted one minute or 100 pulses, whichever

was longer. The order of testing was completely randomized (e.g., electrode 1 at 10 Hz, then electrode 9 at 50 Hz, etc.).

Stimulus artifacts were suppressed in real-time with the SALPA algorithm (Wagenaar and Potter, 2002). The resulting traces were then referenced by the common median to reduce common mode noise (Rolston et al., 2009a). APs were detected in real-time as positive or negative deflections ≥5 × root-mean-square (RMS) noise. Samples that were blanked by artifacts were not included when calculating RMS noise, to prevent spurious depression of the RMS measure during high rates of stimulation.

LFPs were extracted from the raw recordings in real-time, separately from APs, by first linearly interpolating around stimulus artifacts to remove them (Heffer and Fallon, 2008), then filtering the resulting trace between 1-500 Hz (3-pole Butterworth filter).

Closed-loop Driving Experiment

To determine the stimulation frequency at which neural activity was maximally driven, we created a closed-loop stimulation/recording paradigm as follows. For a given electrode, stimulation was delivered at a particular frequency, f, for 20 seconds. Stimuli were ±10 μA biphasic pulses (negative, cathodic phase first), 400 μs in duration per phase. The number of action potentials array wide (APRAW) was computed during each stimulation epoch, and normalized to the sampling duration (i.e., APRAW is measured in units of Hz). The sampling duration was discounted by the duration of artifact blanking, 1 ms per stimulus pulse, to avoid artificial depression of APRAW during high stimulus rates (since no APs can be detected during blanking). At the end of each epoch, the current APRAW is compared to the previous APRAW. If the APRAW is increased, f is changed by Δf (initialized to +10 Hz). If APRAW is decreased, Δf is multiplied by −0.75

and added to *f*. That is, if the last step was "bad" (lowered APRAW), the direction was reversed, but by a smaller amount. This process was repeated until APRAW changed less than 1% between stimulus epochs, or after 100 steps, whichever came first. Additionally, maximum and minimum stimulation rates of 0.1 and 300 Hz were enforced.

To determine APRAW, APs were detected as described above (*Single Electrode Stimulation Trains*).

Results and Discussion

Because this chapter discusses multiple experiments, the results and discussion sections have been combined, so that the interpretation of each experiment is discussed immediately after its presentation. Final conclusions are then presented to discuss the combined experiments.

Results of Single Pulse Stimulation

Single pulses of microstimulation produced a highly heterogeneous assortment of responses in non-epileptic and epileptic animals. Most often, stimulation evoked little or no discernible response when observing APs, even when the electrode was otherwise recording APs (Figure 9-1). In other cases, stimulation evoked population spikes that changed amplitude as the stimulus intensity increased (Figure 9-2). Other responses show single spikes coalescing into population spikes (Figure 9-3), and some show general increases in firing rate that diminish with increased stimulus amplitude (Figure 9-4).

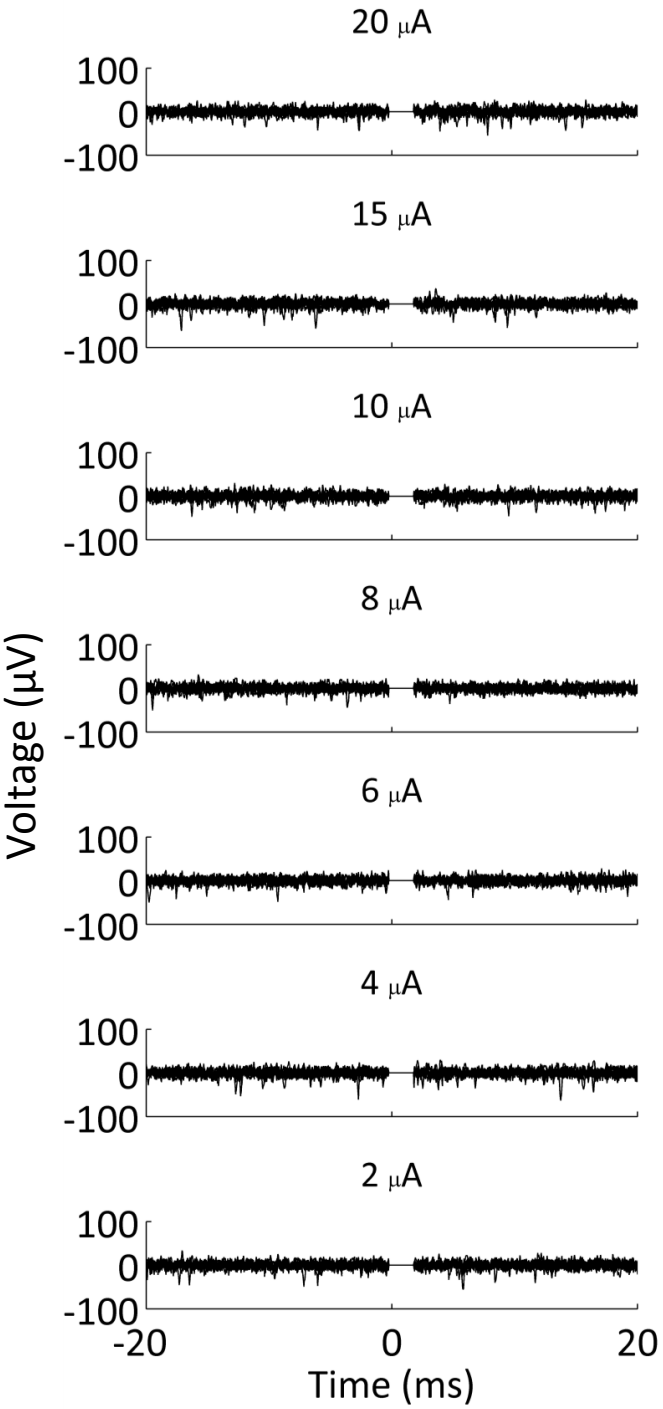

FIGURE 9-1. Responses to single pulses of stimulation at various stimulus amplitudes: no responses. Data from one recording electrode are shown when a separate electrode was stimulated at 2, 4, 6, 8, 10, 15, and 20 μA. Ten trials are overlaid in each panel. Note that at no stimulus amplitude are APs elicited, despite spontaneous APs being recorded.

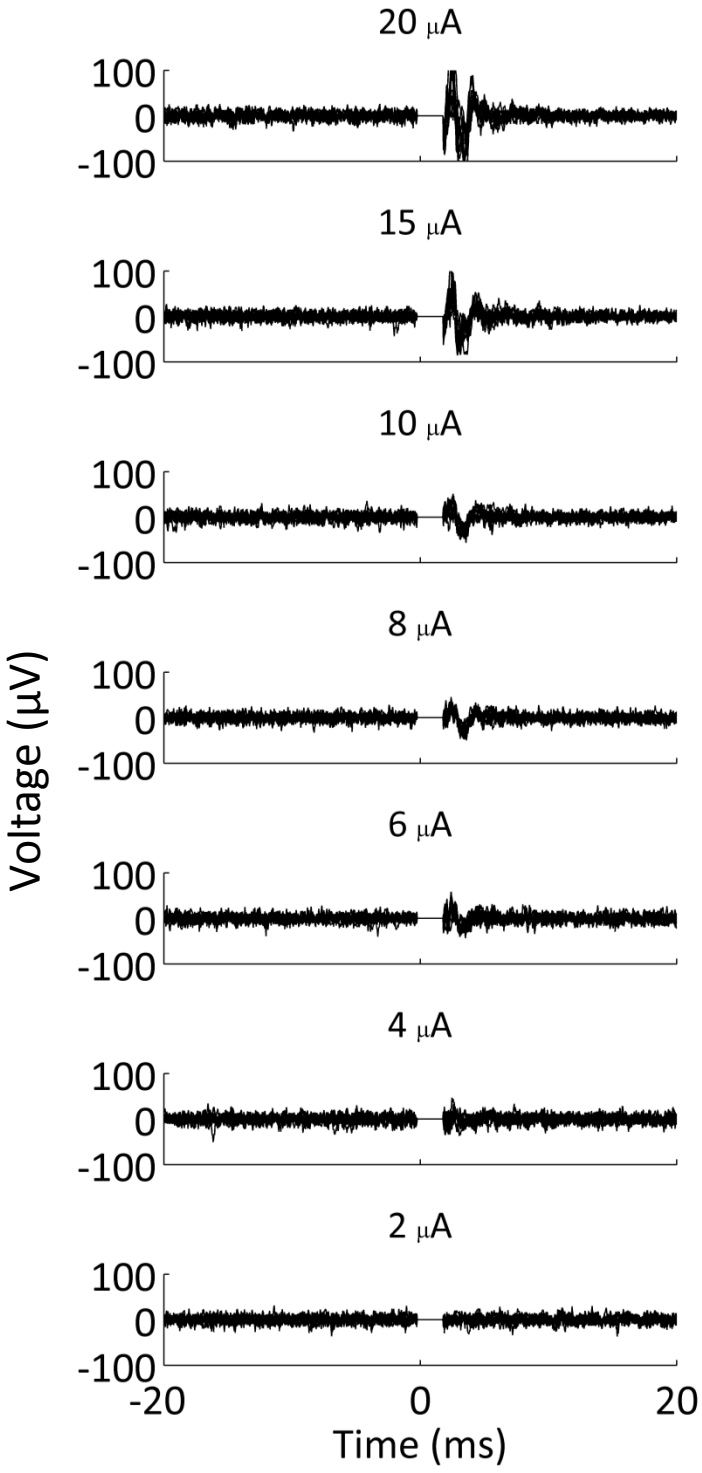

FIGURE 9-2. Responses to single pulses of stimulation at various stimulus amplitudes: population spike.

Presented as in **FIGURE 9-1**. A population spike first appears at 6 μA, reaching maximal amplitude at 20 μA.

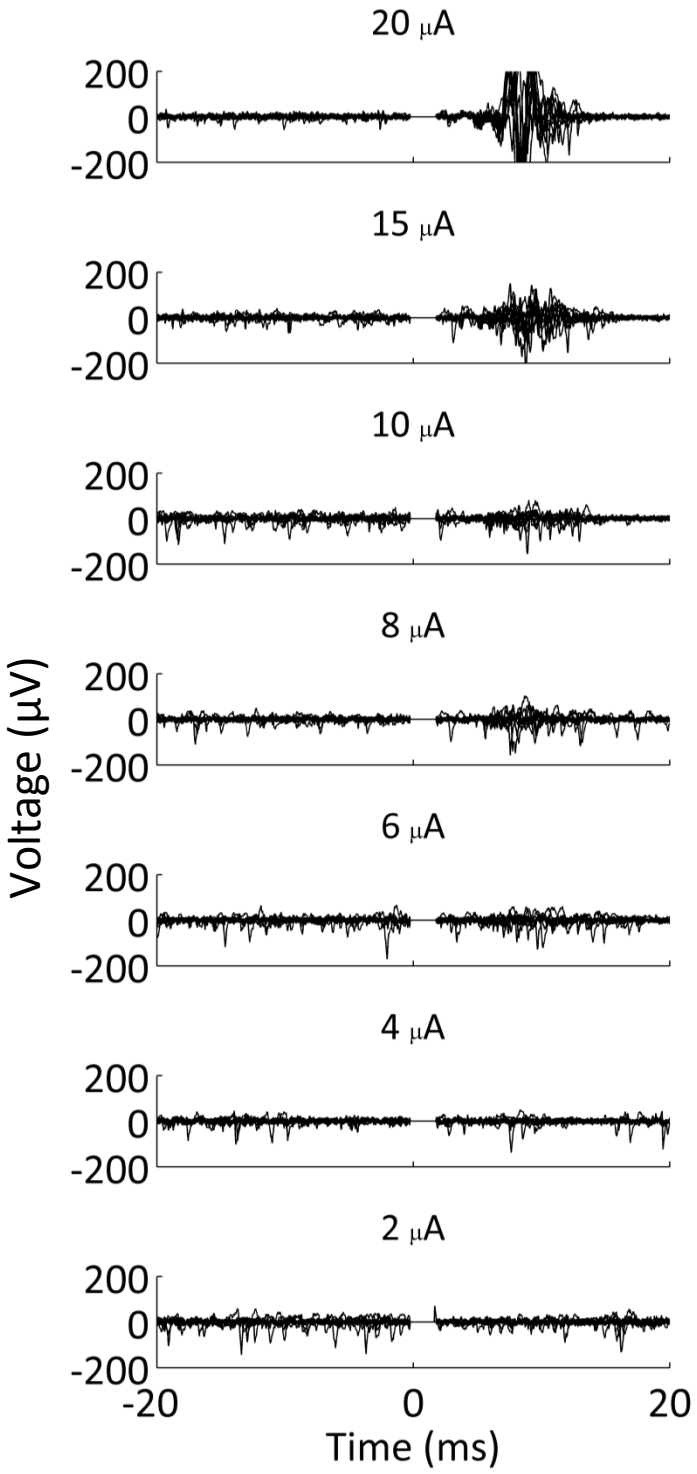

FIGURE 9-3. Responses to single pulses of stimulation at various stimulus amplitudes: coalescing population spike. Presented as in **FIGURE 9-1**. Individual APs are evoked at 6 μA, but coalesce into a population spike by 15 μA.

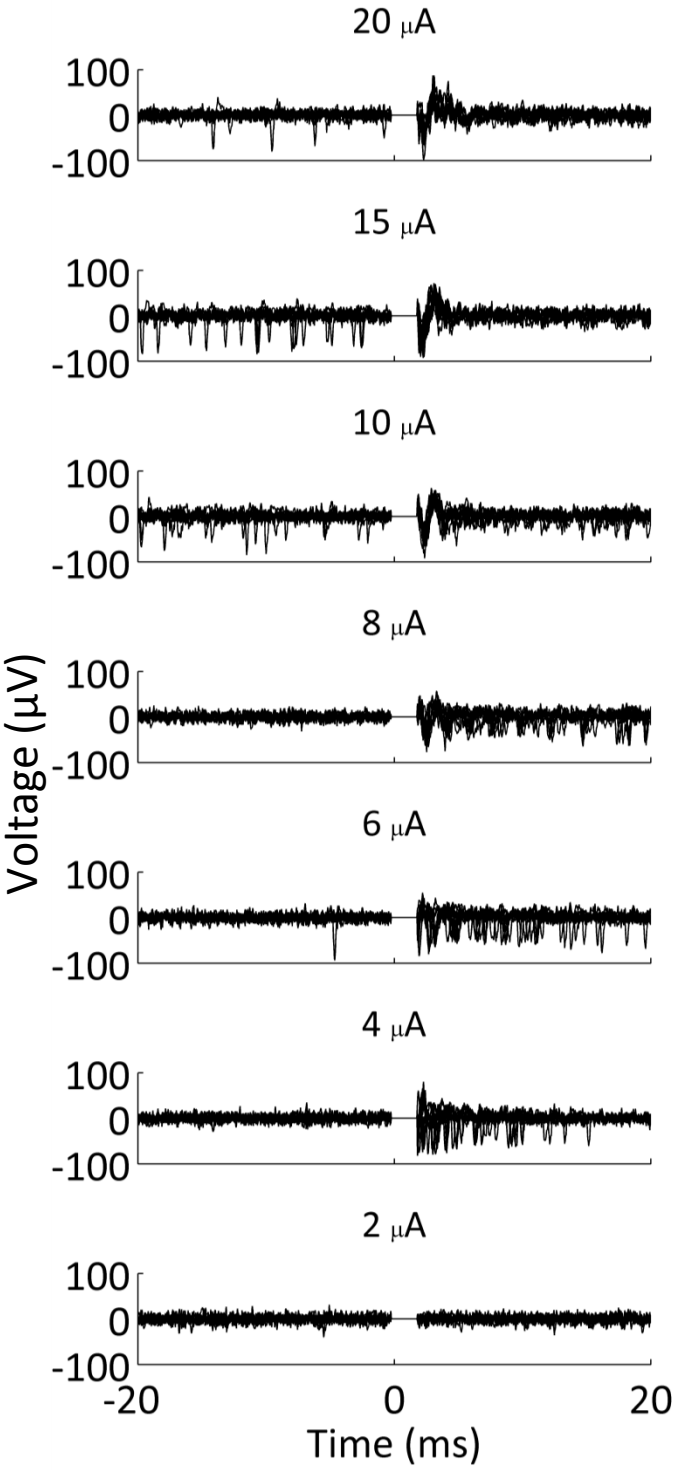

FIGURE 9-4. Responses to single pulses of stimulation at various stimulus amplitudes: increased firing rate. Presented as in **FIGURE 9-1**. APs are evoked at 4 μA, showing an increased firing rate. This response is no longer present at ≥15. μA.

When examining LFPs, similar heterogeneity occurs. Stimulation was observed to cause negative deflections of the extracellular potential (Figure 9-5), positive deflections (Figure 9-6), and minimal deflections (Figure 9-7). Epileptic animals displayed the same LFP responses, with the exception of the frequent phenomenon of evoked high-frequency oscillations (HFOs; see Chapter 8), which were not observed in control animals (Chapter 8). Spectral analysis showed a broadband power increase around the stimulus, likely due to the sharp, Dirac-function-like nature of the evoked response. But no other frequency bands stood out (e.g., gamma, beta, etc.), with again the exception of the evoked HFOs in epileptic animals (Chapter 8).

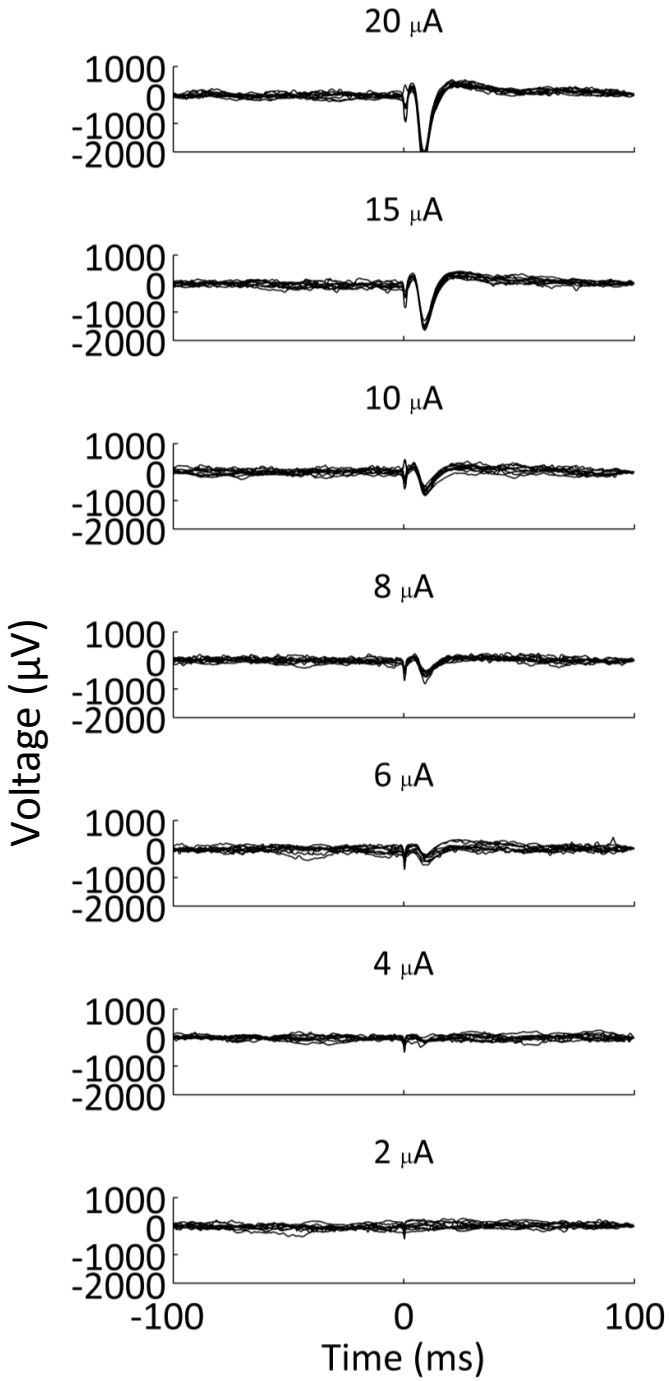

FIGURE 9-5. LFP responses to single pulses of stimulation at various stimulus amplitudes: negative deflection. LFP traces from one recording electrode are shown when a separate electrode was stimulated at 2, 4, 6, 8, 10, 15, and 20 μA. Ten trials are overlaid in each panel. Note that a progressively more negative deflection is produced with increasing stimulus amplitude.

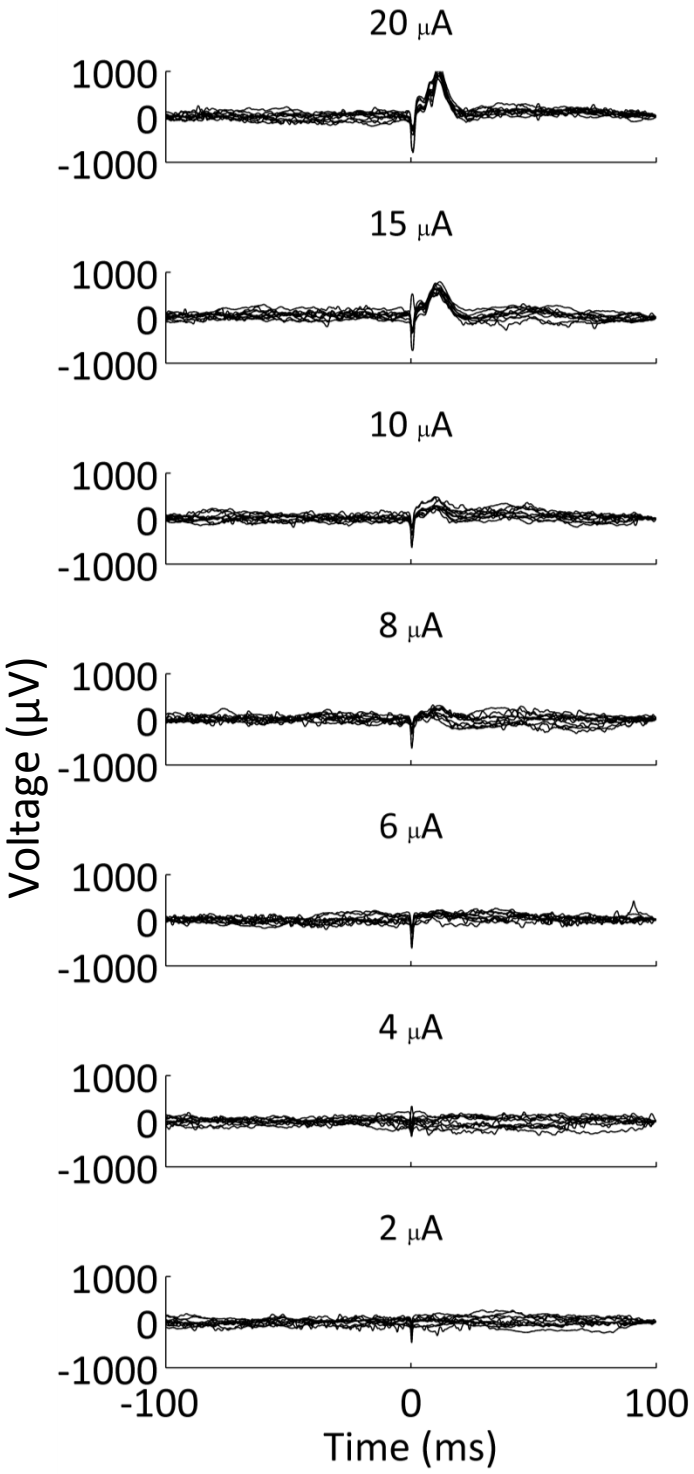

FIGURE 9-6. LFP responses to single pulses of stimulation at various stimulus amplitudes: positive deflections. Presented as in **FIGURE 9-5**. Note the progressively larger positive deflection with increasing stimulus amplitude.

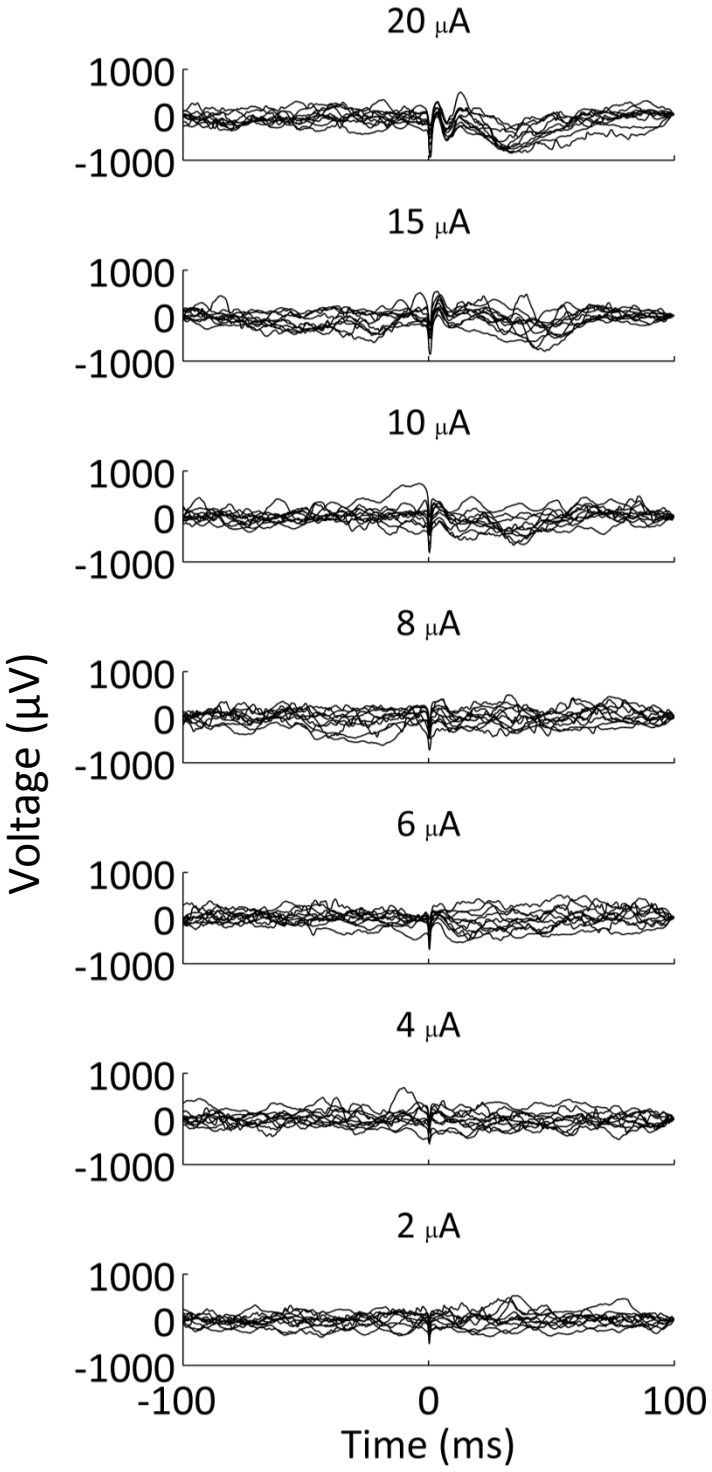

FIGURE 9-7. LFP responses to single pulses of stimulation at various stimulus amplitudes: small deflections. Presented as in **FIGURE 9-5**. In this case, the deflections are small even at the highest intensities.

Discussion of Single Pulse Stimulation

When examining evoked APs using microstimulation in the hippocampus, the main difficulty is heterogeneity. Some responses are robust, others meager. Some increase with increasing stimulus intensity, others decrease. Some display well-isolated single spikes, others show single units coalescing into population spikes. These various classes tend to cluster across stimulation electrodes. That is, nearby stimulation electrodes tend to evoke similar activity. This clustering also applies to recording electrodes: nearby electrodes tend to record similar activity for each stimulation electrode. A side-effect of this clustering of responses based on electrode proximity is that particular classes of activity tend to differ most between animals (i.e., there is more variability in array placement between animals than within animals).

The large differences between animals and the similarities between nearby electrodes suggest that most of the variability arises from electrode location. This is a difficulty of the experimental method. During implantation, microwire electrodes are lowered stereotaxically into the hippocampus while recording neural activity. The electrode array is stopped when a sufficient amount of activity is recorded (this is determined subjectively). Several difficulties arise during surgery that make precise placement difficult. First, we frequently observe swelling of the brain after removal of the dura, and before penetration with the microelectrode array. Once the electrodes are set in place with dental acrylic and the brain swelling subsides, the electrodes are often in a new location than the last recording indicated. Second, any error in stereotactic localization or bend in the microwires (which are very delicate and easily warped with even a slight brush of a finger or surgical instrument) can lead to placement in a different aspect of the hippocampus than other surgeries. For example, if the array has its exposed electrode tips in the stratum radiatum, it is expected that this would produce different

stimulation effects than stimulation in the pyramidal layer or basal dendrites. Indeed, the different polarity of LFP responses suggests that recording electrodes frequently end up in different layers. A further complication of anatomical localization is that different areas of CA3 and CA1 receive different afferents, potentially leading to different responses when directly stimulating the terminal axons of these fiber inputs (e.g, cholinergic vs. serotonergic).

What could be done to minimize these sources of variability? Two approaches seem feasible. First, movable electrodes could be used rather than fixed arrays. Movable microdrives would allow the electrodes to be advanced to known layers of the hippocampus, so homogeneity could be ensured (Kloosterman et al., 2009; Nguyen et al., 2009). The problem with movable arrays is the time required to both assemble the custom drives and then slowly lower the electrodes. The processes can sometime take months, as compared to purchasing a commercially available fixed microwire array, and implanting it in a single surgery to its final depth. Second, silicon probes, with electrodes spaced linearly on each shank's vertical extent (e.g., the "Michigan" probes available from NeuroNexus, Inc.[14]), would allow simultaneous sampling from multiple hippocampal strata (Buzsaki, 2004). Using such vertically distributed recordings would reveal electrophysiologically (via current-source density analysis (Mitzdorf, 1985)) the probable location of each electrode contact, and allow a precise delineation of the effects of stimulation within different strata. Electrode arrays with more contacts spanning more vertical area would also protect against brain shift—that is, if the brain moves in relation to the fixed electrodes, different layers would be aligned with different electrodes, but the most important layers (stratum pyramidale) would still be sampled.

[14] http://www.neuronexustech.com/

Another problem with experiments involving evoked responses in the hippocampus is quantification. In previous characterizations of evoked activity, the number of evoked APs was the figure of merit (Butovas and Schwarz, 2003). In the hippocampus, however, cells are tightly packed, so synchronous single cell discharges superimpose to obscure one another in the form of population spikes (Andersen et al., 1971) (the same problem occurs during interictal spikes and seizures, other forms of synchronous activity (Engel et al., 2009)). Therefore, if such analysis were continued, a metric like multi-unit activity (not simple threshold crossings, but rather a continuous time estimate of high-frequency energy as described by Start et al. (2007)) might be more appropriate. Even still, it is unclear whether multi-unit activity would scale linearly when confronted with population spikes—it likely would not, in fact, since each cell's distance to the electrode and timing (phase in relation to the spike) would determine its contribution to the amplitude of the population spike (Nunez, 1981). Multiunit activity or other energy-based methods might therefore be biased estimators of the true population response, since they conflate number of cells, distance, and synchrony. The optimal method for the densely packed cells of the hippocampus would probably involve isolating single cells and observing their responses independently. To do this at the population level would require optical imaging, as was recently done for microstimulation in the motor cortex (Histed et al., 2009).

Results of Single Electrode Stimulation Trains

Related to the question of the effects of single pulses, delivered at low frequencies, is the question of trains of such pulses. One type of response cannot be predicted from the other, since long- and short-term plasticity of synapses and cells become apparent only with multiple stimuli (e.g., see Iremonger et al. (2006)).

In an attempt to test this, we stimulated electrodes (±10 μA biphasic pulses, negative phase first) at a variety of frequencies (1, 2, 5, 10, 20, 50, 100, and 200 Hz) for one minute or 100 pulses, whichever was greater. In all animals, stimulation at 50 Hz or greater induced electrographic seizures, though not behavioral seizures. In one animal, stimulation at 20 Hz also induced seizures. This is consistent with studies of kindling in rodents, which use currents as low 6 μA (peak-to-peak, so ±3 μA in the terminology of the present chapter) to induce seizures at stimulation frequencies ranging from 20-200 Hz (Goddard, 1967). At 200 Hz, the artifact elimination algorithm saturated the processor (i.e., became too computationally intensive), and prevented the recording from progressing. Lower frequencies were unaffected. An example of a brief evoked seizure is shown in Figure 9-8 and a more sustained seizure in Figure 9-9. The seizures produce bursting which shows up as horizontal bands in the raster plot.

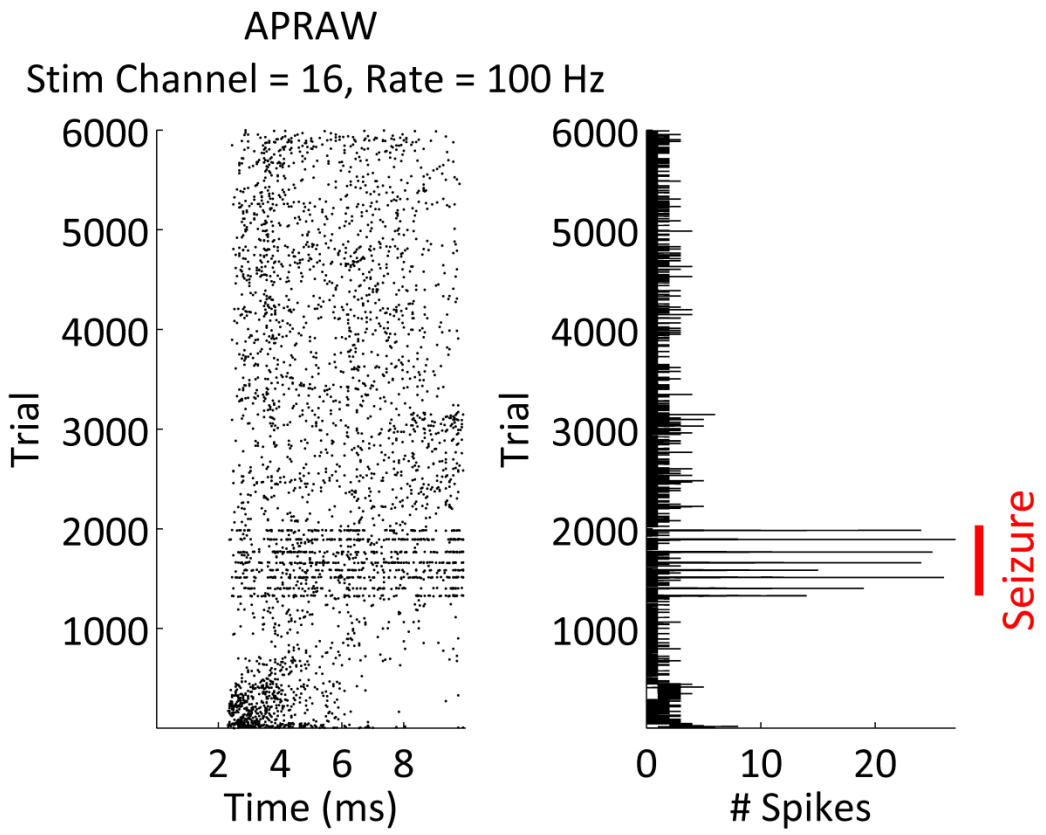

FIGURE 9-8. AP responses to a 100 Hz train of stimuli, lasting one minute. The first stimulus is lowest on the vertical axis (trial 1). No spikes are recorded in the first two ms as a consequence of artifact blanking. The raster on the left of the figure shows each detected AP from any electrode of the array. The plot on the right shows the total number of spikes per trial. Initially, for roughly the first 500 trials, there is an increase in firing rate, which progressively "dissolves." A seizure subsequently began producing population bursting, visible as banding in the raster and spikes in the cumulative spike count from trial 1250-2000 (seizure duration indicated by vertical red line).

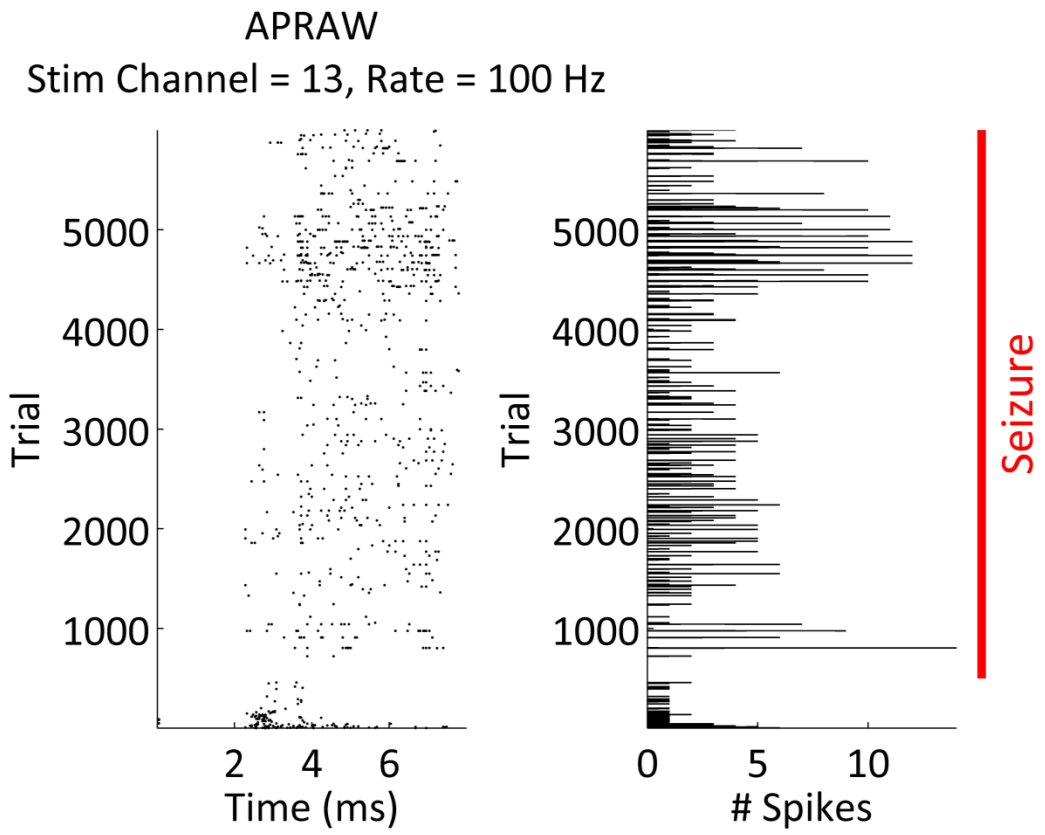

FIGURE 9-9. Seizure evoked by high frequency stimulation. This figure is presented as **FIGURE 9-8**. Here, stimulation produced a long seizure visible in the LFP. Bursting is noted again as banding in the raster and spikes in the cumulative spike count for each trial. Particularly, note that many trials elicit no spikes, likely as at this point the seizure is dominating the dynamics of AP firing. The red line indicates the duration of the induced seizure.

Discussion of Single Electrode Stimulation Trains

The problems that arose when examining responses to single pulses also arose when examining trains of pulses. That is, responses vary from electrode to electrode, likely due to different anatomical localizations, and the responses are difficult to quantify when APs from single cells can no longer be isolated (i.e., when they begin to superimpose and form population spikes; see Discussion of Single Pulse Stimulation above). An additional complication appears due to evoked seizures. Not only do these seizures make interpretation of the ongoing response to stimulation difficult, they often bleed into the

next trial. Such contamination distorts the analysis of these subsequent epochs, which are often at lower stimulation frequencies.

Results of Closed-loop Driving Experiment

The last question we pursued was related to the previous one: can we find the stimulation frequency that evokes the most activity? This time, however, we used the capabilities of our closed-loop stimulation/recording system (Chapter 4 and Chapter 5) to automate this process. The procedure involved stimulating at a frequency, *f*, for 20 seconds, while measuring the total number of APs recorded across the entire electrode array. This metric is termed APRAW (APs recorded array-wide), and was used in the *in vitro* burst quieting experiments of Wagenaar et al. (2005b). At the end of the 20 seconds, the APRAW is compared to the previously recorded APRAW. If APRAW has increased, the frequency is changed in the same direction as it was previously changed (for example, if moving from 10 to 20 Hz increased APRAW, then the frequency will be increased for the next test). If APRAW has decreased, the stimulation frequency is changed in the opposite direction to the previous change, and with $3/4^{th}$ the previous step size (for example, if moving from 30 to 40 Hz decreases APRAW, the next frequency would be 32.5 Hz). The changing step size allows the algorithm to home in on the best frequency gradually. This process continues until APRAW reaches a stable value (i.e., changes are less than 1% from trial to trial), or after 100 trials if no stable regime is found. There were also minimum and maximum frequencies of 0.1 Hz and 300 Hz, respectively.

The algorithm generally failed to find the true maximum. Specifically, looking at the evoked APRAWs during each epoch, and comparing these to the final values before convergence, the average deviation was 10.2 ± 8.3% (i.e., the maximum evoked APRAW

was empirically at least 10% higher than that determined by the algorithm). Only in one case was the deviation <1%, which was the algorithm's aim. The final stimulation frequencies had a mean of 6.4 ± 10.4 Hz (range 0.1–35 Hz; the one successful stimulation frequency was 17.2 Hz).

Discussion of Closed-loop Driving Experiment

What could be the cause of the poor performance? There are several culprits. First, all the caveats listed for the previous two experiments hold (heterogeneous responses and difficulty quantifying APs when they superimpose). More important, though, is the non-stationarity of the APRAW metric. In non-epileptic animals, APRAW varies by as much as 70% between 20 second windows, with a mean of 15.8 ± 15.3 % (Figure 9-10). Since the algorithm is searching for a change of less than 1%, the spontaneous variability is far too high for this to occur.

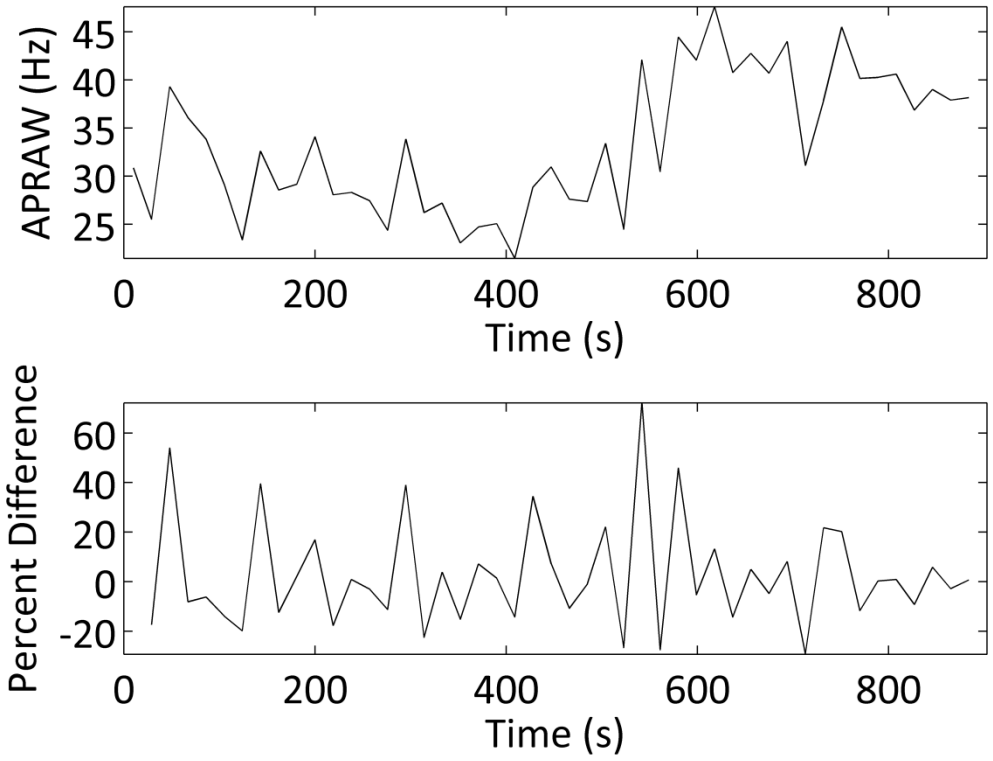

FIGURE 9-10. APRAW is non-stationary. In the top panel, the APRAW for a non-epileptic animal is shown in 20 second windows (to correspond with the closed-loop control scheme). In the bottom panel, the percent difference from one 20 s window to the next 20 s window is shown, matched to the panel above. This shows how variable APRAW is from window to window.

How could this closed-loop experiment be improved? Perhaps longer windows could be used. For example, APRAW appears somewhat stationary over 5 minute intervals in the above graph. But an experiment with each frequency tested for this duration might take hours (up to days for multiple electrodes). Another option is to find a better metric, one that is more stable and more representative of the true neural activity (problems with multiunit activity as applied to population spikes were noted in the Discussion of Single Pulse Stimulation above).

Conclusions

Microstimulation is a potentially powerful means of shaping neural activity in the hippocampus, but the building blocks are not yet known. We desire the situation where a scientist can say, “The activity should look like this, therefore this stimulation pattern should be used.” But we are a long way off. Single pulses produce variable responses depending on the stimulation electrode location, stimulus amplitude, and recording electrode location. Trains of stimuli evoke seizures, which is not productive if our goals are to restore or enhance normal neural function. Closed-loop stimulation is plagued by inherent non-stationarities that cannot yet be overcome with our control mechanism. We know little about these cases, even though these are all primitive stimuli. More complex stimuli, like aperiodic trains or spatially distributed stimuli, are likely to present an even thornier puzzle.

Despite these setbacks, we nevertheless now have the technology to answer these questions. They are not insurmountable. Furthermore, since human microelectrode arrays have been FDA-approved and implanted for decades (Babb et al., 1973), we even have the ability to rapidly translate any successes in animal models to human patients. Microstimulation is an under-investigated area with potentially huge benefits to medical research, such as bidirectional neuroprosthetics and enhanced DBS with greater spatial precision. The field is prepared and awaiting only resources and sustained effort before some of this potential will be realized.

Acknowledgements

I gratefully acknowledge help with rodent surgeries from Nealen G. Laxpati and help with rodent histology from Dr. Claire-Anne Gutekunst, Eric N. Stewart, and Nealen G. Laxpati.

Appendix A

NeuroRighter: Closed-loop Multielectrode Stimulation and Recording for Freely Moving Animals and Cell Cultures[15]

[15] Reprinted, with permission, from *31st Annual International Conference of the IEEE Engineering in Medicine and Biology Society*, "NeuroRighter: Closed-loop Multielectrode Stimulation and Recording for Freely Moving Animals and Cell Cultures," J. D. Rolston, R. E. Gross, S. M. Potter.

Abstract

Closed-loop systems, where neural signals are used to control electrical stimulation, show promise as powerful experimental platforms and nuanced clinical therapies. To increase the availability, affordability, and usability of these devices, we have created a flexible open source system capable of simultaneous stimulation and recording from multiple electrodes. The system is versatile, functioning with both freely moving animals and *in vitro* preparations. Current- and voltage-controlled stimulation waveforms with 1 μs resolution can be delivered to any electrode of an array. Stimulation sequences can be preprogrammed or triggered by ongoing neural activity, such as action potentials (APs) or local field potentials (LFPs). Recovery from artifact is rapid, allowing the detection of APs within 1 ms of stimulus offset. Since the stimulation subsystem provides simultaneous current/voltage monitoring, electrode impedance spectra can be calculated in real time. A sample closed-loop experiment is presented wherein interictal spikes from epileptic animals are used to trigger microstimulation.

Introduction

Multielectrode recording offers rewarding insights into the function of the nervous system, insights otherwise unattainable with alternative techniques (Buzsaki, 2004). The same can be said of electrical stimulation, without which the discovery of long-term potentiation (Cooke and Bliss, 2006) or the motor and sensory maps of Penfield (Penfield and Jasper, 1954) would not exist. We believe that these two modalities, multielectrode stimulation and recording, will be even more powerful when coupled in closed-loop systems (Potter et al., 2006; Arsiero et al., 2007). In fact, research with closed-loop stimulation has already proven useful for suppressing clinical seizures in

humans (Fountas et al., 2005) and exploring new modes of network-level learning in neuronal cultures (Bakkum et al., 2008b).

Unfortunately, no commercial system for closed-loop stimulation and multielectrode recording exists. Furthermore, commercially available systems for multielectrode recording are hampered by long, saturating artifacts, which prevent recording from electrodes following stimulus pulses.

Here we present an integrated system for simultaneous multielectrode recording and stimulation. The software and hardware designs are open-source[16] and freely available online (http://www.johnrolston.com/), reducing the *in vivo* system's cost to <$10,000 for 64-channels of closed-loop recording and stimulation, an order of magnitude less than comparable commercial systems that cannot stimulate. The system recovers from stimulation artifact rapidly and is flexible in use, with both *in vivo* and *in vitro* versions. The current work is an extension of our lab's previous efforts in creating powerful yet inexpensive tools for studying closed-loop systems (Wagenaar and Potter, 2004; Wagenaar et al., 2005a).

System Design

System Overview

The system has four components: 1) multichannel amplifiers, 2) stimulation channel selection circuitry, 3) interface boards for analog filtering, power filtering, and stimulation control, and 4) a standard desktop computer with multifunction data acquisition cards (DAQs). Components 1-2 differ for freely moving animals and *in vitro*

[16] The software is licensed under the GNU Public License (GPL), version 3 (http://www.gnu.org/copyleft/gpl.html), and hardware under the Creative Commons Attribution-Share Alike 3.0 license (http://creativecommons.org/licenses/by-sa/3.0/us/).

preparations, but the software, computer, and DAQs are identical (Figure A-1). Further construction details are available online (http://www.johnrolston.com/).

In Vivo System

A custom-built stimulation headstage (designed with the free ExpressPCB software) connects to a chronically implanted microwire array (Tucker Davis Technologies). A 16-channel 100× gain head-mounting amplifier (Triangle Biosystems) attaches in turn to the stimulator headstage, buffering the signal and minimizing movement artifacts. Solid-state switches (Maxim, Inc.) direct stimuli to the appropriate channel. Current-control and diagnostic circuitry take place off-chip.

Extracellular signals, amplified by the headstage, are band-pass filtered in the interface boards, using a 2-pole active high-pass voltage-controlled voltage-source topology with a cut-off of 1 Hz, and a passive low-pass filter with a cut-off of 8800 Hz.

In Vitro System

A 64-channel MultiChannel Systems preamplifier (1000× gain) amplifies extracellular signals from 60-channel substrate-integrated multielectrode arrays (MEAs; note that the inclusion of the MCS preamp significantly increases the *in vitro* system's cost over that of the *in vivo* system). Custom-designed stimulation modules (ExpressPCB) deliver stimulus waveforms to the appropriate channel.

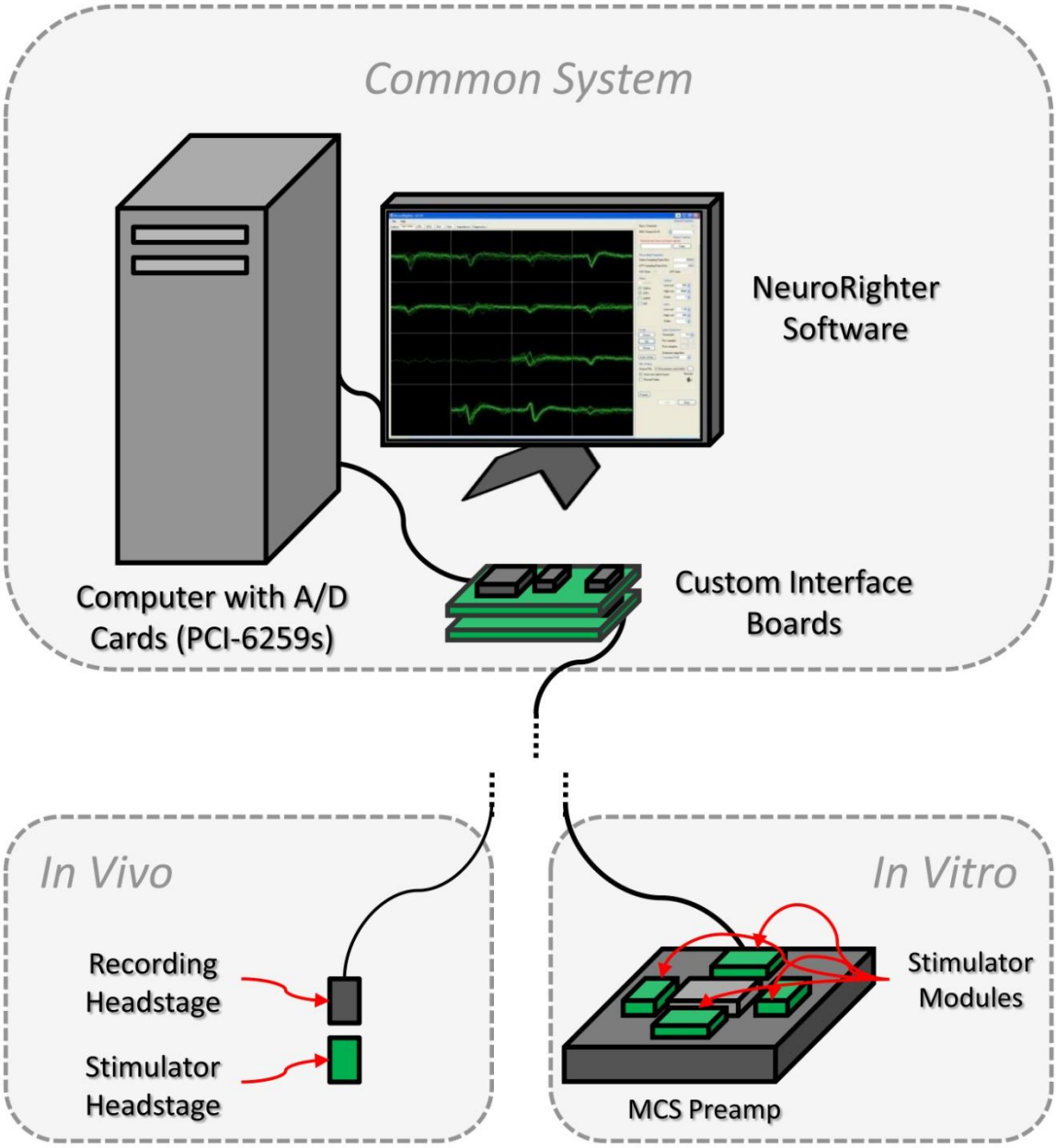

FIGURE A-1. System Schematic. A common system (top), shared by *in vivo* and *in vitro* applications, consists of custom software, data acquisition cards, and a desktop computer. Interface boards handle stimulation control and filtering. In freely moving animals (bottom left) a recording headstage amplifies neural signals and a stimulation headstage routes stimuli to the appropriate channel. *In vitro* (bottom right), an MCS preamp amplifies signals and stimulation modules handle stimulus routing.

Common System

Analog signals are digitized at 25 kHz with 16-bit resolution by PCI-6259 cards (National Instruments). Our NeuroRighter software, a multi-threaded Windows-based application (written in C#), handles online signal processing and stimulation control. Online processing separates the signal into spike and local field potential (LFP) bands and performs real-time spike detection.

Custom-designed printed circuit boards (PCBs; designed with the free PCB123 software) interface the data acquisition cards with the recording and stimulating headstages (*in vivo*) or preamplifiers and modules (*in vitro*).

Voltage or current-controlled stimulation waveforms are specified in software, generated by the PCI-6259 card's D/A converters, and propagate to the interface board. For voltage-controlled stimulation, the D/A signal is buffered and the delivered current is monitored with an instrumentation amplifier. For current-controlled stimulation, the voltage-controlled D/A signal is converted to current through precision resistors and a bank of operational amplifiers. The selection of voltage or current waveforms is made in software, which controls solid-state switches on the interface board.

Power is supplied by rechargable lead-acid batteries; however, the system's ground is tied to that of the acquisition computer (as in many commercial systems, e.g., Plexon). Future versions will incorporate additional isolation.

Experimental Methods

Surgery

All work with animals was conducted in accordance with the National Institutes of Health Guide for the Care and Use of Laboratory Animals and approved by the Emory University Institutional Animal Care and Use Committee. Adult male Sprague-Dawley rats (350-450g) were anesthetized with isoflurane, several anchoring skull screws were implanted, and a craniotomy was drilled over the right dorsal hippocampus. After removing the dura, a 16-channel microwire array (33 μm diameter tungsten wires with polyimide insulation) with two rows of 8 electrodes (row 1, 4 mm long; row 2, 2.8 mm long) was carefully lowered into craniotomy, with the longer row of the array targeted to the CA3 region, and the shorter row to CA1. Proper depth (usually 3-4 mm ventral to pia) was determined by monitoring electrophysiological recordings during implantation, using the NeuroRighter system. The craniotomy was then sealed with dental acrylic and the rat was allowed to recover for 5-8 days before recordings began.

Tetanus toxin (25 ng; Sigma) suspended in 0.5 μl of phosphate-buffered saline with 0.2% bovine serum albumin, was used to induce epilepsy in the closed-loop experimental animals. The injection was targeted to the CA3 region of the dorsal hippocampus (3.3 mm posterior to bregma, 3.2 mm lateral to midline, and 3.1 mm ventral to pia). Spontaneous seizures began in 5-9 days following injection. Unlike status epilepticus models, the tetanus toxin model has no mortality and a shorter latency to seizure onset.

Stimulation Experiment

To screen the effects of different stimulus intensities, rats were moved to a custom-built wooden and Plexiglas enclosure for recording and stimulation. They were tethered but

otherwise freely mobile. Biphasic current-controlled stimulus pulses were then delivered to a subset of the electrode array (those electrodes with single unit activity and some additional electrodes). All cathodic-phase first pulses had a duration of 800 μs (400 μs per phase). Several stimulus amplitudes were used: 2, 4, 6, 8, 10, 15, 25, and 50 μA. 10 trials with each pulse amplitude were delivered to each electrode in random order. Randomization helped to control for neural adaptation.

Impedance Measurements

Impedances were measured by delivering current-controlled sine waves across a spectrum of frequencies to each electrode in turn. The delivered voltage was measured, a matched filter was applied, and the ratio of RMS voltage over RMS current was used to calculate the impedance at a given frequency.

Closed-loop Experiment

To illustrate the closed-loop experiments possible with the NeuroRighter system, we created an algorithm that delivered stimulation to a single electrode when an interictal spike was detected in the LFP. Interictal spikes were defined as deviations exceeding 7.5× the signal's RMS. This high threshold ensured a very high specificity (100% based on 45 minutes of test data immediately preceding the experiment) but at the expense of sensitivity (10%), as determined by an expert reviewer. Biphasic 10 μA, 400 μs per phase pulses were delivered after each detection.

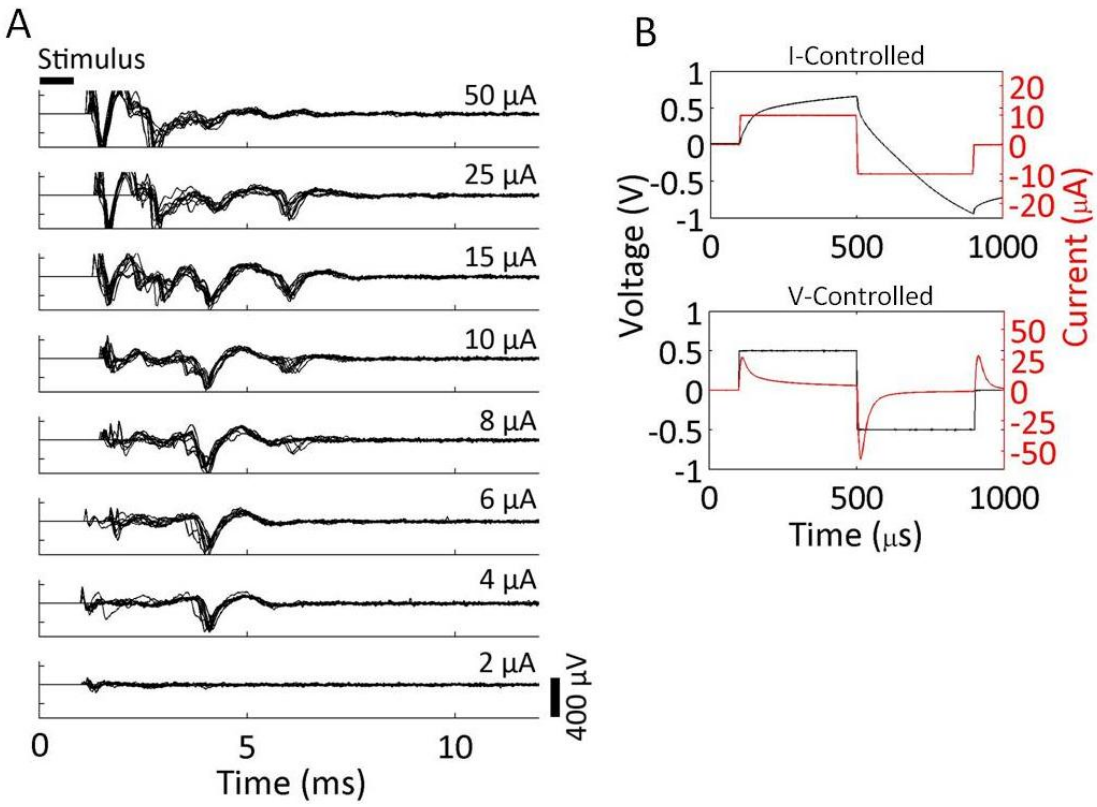

FIGURE A-2. Stimulation evokes action potentials (APs). (A) Biphasic current-controlled pulses of varying amplitudes are delivered to an electrode. Ten trials of evoked activity are overlaid for each intensity. The first APs are evoked at 4 µA, with additional APs emerging at higher intensities (15 µA). Spikes are detected less than 1 ms after stimulus offset. (B) The stimulator can operate in current- or voltage-controlled modes. The delivered current and voltage are simultaneously monitored during each pulse. This information can be used to measure impedance spectra when sinusoidal waves are used rather than biphasic pulses.

Results

We created a combined recording and stimulation system for multielectrode arrays. The system is capable of recording LFPs and APs from freely moving animals. Both current- and voltage-controlled stimulation waveforms can be delivered to any recording electrode, and impedance spectra can be acquired in real-time. Stimulus pulses readily evoke APs which are recorded at short latency (Figure A-2A).

Noise and Cross-talk

Broadband root-mean-square (RMS) noise values for the *in vivo* system are 6.1 ± 0.2 μV (mean ± standard error across channels) when using a grounded reference, and 8.4 ± 0.2 μV when using an active reference. Restricted to bands containing action potential data (>300 Hz), the RMS noise is 3.9 ± 0.1 μV for grounded reference, 5.5 ± 0.1 μV for true reference. The increased noise when using a true reference arises from the superposition of the reference channel's noise and that of the signal channel (the combined noise is a factor of √2 larger). The headstage manufacturer, Triangle Biosystems, specifies the broadband RMS noise as 6.2 μV, so our system is not introducing additional noise through the interface boards, cables, or A/D conversion process.

For the *in vitro* setup, where an MCS preamplifier is used, the broadband RMS noise is 3.2 μV.

The observed cross-talk was −66 dB for adjacent channels, −69 dB for non-adjacent. This is in agreement with the headstage manufacturer's reported cross-talk (−63 dB for adjacent channels; personal communication with TBSI).

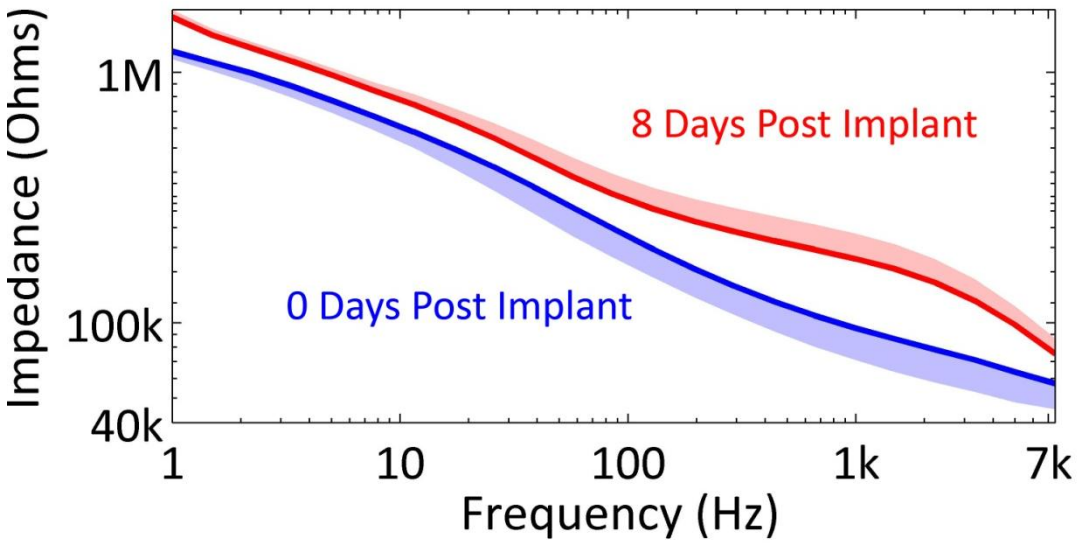

FIGURE A-3. Impedance spectra. The ability to simultaneously monitor delivered current and voltage allows the NeuroRighter system to calculate impedance spectra in real-time from freely moving animals. The above impedance spectra were taken from a microwire array implanted in rat hippocampus immediately after surgery (blue) and 8 days post-op (red). Dark lines indicate population averages (across the array's 16 electrodes); shading indicates one standard deviation (shown on ones side only, for clarity).

Impedance Spectra

Impedance spectra were calculated at several time points across several animals. Example traces are shown in Figure A-3, highlighting the gradual increase of electrode impedance after the initial array implant.

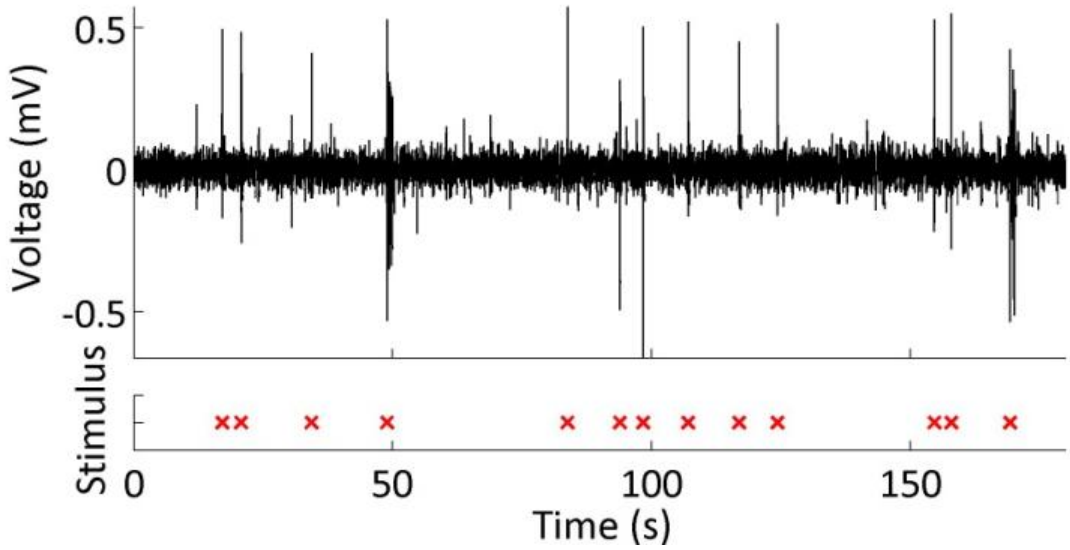

FIGURE A-4. Closed-loop stimulation. Stimuli (red x's) are triggered by the detection of interictal spikes in the LFP (top trace). The animal was freely mobile during this experiment.

To test our system's closed-loop capabilities, we programmed a sample experiment wherein a single 10 μA stimulation pulse was delivered to an electrode when interictal spikes were detected (Figure A-4). The mean time between detection of interictal spikes and stimulus delivery was 4.4 ± 1.2 ms (± standard deviation). Though stimulation pulses readily evoked neural responses (Figure A-2), stimulation nevertheless had no discernible effects on interictal spikes in CA1 or CA3 of epileptic animals (the stimulating channel was located in CA3).

Discussion

The NeuroRighter system is an integrated software and hardware suite for conducting closed-loop multielectrode experiments. It has several notable features. 1) *Open source software and hardware.* Because the software and circuit layouts are free and permissively licensed, users can readily modify the code or circuitry to add features (e.g.,

new device drivers, new spike detection methods), improve functionality, or customize their experiments. The free licensing also leads to a total *in vivo* system cost of less than $10,000 for 64-channels, 4-10× cheaper than comparable commercial systems that cannot conduct closed-loop stimulation. 2) *Flexibility*. NeuroRighter has circuitry for both *in vitro* and *in vivo* experiments, providing a consistent platform for both fields of research. Stimulation is also flexible, with software toggling between voltage and current control, and the capability to produce waveforms of arbitrary complexity (e.g., "replaying" a previously recorded LFP). 3) *Stimulation*. Others have previously reported multielectrode stimulation systems with short stimulation artifacts (Jimbo et al., 2003; Brown et al., 2008; Venkatraman et al., 2009), though these use specialized (in one case patented) artifact-reduction circuitry. Our system relies only on a low-gain front-end (100×) with no subsequent second-stage amplification, possible due to our 16-bit A/D resolution. This simplicity improves cost while still recovering from artifacts within 1 ms (the stimulating channel takes longer (~60 ms) to recover, however, due to capacitive coupling to the medium). 4) *Real-time impedance spectroscopy*. Impedance spectroscopy has the potential to reveal additional information about electrode viability and tissue composition proximal to the electrode (Merrill and Tresco, 2005; Williams et al., 2007). The NeuroRighter system provides push-button acquisition of these spectra. Preliminary results (Figure A-3) corroborate previous reports of increased impedance following electrode implantation (Williams et al., 2007), illustrating the system's utility. 5) *Closed-loop experimentation*. Few systems exist for conducting closed-loop multielectrode electrophysiology, and there are fewer still for use in freely moving animals. To illustrate the system's capabilities, we conducted a simple experiment wherein stimulation was delivered to CA3 upon detection of interictal spikes (de Curtis and Avanzini, 2001) in a freely moving rat. Some authors propose that stimulation following seizure detection can prevent full-blown seizures or shorten their duration

(Morrell, 2006; Fountas and Smith, 2007). Though our stimulation evokes APs (Figure A-2), interictal spikes, which share pathophysiological features of seizures, were unaffected, even in the downstream CA1 region. This implies that the amount of tissue we affect is insufficient to suppress these spikes, or that the generating mechanism is resistant to perturbation by stimulation.

Conclusion

The NeuroRighter system offers a streamlined platform for closed-loop experimentation using microwire arrays both in culture and in awake, behaving animals. It is our hope that the features and usability of the system will encourage additional researchers to capitalize on the exciting possibilities inherent in closed-loop devices.

Acknowledgment

We gratefully acknowledge technical support from Claire-Anne Gutekunst, Edgar Brown, Lissa Jackson, and the Gross and Potter labs.

Appendix B

NeuroRighter Construction Manual[17]

[17] A "living" version of this document can be found at http://sites.google.com/site/neurorighter/.

System Overview

The system is made of headstages, interface boards, data acquisition cards, a computer, and connecting cables.

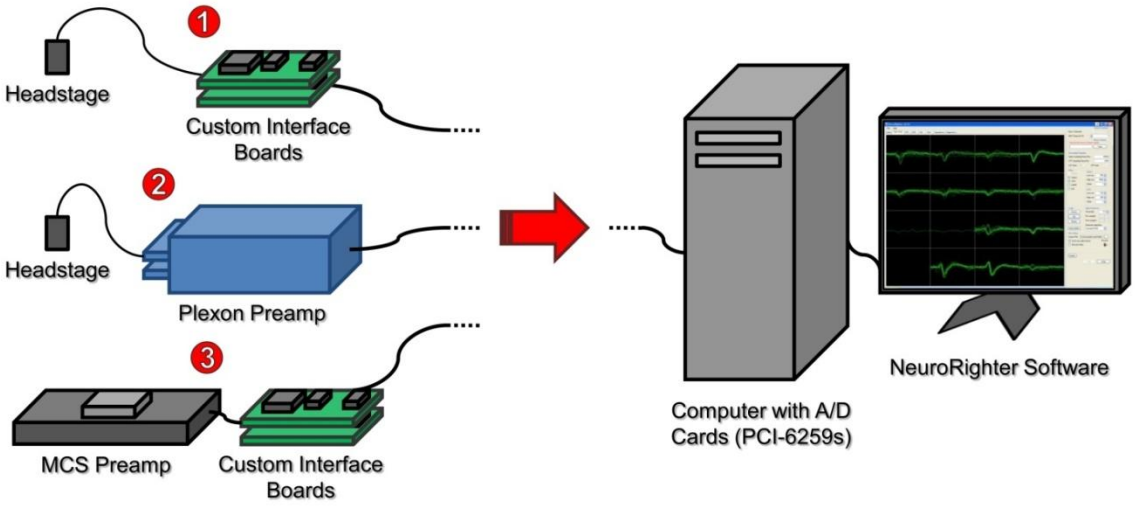

FIGURE B-1. Overview of NeuroRighter System. ❶ Shows the standard *in vivo* setup, with a Triangle Biosystems (TBSI) recording headstage, and custom interface boards. ❷ Shows a hybrid system using a Plexon headstage and preamplifier. ❸ Shows an *in vitro* hybrid system, using a preamp from MultiChannel Systems. All setups converge to a desktop computer with multiple data acquisition cards (National Instruments PCI-6259 or PCIe-6259).

Parts to Order

The following is a detailed list of what to order and where to get it from. There are multiple configurations for the NeuroRighter System. Each requires different parts, though some are shared.

In Vivo Parts (❶ in Figure B-1)

1. **Recording Headstage:** 16-channel tethered headstage, gain 100 (Triangle Biosystems (TBSI), http://www.tbsi.biz). You will need one of these for every 16 channels you'd like to record.

FIGURE B-2. Recording headstage.

2. Recording Headstage Cable: This is a custom cable to connect the headstage to the interface boards. This should be ordered from TBSI along with the headstage. Specify that you'd like stripped leads on one end of the cable (the end that doesn't plug into the headstage—the end that does plug into the headstage will have an Omnetics connector on it). You will solder these free leads to a printed circuit board (PCB) later.

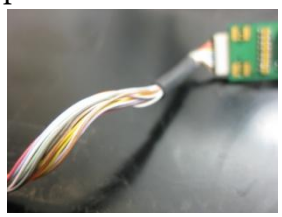

FIGURE B-3. Recording Headstage Cable.

3. **Stimulator Headstage:** These can be ordered from ExpressPCB (http://www.expresspcb.com/) via their layout software, ExpressPCB (nb: this is a different software and vendor than is used for the interface boards). Open the layout file stimModule070801_FP.pcb. Then use the software's built-in ordering function to order boards. A soldermask is essential to avoid shorts when connecting the fine-pitch Omnetics connectors (http://www.omnetics.com/).

FIGURE B-4. Stimulator headstage.

   a. **Components for Headstage**
      i. Omnetics A9512-001 (connects to recording headstage)
      ii. Omnetics A8783-001 (connects to MEA)
      iii. Maxim MAX306 16-channel multiplexer
      iv. 2x Nichion F93 SMT (surface-mount) tantalum capacitors, 1 μF
   b. **Solder stencil:** We used Pololu (http://www.pololu.com) to manufacture transparent Mylar stencils for our boards. To do the same, send them the top/bottom DXF files of the stimulator headstage layout: stimModule070801_FP_BOTTOM.dxf and stimModule070801_FP_TOP.dxf.

4. **Interface Boards:** These can be ordered from PCBExpress (http://www.pcbexpress.com/) via their layout software, PCB123. First, download the software: http://www.pcb123.com/. Once installed, load the stimulator/power board layout: Interface_Stim_V0_7.123. When the file is loaded, use the built-in controls to order boards. [Note: The PCB123 software generates multiple DRC errors when testing the boards. These can all be safely ignored.] You will need one board for each NeuroRighter setup, but the minimum order is two boards. There is no need for solder masks or silkscreens (unless you'd like the board to look prettier). Not using these features will reduce the boards' prices. The next board to order is the headstage filtering board. Load the layout: Interface_Headstage_V0_7.123. Again, use the built-in controls to order boards. You will need one board for each 16 channels of recording.

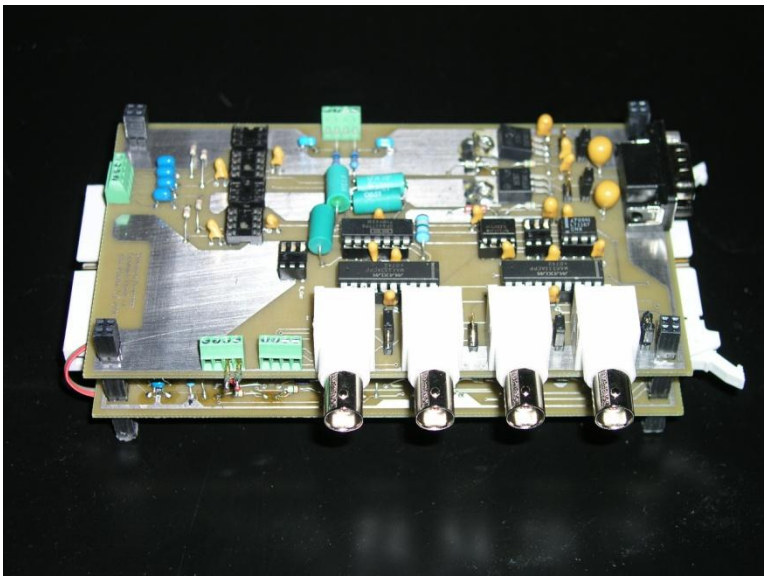

FIGURE B-5. Stacked interface boards.

5. **Computer:** Any standard PC will do. However, ensure that it has enough PCI or PCIe slots (either PCI or PCIe works fine) to handle your data acquisition cards. You will need one card for every 32 channels of recording, and one additional card for stimulation (e.g., a 64-channel system will have three cards, two for

recording and one for stimulation). Multi-core processors are preferred and high speed hard drives will be useful if writing raw traces to disk. Our software works and has been tested on Windows XP and Windows Vista (32-bit). We expect it to work on 64-bit versions of these operating systems, as well.

6. **Data Acquisition Cards:** We use the PCI-6259 or PCIe-6259 32-channel multi-function data acquisition cards from National Instruments (http://www.ni.com), along with their associated cables and breakout boxes and RTSI cables.
    a. **PCI- or PCIe-6259 multi-function data acquisition cards** (http://sine.ni.com/nips/cds/view/p/lang/en/nid/201814). PCIe cards are preferred over PCI cards (since they have a faster data transfer rate), though we have not seen any performance increase in practice. You will need one card for every 32 channels of data acquisition. One additional card is currently required for stimulation (this requirement can be removed, if you wish to do some reprogramming of the NeuroRighter software).
    b. **Shielded cables.** Each card requires two shielded cables (SHC68-68-EPM Cable (2m)) to connect to the card's breakout boxes. The shielded cables can be any length, but 2 m will give you more flexibility in setting up your system.
    c. **Breakout boxes.** Two breakout boxes (SCB-68 – Shielded) are required per card.
    d. **RTSI cable.** You will need a RTSI cable (http://sine.ni.com/nips/cds/view/p/lang/en/nid/12631) to connect the data acquisition cards, so that they can share timing information while recording or stimulating.
7. **Circuit board components:** Most of these can be ordered from Digi-Key (http://www.digikey.com) or Newark (http://www.newark.com). Stack-through connectors (four for each board) are generally not sold through Digi-Key or Newark, however, and should be ordered via the manufacturer, Samtec (http://www.samtec.com).

Components for Stimulator/Interface Command Board, r7

From Digi-Key:

4x BNCs: ARF1065NW
4x 4-pin terminal strips: 277-1275
22pins of header strip: (e.g., 1x A26513-40)
1x DB9: 182-809ME
4x 6-pin sockets: A9406

2x MAX333A: MAX333ACPP+
3x LT1167: LT1167ACN8 (two for EEG, one for V-controlled stimulation)
1x OPA4277: OPA4277PA
1x OPA277: OPA277PA
1x LM317: 296-21576-5 (TI) or LM317BTGOS (ON)
1x LM337: 296-21577-5 (TI) or LM337BTGOS (ON)

1x 910 Ohm 1%: P910CACT (for LM317) (to make 6V supply)

1x 453 Ohm 1%: CMF453HFCT (for LM337) (to make 6V supply)
1x 120 Ohm 1%: P120CACT (for LM337) (to make 6V supply)
1x 240 Ohm 1%: P240CACT (for LM317) (to make 6V supply)
4x100k Ohm 0.01%: MR106-100k-.01 (for OPA4277)
Assorted 1% resistors for OPA4277 measurements
Assorted 1% resistors for Rg and Rm
1x 6.8 MOhm 1%: PPCHF6.80MCT
4x 22 kOhm 1% resistors (for EEG 0.7 Hz high pass): P22.0KCACT
2x 1 kOhm 1% (for EEG 500 Hz low pass): P1.00KCACT

4x 10 uF capacitors (EEG high pass): 445-2887
2x 0.33 uF capacitors (EEG low pass): 490-3832
16x 1 uF tantalum capacitors (decoupling caps and two of the voltage regulator caps): 478-1833
2x 100 uF tantalum capacitors (board power in): 478-1847
2x 10 uF tantalum capacitors (voltage regulation, near adj pins): 478-1840

From Samtec:
4x ESQ-102-39-G-D

Components for Interface Board, r7
From Digi-Key:
1x 34-pin right angle header: HRL34H
1x 40-pin right angle header: HRL40H

4x OPA4277: OPA4277PA
1x LM317: 296-21576-5 (TI) or LM317BTGOS (ON)
1x LM337: 296-21577-5 (TI) or LM337BTGOS (ON)

2x 120 Ohm 1%: P120CACT (for LM337) (to make 2.5V supply)
2x 240 Ohm 1%: P240CACT (for LM317) (to make 2.5V supply)
34x 1uF ceramic capacitor (active filters): 445-2858
17x 180 Ohm resistors (low pass): P180CACT
17x 100 nF ceramic capacitors (low pass): BC1114CT
34x 150k resistors (active filters): P150KCACT
17x 100k resistors (active filters): P100KCACT
17x 59k resistors (active filters): CMF59.0KQFCT
12x 1 uF tantalum capacitors (decoupling caps and two of the voltage regulator caps): 478-1833
2x 100 uF tantalum capacitors (board power in): 478-1847
2x 10 uF tantalum capacitors (voltage regulation, near adj pins): 478-1840

From Samtec:
4x ESQ-102-39-G-D

8. **Cabling.** Cables are needed to provide power to the stimulator/interface boards, and cables are needed to transmit data from the interface boards to the data acquisition cards. All of this can be ordered through Digi-Key (http://www.digikey.com).
    a. *Power cable* (1 per stimulator/power board)
        i. DB-9 solder-cup (to plug into board): AE10095-ND

ii. Shielded multi-conductor cable, with at least 4 conductors: W504-100-ND

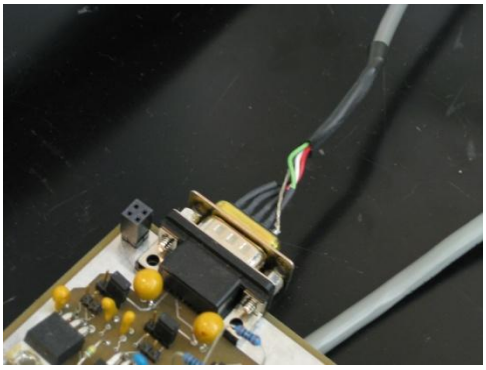

FIGURE B-6. Power cable.

b. *Data cable* (1 per headstage)

i. 34-conductor shielded flat ribbon cable: MB34H-100-ND (nb: shielding is optional, but important for reducing EMI, in our experience)

ii. 34-pin ribbon header (to plug cable into board): MSC34A-ND

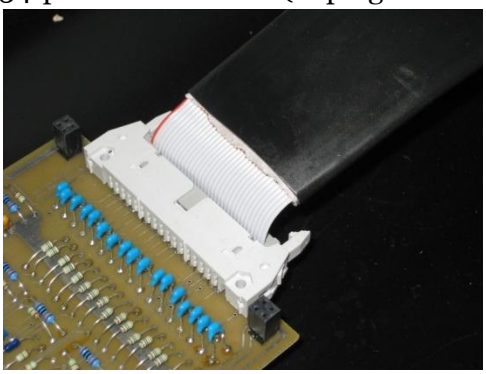

FIGURE B-7. Data cable.

c. *Stimulator cable*

i. Shielded multi-conductor cable: C0755-100-ND

ii. Thin-gauge wire (for last few feet of cable, going to the animal's head): e.g., 3749/16 100-ND

9. Power Supply. We currently use lead-acid batteries to provide power to our system and reduce line noise (60 Hz noise). To create a bipolar ±6V power supply, we use two 6V batteries in serial. These are controlled with a simple toggle switch and some hook-up wire. A battery charger is also required. Batteries of higher voltage can be used, but not less. If higher voltages are used, make sure to properly configure the on-board voltage regulators on the

stimulator/power board (described below).

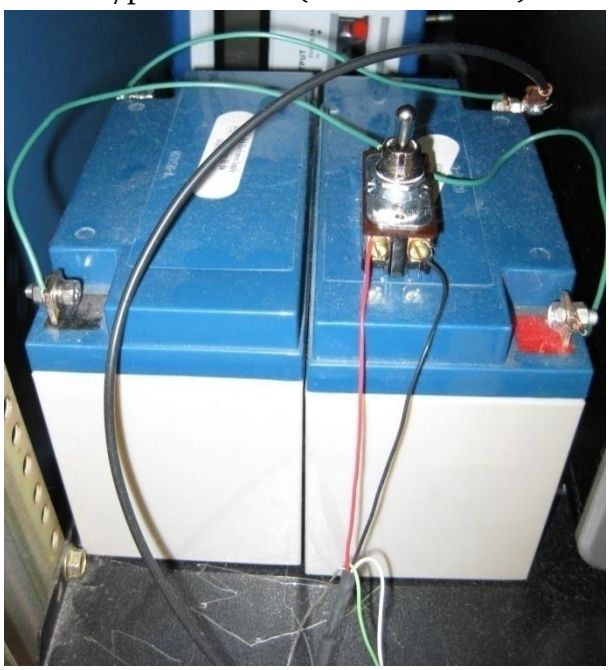

FIGURE B-8. Batteries.

a. **Batteries.** We used Power-Sonic 20 amp-hour lead-acid batteries from Ack Electronics (http://www.acksupply.com/). However, comparable batteries can be obtained from Digi-Key (e.g., P231-ND).
b. **Recharger.** We used a Power-Sonic PSC-124000A-C Automatic Battery Charger (PSC-124000A-C) to recharge the lead-acid batteries. A comparable product from Digi-Key might be 271-2386-ND (though this hasn't been tested).
c. **Switch.** We prefer a double-pole single-throw (DPST) toggle switch to turn the interface board power on and off. From Digi-Key, 432-1087-ND.

In Vitro Parts (Multichannel Systems hybrid) (❸ in Figure B-1)

Multichannel Systems setup. If creating a NeuroRighter setup for *in vitro* use, the parts required are different. You will not need items 1-3 above. For item 4, only order the stimulator/control board. Do not order the interface board (which is for *in vivo* applications). Instead, order the MCS Converter board (MCS_Converter_V01.123). [Note: The PCB123 software generates multiple DRC errors when testing the boards. These can all be safely ignored.]

For item 8, cabling, the power cable remains identical. Ribbon cable should still be used to carry signals from the converter board to the DAQs, but you will now need four separate cables (4x MSC34A). Currently, the stimulator cable must be manufactured by the end user.

Stimulator headstages are required for the MCS preamplifier. These are identical to those of Daniel Wagenaar's RACS setup. For now, see his documentation for parts and board designs. The only required parts are the "stim mods" (stimulator modules), which have 2x 8-channel multiplexors, header pins, and decoupling capacitors.

Item 8, the battery supply, is the same as for the *in vivo* setup.

You will need only part of item 7, those components for the stimulator/command board. However, you will need additional components for the MCS interface board (MCS_Converter_V01.123). These are tabulated below:

Components for MCS Interface Board

From Digi-Key:

4x 34-pin right angle header: MHD34K
1x 68-pin right angle female SCSI: A33512

1x LM317: 296-21576-5 (TI) or LM317BTGOS (ON)
1x LM337: 296-21577-5 (TI) or LM337BTGOS (ON)

1x 910 Ohm 1%: P910CACT (for LM317) (to make 6V supply)
1x 453 Ohm 1%: CMF453HFCT (for LM337) (to make 6V supply)
1x 120 Ohm 1%: P120CACT (for LM337) (to make 6V supply)
1x 240 Ohm 1%: P240CACT (for LM317) (to make 6V supply)
2x 1 uF tantalum capacitors (voltage regulator caps): 478-1833
2x 100 uF tantalum capacitors (board power in): 478-1847
2x 10 uF tantalum capacitors (voltage regulation, near adj pins): 478-1840

From Samtec:

4x ESQ-102-39-G-D

Assembly

Assembly instructions are presented with the common items first (computer, software, data acquisition cards), and then the items specific to each setup (❶-❸ in Figure B-1 above).

Computer

Follow the computer supplier's setup instructions.

Data Acquisition Cards

Refer to National Instruments installation instructions when installing your PCI- or PCIe-6259 cards and their associated RTSI cable(s). RTSI cable installation instructions can be found here: http://www.ni.com/pdf/manuals/371343a.pdf. Refer to the National Instruments instructions when connecting the shielded cables and breakout boxes. Instructions for connecting the interface boards to the breakout boxes are given below.

Software

Two software installation tasks must be performed: install the National Instruments drivers (NI-DAQmx) and install the NeuroRighter software. After installing the data acquisition cards and their drivers, you must also configure the RTSI cable through National Instruments' Measurement and Automation Explorer application.

Installing the NI-DAQmx drivers

The data acquisition cards should come with a CD or DVD containing the NI-DAQmx drivers. Follow the instructions accompanying this software to install the NI-DAQmx software. The drivers can also be found online at National Instruments web site, by searching for NI-DAQmx (http://www.ni.com/).

Configuring RTSI Bus

After physically installing the NI data acquisition cards, installing the RTSI cable between the cards, and installing the NI-DAQmx cards, you must manually add the RTSI cable to each NI card's software attributes. To do this, start Measurement and Automation Explorer (usually in the National Instrument folder in your Start Menu). The screen should look something like the screenshot below:

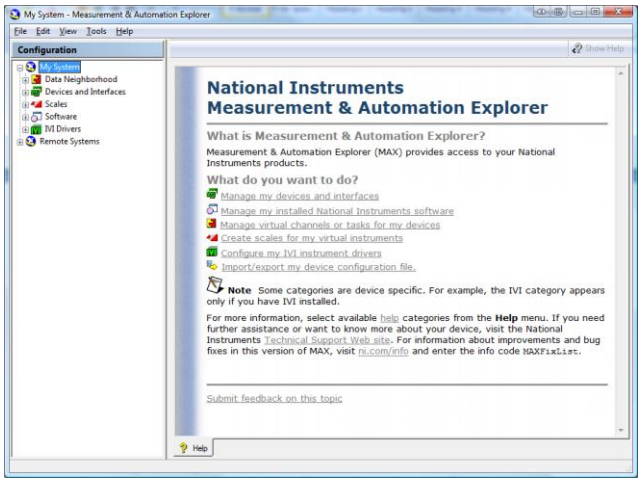

FIGURE B-9. Measurement and Automation Explorer screenshot.

In the left panel, select "Devices and Interfaces", then "NI-DAQmx Devices". Right-click on "NI-DAQmx Devices" and select "Create New NI-DAQmx Device" and choose "RTSI Cable". The RTSI cable will now show up as one of your NI-DAQmx devices.

To connect each PCI or PCIe card to the RTSI bus, right-click on each card in the left-

hand menu, and select “Properties”. A dialog box similar to the following should appear:

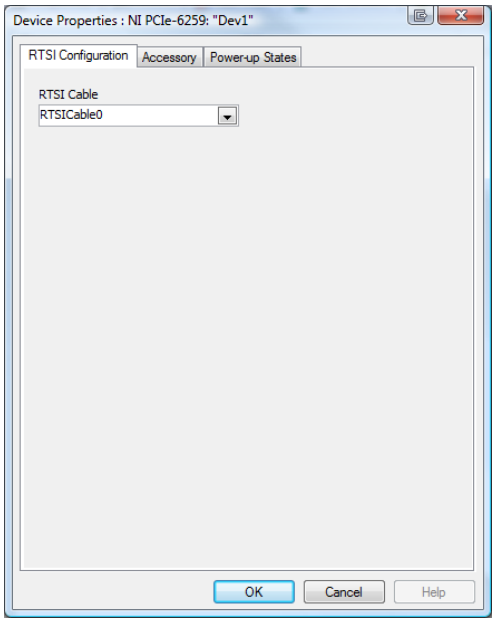

FIGURE B-10. RTSI configuration screenshot.

In the RTSI Cable box, select your recently added RTSI cable. Do this for each device you wish to connect to the bus.

Installing NeuroRighter

Download the latest version of the NeuroRighter software from http://www.johnrolston.com/. This is usually distributed as a ZIP file. Decompress the ZIP file and refer to the user manual for more detailed installation instructions. (Installation typically requires executing the setup.exe file, but refer to the specific instructions to be certain.)

Power Supply

Connect the two 6V batteries in serial: that is, connect the negative terminal of one to the positive terminal of the other. You now have a 12V battery. Using the “center” of the

battery as ground (calling the terminals you connected ground), gives you a ±6V power supply. The unconnected negative terminal is -6V in reference to ground, and the unconnected positive terminal is +6V in reference to ground.

Now, connect the free (unconnected) positive and negative terminals to the toggle switch. To secure the toggle switch, we use super glue (cyanoacrylate glue) to fix it to one of the batteries. This is for convenience, and not necessary. At this point, when the toggle switch is turned on, the terminals of the switch will now have -6V on one terminal and +6V on the other. Using a multimeter should measure a difference of ~12V between the two. The voltage is usually a little higher, since the actual voltage of a "6V" battery is about 6.5V.

See the picture below for more details. [Note: In the picture below, the red wire of the power cable is -6V, the black wire is +6V. This is unconventional. Traditionally, red would be positive voltage. The colors are arbitrary. You can use whatever scheme you'd like, as long as it is consistent.]

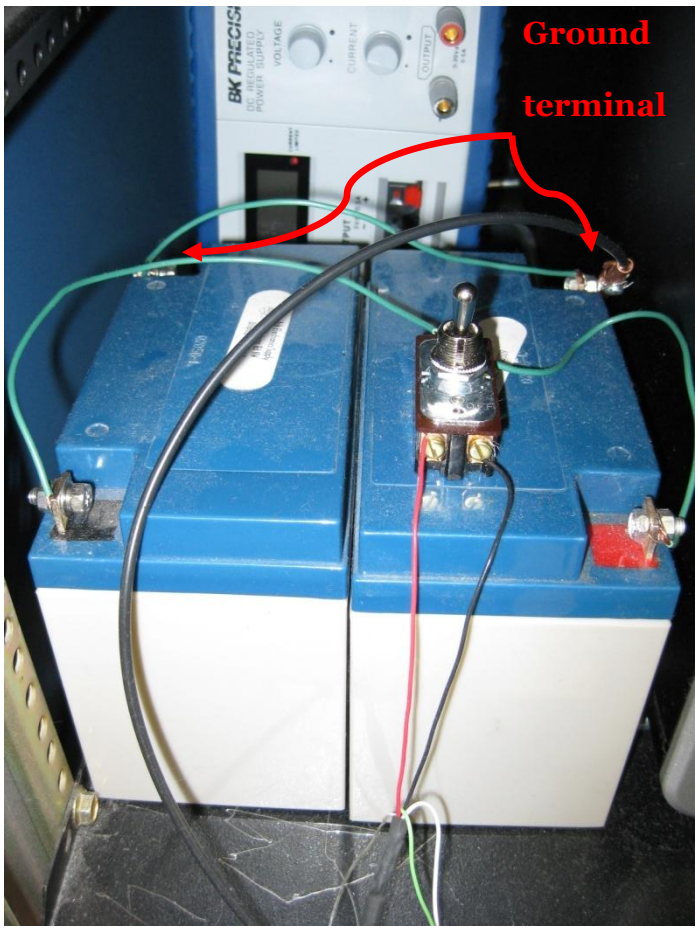

FIGURE B-11. Battery connections.

In Vivo Interface Boards and Cables

This section requires a great deal of soldering to assemble the printed circuit boards (PCBs) and cables. If you are unfamiliar with soldering, you can look online for tutorials—there are hundreds, all free and high quality. If you would rather not solder the boards yourself, you can hire a company to do it for you. For example, Screaming Circuits (http://www.screamingcircuits.com/) can create all of the boards shown below for a reasonable price. Screaming Circuits will even order the components for you.

Power Cable

This cable connects the batteries to the stimulator/power board, providing power for the recording headstage, the interface board, and the stimulator circuitry. This requires three wires: V+, V-, and GND (ground). A fourth wire controls whether the board is delivering current- or voltage-controlled stimulation. If the signal on the fourth wire is "high" (+5V), the stimulation will be current-controlled. If the signal is "low" (ground or 0V), the stimulation will be voltage-controlled. This wire will be controlled by the National Instruments cards.

Use a sufficient length of cable to reach the stimulator/control board from the location of the batteries and National Instruments breakout boxes. Remove the shielding and a few inches of the outer insulation from both ends of the cable. Strip a few mm of each individual wire's insulation on both ends.

On one end of the cable, solder the wires to the DB9 solder-cup connector, as shown in the picture below. We used heat-shrink tubing around the end of each wire, to prevent the deinsulated wires from touching and causing shorts. A similar effect could be achieved with electrical tape or epoxy.

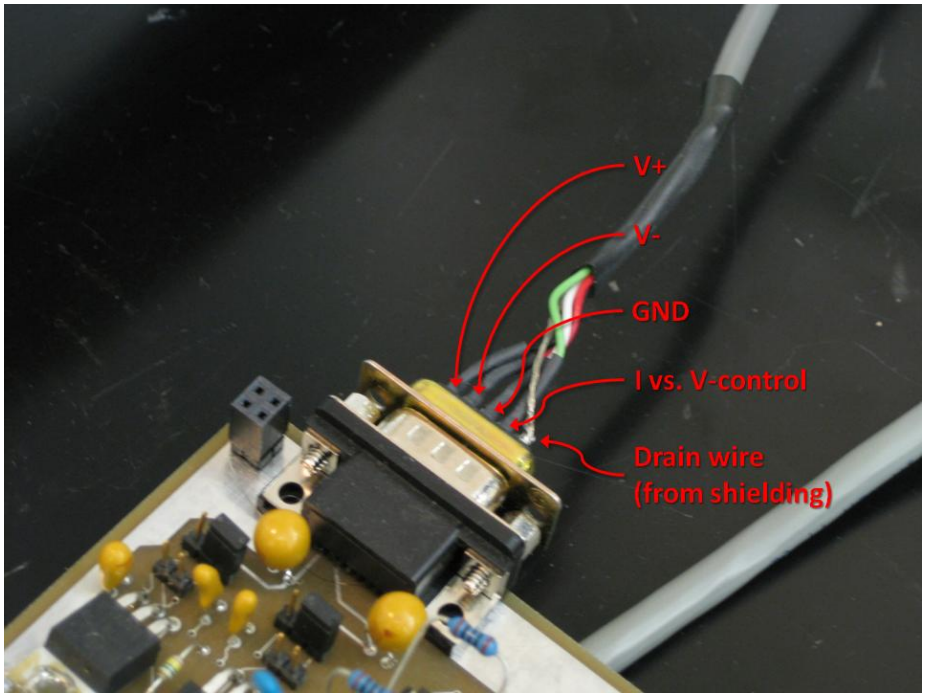

FIGURE B-12. Power cable connections.

The other end of the cable should be attached to the battery supply's toggle switch, as depicted in the power supply section. The ground wire (white in the above pictures) should be connected to the "ground" terminals of the batteries (i.e., the terminals of the two batteries that are connected to each other). In the figure above, this is down with a short length of black wire with alligator clips on both ends: one end clamps on the ground terminal, the other clamps on the power cable's ground wire. This could also have been accomplished by directly connecting the power cable's ground wire to one of the battery's ground terminals. There is no reason to use a switch for the ground wire.

Stimulator/power board

Below are several pictures of the stimulator/power board. Construct the board as shown. Refer to the board schematics for additional help (included with board layouts).

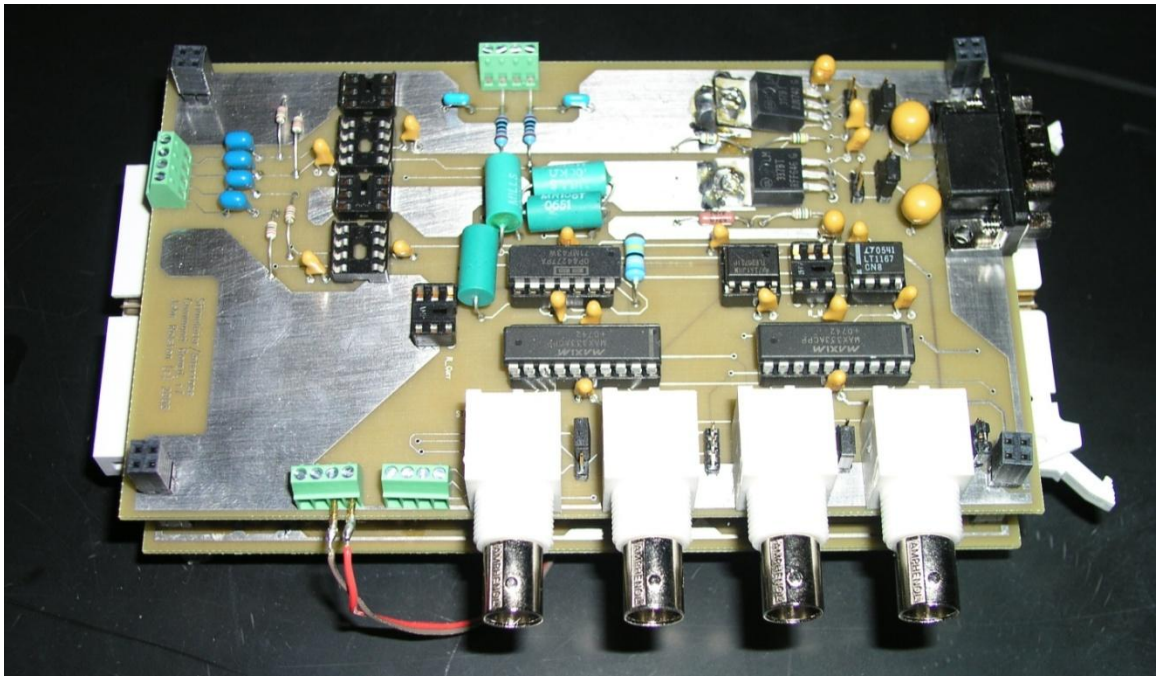

FIGURE B-13. Power/stimulator board.

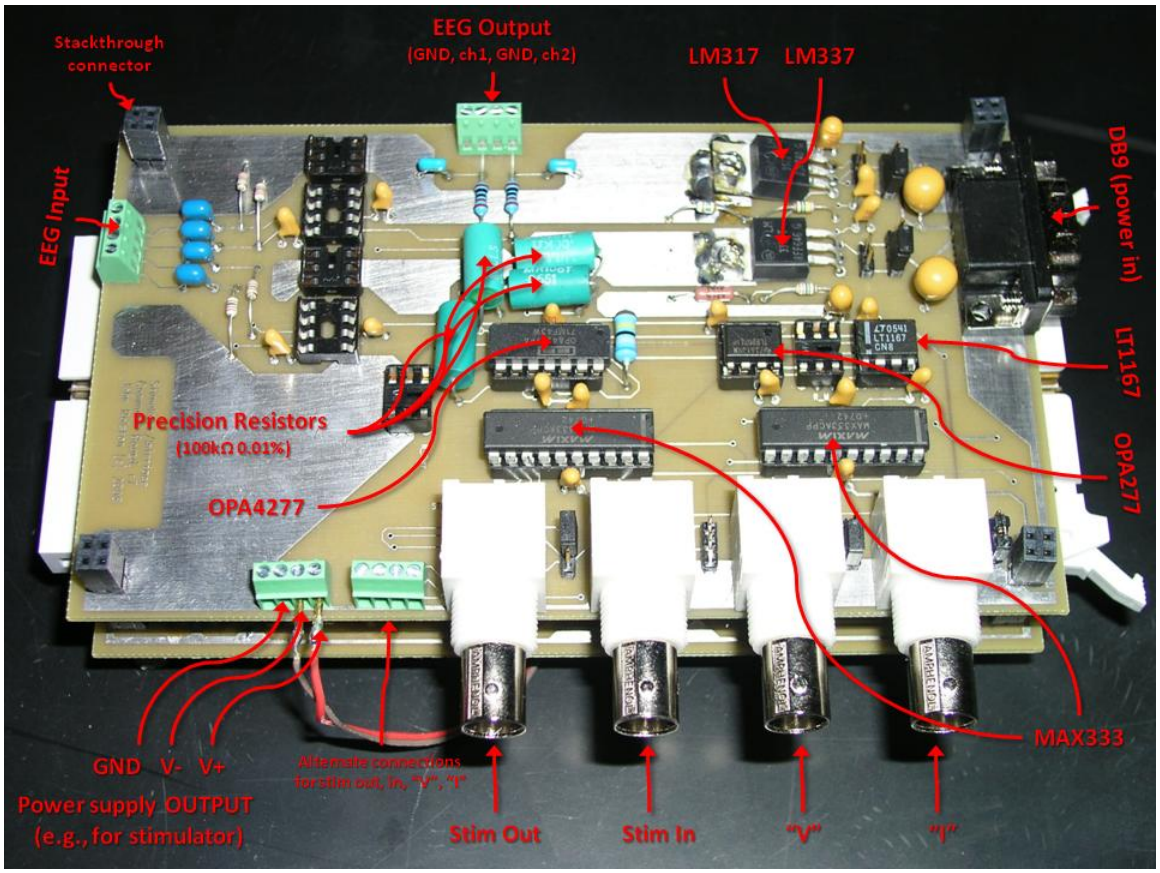

FIGURE B-14. Stim/power board components 1.

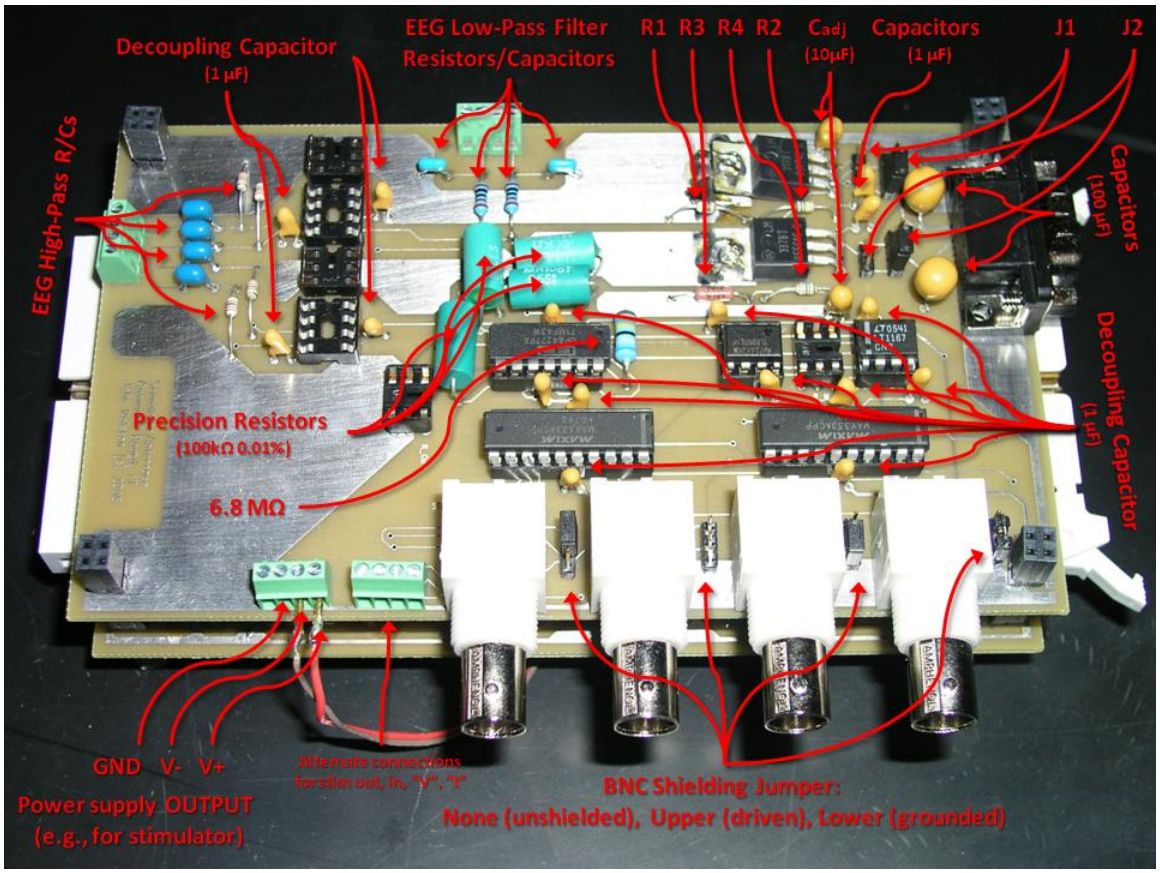

FIGURE B-15. Power/stim board components II. R1, R2, R3, R4 determine voltage output of voltage regulators. R1 = 910 Ω, R2 = 240 Ω, R3 = 453 Ω, R4 = 120 Ω. J1 and J2 (one set per regulator) can be used to engage or bypass voltage regulators (see **FIGURE B-16**ERROR! REFERENCE SOURCE NOT FOUND. for more details).

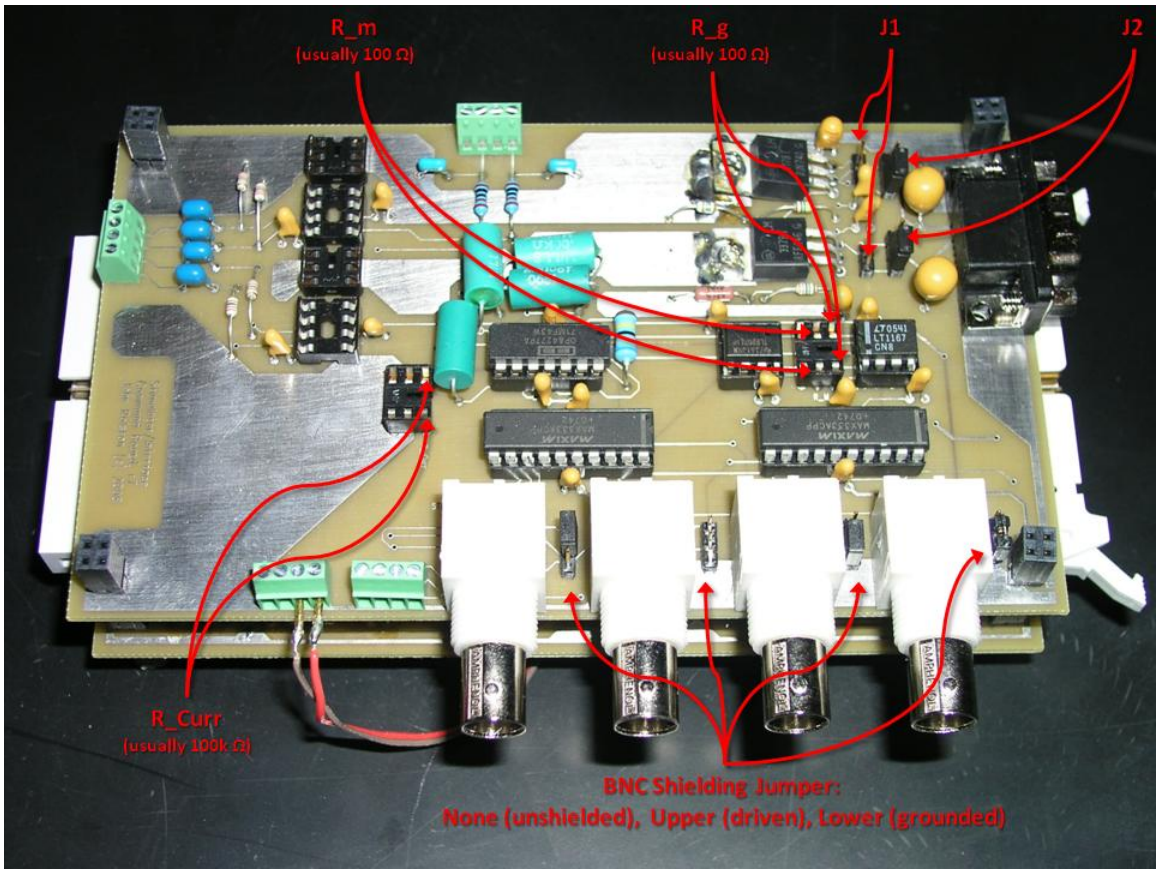

FIGURE B-16. Stim/power board components III. R_curr is used to divide the stim-in input voltage into current for current-controlled stimulation (e.g., 1V input -> 1 μA when R_curr = 100 kΩ). R_m and R_g determine the gain of "I" (the current-monitor) when delivering voltage-controlled stimulation. J1 and J2 (one set per regulator) can be used to engage or bypass voltage regulators (e.g., you'd want to bypass these if using two 6V batteries for your power supply). Setting J1 empty and J2 low bypasses the voltage regulators. Setting J1 and J2 high engages voltage regulators.

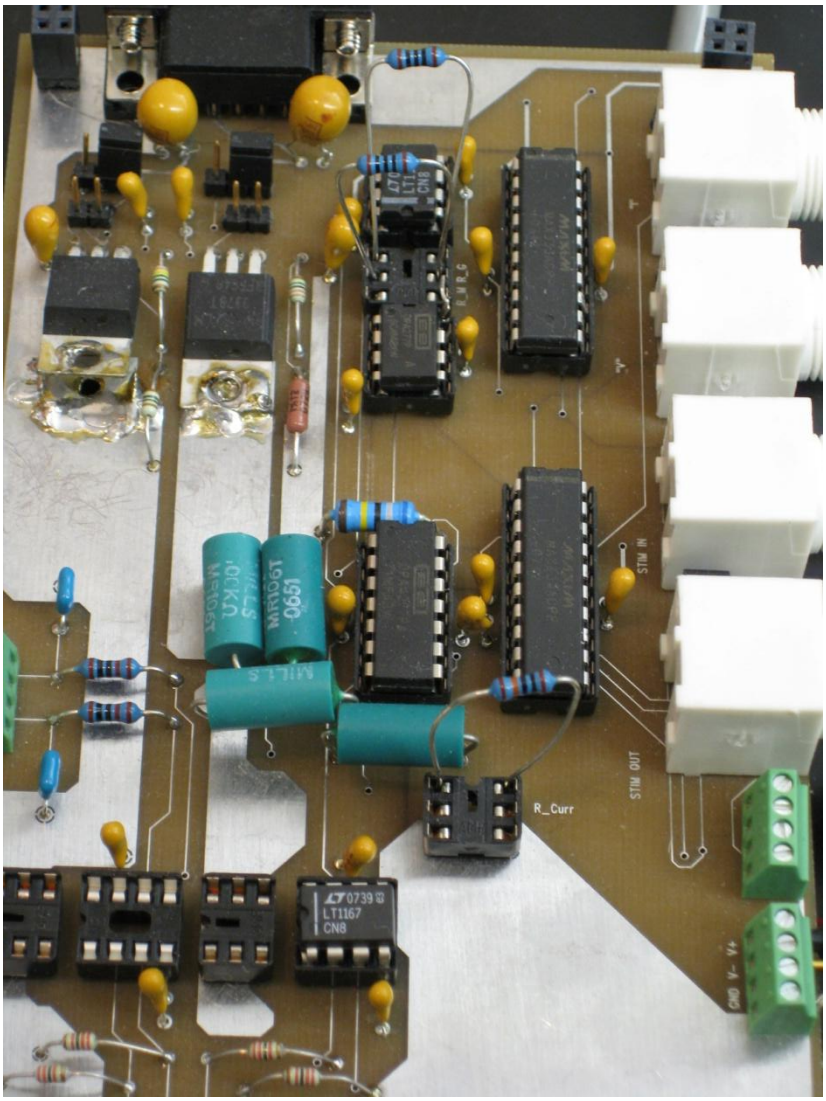

FIGURE B-17. Current and voltage-controlled stimulation resistors. The resistor R_curr (bottom) changes the voltage-to-current conversion factor. Resistors R_m and R_g (top) change the gain of the current monitor (output BNC "I").

Once the stimulator/power board is assembled, there are several customizable components.

- Voltage regulator jumpers (J1-J2): The power supply to the board must be ±5.5V or higher. Two 6V batteries will provide ±6V. If the power supply is ±8.5V or higher, you have the option of running the power supply through the power board's voltage regulators. This will bring the board's voltage down to ±6V (if R1-

4 are set as described in Figure B-15's legend), provide noise protection, and improve linearity of stimulation responses.

To set the board **to bypass the regulators**, leave J1 unpopulated, and set J2 to the lower setting (closer to the BNCs).

To **use the voltage regulators**, connect J1, and set J2 to the upper setting (further from the BNCs).

- Current-controlled stimulation: R_curr is used to divide the stimulator input voltage (from the stim-in BNC or screw terminal) into current for current-controlled stimulation. The equation is Ohm's law: I = V/R (e.g., 1V input → 1 μA when R_curr = 100 kΩ).
- Voltage-controlled stimulation: R_m and R_g determine the gain of "I" (the current-monitor) when delivering voltage-controlled stimulation. The gain of "I" is determined by the following equation: g = R_m x (1 + (49.4 kΩ/R_g)). Changing the values of these resistors can change the stability of the "I" monitor. These resistors have no effect on "I" during current-controlled stimulation.
- BNC shielding: The BNC stimulator inputs, outputs, and voltage and current monitors can be shielded. The jumper to the right of each BNC determines the shielding for that BNC. This has no effect if screw terminals are used.

  For no shielding, leave the jumper vacant.
  For driven shielding, set the jumper high (away from the connector's mating end).
  For grounded shielding, set the jumper low (toward the connector's mating end).

Recording Headstage Interface Board

The recording headstage interface board will be printed by PCBExpress with two recording headstage connectors attached. These should be separated from the main interface board with a band saw of similar tool.

Assemble the board (one for each 16-channel headstage) according to the pictures below. Some components can be changed to alter the function of the board, such as the filter resistors and capacitors.

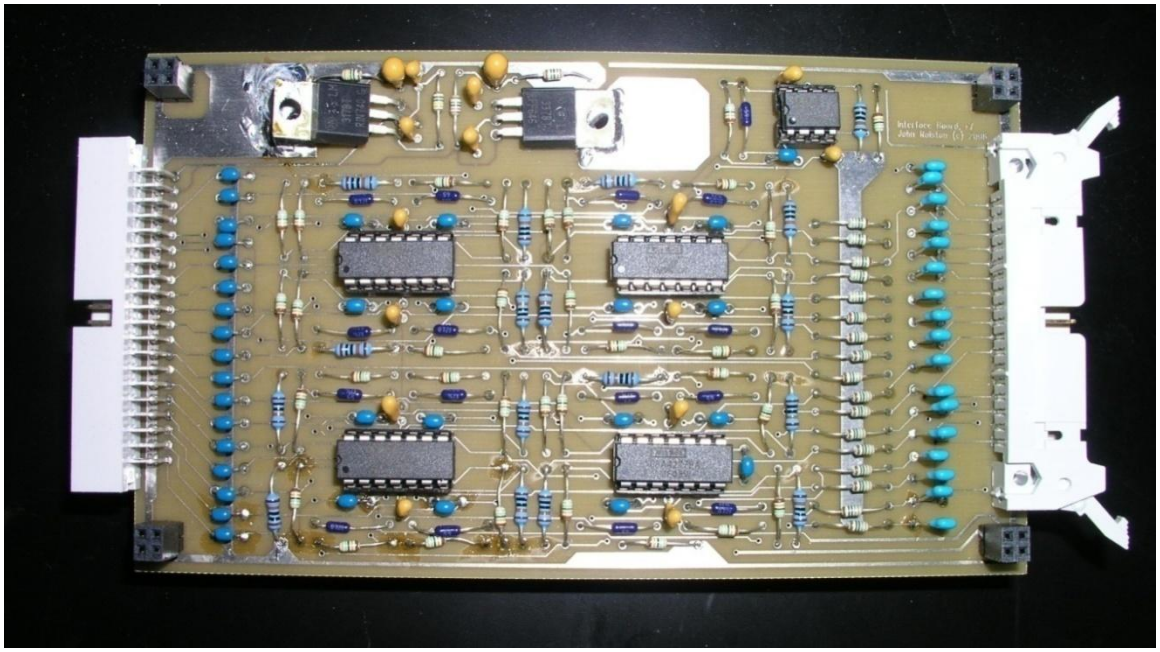

FIGURE B-18. Recording interface board.

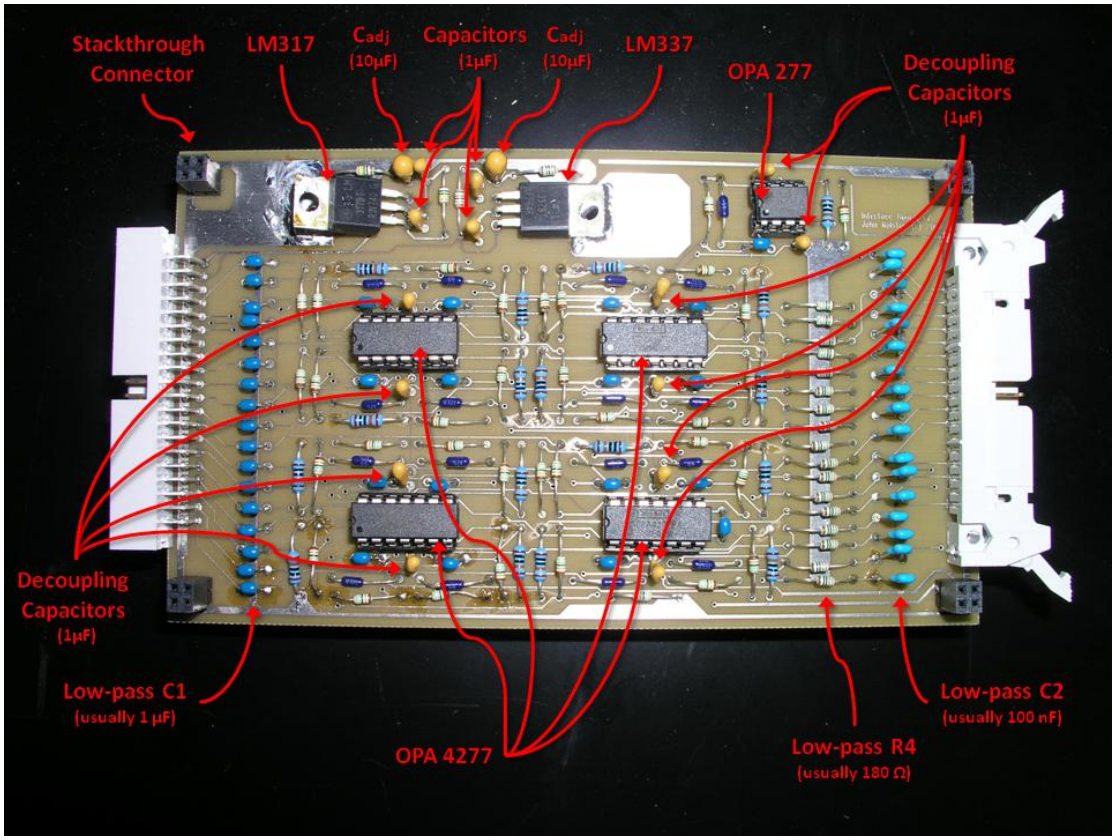

FIGURE B-19. Recording interface board components.

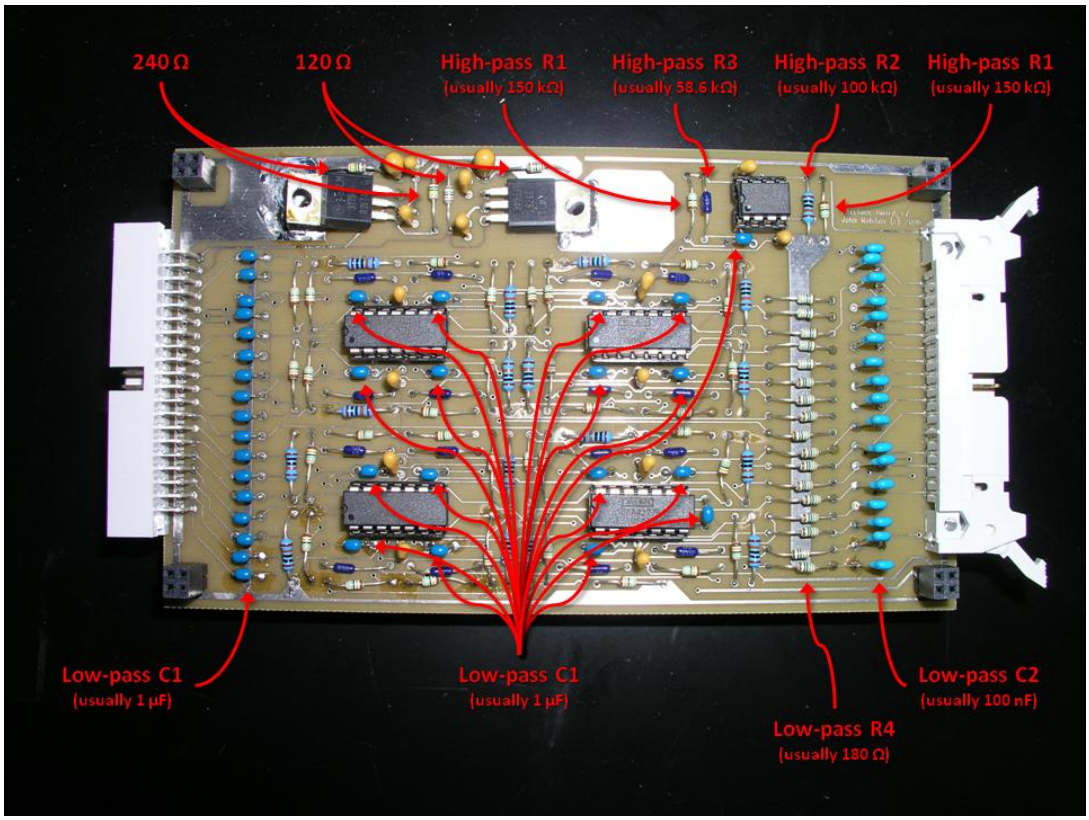

FIGURE B-20. Recording interface board filters. C1-2, R1-4 determine low and high-pass filters cut-offs of the interface board. The unlabelled resistors are R1, R2, or R3. Use the colors of the labeled R1-3 to determine the unlabeled resistor values.

Analog filters: The −3dB points of the low- and high-pass filters are determined by the standard equation $f_C = 1/(2\pi RC)$. The high-pass uses R1 and C1 in this equation, and the low-pass uses R4 and C2. For the values listed in the figure, the −3dB points of the system will be 1 Hz and 8840 Hz. These can be changed by replacing the appropriate resistors and capacitors. For example, if you wish to only record action potentials, and not LFPs, you could raise the −3dB point of the high-pass filter to 160 Hz: R1 = 1 kΩ and C1 = 1 µF.

Recording Headstage Cable

Use the connector boards separated from the recording headstage interface board to form the connectors for the recording headstage cable, as shown below. Do not connect GND BUF (buffered ground).

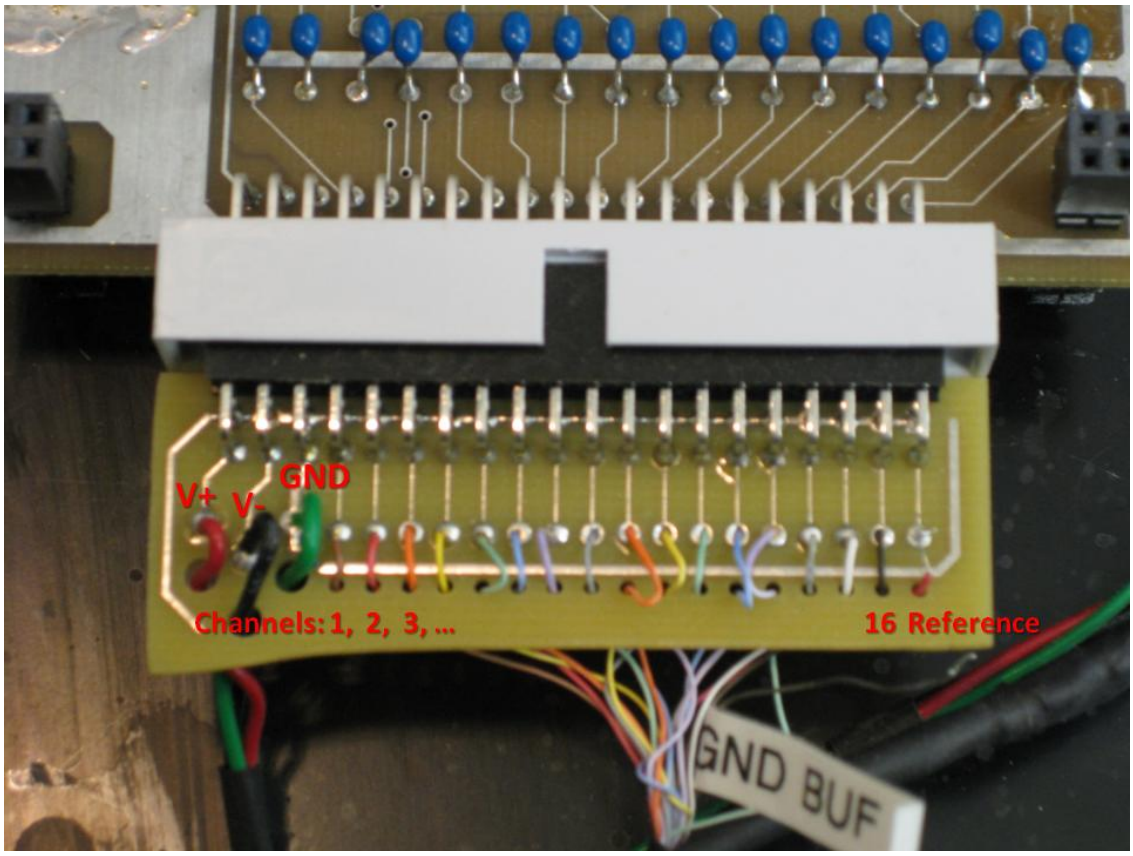

FIGURE B-21. Recording headstage cable.

In the picture above, the large red wire is +2.5V, the black is -2.5V, and the green is ground (TBSI should label these for you). The smaller wires are for the recording channels (channel 1 is left-most, 16 is the 2nd to last on the right). The right-most channel is the reference channel. This can be switched to GND BUF (buffered ground) if desired, though we find better signals when using a reference. To appropriately assign channels, you should request channel-color labels from Triangle Biosystems.

Alternatively, you can use a multimeter to determine conductance from the Omnetics connector end (that mates with the recording headstage) to the free ends (that will be soldered into custom PCB shown above).

Data Cables

For each headstage interface board, you will need one cable to carry data to the data acquisition cards. Add a rectangular header connector to one side (that will mate with the interface PCB), as shown below. The rectangular connector is of the IDC (insulation displacement connector) type, meaning that it pierces the ribbon cable's insulation when clamped down. The best way we've found for attaching these is with a vise, slowly tightening the vise until the connector is firmly "clicked" into place, having penetrated the insulation and made good electrical contact.

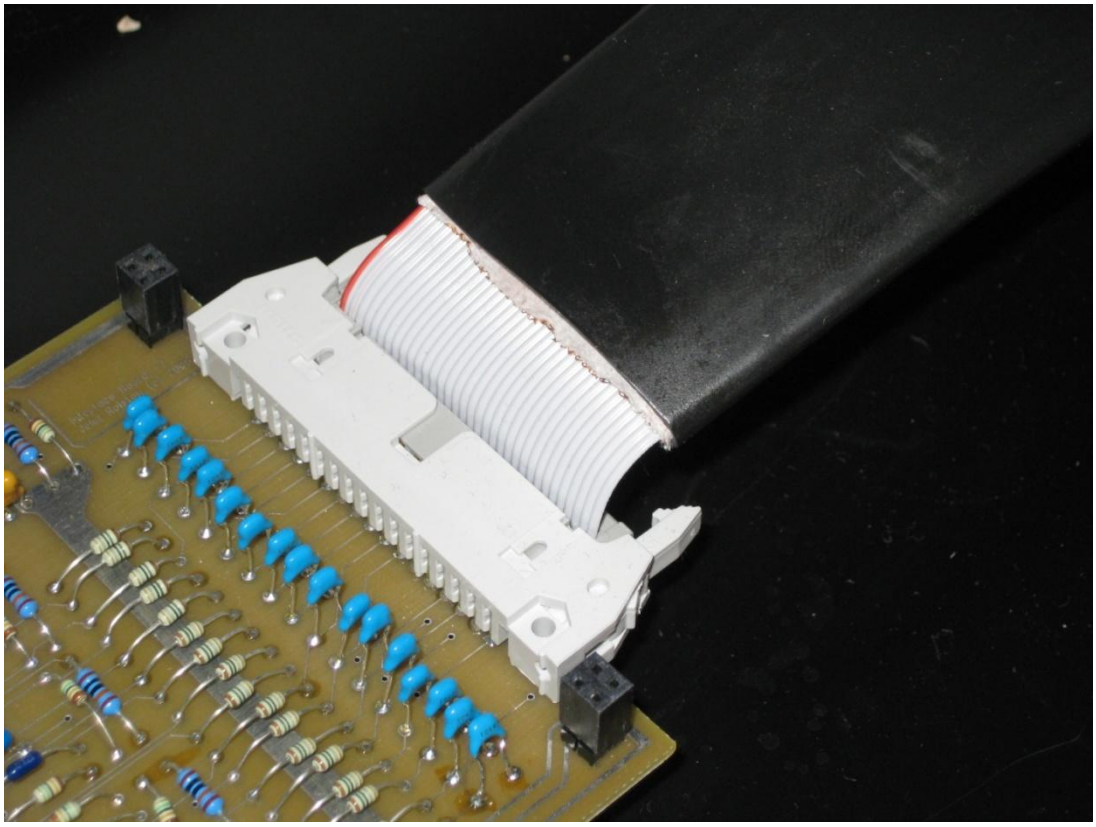

FIGURE B-22. Data cable.

The other end of the cable will connect with a National Instruments breakout box. This end of the data cable should have several inches of each wire separated out, to allow the wires to reach the appropriate terminals. The last 2-5 mm should be stripped.

In Vitro Interface Boards and Cables

The stimulator/power board is identical to that used in the *in vivo* setup, described above.

Connections

Connections to Breakout Boxes

The most intricate connections in the setup involve the National Instruments breakout boxes, for both stimulation and recording. These are described in detail here.

Recording (Analog Input)

For each 16-channel recording headstage (or each 16-channel cable of a 64-channel *in vitro* setup), one ribbon cable will interface with one National Instruments breakout box (SCB-68). Connect channels 1-16 of the recording boards to AI0-15 of the SCB-68. Connect the reference wire to AI SENSE. Repeat this for each additional breakout box (e.g., channels 17-32 will connect to AI16-31, channels 33-48 will connect to AI0-15 of a second A/D board). See *SCB-68 Quick Reference Labels* for more information on where to connect each wire. See picture below for an example connection.

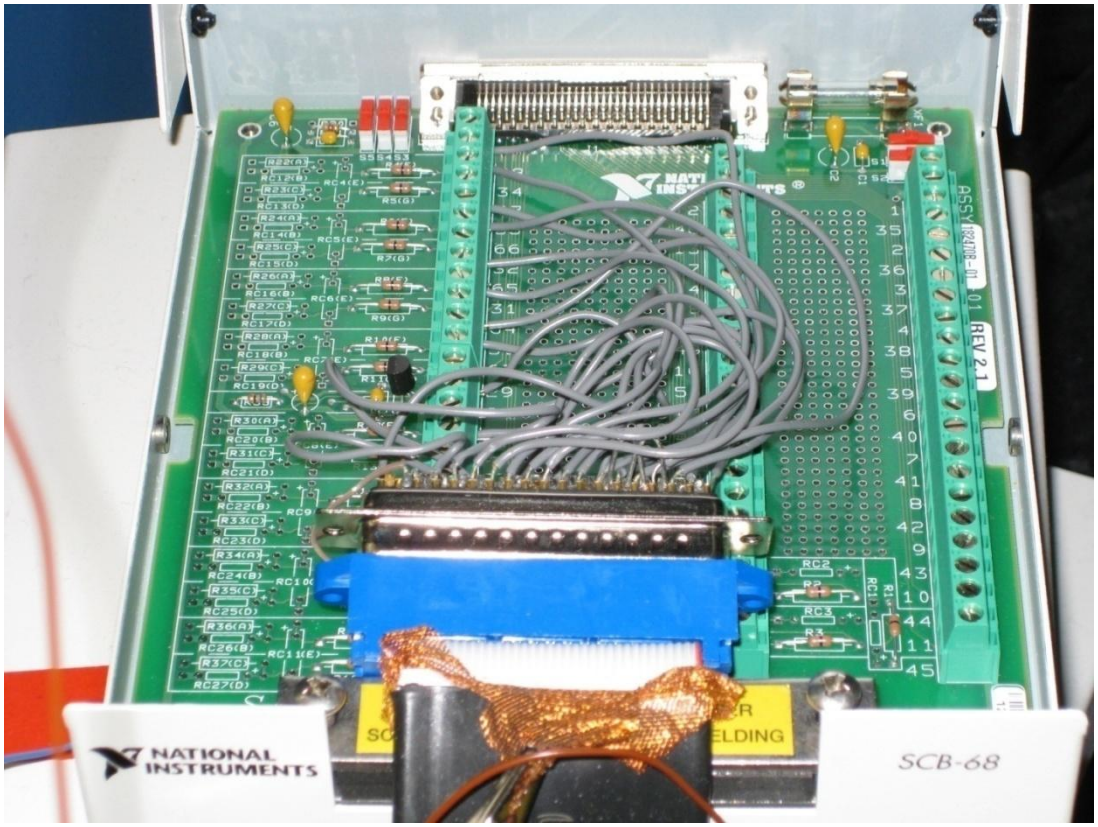

FIGURE B-23. Recording breakout box. [Note: We use additional connectors to convert the ribbon cable to free wires. This is not strictly necessary, and not described above.] Channels are connected to AI0-15 (recording headstage channels 1-16. The reference wire is connected to AI-SENSE. The copper shielding is connected to "central ground" with a short length of wire and alligator clips.

The shielding of this cable must be connected to ground to prevent noise. The preferred method is to connect the shield to the "central ground" of the system ("central ground" is discussed below).

Stimulator Output

The stimulator cable has wires for A0-3, EN, and V.Stim. Connect A0-3 to P0.8-11 (of the second connector block). Connect EN to P0.12. Connect V.Stim to AO 2.

You must also connect P0.7 to PFI 6/AO START TRIG (same PCI-6259 card, but the other breakout box). This allows the digital and analog parts of the stimulation pulses to be synchronized.

To monitor stimulation timing while recording and conduct closed-loop experiments, connect the stimulator SCB-68's AO 3 to the same SCB-68's AI16. Additionally, connect an AO GND to AI SENSE of the same breakout box. Lastly, in the same card's other breakout box, connect AO 0 to AI 0.

Stimulator power should be obtained from the stimulation/power interface board, via the voltage output screw terminals.

The stimulator power cable's line for current- vs. voltage-controlled stimulation should be connected to P1.0 of the "Cineplex" device (this device is labeled in software, and can be any of the recording boards).

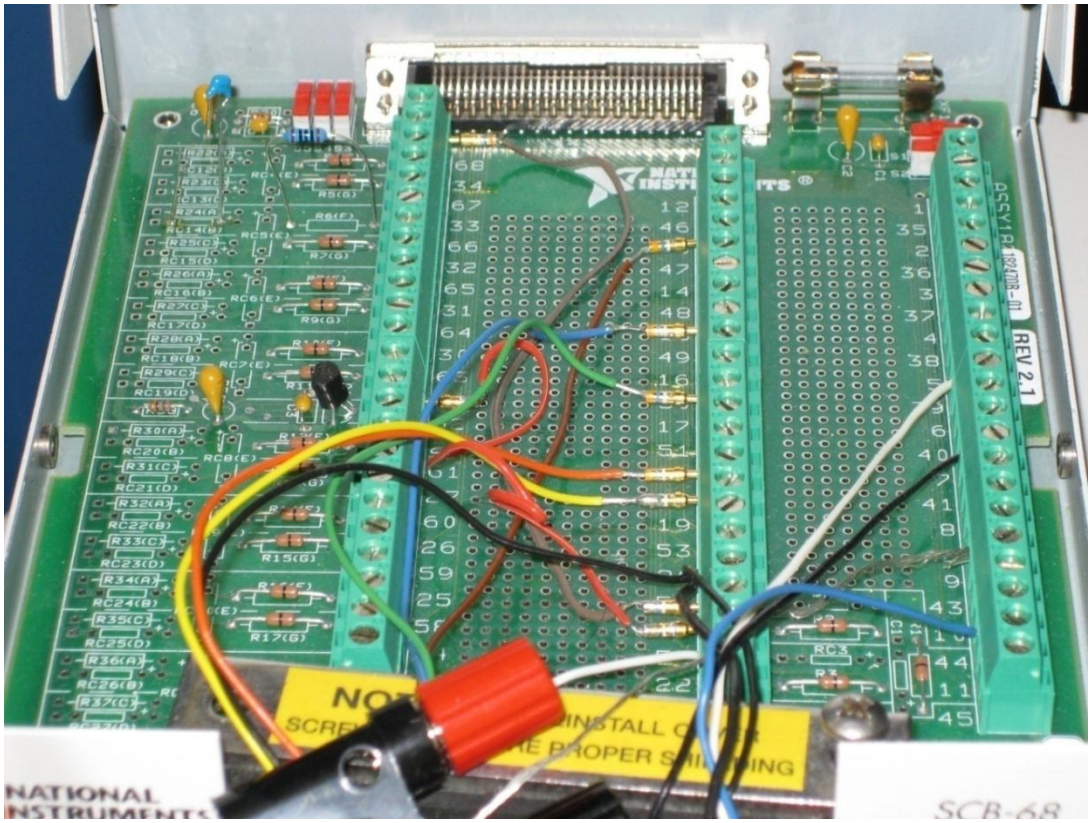

FIGURE B-24. Stimulator breakout box.

Stimulator Cable

The stimulator cable is actually 4-5 cables combined (see ❶ in the following figure). We hope to minimize the number of cables in future versions. One cable brings switching information from the PCI-6259 card to the headstage. A second cable brings the stimulation pulse from the PCI-6259 card to the stimulator/control interface board, where it is converted to a current-controlled pulse (if applicable), and current and voltage monitoring takes place. A third cable brings the stimulation output pulse from the interface board to the headstage. And a third cable brings power from the stimulator/power interface board to the stimulator headstage. Optionally (and we prefer this), some of these cables are bundled together prior to connecting to the headstage (see

❷ in the figure below). This provides a convenient bundling when using with a tethered animal. This optional connector can be built in many ways. The simplest would be to use two mating DB9 connectors, with solder cup terminals.

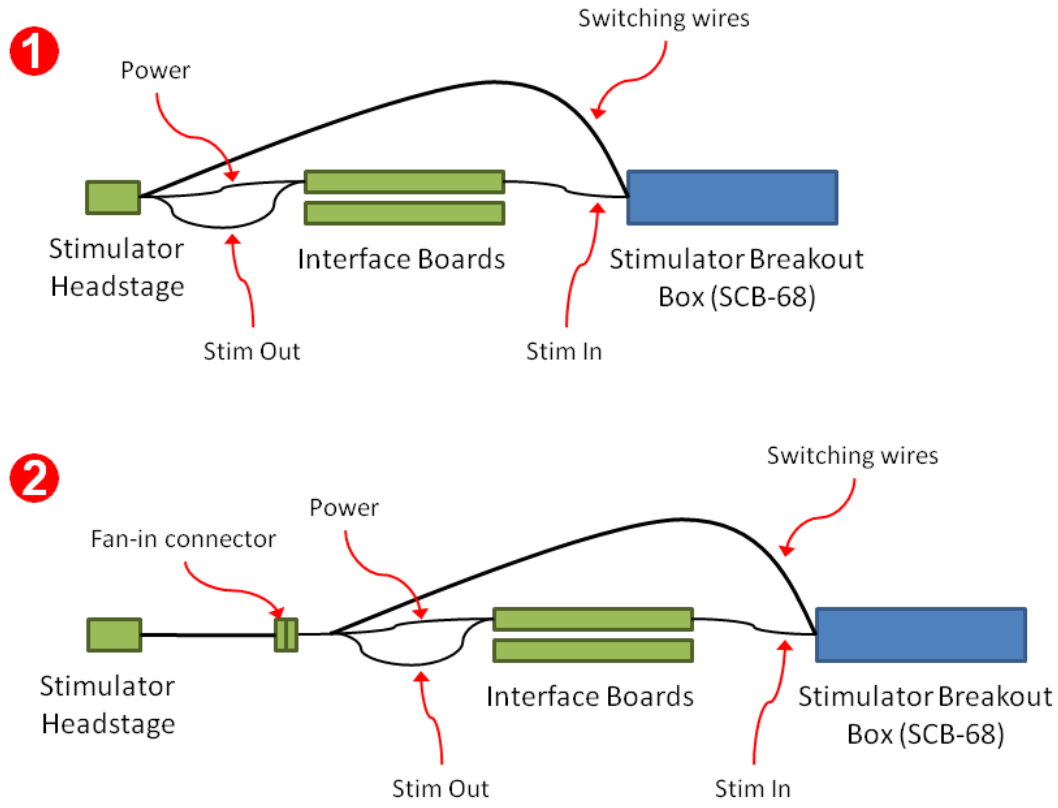

FIGURE B-25. Stimulator cable connections.

Connect the power wires into the stimulator/power interface board's power output screw terminals (to the far left of the BNCs). Connect the stimulator switching lines to the National Instruments breakout box, as described above (Stimulator Output). Connect the Stim In wire to the breakout box on one end, and the interface board's "Stim In" terminal on the other. Connect the Stim Out cable to the interface borad's "Stim Out" terminal on one end, and the headstage on the other.

Data Cable

Connect one end of the data cable to the recording headstage interface board. Connect the other into the National Instruments breakout box, as described above (Recording (Analog Input)).

Recording Headstage Cable

Connect one end of the cable (with the small Omnetics connector) into the recording headstage. Connect the other into the recording interface board (this uses the custom-made connector you assembled above).

Power Cable

Connect the +6V, -6V, and GND wires of the power cable to the battery supply, as described above (Power Supply). Connect the other end (with the DB9 connector) to the stimulator/power interface board. Lastly, connect the current- vs. voltage-controlled stimulation wire to P0.8 of the "Cineplex" data acquisition card's breakout box. The "Cineplex" card can be any card that is not already using digital output, such as one of the recording cards.

Impedance Measurement Cables

To measure impedances, information from the "I" and "V" BNC or strip terminals needs to be accessed by the NeuroRighter software. This is enabled by connecting the "V" terminal to channel ai2 of the "Impedance Device" (the NI-DAQ breakout box on which the impedances will be measured), and the "I" terminal to the "Impedance Device" channel ai3. The Impedance Device is specified in software by selecting File -> Hardware Settings and then selecting the "Miscellaneous" tab.

Grounding

This section is primarily concerned with grounding and noise. First, a brief outline of noise sources is presented. Second, a recommended grounding configuration is presented.

Sources of noise

One of the main sources of recording noise arises from improper grounding of the experimental preparation and equipment. This noise often manifests as a ripple at 60 Hz and its harmonics (120, 180, etc.). In Europe, this noise arises at 50 Hz and its harmonics. However, improper grounding can often lead to pickup of environmental noise at bizarre and unpredictable frequencies (1.25 kHz, 6 kHz, etc.). This noise comes from switching power supplies, monitors, lights, etc. Essentially, if there is a ground loop in the system, and these devices can find some electrical path to the recording equipment's ground (or grounds), they will leak power into the recording circuitry, and oscillations at these higher frequencies will be detected.

What is a ground loop? A ground loop occurs when there are multiple paths to ground for a particular piece of equipment (or, more generally, any wire or pin or trace of any circuit). Since all wires, traces, pins, etc. have a finite resistance and capacitance, they will all have different voltage offsets from "ground." Thus, if there are multiple paths to ground, and each "ground" has a different voltage offset, it is almost inevitable that one "ground" will have a higher voltage than another "ground." Because of this voltage difference, current will flow between the grounds. Another effect of ground loops, and loops in general, is that magnetic fields induce currents in closed circuits. Thus, any ground loop will amplify any radiated noise from nearby equipment.

A related source of noise results from electromagnetic induction (EMI). This affects any wire or trance of a circuit, basically forcing them to act like antennae for the electromagnetic radiation from nearby (and distant) devices. Longer wires (e.g., data cables, power cables) are especially sensitive. The best solution to this is "shield" the cable or traces. This involves surrounding the circuitry or wires with a conductive shell. This shell acts as a "Faraday cage," conducting most of the ambient radiation and protecting the inside of the shield.

Suggested Ground Configuration

Two steps should be taken to reduce noise:

1. All grounding should connect to the building/laboratory ground at only one point: what we term the "central ground"
2. All long wires and cables should be shielded, with the shield connected to ground.

Central Ground

To ensure that all grounds connect to a common point, we will first list the grounds of the system:

1. Computer
2. Monitor
3. Data acquisition cards
4. Breakout boxes
5. Power supply (batteries)
6. Interface boards
7. Recording headstage
8. Stimulation headstage

Our goal is to connect all devices to the building ground (third prong of a wall outlet) at one point. The monitor and computer both have three-pronged plugs and both require a connection to the building's main power supply. Therefore, they should both be connected to a shared surge protector, which is then connected to the wall outlet.

Data acquisition cards receive their ground from the computer (which is connected to a surge protector, then building ground). The breakout boxes receive their grounds from the data acquisition cards.

The power supply ground is floating, unless it is directly connected to another ground. To reduce recording noise, this should be connected to the common ground of the system. This common ground is (as we've seen from the analysis above) present in the breakout boxes. Therefore, the "ground" terminals of the power supply batteries should be connected to a ground terminal of a breakout box. We use AO GND of the stimulator board's breakout box.

The interface boards are grounded through the power supply, and the recording and stimulation headstages are grounded through the interface boards.

Cable shielding

All cables should be shielded, with their shields grounded to reduce noise. The three main cables of the system are the data cables, the power supply cable, and the stimulator cable. If the power supply cable's drain wire is soldered to the DB9 connector, as illustrated in the assembly section, then this shielding will be grounded whenever the cable is connected to the interface boards. For data cable shielding and stimulator cable shielding, we manually connect these to the "central ground" (AO GND of the stimulator board).

Appendix C

NeuroRighter User's Manual[18]

[18] A "living" version of this document can be found at http://sites.google.com/site/neurorighter/.

Overview

The NeuroRighter system has several configurations. The main two are the *in vivo* (❶ in the figure below) and *in vitro* setups (❷ in the figure below).

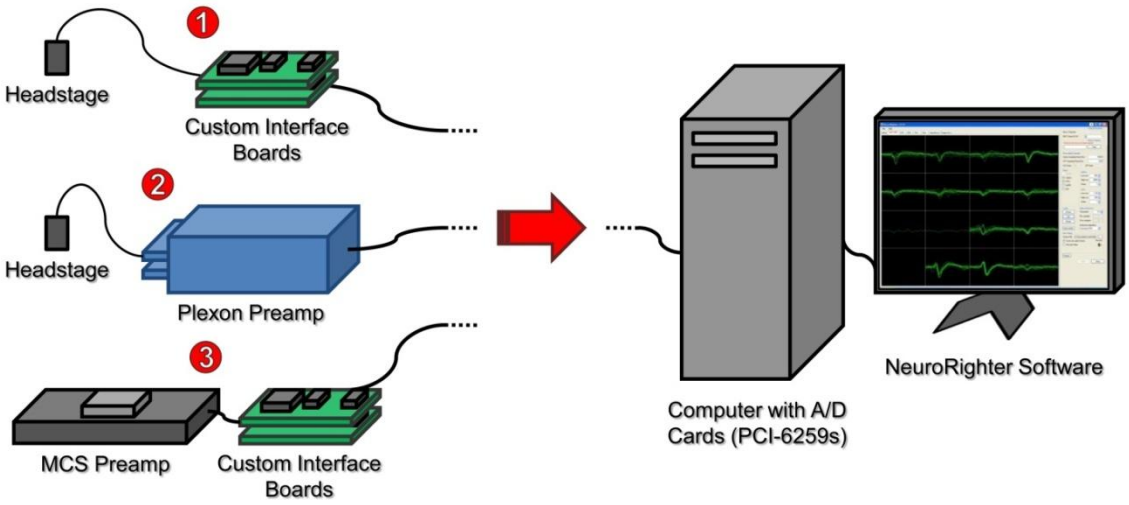

FIGURE C-1. Overview of NeuroRighter System. ❶ Shows the standard *in vivo* setup, with a Triangle Biosystems (TBSI) recording headstage, and custom interface boards. ❷ Shows a hybrid system using a Plexon headstage and preamplifier. ❸ Shows an *in vitro* hybrid system, using a preamp from MultiChannel Systems. All setups converge to a desktop computer with multiple data acquisition cards (National Instruments PCI-6259 or PCIe-6259).

In Vivo Setup

For recordings of awake, behaving animals, a lightweight recording headstage is used, connected to custom interface boards. The custom interface boards handle analog filtering, power conditioning, and stimulation control. The boards then interface with National Instruments data acquisition cards, installed in a standard desktop computer, running the NeuroRighter software.

In Vitro Setup

For recordings from neural or cardiac cultures, a MultiChannel Systems (MCS) preamplifier (http://www.multichannelsystems.com/) is connected to custom interface boards. These boards provide power conditioning, stimulation control, and convert the MCS cables to cables suitable for use with National Instruments data acquisition cards. The custom boards interface with a standard desktop computer, running the NeuroRighter software.

Preparing the System

Connections

Before initiating a recording, ensure that all cables are properly connected (see the NeuroRighter Construction Manual for details). This includes:

- Power cable from power supply to interface boards
- Recording cables:
    - Cable from recording headstage to interface board
    - Data cable from interface board to data acquisition card
- Stimulation cables
    - Stimulation input cable from National Instruments card to interface board
    - Stimulation switching control cable from National Instruments card to stimulator headstage
    - Stimulation output cable from interface board to stimulator headstage
    - Stimulator power cable from interface board to stimulator headstage
    - Current- vs. voltage-control cable from National Instruments card to interface board
- National Instruments cards
    - The breakout boxes should be connected with the PCI-6259 (or similar) cards
    - The National Instruments cards should be connected to each other with a RTSI cable

If using an *in vitro* system, ensure that the MCS preamp is connected to the recording interface board (via an MCS SCSI cable, see figure at right). This cable powers the preamp, and carries recorded signals to the interface boards. For an *in vitro* system, one stimulator module should be plugged into each of the preamp's four banks of headers (for a total of four modules; see image at right). Ensure that the 15th pin (for MCS MEAs) is grounded.

FIGURE C-2. MCS 68-pin SCSI cable. Connects the MCS preamp to the recording interface board.

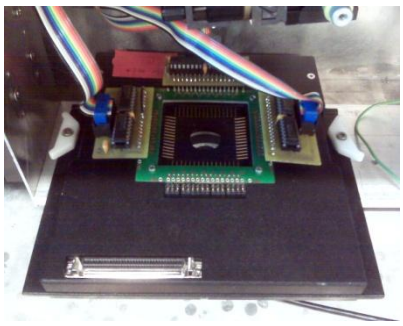

FIGURE C-3. MCS preamp with stimulator modules. The bottom module has been removed for clarity. The SCSI connector cables in not plugged in.

Power Supply

Ensure that the batteries are charged prior to system use. When the system is not in use, turn the power supply's toggle switch to "Off." When the system is ready to be used, switch the supply to "On."

IMPORTANT: It is good practice to have all headstages, preamps, etc. *connected* ***before*** *turning the power on*. Connecting or disconnecting components while powered can have unpredictable results.

Software

Ensure that the NeuroRighter software is installed on your desktop computer, the same computer with the National Instruments cards. The software can be downloaded at http://www.johnrolston.com/.

Software Installation

To install the NeuroRighter software, download the compressed archive from http://www.johnrolston.com/ (this is usually a ZIP file). Decompress the files to disk. Run the "setup.exe" file (not the MSI file). Follow the on-screen prompts.

Stimulation Hardware Settings

The stimulator board has three spaces for resistors: R_curr, R_m, and R_g. These resistors determine aspects of stimulation and impedance measurements. R_curr determines the voltage-to-current conversion factor for current-controlled stimulation. R_g and R_m determine the gain of the current monitor for voltage-controlled stimulation. R_curr must be present for current-controlled stimulation. R_m must be present for voltage-controlled stimulation. R_g is only necessary when monitoring "I" during voltage-controlled stimulation. See the picture below for the resistors' locations.

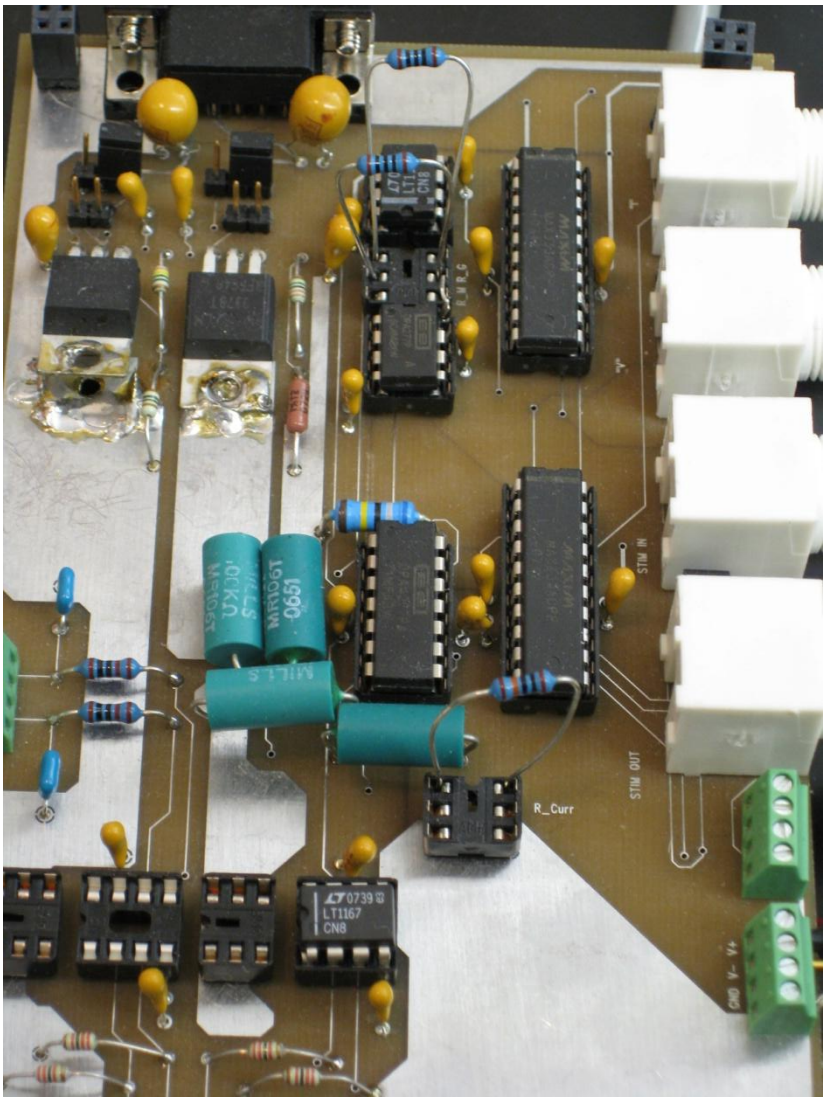

FIGURE C-4. Current and voltage-controlled stimulation resistors. The resistor R_curr (bottom) changes the voltage-to-current conversion factor. Resistors R_m and R_g (top) change the gain of the current monitor (output BNC "I").

R_curr

R_curr is used to divide the stimulator input voltage (from the stim-in BNC or screw terminal) into current for current-controlled stimulation. The equation is Ohm's law: I = V/R (e.g., 1V input → 1 μA when R_curr = 100 kΩ).

R_m and R_g

R_m and R_g determine the gain of "I" (the current-monitor) when delivering voltage-controlled stimulation. The gain of "I" is determined by the following equation: g = R_m x (1 + (49.4 kΩ/R_g)). Changing the values of these resistors can change the stability of the "I" monitor. These resistors have no effect on "I" during current-controlled stimulation.

Software Usage

FIGURE C-5. NeuroRighter Icon.

Starting NeuroRighter

NeuroRighter installs shortcuts in the user's Start Menu (in the NeuroRighter folder), as well as on the desktop. To start the program, double-click on the desktop icon (shown in figure at right).

You will be presented with a screen similar to Figure C-6.

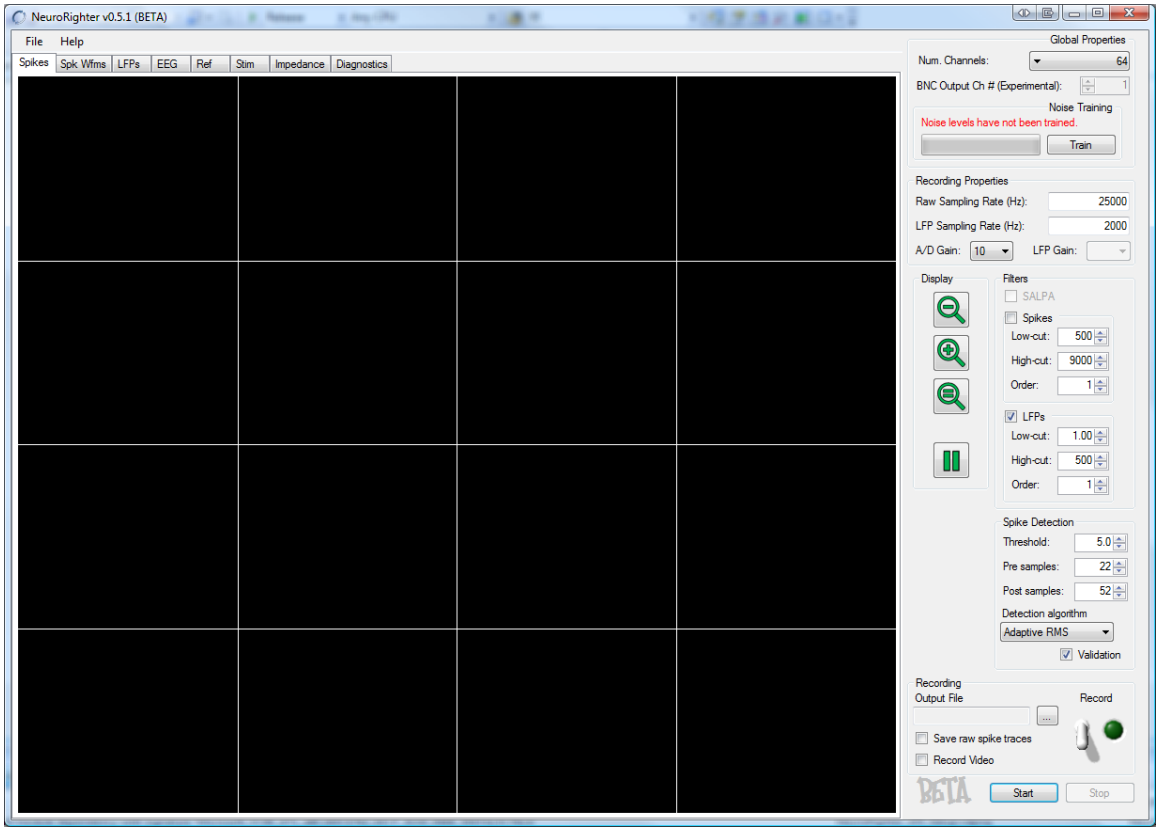

FIGURE C-6. Software screenshot.

Configuring Settings

There are three groups of settings, available by selecting the File Menu in the NeuroRighter software: Display Settings, Hardware Settings, and Processing Settings.

Display Settings

Clicking on “Display Settings” opens a dialog box, like that shown below.

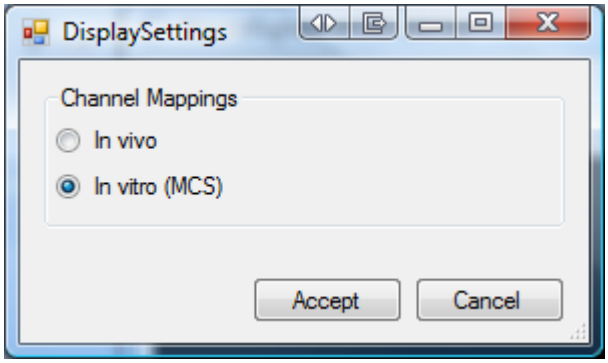

FIGURE C-7. Display settings.

There are two options: “In vivo” and “In vitro (MCS).”

In vivo

The in vivo setting maps channels 1-N (where N is the number of channels) in linear order. That is, channel 1 (the first analog channel recorded from the first National Instruments card) will be displayed in the first channel window of the software.

In vitro (MCS)

The in vitro setting maps channels as they would appear when looking down upon an MCS substrate integrated multi-electrode array.

Hardware Settings

Clicking on “Hardware Settings” opens a dialog box like the one shown below.

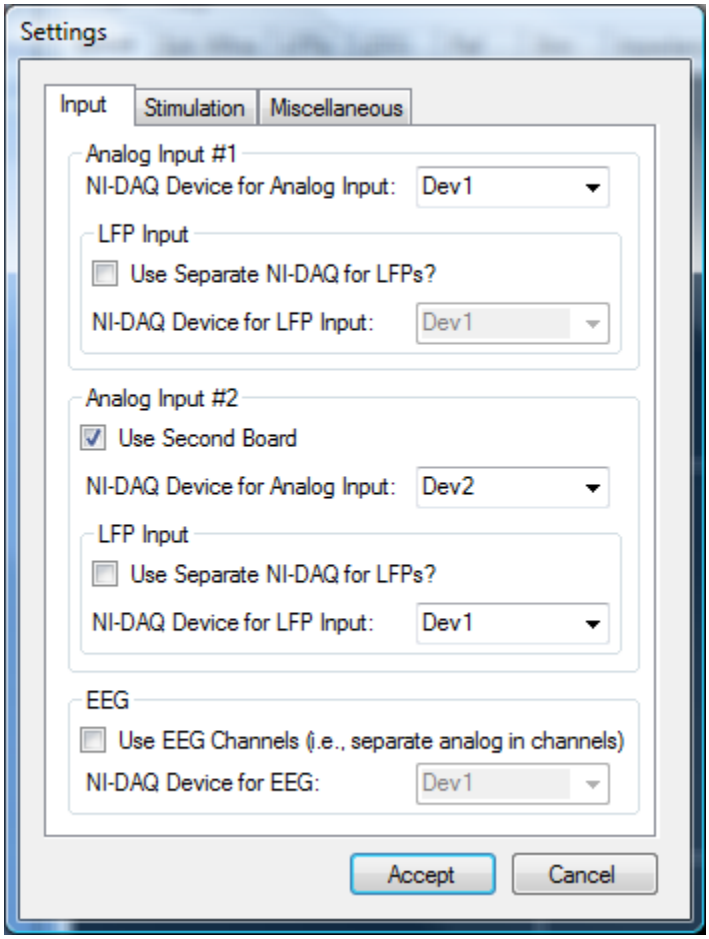

FIGURE C-8. Input settings.

There are three tabs, representing three types of settings: Input, Stimulation, and Miscellaneous.

Input

Here you select the National Instruments card (NI-DAQ) that will record the first 16-32 channels of analog data (e.g., Dev1, Dev3, etc.). All installed devices will automatically be listed as options. For more information on device numbering, see your National Instruments device's literature, or examine the Measurement and Automation tool, distributed with National Instruments data acquisition hardware.

If you use a second board for dedicated LFP acquisition (for example, if you are using a Plexon system, as in Figure 1, case ❷, above), check the appropriate box and choose the connected device.

If you are using multiple analog input boards for acquisition of raw/spike data (for example, if you are recording from 64 channels, or recording from a MultiChannel Systems preamp), you should select the "Use Second Board" option, and select the appropriate device.

If you are using the EEG functionality of the NeuroRighter system, select the "Use EEG Channels" checkbox and select the appropriate device.

Stimulation

An example of this dialog is shown below.

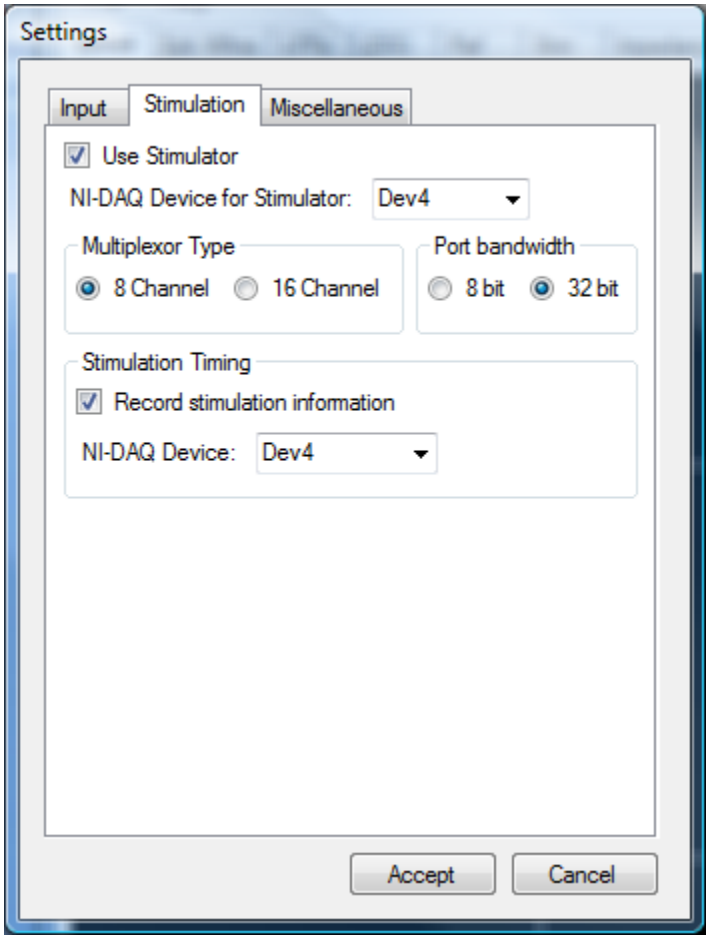

FIGURE C-9. Stimulation settings.

If you are using stimulation, select the checkbox, and then the appropriate device.

Multiplexor Type

You will also be required to select the multiplexor type of your stimulation modules or stimulation headstage. If you are using the *in vivo* stimulation headstage, you are using a 16-channel multiplexor. If you are using the stimulator modules for a MultiChannel Systems preamplifier, you are using 8-channel multiplexors. [These assignments might change in the future. To be absolutely certain which type of multiplexor you are using, look at the multiplexor's part number, and find its documentation online.]

Port Bandwidth

Depending on the type of National Instruments card you are using, you will select either an 8-bit port width or a 32-bit port width. If you are using a PCI-6259 or PCIe-6259 for stimulation, set the bandwidth to 32-bits. If you are using a PCI-6221, set the bandwidth to 8-bits.

Stimulation Timing

If you wish to record stimulation timing information synchronized to your experiment, you will need to check this box, and select the device on which this recording occurs. See the NeuroRighter Construction Manual for pin assignments (i.e., where to connect wires).

Miscellaneous

The miscellaneous tab appears as below.

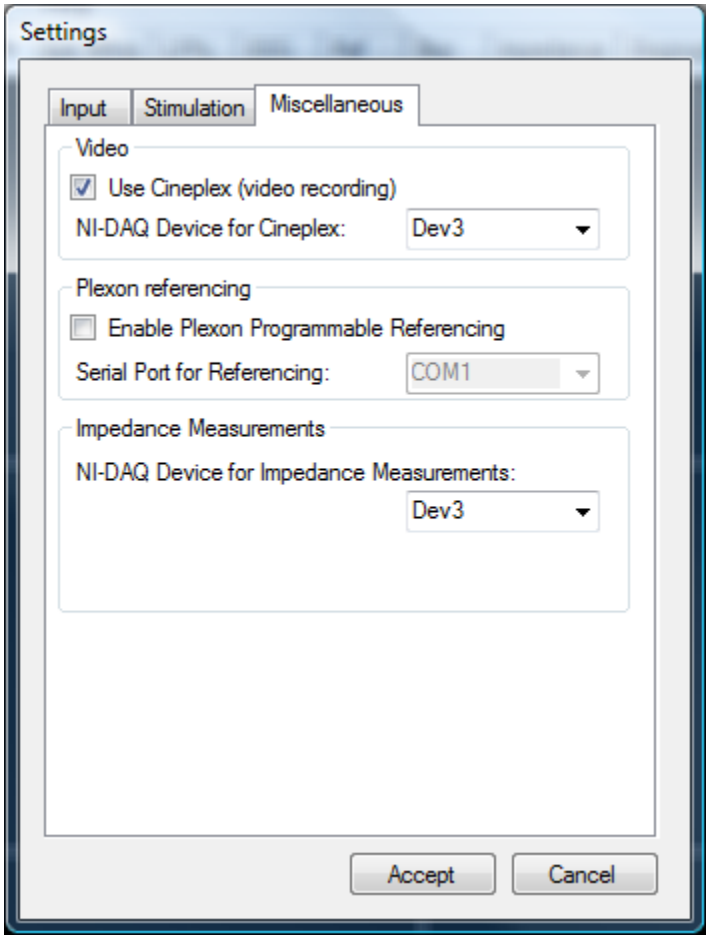

FIGURE C-10. Miscellaneous settings.

If you wish to use the NeuroRighter software to control a Cineplex camera system, check the appropriate box and select the correct device.

If you are using a Plexon preamplifier, and wish to control its programmable referencing through your serial port, check the "Enable Plexon Programmable Referencing" box, and select the appropriate serial port.

When conducting impedance measurements, select the device that is receiving the "V" and "I" outputs of the stimulation interface board (ai2 and ai3, respectively).

Processing Settings

Processing settings determine how data is handled after acquisition. There is currently only one setting, "Process LFPs." If this setting is enabled, LFPs are either acquired directly from an A/D card, or processed from the raw acquired data. If data is being recorded, LFPs will automatically be save to disk (see Recording below). If this setting is not enabled, LFPs will not be processed, graphed or saved in any circumstance. This can be useful to minimize computation and disk usage for recordings when LFPs are not desired. A sample of the Processing Settings dialog box is shown below.

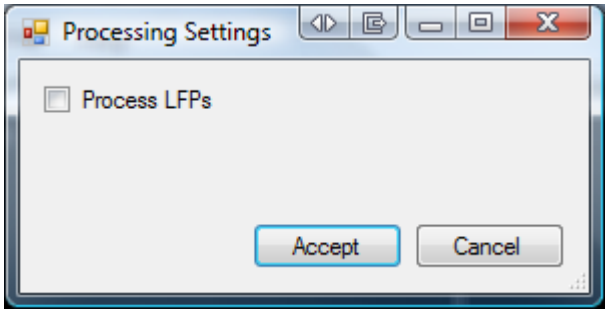

FIGURE C-11. Processing settings.

Acquiring Data

Before acquiring data, you should set experimental parameters.

1. Select the number of channels. NeuroRighter currently supports 16, 32, and 64 channel recordings.
2. Select the raw data's sampling rate and LFP sampling rates. *Note: If not using a separate card for LFP recording, the LFP signals are created by filtering and downsampling the raw data. The new signals are downsampled to the specified LFP sampling rate.* This has no effect if "Processing LFPs" is not enabled (see Processing Settings above).
3. Select the A/D gain for analog input. This is a multiplier that determines the range and resolution of your analog data acquisition. The PCI-6259, for instance, has a maximum range of ±10 V and a resolution of 16 bits. If the A/D gain is 1, the full voltage range is used, and the 16 bits are allocated to this full range. If the A/D gain is 2, the voltage range is reduced by half to ±5 V, but the 16 bit

resolution is now allocated to this smaller voltage range, increasing the acquisition's precision.

Important: You want to choose a range that will prevent clipping. If the input exceeds the voltage range, the data "clips" and the signals are lost for the duration of the clipping. You want to find a good balance between minimizing clipping, and having as high a resolution as possible. Fortunately, 16-bit resolution provides very high voltage resolution even at low gains. So an A/D gain of 2 or even 1 will easily resolve action potentials.

4. If you plan to record the acquired data to disk, configure recording options now: select an output file and set the toggle switch to record (this will illuminate the recording "LED"). You can optionally elect to record video data (with an attached Cineplex system) and write all of the raw data to disk (by checking the "save raw spike traces" box). Writing data to file is covered in more detail below.

When your parameters are configured, press the **Start** button to begin acquiring data. [The power supply should have been turned on at this point, or else only noise will be recorded. The software, however, can run whether or not the hardware is powered.]

Recording

NeuroRighter saves 4 types of files: raw, spike waveform, LFP, and stimulation. Not all files are written for all recordings. The types are determined by the user. Files are only saved if the recording toggle switch is "up." When recordings are occurring, the recording "LED" will flash between green and red.

Raw files

Raw files are not saved by default. To save raw files, ensure that the "Save raw spike traces" box is checked (bottom right of software window). Raw files include every sample of data recorded. The saved data is not filtered, regardless of what filters you have set for visualization or spike detection.

Spike Waveform files

Spike waveform files include information on all spikes detected. The time of the spike, the channel it occurred on, and a number of samples before and after the spike threshold crossing are stored. The number of samples is determined by the "Pre samples" and "Post samples" controls. The default is 22 samples before and 52 after the threshold, giving 75 samples per waveform (22 pre + 1 triggering sample + 52 post).

LFP files

LFP files are currently saved by default. These files contain the filtered and downsampled data that is visualized in the LFP graph. LFPs are not saved if "Processing LFPs" is not enabled (see Processing Settings above).

Stimulation files

These files record information about the stimulation that occurred during an experiment. For each stimulation pulse, the time, channel, voltage, and pulse width are recorded.

Controls

There are several ways to interact with the acquired data while it's being visualized or before the recording has begun. Below are descriptions of these controls.

Noise Training

The SALPA filter (Wagenaar, D. A. and S. M. Potter (2002). "Real-time multi-channel stimulus artifact suppression by local curve fitting." J. Neurosci. Methods 120: 113-120) requires an estimate of recording noise before filtering. By pressing the "Train" button, before recording, NeuroRighter records 3 seconds of data to determine noise levels on all

channels. Once the training is complete, the SALPA checkbox in the filters section becomes selectable.

Display

When a recording begins, the visual display of data shows the A/D card's full range (factoring in the A/D gain). For instance, with an A/D gain of 10, each channel will have a vertical range of ±1 V (assuming a ±10 V card, like the PCI-6259). By clicking the magnifying glass with a "+" inside, the range is halved. Each click of the magnifying glass increases the visual gain by another factor of 2. Similarly, clicking the magnifying glass with a "-" increases the range by a factor of 2. The magnifying glass with a "=" inside returns the display to the default visual gain.

There is also a pause button ("||"). This button freezes the display.

Filters

There are currently three filters that can be used while acquiring data: SALPA, spikes, and LFPs.

SALPA

The SALPA filter (Wagenaar, D. A. and S. M. Potter (2002). "Real-time multi-channel stimulus artifact suppression by local curve fitting." J. Neurosci. Methods 120: 113-120) removes stimulation artifacts from the raw data, allowing better visualization of action potentials. To select this filter, noise levels must have been trained prior to beginning the recording (i.e., before pressing "Start").

Spikes

The "spikes" filter is a Butterworth bandpass filter with -3 dB points specified in the "Low-cut" and "High-cut" boxes. The number of poles is also selectable. This filtering takes place after the SALPA filter, if applied.

LFPs

LFP signals can be acquired in one of two ways:

1. derived from the raw analog input channels, then filtered and downsampled, or
2. directly acquired from a dedicated analog input A/D card (as in scenario ❷ of figure 1 above).

In the first case, the LFP filter (Butterworth bandpass with cut-offs specified in the "Low-cut" and "High-cut" boxes) is applied to the raw acquired data, then downsampled to a frequency specified in the "LFP Sampling Rate (Hz)" box. It is strongly recommended that a filter always be used when downsampling LFPs in this manner.

In the second case, the data is acquired at the frequency specified in the "LFP Sampling Rate (Hz)" box, then filtered according to the characteristics of the LFP filter.

This has no effect if "Processing LFPs" is not enabled (see Processing Settings above).

Spike Detection

Spike detection is the process of finding candidate action potentials from raw data. No method currently available is 100% specific and 100% sensitive—there will always be false positives and false negatives in a practical experimental setup.

In the NeuroRighter software, spikes are detected by first calculating an estimate of the noise level for each channel, σ. A threshold is calculated from this number using the entry, *T*, in the "Threshold" box. Any time the acquired data crosses this threshold, *T*σ, a

spike is detected. The threshold is symmetric, meaning that samples greater than $T\sigma$ and less than $-T\sigma$ all trigger spike detection. An typical value of T is 5.

There are four methods for spike detection currently implemented in NeuroRighter: Adapative RMS, Fixed RMS, Median, and LimAda.

Fixed RMS

This method computes σ as the root-mean-squared value of the samples within the first 40 ms of data acquisition.

Adaptive RMS

With adaptive RMS, σ is computed as the root-mean-squared value of the last 250 ms of acquired data. The window is updated every 10 ms.

Median

Here, σ is computed as the median of the absolute value of the data in the last 250 ms. This is an adaptive method. The 250 ms is updated every 10 ms.

LimAda

This method is identical to that used by Daniel Wagenaar's MEABench software: http://www.its.caltech.edu/~daw/meabench/. See his documentation for details. **This method has not been thoroughly tested**, as have the previous three.

Referencing

Digital and analog referencing of channels can be set through the "Ref" tab, as shown below.

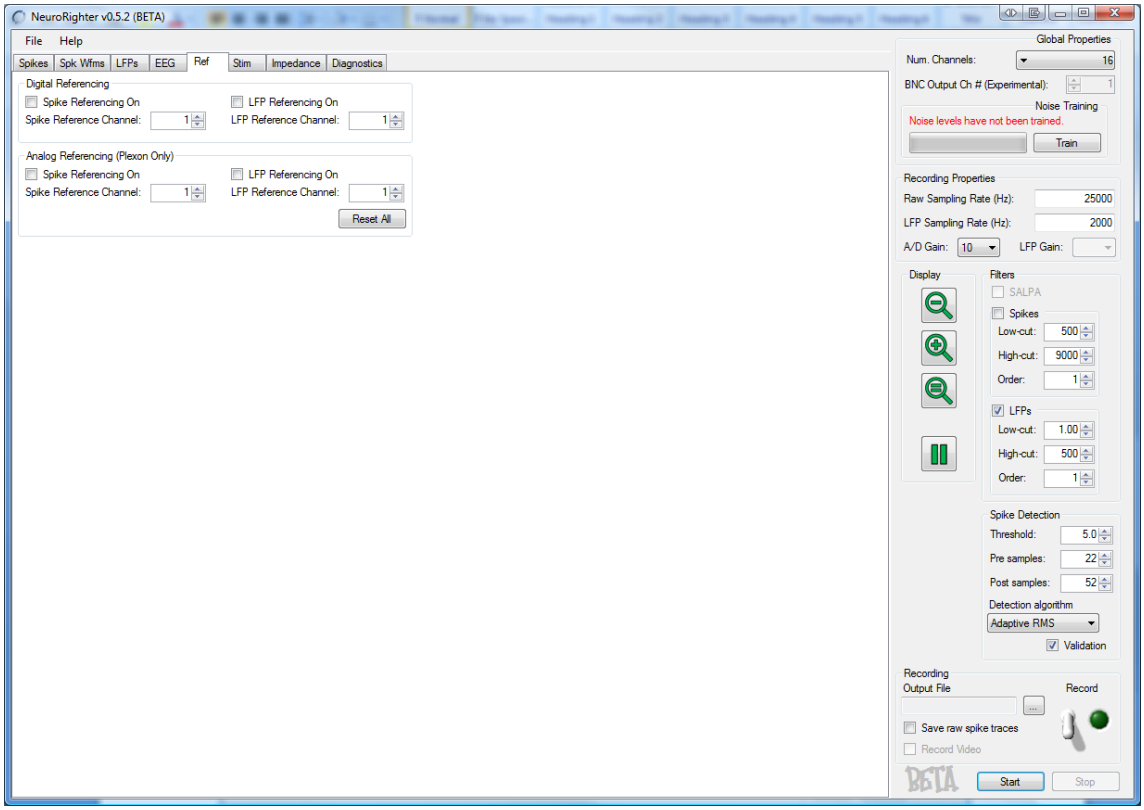

FIGURE C-12. Referencing tab.

Digital Referencing

Selecting "Spike Referencing On" will digitally subtract the selected channel from all other channels. This can be useful when dealing with movement artifacts or related correlated noise. This has no effect on the LFP channels, nor data saved with the "Save raw spike traces" command. It will affect the data sent to the spike detection algorithms.

Selecting "LFP Referencing On" accomplishes identical referencing for the LFP channels.

Analog Referencing

If a Plexon preamp is being used, analog referencing can be controlled similarly to digital referencing.

Stimulation

Before stimulating, ensure the stimulation modules are properly connected (see NeuroRighter Construction Manual and Stimulation Hardware Settings above).

Stimulation commands are available in the "Stim" tab in the NeuroRighter application. Before stimulating, set the "Global Parameters." Then choose a type of stimulation, set parameters for that type, and start stimulation. Available stimulation modalities are:

- On Demand (single pulses or brief trains),
- Open Loop (continuous stimulation delivered in pseudo-random fashion)
- Electrode Screening (cycles randomly through a selection of stimulation parameters)
- Electrolesioning (sends "DC" current for a given length of time, useful for electrocoagulation)
- IIS Zapper (an experimental closed-loop application that stimulates when an interictal spike is detected on an LFP channel)
- Closed-loop Learning (an experimental closed-loop application mimicking the experiment of Bakkum, Chao, and Potter 2008)

A screenshot of the interface follows. Settings for each stimulation type are described below.

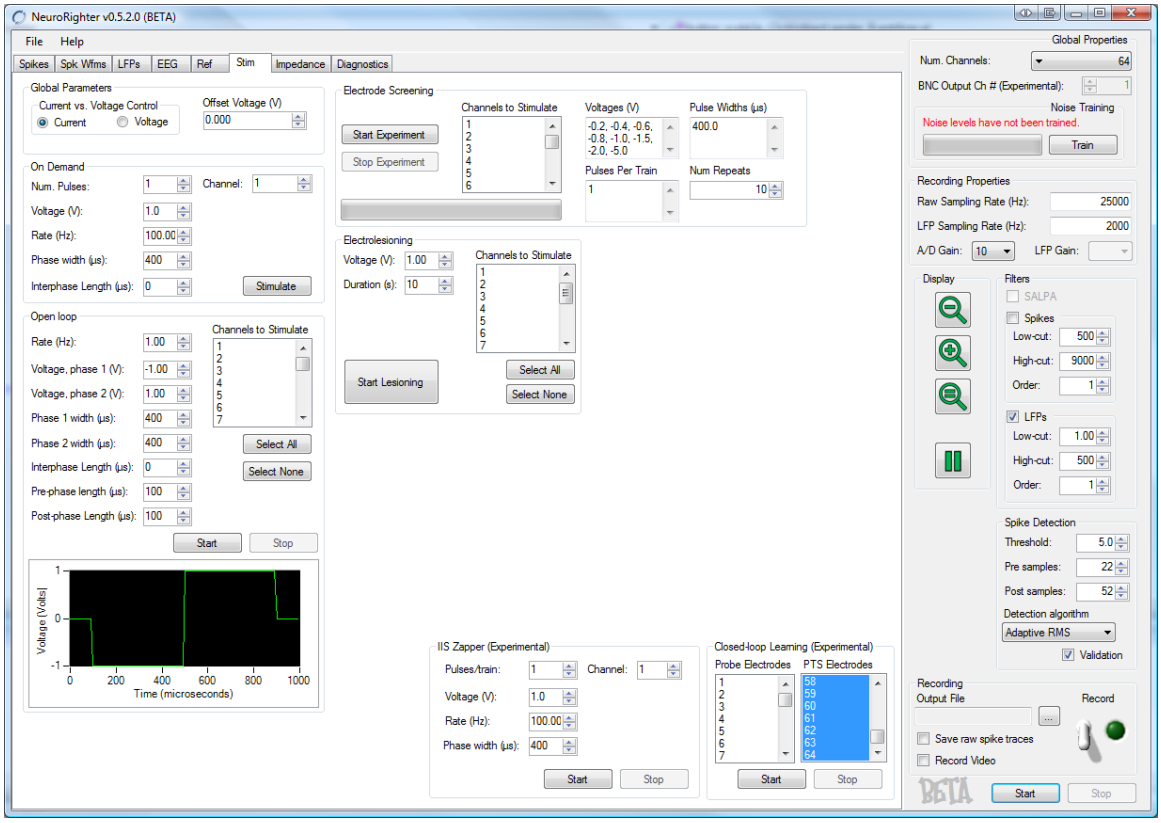

FIGURE C-13. Stimulation tab.

Global Parameters

These parameters affect all stimulation types.

Current vs. Voltage Control

This setting determines whether stimulation is voltage- or current-controlled. The current for current-controlled stimulation is specified as a voltage, and delivered as a voltage by a National Instruments D/A output. This voltage is then converted to current on the stimulation/power interface board through the resistor R_curr (see Stimulation Hardware Settings above). So, to deliver a 10 µA pulse, for example, you would deliver a 1 V pulse with R_curr = 100 kΩ.

Offset Voltage

The offset voltage is added to the entire stimulation waveform. This can be used to account for offsets induced by the electrode's electrochemical shift, or to provide a constant bias current.

On Demand

On demand stimulation provides à la carte stimulation pulses or pulse trains. All pulses are biphasic with phase widths of equal length. The specified voltage is for the first phase, and the second phase is the negative of the first phase (e.g., if the first phase is 1V, the second will be -1V).

Num Pulses

This specifies the number of pulses or pulse trains that will be delivered.

Voltage

This specifies the voltage of the first phase of the biphasic stimulation pulse. The second phase is the negative of this voltage (e.g., if the first phase is 1V, the second will be -1V). If stimulation is current-controlled, this voltage determines the current, after accounting for the voltage-to-current conversion resistor.

Rate

This determines the stimulation rate at which multiple pulses are given. This has no effect if the number of pulses is equal to one.

Phase Width

The phase width is the length of time for each phase of the biphasic stimulus pulse. For example, if the phase width is 400 μs, the total pulse will be 800 μs (400 for each of the two phases).

Interphase Length

A brief period where the stimulation voltage is set to 0 V (or 0 A) can be inserted between the two phases of the biphasic stimulation pulse. This has been suggested by some authors to reduce tissue damage or provide different excitatory effects (e.g., see Merrill DR, Bikson M, Jefferys JG 2005). If the offset voltage is non-zero, the interphase voltage will equal the offset.

Channel

The electrode on which the stimulation is delivered is specified in the "Channel" box. [For curious computer scientists this is 1-based, not 0-based.]

Open Loop

Stimulation is delivered in a pseudorandom order from the specified set of electrodes. The aggregate stimulation rate determines the time between pulses (e.g., if the rate is 100 Hz, and 10 electrodes are selected, each electrode will be asynchronously stimulated at 10 Hz).

Rate

The selected set of electrodes is stimulated asynchronously at the specified rate (e.g., if the rate is 100 Hz, and 10 electrodes are selected, each electrode will be asynchronously stimulated at 10 Hz).

Voltage

The voltage (or current) of each phase of the biphasic stimulation pulse can be set independently. If stimulation is current-controlled, this voltage determines the current, after accounting for the voltage-to-current conversion resistor.

Phase Width

The phase width is the length of time for each phase of the biphasic stimulus pulse. The two phases can be determined independently. For example, if the phase width is 400 μs, the total pulse will be 800 μs (400 for each of the two phases).

Interphase Length

A brief period where the stimulation voltage is set to 0 V (or 0 A) can be inserted between the two phases of the biphasic stimulation pulse. This has been suggested by some authors to reduce tissue damage or provide different excitatory effects (e.g., see Merrill DR, Bikson M, Jefferys JG 2005). If the offset voltage is non-zero, the interphase voltage will equal the offset.

Pre and Post Phase Length

A brief period where the stimulation voltage is set to 0V (or 0A) is usually present at the beginning and end of each pulse. In our experience, this helps control stimulation artifacts. If the offset voltage is non-zero, the pre and post-phase voltage will equal the offset.

Channels

The set of channels to stimulate is determined before beginning the open-loop stimulation experiment. The number of selected channels can be 1 to *N*, where *N* is the number of available channels.

Electrode Screening

The electrode screening experiment cycles through a selected set of stimulation parameters on a set of electrodes in a random ordering. Each selected electrode will be stimulated with all possible permutations of stimulation parameters. Each permutation will be delivered the specified number of times (the “Num repeats” box), again in a

random order. The randomization of ordering minimizes habituation effects between stimulation pulses. The rate of stimulation is 1 Hz (i.e., one permutation on one electrode every second).

Channels

The set of channels to stimulate is specified here. 1-*N* channels can be selected, where *N* is the total number of electrodes.

Voltages

The specified voltage determines the amplitude of the biphasic stimulation pulse. The given number is the amplitude of the first phase, and the second phase is the negative of this voltage (e.g., if the first phase is 1V, the second will be -1V). If stimulation is current-controlled, this voltage determines the current, after accounting for the voltage-to-current conversion resistor. Multiple values should be separated by commas, spaces, tabs, newlines, or colons.

Pulses per Train

Pulse trains can be delivered in addition to single pulses. If a value of "1" is provided here, single pulses are delivered. If larger numbers are specified, then a rapid train of pulses is delivered, at a rate of 200 Hz (5 ms between pulses). Multiple values should be separated by commas, spaces, tabs, newlines, or colons.

Pulse Widths

The phase width is the length of time for each phase of the biphasic stimulus pulse. For example, if the phase width is 400 μs, the total pulse will be 800 μs (400 for each of the two phases). Multiple values should be separated by commas, spaces, tabs, newlines, or colons.

Num Repeats
The number of times each permutation is presented is specified here.

Electrolesioning

To localize electrode tips for histology, it is often suggested to deliver direct current (DC) stimulation prior to animal perfusion. This component of NeuroRighter allows this to be done easily.

Voltage
The voltage of the electrode for the duration of the stimulation is specified here. If stimulation is current-controlled, this voltage determines the current, after accounting for the voltage-to-current conversion resistor.

Duration
The duration for which the voltage is provided for each electrode is specified here. Typical values are in the 1-30 second range.

Channels to Stimulate
The set of channels to lesion is specified here. 1-*N* channels can be selected, where *N* is the total number of electrodes.

IIS Zapper

This is an experimental closed-loop application. Please review the code thoroughly before using, and ask the author, John Rolston (rolston2@gmail.com), for help. This application has not been thoroughly tested (though it has worked for the code's author on several occasions). **Important: data acquisition should be started prior to the closed-loop experiment.**

Closed-loop Learning

This is an experimental closed-loop application, based on the paper by Bakkum DJ, Chao Z, and Potter SM (2008). Please review the code thoroughly before using, and ask the author, John Rolston (rolston2@gmail.com), for help. This application has not been thoroughly tested. **Important: data acquisition should be started prior to the closed-loop experiment.**

Impedance Measurements

NeuroRighter is capable of measuring impedance spectra in real time, using the stimulator and its current- or voltage-monitoring outputs. The essential idea is that, if a voltage-controlled sine wave us used to stimulate an electrode, the monitored current can be used to calculated electrode impedance at the sine wave's frequency. This is also true when using current-controlled sine waves and monitoring the delivered voltage.

The results are presented in a table (under "Results") and depicted graphically in a plot. Clicking "Copy Data to Clipboard" copies the contents of the "Results" box to the clipboard. Clicking "Save Data as Matlab MAT File" saves the data in MAT format (useful for later analysis in Matlab).

Before taking impedance measurements, ensure that the "V" and "I" terminals of the stimulator interface board (either BNC or screw terminals) are connected to the Impedance Device's ai2 and ai3 inputs, respectively (see the NeuroRighter Construction Manual for more details). The Impedance Device is specified File -> Hardware Settings under the "Miscellaneous" tab.

Important: Impedance measurements are difficult for a number of reasons. ***First, impedance values range over several orders of magnitude.*** Therefore, some measurements will be very small, and likely buried in noise. Other measurements will be very large, and clip at the power supply rails. **It is therefore strongly recommended that the actual data be monitored first with an oscilloscope before relying on the computed values.** An oscilloscope can be used by hooking up the appropriate BNC outputs, and executing an impedance measurement. As an example, take a current-controlled measurement of impedance. What's measured is the actual delivered voltage. If the impedance is very high (e.g., at low frequencies in standard electrodes), the voltage required to deliver that current will be very high. This can lead to clipping (e.g,. if the required voltage is 8 V, but the power supply is limited to 6 V). If the impedance is very low, the voltage required will be very low. If the noise is, for example, 10 mV peak-to-peak, at the delivered voltage is 10 mV, this will be obscured by the noise. However, filtering might be able to recover the desired voltage.

Second, impedance is affected by stray capacitance. There are many places where the stimulation signal is carried near other wires and conducting objects, after it has left the stimulation interface board. Along this path, a voltage or current-controlled pulse will wind up charging these other objects and wires (stray capacitance). Since the stimulation current and voltage are measured on the interface board, these stray capacitances will be included in the measured impedance. Therefore, what is truly being measured is the impedance of the electrode, and the cables leading to it. With short cables, this effect is negligible, especially when higher amplitude test currents or voltages are used. However, the effect can be large when using long cables and low amplitude test waves. **It is therefore recommended that you test a known impedance to estimate your error.** A good source of a known impedance is the MultiChannel Systems test MEA, which has a known resistance and capacitance in parallel. However, any custom-built resistor and capacitor in parallel will do.

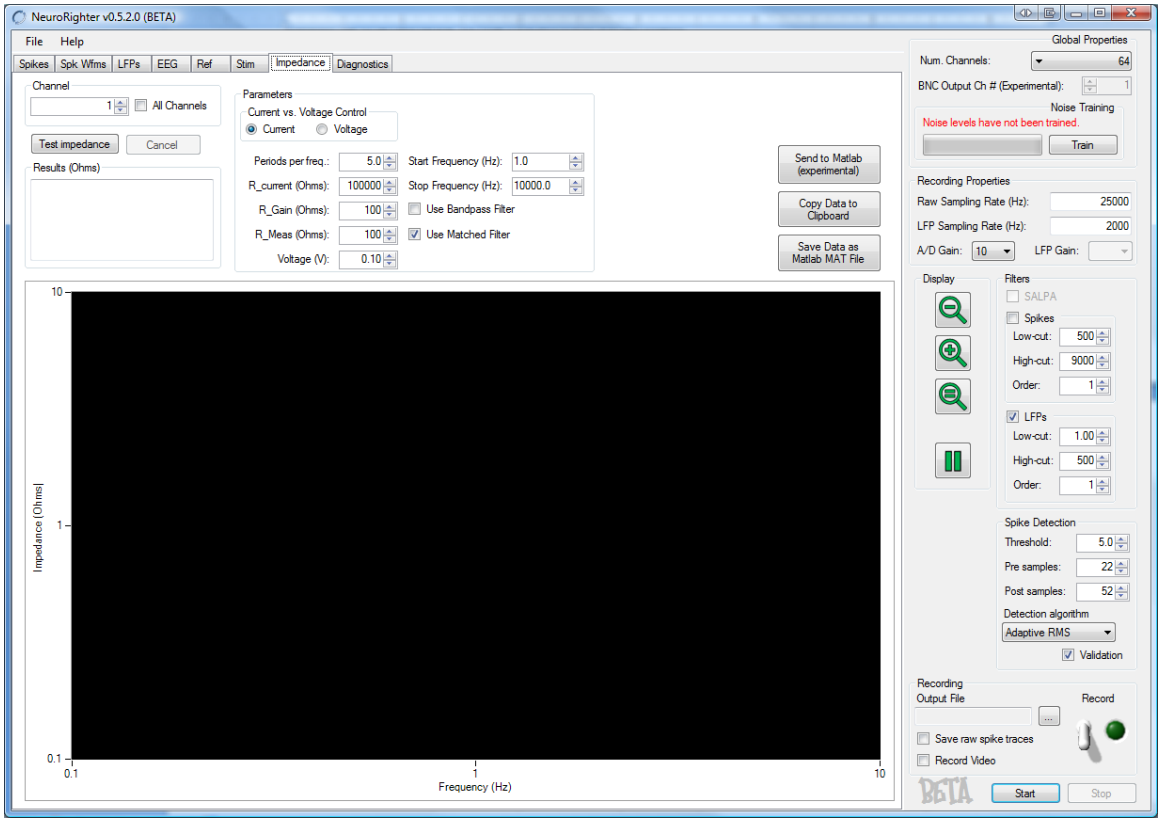

FIGURE C-14. Impedance tab.

Channel

Impedance measurements can be taken from a single channel, or all channels in sequence (by checking the “all channels” box).

Current vs. Voltage Control

Impedance measurements can be conducted by delivering current-controlled sine waves and measuring the delivered voltage, or by delivering voltage-controlled sine waves and measuring the delivered current. The amplitude of the sine wave is always specified as a voltage (since this is what the National Instruments D/A emits) but the voltage is converted to current through R_curr if the stimulation is current-controlled (see Stimulation Hardware Settings).

Periods per Frequency

Each sine wave is presented for the specified number of periods, to help estimate the average amplitude of the measured wave. However, to improve results, the minimum duration of any test wave is 100 ms.

R_curr

When measuring impedance with current-controlled stimulation, NeuroRighter requires the value of R_curr. Knowing this, the software can then calculate the delivered current, and use that to compute the measured impedance.

R_m and R_g

When measuring impedance with voltage-controlled stimulation, NeuroRighter requires the values of R_m and R_g. Knowing these, the software can calculate the gain of the current monitoring circuitry, and then use this to calculate the measured impedance.

Voltage

The amplitude of the delivered sine wave is specified here. If stimulation is current-controlled, this voltage determines the current, after accounting for the voltage-to-current conversion resistor.

Start and Stop Frequencies

The impedance spectrum is measured over the specified range of frequencies. The actual frequencies measured begin with the start frequency, and then every multiple of 1.5 thereafter, in a semi-logarithmic fashion. For example, if the start and stop frequencies are 1 and 10 Hz, the tested frequencies are 1, 1.5, 2.25, 3.375, 5.0625, and 7.5938. To test a single frequency, set the start and stop frequencies equal to each other (e.g., to

measure impedance at 1 kHz, set the start frequency to 1000 Hz and the stop frequency to 1000 Hz).

Filters

It is occasionally necessary to filter the measured signals to improve the measurement quality. This is especially true if the signals are present on a large background of noise. Two filters are available: a matched filter and a bandpass filter.

Matched Filter

The matched filter will convolve the measured signal with the original sine wave. This is the optimal matched filter assuming a Gaussian distribution of noise. This is our preferred method.

Bandpass filter

This bandpass filter is a 1-pole filter with -3 dB points at the ±0.25 * *f*, where *f* is the frequency of interest. [This tends to over-estimate the impedance in our experience.]

Diagnostics

The diagnostics section is provided to help verify that the recording equipment is amplifying with an appropriate bandpass filter and gain. This works nearly identical to impedance measurements. However, unlike impedance testing, the measured signals will be recorded by the recording headstage or preamplifier. All input sine waves should be voltage-controlled. With a known voltage-controlled sine wave of a know frequency, the measured signals from the headstage or preamplifier can be used to determine the system's gain at that frequency. When computed at multiple frequencies, the system's transfer function can be estimated.

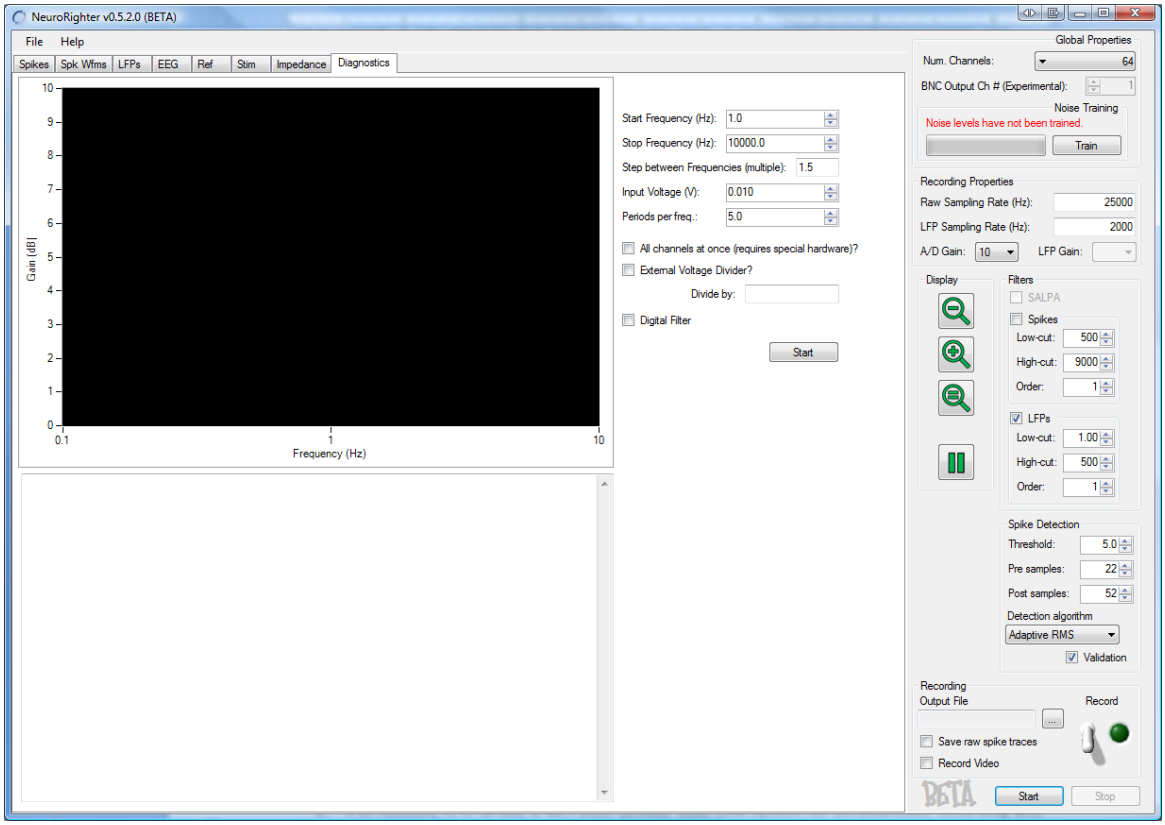

FIGURE C-15. Diagnostics tab.

Basic Features

These features are identical to those used for impedance measurements. Please refer to that section for more information.

Special Features

All channels at once

Selecting this requires a way to deliver stimulation to all channels simultaneously. This capability is not present with the normal stimulator headstages. In our case, we use a Plexon Headstage Test Unit, which provides a common signal to all electrodes.

External voltage divider

The National Instruments analog output, used to generate stimulation pulses and test waves, has a finite accuracy (16-bits with a range of ±5 V). Therefore, very small amplitude sine waves (e.g., 1 mV), will have poor resolution. To account for this, we often use an external voltage divider, to divide down a 1 V sine wave to something smaller (e.g., 100 μV). Entered the division factor will allow the software to automatically account for this.

Digital Filter

This filter is identical to the bandpass filter used in the impedance measurement section.

Appendix D

SCB-68 Quick Reference Labels

Use these figures to properly connect analog input channels, analog output channels, and digital input output channels. Each PCI-6259 or PCIe-6259 will connect to two SCB-68 breakout boxes, which is why there is a "connector 0" and "connector 1" reference sheet below. These sheets were taken from http://digital.ni.com/public.nsf/allkb/F011AD8B0F4BD35086257050006CBB70 on February 3, 2009.

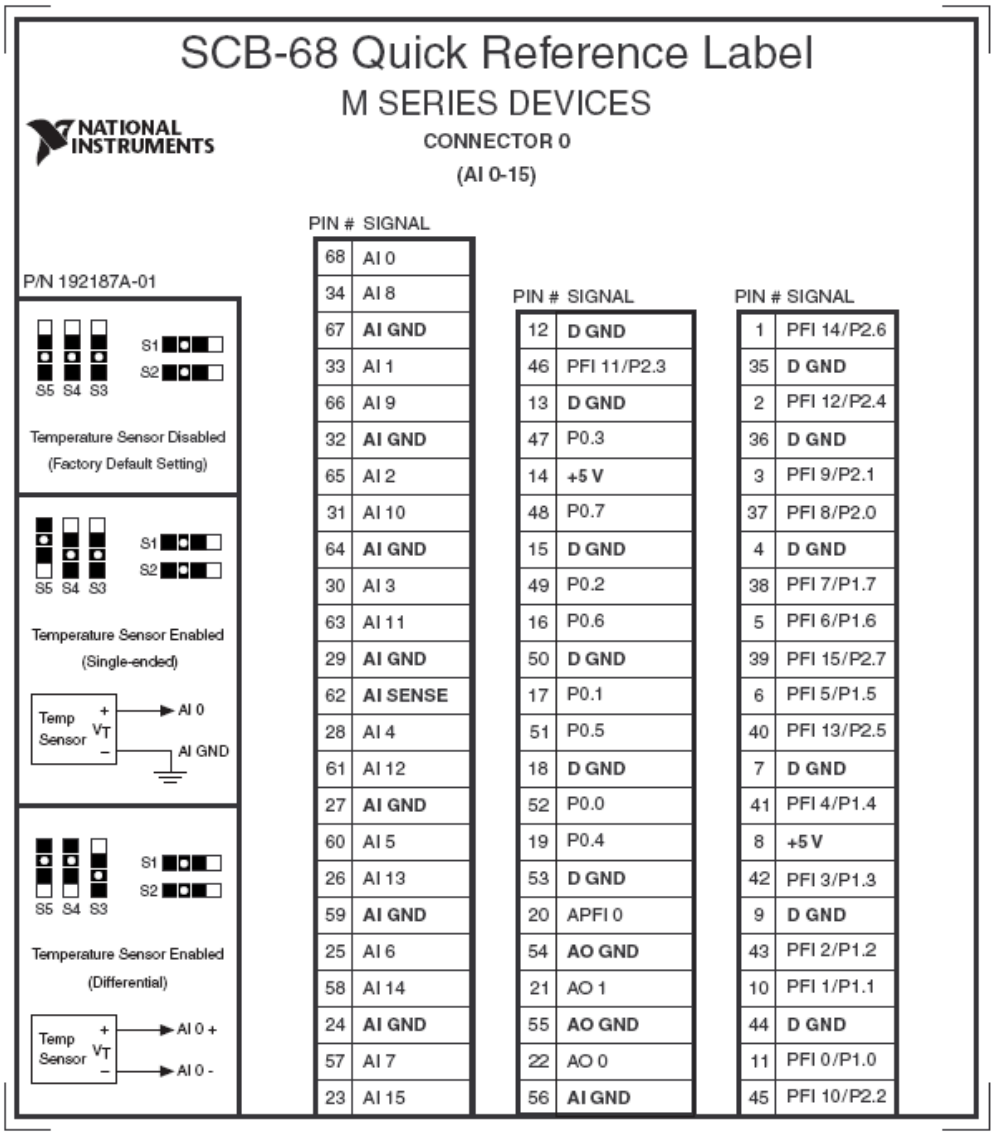

FIGURE D-1. Connector 0.

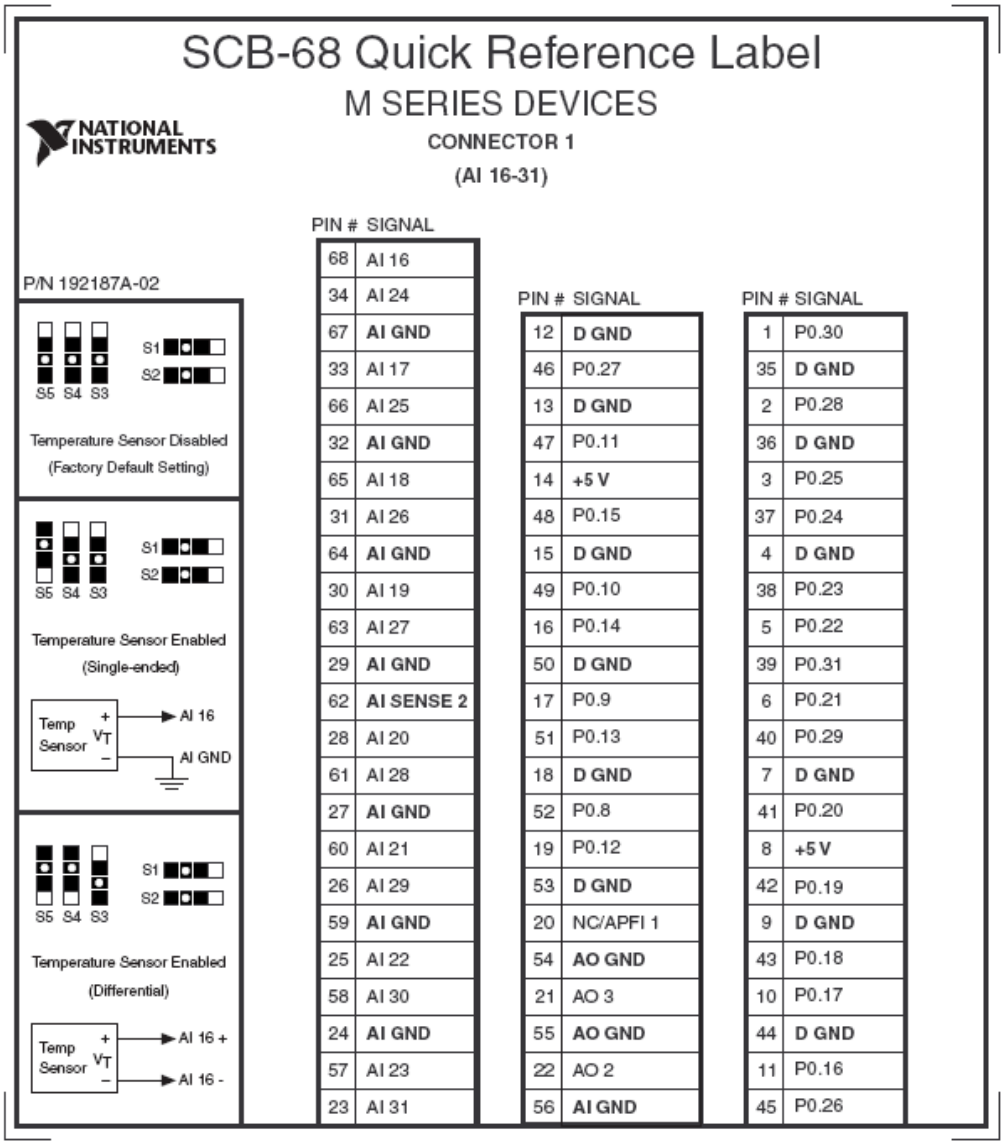

FIGURE D-2. Connector 1.

References

Abadir KM (2005) The Mean-Median-Mode Inequality: Counterexamples. Econometric Theory 21:477-482.

Abeles M (1991) Corticonics: neural circuits of the cerebral cortex. New York, NY: Cambridge University Press.

Abeles M, Gerstein GL (1988) Detecting spatiotemporal firing patterns among simultaneously recorded single neurons. J Neurophysiol 60:909-924.

Abeles M, Bergman H, Margalit E, Vaadia E (1993) Spatiotemporal firing patterns in the frontal-cortex of behaving monkeys. J Neurophysiol 70:1629-1638.

Aertsen A, Diesmann M, Gewaltig MO (1996) Propagation of synchronous spiking activity in feedforward neural networks. J Physiol Paris 90:243-247.

Andersen P (2007) The hippocampus book. Oxford; New York: Oxford University Press.

Andersen P, Bliss TV, Skrede KK (1971) Unit analysis of hippocampal polulation spikes. Exp Brain Res 13:208-221.

Arsiero M, Luscher HR, Giugliano M (2007) Real-time closed-loop electrophysiology: towards new frontiers in in vitro investigations in the neurosciences. Arch Ital Biol 145:193-209.

Avoli M (2001) Do interictal discharges promote or control seizures? Experimental evidence from an in vitro model of epileptiform discharge. Epilepsia 42 Suppl 3:2-4.

Babb TL, Carr E, Crandall PH (1973) Analysis of extracellular firing patterns of deep temporal lobe structures in man. Electroencephalogr Clin Neurophysiol 34:247-257.

Bak P (1996) How nature works: the science of self-organized criticality. New York, NY, USA: Copernicus.

Bak P, Tang C, Wiesenfeld K (1987) Self-organized criticality: An explanation of the 1/f noise. Phys Rev Lett 59:381-384.

Bakkum DJ, Chao ZC, Potter SM (2008a) Long-term activity-dependent plasticity of action potential propagation delay and amplitude in cortical networks. PLoS ONE 3:e2088.

Bakkum DJ, Chao ZC, Potter SM (2008b) Spatio-temporal electrical stimuli shape behavior of an embodied cortical network in a goal-directed learning task. Journal of Neural Engineering 5:310-323.

Banker G, Goslin K (1998) Culturing nerve cells, 2nd Edition. Cambridge, Mass.: MIT Press.

Barbarosie M, Avoli M (1997) CA3-Driven Hippocampal-Entorhinal Loop Controls Rather than Sustains In Vitro Limbic Seizures. J Neurosci 17:9308-9314.

Barsoukov E, Macdonald JR (2005) Impedance spectroscopy : theory, experiment, and applications, 2nd Edition. Hoboken, N.J.: Wiley-Interscience.

Bedard C, Kroger H, Destexhe A (2006) Does the 1/f frequency scaling of brain signals reflect self-organized critical states? Phys Rev Lett 97:118102.

Beggs JM, Plenz D (2003) Neuronal avalanches in neocortical circuits. J Neurosci 23:11167-11177.

Beggs JM, Plenz D (2004) Neuronal avalanches are diverse and precise activity patterns that are stable for many hours in cortical slice cultures. J Neurosci 24:5216-5229.

Benke TA, Swann J (2004) The tetanus toxin model of chronic epilepsy. Adv Exp Med Biol 548:226-238.

Berger TW, Glanzman D (2005) Toward replacement parts for the brain: implantable biomimetic electronics as neural prostheses. Cambridge, Mass.: MIT Press.

Berger TW, Ahuja A, Courellis SH, Deadwyler SA, Erinjippurath G, Gerhardt GA, Gholmieh G, Granacki JJ, Hampson R, Hsaio MC, LaCoss J, Marmarelis VZ,

Nasiatka P, Srinivasan V, Song D, Tanguay AR, Wills J (2005) Restoring lost cognitive function. IEEE Eng Med Biol Mag 24:30-44.

Bienenstock E (1996) On the dimensionality of cortical graphs. J Physiol Paris 90:251-256.

Bland JM, Altman DG (1995) Multiple significance tests: the Bonferroni method. BMJ (Clinical research ed 310:170.

Blum R, Ross J, Das S, Brown E, Deweerth S (2004) Models of stimulation artifacts applied to integrated circuit design. Conf Proc IEEE Eng Med Biol Soc 6:4075-4078.

Blum RA, Ross JD, Brown EA, DeWeerth SP (2007) An integrated system for simultaneous, multichannel neuronal stimulation and recording. IEEE Trans Circuits Syst I-Regul Pap 54:2608-2618.

Bontorin G, Renaud S, Garenne A, Alvado L, Le Masson G, Tomas J (2007) A Real-Time Closed-Loop Setup for Hybrid Neural Networks. In: Engineering in Medicine and Biology Society, 2007. EMBS 2007. 29th Annual International Conference of the IEEE, pp 3004-3007.

Bragin A, Wilson CL, Engel J, Jr. (2000) Chronic epileptogenesis requires development of a network of pathologically interconnected neuron clusters: a hypothesis. Epilepsia 41 Suppl 6:S144-152.

Bragin A, Engel J, Wilson CL, Fried I, Buzsáki G (1999) High-frequency oscillations in human brain. Hippocampus 9:137-142.

Bragin A, Wilson CL, Almajano J, Mody I, Engel J, Jr. (2004) High-frequency oscillations after status epilepticus: epileptogenesis and seizure genesis. Epilepsia 45:1017-1023.

Brinkmann BH, Bower MR, Stengel KA, Worrell GA, Stead M (2009) Large-scale electrophysiology: acquisition, compression, encryption, and storage of big data. J Neurosci Methods 180:185-192.

Brodie MJ, Shorvon SD, Canger R, Halasz P, Johannessen S, Thompson P, Wieser HG, Wolf P (1997) Commission on European Affairs: appropriate standards of epilepsy care across Europe.ILEA. Epilepsia 38:1245-1250.

Brown EA, Ross JD, Blum RA, Yoonkey N, Wheeler BC, DeWeerth SP (2008) Stimulus-artifact elimination in a multi-electrode system. IEEE Trans Biomed Circuit Syst 2:10-21.

Butovas S, Schwarz C (2003) Spatiotemporal effects of microstimulation in rat neocortex: a parametric study using multielectrode recordings. J Neurophysiol 90:3024-3039.

Buzsaki G (1986) Hippocampal sharp waves: Their origin and significance. Brain Research 398:242-252.

Buzsaki G (1989) Two-stage model of memory trace formation: A role for "noisy" brain states. Neuroscience 31:551-570.

Buzsaki G (2004) Large-scale recording of neuronal ensembles. Nat Neurosci 7:446-451.

Buzsáki G (2006) Rhythms of the brain. New York: Oxford University Press.

Chandra SS, Chandra K (2005) A comparison of Java and C#. J Comput Small Coll 20:238-254.

Chao ZC, Bakkum DJ, Potter SM (2008) Shaping embodied neural networks for adaptive goal-directed behavior. PLoS Comput Biol 4:e1000042.

Chao ZC, Bakkum DJ, Wagenaar DA, Potter SM (2005) Effects of random external background stimulation on network synaptic stability after tetanization: a modeling study. Neuroinformatics 3:263-280.

Cockerell OC, Johnson AL, Sander JW, Hart YM, Shorvon SD (1995) Remission of epilepsy: results from the National General Practice Study of Epilepsy. Lancet 346:140-144.

Cooke SF, Bliss TVP (2006) Plasticity in the human central nervous system. Brain 129:1659-1673.

Csicsvari J, Jamieson B, Wise KD, Buzsaki G (2003) Mechanisms of gamma oscillations in the hippocampus of the behaving rat. Neuron 37:311-322.

D'Arcangelo G, Panuccio G, Tancredi V, Avoli M (2005) Repetitive low-frequency stimulation reduces epileptiform synchronization in limbic neuronal networks. Neurobiol Dis 19:119-128.

Dan Y, Poo M-M (2006) Spike timing-dependent plasticity: from synapse to perception. Physiol Rev 86:1033-1048.

de Curtis M, Avanzini G (2001) Interictal spikes in focal epileptogenesis. Progress in Neurobiology 63:541-567.

Dichter MA (1978) Rat cortical neurons in cell culture: culture methods, cell morphology, electrophysiology, and synapse formation. Brain Res 149:279-293.

DiLorenzo DJ, Bronzino JD (2008) Neuroengineering. Boca Raton: CRC Press.

Donoho DL, Johnstone IM (1994) Ideal Spatial Adaptation by Wavelet Shrinkage. Biometrika 81:425-455.

Droge MH, Gross GW, Hightower MH, Czisny LE (1986) Multielectrode analysis of coordinated, multisite, rhythmic bursting in cultured CNS monolayer networks. J Neurosci 6:1583-1592.

Echlin FA, Peck D, Schmer C, Brown L (1959) The supersensitivity of chronically "isolated" cerebral cortex as a mechanism in focal epilepsy. Electroencephalography and Clinical Neurophysiology 11:697-722.

Engel J, Jr., Bragin A, Staba R, Mody I (2009) High-frequency oscillations: what is normal and what is not? Epilepsia 50:598-604.

Eytan D, Marom S (2006) Dynamics and effective topology underlying synchronization in networks of cortical neurons. J Neurosci 26:8465-8476.

Faraday M (1834) On Electrical Decomposition. Philosophical Transactions of the Royal Society.

Foffani G, Uzcategui YG, Gal B, Menendez de la Prida L (2007) Reduced spike-timing reliability correlates with the emergence of fast ripples in the rat epileptic hippocampus. Neuron 55:930-941.

Fountas KN, Smith JR (2007) A novel closed-loop stimulation system in the control of focal, medically refractory epilepsy. Acta Neurochir Suppl 97:357-362.

Fountas KN, Smith JR, Murro AM, Politsky J, Park YD, Jenkins PD (2005) Implantation of a closed-loop stimulation in the management of medically refractory focal epilepsy: a technical note. Stereotact Funct Neurosurg 83:153-158.

Frey U, Egert U, Heer F, Hafizovic S, Hierlemann A (2009) Microelectronic system for high-resolution mapping of extracellular electric fields applied to brain slices. Biosens Bioelectron 24:2191-2198.

Frostig RD, Frostig Z, Harper RM (1984) Information trains. The technique and its uses in spike train and network analysis, with examples taken from the nucleus parabrachialis medialis during sleep-waking states. Brain Res 322:67-74.

Gaito J (1980a) Gradient of interference by various frequencies on 60 Hz kindling behavior. Can J Neurol Sci 7:223-226.

Gaito J (1980b) The effect of variable duration one hertz interference on kindling. Can J Neurol Sci 7:59-64.

Gaito J, Nobrega JN, Gaito ST (1980) Interference effect of 3 Hz brain stimulation on kindling behavior induced by 60 Hz stimulation. Epilepsia 21:73-84.

Goaillard JM, Marder E (2006) Dynamic clamp analyses of cardiac, endocrine, and neural function. Physiology (Bethesda) 21:197-207.

Goddard GV (1967) Development of epileptic seizures through brain stimulation at low intensity. Nature 214:1020-1021.

Greenberg DS, Houweling AR, Kerr JND (2008) Population imaging of ongoing neuronal activity in the visual cortex of awake rats. Nat Neurosci 11:749-751.

Gross GW (1979) Simultaneous single unit recording in vitro with a photoetched laser deinsulated gold multimicroelectrode surface. IEEE Trans Biomed Eng 26:273-279.

Gross RE (2004) Deep brain stimulation in the treatment of neurological and psychiatric disease. Expert Rev Neurother 4:465-478.

Gross RE, Rolston JD (2008) The clinical utility of methods to determine spatial extent and volume of tissue activated by deep brain stimulation. Clinical Neurophysiology 119:1947-1950.

Gross RE, Krack P, Rodriguez-Oroz MC, Rezai AR, Benabid AL (2006) Electrophysiological mapping for the implantation of deep brain stimulators for Parkinson's disease and tremor. Mov Disord 21 Suppl 14:S259-283.

Gutig R, Sompolinsky H (2006) The tempotron: a neuron that learns spike timing-based decisions. Nat Neurosci 9:420-428.

Hammack SE, Mania I, Rainnie DG (2007) Differential Expression of Intrinsic Membrane Currents in Defined Cell Types of the Anterolateral Bed Nucleus of the Stria Terminalis. J Neurophysiol 98:638-656.

Hebb DO (1949) The organization of behavior: a neuropsychological theory. New York, NY: Wiley.

Heffer LF, Fallon JB (2008) A novel stimulus artifact removal technique for high-rate electrical stimulation. J Neurosci Methods 170:277-284.

Henze DA, Borhegyi Z, Csicsvari J, Mamiya A, Harris KD, Buzsaki G (2000) Intracellular features predicted by extracellular recordings in the hippocampus in vivo. J Neurophysiol 84:390-400.

Herrmann M, Hertz JA, Prugelbennett A (1995) Analysis of synfire chains. Network 6:403-414.

Hille B (2001) Ion channels of excitable membranes, 3rd Edition. Sunderland, Mass.: Sinauer.

Histed MH, Bonin V, Reid RC (2009) Direct activation of sparse, distributed populations of cortical neurons by electrical microstimulation. Neuron 63:508-522.

Horowitz P, Hill W (1989) The art of electronics, 2nd Edition. New York: Cambridge University Press.

Houweling AR, Bazhenov M, Timofeev I, Steriade M, Sejnowski TJ (2005) Homeostatic synaptic plasticity can explain post-traumatic epileptogenesis in chronically isolated neocortex. Cereb Cortex 15:834-845.

Huber PJ, Ronchetti E (2009) Robust statistics, 2nd Edition. Hoboken, N.J.: Wiley.

Hufnagel A, Dumpelmann M, Zentner J, Schijns O, Elger CE (2000) Clinical relevance of quantified intracranial interictal spike activity in presurgical evaluation of epilepsy. Epilepsia 41:467-478.

Ikegaya Y, Aaron G, Cossart R, Aronov D, Lampl I, Ferster D, Yuste R (2004) Synfire chains and cortical songs: temporal modules of cortical activity. Science 304:559-564.

Imfeld K, Neukom S, Maccione A, Bornat Y, Martinoia S, Farine PA, Koudelka-Hep M, Berdondini L (2008) Large-scale, high-resolution data acquisition system for extracellular recording of electrophysiological activity. IEEE Trans Biomed Eng 55:2064-2073.

Iremonger KJ, Anderson TR, Hu B, Kiss ZH (2006) Cellular mechanisms preventing sustained activation of cortex during subcortical high-frequency stimulation. J Neurophysiol 96:613-621.

Izhikevich EM (2006) Polychronization: computation with spikes. Neural Comput 18:245-282.

Izhikevich EM, Gally JA, Edelman GM (2004) Spike-timing dynamics of neuronal groups. Cereb Cortex 14:933-944.

Jackson A, Mavoori J, Fetz EE (2006) Long-term motor cortex plasticity induced by an electronic neural implant. Nature 444:56-60.

Jacobs J, LeVan P, Chander R, Hall J, Dubeau F, Gotman J (2008) Interictal high-frequency oscillations (80-500 Hz) are an indicator of seizure onset areas independent of spikes in the human epileptic brain. Epilepsia 49:1893-1907.

Jahanshahi A, Mirnajafi-Zadeh J, Javan M, Mohammad-Zadeh M, Rohani R (2009) The antiepileptogenic effect of electrical stimulation at different low frequencies is accompanied with change in adenosine receptors gene expression in rats. Epilepsia.

Jefferys JG, Walker MC (2005) Tetanus Toxin Model of Focal Epilepsy. In: Models of Seizures and Epilepsy (Pitkanen A, Schwartzkroin PA, Moshé SL, eds). Burlington, MA: Elsevier.

Jefferys JG, Borck C, Mellanby J (1995) Chronic focal epilepsy induced by intracerebral tetanus toxin. Ital J Neurol Sci 16:27-32.

Jefferys JG, Evans BJ, Hughes SA, Williams SF (1992) Neuropathology of the chronic epileptic syndrome induced by intrahippocampal tetanus toxin in rat: preservation of pyramidal cells and incidence of dark cells. Neuropathol Appl Neurobiol 18:53-70.

Jimbo Y, Kasai N, Torimitsu K, Tateno T, Robinson HPC (2003) A system for MEA-based multisite stimulation. Biomedical Engineering, IEEE Transactions on 50:241-248.

Jobst B (2009) Brain stimulation for surgical epilepsy. Epilepsy Res.

Kandel ER, Spencer WA, Brinley FJ, Jr. (1961) Electrophysiology of hippocampal neurons. I. Sequential invasion and synaptic organization. J Neurophysiol 24:225-242.

Kandel ER, Schwartz JH, Jessell TM (2000) Principles of neural science, 4th Edition. New York: McGraw-Hill, Health Professions Division.

Kerkut GA, Wheal HV (1981) Electrophysiology of isolated mammalian CNS preparations. London ; New York: Academic Press.

Kerr JND, Denk W (2008) Imaging in vivo: watching the brain in action. Nat Rev Neurosci 9:195-205.

Kipke DR, Shain W, Buzsaki G, Fetz E, Henderson JM, Hetke JF, Schalk G (2008) Advanced Neurotechnologies for Chronic Neural Interfaces: New Horizons and Clinical Opportunities. J Neurosci 28:11830-11838.

Kloosterman F, Davidson TJ, Gomperts SN, Layton SP, Hale G, Nguyen DP, Wilson MA (2009) Micro-drive array for chronic in vivo recording: drive fabrication. J Vis Exp.

Kwan P, Brodie MJ (2000) Early identification of refractory epilepsy. The New England journal of medicine 342:314-319.

Lapish CC, Kroener S, Durstewitz D, Lavin A, Seamans JK (2007) The ability of the mesocortical dopamine system to operate in distinct temporal modes. Psychopharmacology (Berl) 191:609-625.

Lee AK, Epsztein J, Brecht M (2009) Head-anchored whole-cell recordings in freely moving rats. Nat Protoc 4:385-392.

Lempka SF, Miocinovic S, Johnson MD, Vitek JL, McIntyre CC (2009) In vivo impedance spectroscopy of deep brain stimulation electrodes. J Neural Eng 6:46001.

Lesser RP, Kim SH, Beyderman L, Miglioretti DL, Webber WR, Bare M, Cysyk B, Krauss G, Gordon B (1999) Brief bursts of pulse stimulation terminate afterdischarges caused by cortical stimulation. Neurology 53:2073-2081.

Lewicki MS (1998) A review of methods for spike sorting: the detection and classification of neural action potentials. Network 9:R53-78.

Liberty J, Xie D (2008) Programming C# 3.0, 5th Edition. Sebastopol, CA: O'Reilly.

Loddenkemper T, Pan A, Neme S, Baker KB, Rezai AR, Dinner DS, Montgomery EB, Jr., Luders HO (2001) Deep brain stimulation in epilepsy. J Clin Neurophysiol 18:514-532.

Luders H, ed (2004) Deep Brain Stimulation and Epilepsy. Independence, KY: Taylor & Francis.

Ludwig KA, Miriani RM, Langhals NB, Joseph MD, Anderson DJ, Kipke DR (2009) Using a Common Average Reference to Improve Cortical Neuron Recordings From Microelectrode Arrays. J Neurophysiol 101:1679-1689.

MacLean JN, Watson BO, Aaron GB, Yuste R (2005) Internal dynamics determine the cortical response to thalamic stimulation. Neuron 48:811-823.

Madhavan R, Chao ZC, Potter SM (submitted) Plasticity of recurring spatiotemporal activity patterns in dissociated cortical networks.

Mavoori J, Jackson A, Diorio C, Fetz E (2005) An autonomous implantable computer for neural recording and stimulation in unrestrained primates. Journal of Neuroscience Methods 148:71-77.

Mellanby J, George G, Robinson A, Thompson P (1977) Epileptiform syndrome in rats produced by injecting tetanus toxin into the hippocampus. J Neurol Neurosurg Psychiatry 40:404-414.

Merrill DR, Tresco PA (2005) Impedance characterization of microarray recording electrodes in vitro. Biomedical Engineering, IEEE Transactions on 52:1960-1965.

Merrill DR, Bikson M, Jefferys JGR (2005) Electrical stimulation of excitable tissue: design of efficacious and safe protocols. Journal of Neuroscience Methods 141:171-198.

Mitra P, Bokil H (2008) Observed brain dynamics. New York: Oxford University Press.

Mitzdorf U (1985) Current source-density method and application in cat cerebral cortex: investigation of evoked potentials and EEG phenomena. Physiol Rev 65:37-100.

Morrell M (2006) Brain stimulation for epilepsy: can scheduled or responsive neurostimulation stop seizures? Curr Opin Neurol 19:164-168.

Mountcastle VB (1998) Perceptual neuroscience: the cerebral cortex. Cambridge, Mass.: Harvard University Press.

Muller HM, Kenny EE, Sternberg PW (2004) Textpresso: an ontology-based information retrieval and extraction system for biological literature. PLoS biology 2:e309.

Nadasdy Z, Hirase H, Czurko A, Csicsvari J, Buzsaki G (1999) Replay and time compression of recurring spike sequences in the hippocampus. J Neurosci 19:9497-9507.

Nguyen DP, Layton SP, Hale G, Gomperts SN, Davidson TJ, Kloosterman F, Wilson MA (2009) Micro-drive array for chronic in vivo recording: tetrode assembly. J Vis Exp.

Nicolelis MAL (2008) Methods for neural ensemble recordings, 2nd Edition. Boca Raton: CRC Press.

Novellino A, D'Angelo P, Cozzi L, Chiappalone M, Sanguineti V, Martinoia S (2007) Connecting neurons to a mobile robot: an in vitro bidirectional neural interface. Comput Intell Neurosci:12725.

Nunez PL (1981) Electric fields of the brain : the neurophysics of EEG. New York: Oxford University Press.

Nunez PL, Srinivasan R (2006) Electric fields of the brain : the neurophysics of EEG, 2nd Edition. New York: Oxford University Press.

O'Doherty JE, Lebedev MA, Hanson TL, Fitzsimmons NA, Nicolelis MA (2009) A brain-machine interface instructed by direct intracortical microstimulation. Front Integr Neurosci 3:20.

Olsson RH, 3rd, Buhl DL, Sirota AM, Buzsaki G, Wise KD (2005) Band-tunable and multiplexed integrated circuits for simultaneous recording and stimulation with microelectrode arrays. IEEE Trans Biomed Eng 52:1303-1311.

Penfield W, Jasper HH (1954) Epilepsy and the functional anatomy of the human brain, [1st Edition. Boston: Little.

Pine J (1980) Recording action potentials from cultured neurons with extracellular microcircuit electrodes. J Neurosci Methods 2:19-31.

Pitkanen A, schwartzkroin PA, Moshé SL (2006) Models of Seizures and Epilepsy. Burlington, MA: Elsevier Academic Press.

Potter SM (1996) Vital imaging: two photons are better than one. Curr Biol 6:1595-1598.

Potter SM (2005) Two-photon microscopy for 4D imaging of living neurons. In: Imaging in Neuroscience and Development: A Laboratory Manual, 2nd Edition, Second Edition (Yuste R, Konnerth A, eds), pp 59-70. Woodbury, NY: Cold Spring Harbor Laboratory Press.

Potter SM, DeMarse TB (2001) A new approach to neural cell culture for long-term studies. J Neurosci Methods 110:17-24.

Potter SM, Wagenaar DA, DeMarse TB (2006) Closing the Loop: Stimulation Feedback Systems for Embodied MEA Cultures. In: Advances in Network Electrophysiology Using Multi-Electrode Arrays (Taketani M, Baudry M, eds). New York: Springer.

Prince DA, Tseng GF (1993) Epileptogenesis in chronically injured cortex: in vitro studies. J Neurophysiol 69:1276-1291.

Quiroga RQ, Nadasdy Z, Ben-Shaul Y (2004) Unsupervised spike detection and sorting with wavelets and superparamagnetic clustering. Neural Comput 16:1661-1687.

Rampp S, Stefan H (2006) Fast activity as a surrogate marker of epileptic network function? Clin Neurophysiol:2111-2117.

Raymond ES (2001) The cathedral and the bazaar: musings on Linux and Open Source by an accidental revolutionary, Rev. Edition. Cambridge, Mass.: O'Reilly.

Reed WJ, Hughes BD (2002) From gene families and genera to incomes and internet file sizes: why power laws are so common in nature. Phys Rev E Stat Nonlin Soft Matter Phys 66:067103.

Robinson HPC, Kawahara M, Jimbo Y, Torimitsu K, Kuroda Y, Kawana A (1993) Periodic synchronized bursting and intracellular calcium transients elicited by low magnesium in cultured cortical-neurons. J Neurophysiol 70:1606-1616.

Rolston JD, Wagenaar DA, Potter SM (2007a) Precisely timed spatiotemporal patterns of neural activity in dissociated cortical cultures. Neuroscience 148:294-303.

Rolston JD, Gross RE, Potter SM (2007b) An inexpensive closed-loop, all-channel stimulator for in vivo microelectrode arrays. In: 37th Annual Meeting of the Society for Neuroscience. San Diego, CA.

Rolston JD, Gross RE, Potter SM (2008) Low-Cost System for Simultaneous Recording and Stimulation with Multi-microelectrode Arrays. In: 6th International Meeting

on Substrate-Integrated Micro Electrode Arrays (SIMEA), pp 341-342. Reutlingen, Germany: BIOPRO Baden-Württemberg GmbH.

Rolston JD, Gross RE, Potter SM (2009a) Common Median Referencing for Improved Action Potential Detection with Multielectrode Arrays. In: 31st Annual International Conference of the IEEE Engineering in Medicine and Biology Society. Minneapolis, MN.

Rolston JD, Gross RE, Potter SM (2009b) A low-cost multielectrode system for data acquisition enabling real-time closed-loop processing with rapid recovery from stimulation artifacts. Frontiers in Neuroengineering 2:12.

Rosenow F, Luders H (2001) Presurgical evaluation of epilepsy. Brain 124:1683-1700.

Ross JD, O'Connor SM, Blum RA, Brown EA, DeWeerth SP (2004) Multielectrode impedance tuning: reducing noise and improving stimulation efficacy. Conf Proc IEEE Eng Med Biol Soc 6:4115-4117.

Roux E, Borrel A (1898) Tétanos cérébral et immunité contre le tétanos. Ann Inst Pasteur 4:225-239.

Santhanam G, Linderman MD, Gilja V, Afshar A, Ryu SI, Meng TH, Shenoy KV (2007) HermesB: a continuous neural recording system for freely behaving primates. IEEE Trans Biomed Eng 54:2037-2050.

Segev R, Baruchi I, Hulata E, Ben-Jacob E (2004) Hidden neuronal correlations in cultured networks. Phys Rev Lett 92:118102.

Sodagar AM, Wise KD, Najafi K (2007) A fully integrated mixed-signal neural processor for implantable multichannel cortical recording. IEEE Trans Biomed Eng 54:1075-1088.

Stark E, Abeles M (2007) Predicting movement from multiunit activity. J Neurosci 27:8387-8394.

Steriade M (2001) The intact and sliced brain. Cambridge, Mass.: MIT Press.

Steriade M, Timofeev I (2003) Neuronal Plasticity in Thalamocortical Networks during Sleep and Waking Oscillations. Neuron 37:563-576.

Steriade M, Nunez A, Amzica F (1993) A novel slow (< 1 Hz) oscillation of neocortical neurons in vivo: depolarizing and hyperpolarizing components. J Neurosci 13:3252-3265.

Sun FT, Morrell MJ, Wharen Jr RE (2008) Responsive Cortical Stimulation for the Treatment of Epilepsy. Neurotherapeutics 5:68-74.

Suner S, Fellows MR, Vargas-Irwin C, Nakata GK, Donoghue JP (2005) Reliability of signals from a chronically implanted, silicon-based electrode array in non-human primate primary motor cortex. IEEE Trans Neural Syst Rehabil Eng 13:524-541.

Taketani M, Baudry M (2006a) Advances in network electrophysiology: using multiple-electrode arrays. New York, NY: Springer.

Taketani M, Baudry M (2006b) Advances in network electrophysiology: using multi-electrode arrays. New York, NY: Springer.

Theodore WH (2005) Brain stimulation for epilepsy. Nat Clin Pract Neurol 1:64-65.

Tukey JW (1977) Exploratory data analysis. Reading, Mass.: Addison-Wesley Pub. Co.

Turrigiano GG (1999) Homeostatic plasticity in neuronal networks: the more things change, the more they stay the same. Trends Neurosci 22:221-227.

Urrestarazu E, Jirsch JD, LeVan P, Hall J (2006) High-Frequency Intracerebral EEG Activity (100-500 Hz) Following Interictal Spikes. Epilepsia 47:1465-1476.

Venkatraman S, Elkabany K, Long JD, Yao Y, Carmena JM (2009) A System for Neural Recording and Closed-Loop Intracortical Microstimulation in Awake Rodents. Biomedical Engineering, IEEE Transactions on 56:15-22.

Vogels TP, Rajan K, Abbott LF (2005) Neural network dynamics. Annu Rev Neurosci 28:357-376.

W. R. van Zwet (1979) Mean, median, mode II. Statistica Neerlandica 33:1-5.

Wagenaar DA, Potter SM (2002) Real-time multi-channel stimulus artifact suppression by local curve fitting. J Neurosci Methods 120:113-120.

Wagenaar DA, Potter SM (2004) A versatile all-channel stimulator for electrode arrays, with real-time control. J Neural Eng 1:39-45.

Wagenaar DA, Pine J, Potter SM (2004) Effective parameters for stimulation of dissociated cultures using multi-electrode arrays. J Neurosci Methods 138:27-37.

Wagenaar DA, DeMarse TB, Potter SM (2005a) MeaBench: A toolset for multielectrode data acquisition and on-line analysis In: IEEE EMBS Conference on Neural Engineering, pp 518-521. Arlington, VA: IEEE.

Wagenaar DA, Nadasdy Z, Potter SM (2006a) Persistent dynamic attractors in activity patterns of cultured neuronal networks. Phys Rev E Stat Nonlin Soft Matter Phys 73:051907-051908.

Wagenaar DA, Pine J, Potter SM (2006b) An extremely rich repertoire of bursting patterns during the development of cortical cultures. BMC Neurosci 7:11.

Wagenaar DA, Madhavan R, Pine J, Potter SM (2005b) Controlling bursting in cortical cultures with closed-loop multi-electrode stimulation. J Neurosci 25:680-688.

Wiener N (1948) Cybernetics. New York,: J. Wiley.

Wilkens L (2003) The joy of teaching with C#. J Comput Small Coll 19:254-264.

Williams JC, Hippensteel JA, Dilgen J, Shain W, Kipke DR (2007) Complex impedance spectroscopy for monitoring tissue responses to inserted neural implants. Journal of Neural Engineering 4:410-423.

Worrell GA, Parish L, Cranstoun SD, Jonas R, Baltuch G, Litt B (2004) High-frequency oscillations and seizure generation in neocortical epilepsy. Brain 127:1496-1506.

Worrell GA, Gardner AB, Stead SM, Hu S, Goerss S, Cascino GJ, Meyer FB, Marsh R, Litt B (2008) High-frequency oscillations in human temporal lobe: simultaneous microwire and clinical macroelectrode recordings. Brain 131:928-937.

Wyler AR, Ojemann GA, Ward AA, Jr. (1982) Neurons in human epileptic cortex: correlation between unit and EEG activity. Ann Neurol 11:301-308.

Xu J, Clancy CE (2008) Ionic mechanisms of endogenous bursting in CA3 hippocampal pyramidal neurons: a model study. PLoS ONE 3:e2056.

Ye X, Wang P, Liu J, Zhang S, Jiang J, Wang Q, Chen W, Zheng X (2008) A portable telemetry system for brain stimulation and neuronal activity recording in freely behaving small animals. Journal of Neuroscience Methods 174:186-193.

Zhang F, Aravanis AM, Adamantidis A, de Lecea L, Deisseroth K (2007) Circuit-breakers: optical technologies for probing neural signals and systems. Nat Rev Neurosci 8:577-581.